Fatigue behaviour of Inconel 625 produced by Directed Energy Deposition

Duarte de Araújo Maciel

Dissertation submitted to
Faculty of Engineering of the University of Porto
for the degree of

Masters in Mechanical Engineering

Advisor:
Prof. Dr. Abílio de Jesus

Co-advisors:
Eng. Miguel Figueiredo
MSc. Felipe Fiorentin
MSc. Jorge Gil

Department of Mechanical Engineering
Faculty of Engineering of the University of Porto

June 28th, Porto, 2021

The work presented in this dissertation was performed at
Advanced Manufacturing Processes Unit (UTAF)
Institute of Science and Innovation in Mechanical
and Industrial Engineering (INEGI)
Porto, Portugal.

Duarte de Araújo Maciel
E-mail: duarma@live.com.pt

Instituto de Ciência e Inovação em Engenharia Mecânica
e Engenharia Industrial
Unidade de Tecnologias Avançadas de Fabrico
Rua Dr. Roberto Frias s/n
4200-465 Porto
Portugal

Abstract

Additive manufacturing has outgrown its initial purpose of building prototypes for product development. Nowadays, it is frequently used for the production of fully functional parts, with complex geometries for many demanding industries, which require the performance of extensive research in characterisation of the material and their production process. Fatigue is one of the most common mechanical types of failure, due to the fact that components are frequently subjected to cyclic loading during their service life.

The main goal of this dissertation is to characterise the fatigue behaviour of the Nickel-based superalloy Inconel 625 produced by Directed Energy Deposition. In order to accomplish the goal, four point bending fatigue tests were performed with different load levels to obtain a S-N curve. The production process of the specimen was developed and accompanied from the beginning, starting from the CAD design to the process parameters parametrisation and specimen production by Directed Energy Deposition. Fatigue tests were carried out using miniature specimens to reduce monetary costs. The machine utilised was not prepared to run tests on miniature specimen, so a gripping mechanism was developed and validated through the usage of strain gauges. Moreover, the three-point bending machine was modified to run four-point bending tests and new load cells were added.

A finite element model was created in Abaqus, firstly to validate the gripping mechanism and then to establish comparisons between the experimental and numerical values. A convergence study was carried out and the influence of some input variables was tested to better grasp the behaviour of the gripping mechanism during testing. The numerical model was able to replicate the experimental setup with some precision.

A metallographic analysis of the material was performed through optical observation with the intent of evaluating microstructural features, porosity levels and defects. The fatigue fracture surface was also analysed. Moreover, hardness and surface roughness measurements were made.

In addition, tensile tests were performed, coupled with digital image correlation techniques to measure strain during the elastic and plastic regimes, in order to characterise the material's behaviour.

Finally, a fatigue life prediction was made based on hardness, resorting to analytical models proposed for steels. The S-N curve obtained experimentally was compared to curves from the reviewed literature. The material produced presented a fatigue behaviour in line with those in the reviewed literature, while the other measured properties were similar to the values obtained by other authors.

Keywords: Metallic Additive Manufacturing, Directed Energy Deposition, Inconel 625, Fatigue Behaviour, Miniature Specimen, Finite Element Method, Four-point Bending

Resumo

O fabrico aditivo superou o seu objetivo inicial de produção de protótipos no desenvolvimento de produto. Atualmente, é frequentemente usado na produção de peças funcionais, com geometrias complexas para várias indústrias de precisão, que exigem a realização de extensa pesquisa na caracterização de materiais e do seu processo produtivo. A fadiga é um dos tipos mais comuns de falha mecânica, devido ao facto dos componentes serem solicitados com cargas cíclicas durante a sua vida em serviço.

O objetivo principal desta dissertação é a caracterização do comportamento à fadiga da superliga de Níquel, Inconel 625, produzido por *Directed Energy Deposition*. De modo a alcançar tal objetivo, ensaios de fadiga de flexão em quatro pontos foram realizados com diferentes níveis de carga, com vista à obtenção de uma curva S-N. O processo produtivo dos provetes foi desenvolvido e acompanhado desde o início, começando pelo desenho CAD até à otimização dos parâmetros do processo de fabrico e à produção dos provetes por *Directed Energy Deposition*. Os testes à fadiga foram realizados com provetes miniatura de modo a reduzir os custos monetários. A máquina utilizada não estava preparada para realizar testes em provetes miniatura, por isso foram projetadas umas amarras e, posteriormente, validadas com recurso à extensometria. Além disso, a máquina foi adaptada para realizar testes de flexão em quatro pontos, ao invés de flexão em três pontos, e nela foram colocadas células de carga novas.

Foi criado um modelo de elementos finitos em Abaqus, primeiramente para validar as amarras projetadas e, posteriormente, para realizar comparações entre os valores experimentais e os numéricos. Foi feito um estudo de convergência e a influência de algumas variáveis de entrada foi testada para melhor compreender o comportamento das amarras durante os testes. O modelo numérico foi capaz de replicar o modelo experimental com alguma precisão.

Foi realizada uma análise metalográfica através de observação por microscópico ótico com o intuito de avaliar a microestrutura, níveis de porosidade e defeitos. A superfície de fratura de fadiga foi, também, analisada. Adicionalmente, foram efetuadas medições de dureza e de rugosidade superfícial.

Foram realizados ensaios de tração, aliados à técnica de correlação digital de imagem para medir as deformações durante o regime elástico e plástico, de modo a caracterizar o comportamento do material.

Finalmente, foi executada uma previsão de vida à fadiga baseada nos valores de dureza, recorrendo a modelos analíticos propostos para aços. A curva tensão-vida obtida experimentalmente foi comparada com curvas existentes na literatura consultada. O material produzido apresentou uma vida à fadiga semelhante aos valores encontrados na literatura, enquanto que as outras propriedades mecânicas medidas estão de acordo com os valores apresentados por outros autores.

Palavras-chave: Fabrico Aditivo Metálico, Directed Energy Deposition, Inconel 625, Comportamento à Fadiga, Provetes Miniatura, Método dos Elementos Finitos, Flexão em Quatro Pontos

To my parents

'I would rather have questions that can't be answered than answers that can't be questioned.'

Richard P. Feynman

Acknowledgements

It took an immense amount of work, time and resilience, but this thesis would not be possible without the fundamental contribution of my family, friends and coworkers. I would like to express my deep gratitude:

To Professor Dr. Abílio de Jesus, whose expertise was crucial in formulating the work's methodology and timely steered me into the right direction whenever it was needed;

To FCT, whose support towards the Add.Strength project allowed this thesis to exist;

To Engineer Felipe Fiorentin, who helped me in every step of the way, often placing his work after mine. His time, patience and knowledge were essential to the success of this project;

To Engineer Jorge Wolfs, whose attention to detail, valuable input and daily support were always welcomed;

To Engineer Miguel Figueiredo and Engineer Rui Silva, who were always prompt and willing to help in the experimental tests. Their critical opinion made me questioning and rethink;

To LET, for all the support during all the experimental procedures;

To all INEGI collaborators, who welcomed me and made me feel included;

To Mr. Domingos Carvalho for machining the specimen and being helpful when time was limited;

To Armanda Teixeira and Emilia Soares for the specimen preparation and contribution;

To my parents, whose unconditional love raised me up when I was weary. They always gave me the strengths to pursue my dreams and made me the man I am today;

To my brother, who I had the pleasure to grow up with. The moments we shared together will be kept forever;

To Catarina Oliveira, whose continuous support and patience will not be forgotten, as we keep learning from each other;

To all my friends, who accompanied me during my journey and with whom I created so many memories.

To all of you, thank you.

Duarte de Araújo Maciel

Institutional acknowledgements

The Add.Strength project (Reference PTDC/EME-EME/31307/2017) entitled "Enhanced Mechanical Properties in Additive Manufactured Components" funded by the Programa Operacional Competitividade e Internacionalização, and Programa Operacional Regional de Lisboa funded by FEDER and National Funds (FCT) is acknowledged. The BIC scholarship funded by the Add.Strength project is also acknowledged.

The MAMTool project (Reference PTDC/EME-EME/31895/2017) entitled "Machinability of Additive Manufactured Parts for Tooling Industry" funded by the Programa Operacional Competitividade e Internacionalização, and Programa Operacional Regional de Lisboa funded by FEDER and National Funds (FCT) is acknowledged.

The ADDing project (Reference POCI-01-0145-FEDER-030490) entitled "Multi-scale Modelling of ADDitive Manufacturing by Direct Energy Deposition of Metallic Powders" funded by the Programa Operacional Competitividade e Internacionalização, and Programa Operacional Regional de Lisboa funded by FEDER and National Funds (FCT) is acknowledged.

The GCYCLEFAT project (Reference PTDC/EME-EME/7678/2021) entitled "Gigacycle fatigue behaviour of engineering metallic alloys" funded by National Funds (FCT) is acknowledged.

Contents

List of Figures

List of Tables

Abbreviations

AEM Analytical Electron Microscopy xxiii, 63

AM Additive Manufacturing xv, 3, 4, 5, 6, 7, 9, 10, 15, 21, 28, 29, 32, 33, 34, 36, 37, 38, 39, 55, 68, 70, 73, 74, 75, 77, 78, 79, 80, 81, 87, 94, 100, 101, 191

ASTM American Society for Testing and Materials 104

BCT Body-centered Tetragonal 67

CAD Computer Aided Design 4, 95

CCT Continuous Cooling Transformation 142, 143

CNC Computer Numerically Controlled 6

CT Compact Tension 137, 138

CW Continuous Wave 11

DC Direct Current 100

DED Directed Energy Deposition xv, xvii, xviii, xxiii, 1, 3, 4, 7, 8, 9, 10, 11, 13, 14, 15, 16, 17, 18, 20, 21, 22, 24, 25, 28, 29, 32, 34, 38, 39, 55, 70, 85, 86, 90, 92, 93, 95, 96, 98, 120, 124, 130, 131, 133, 139, 142, 144, 162, 163, 173, 189

DIC Digital Image Correlation 2, 105, 146, 147, 149, 150, 190

DMD Direct Metal Deposition 9

EBM Electron Beam Melting 7

EDM Electrical Discharge Machining 38

FCC Face Centered Cubic 67

FEA Finite Element Analysis 2

FEM Finite Element Method 109, 111, 127, 186, 190

FEUP Faculty of Engineering, University of Porto 101, 106

HAZ Heat Affected Zone xv, xix, 22, 23, 25, 36, 131, 132, 134, 135, 142, 143, 144

HCP Hexagonal Close Packed 63

HIP Hot Isostatic Pressing 7, 10, 39, 101

INEGI Institute for Science and Innovation in Mechanical and Industrial Engineering 1, 86, 90, 98, 100, 103, 122

L-DED Laser Based Directed Energy Deposition 73

LEFM Linear Elastic Fracture Mechanics 48, 49

LENS Laser Engineered Net Shaping 9

LET Laboratório de Ensaios Tecnológicos 101, 106

L-PBF Laser Powder Bed Fusion xvii, 7, 80, 81

LMD Laser Metal Deposition xvii, 9, 70, 71, 74, 75, 76, 77, 78, 144

MAM Metal Additive Manufacturing 1, 7, 85

MVC Microvoid Coalescence 82

OES Optical Emission Spectroscopy 98, 128

PBF Powder Bed Fusion xv, 7, 10, 28, 29, 38, 39, 55

REP Rotating Electrode Process 27

SEM Scanning Electron Microscopy xvii, 30, 70, 71, 74, 75, 76, 122, 190

SLM Selective Laser Melting xvi, xvii, 3, 7, 31, 37, 70, 71, 74, 75, 76, 77, 78, 139

SLS Selective Laser Sintering 7

UAM Ultrasonic Additive Manufacturing 6

USB Universal Serial Bus 96

UTAF Advanced Manufacturing Processes Unit 1

WAAM Wire Arc Additive Manufacturing 9, 71, 74

Nomenclature

β	Bulk absorption coefficient
β_m	Modification factor
$\Delta\delta F$	Experimental displacement range
$\Delta\sigma$	True stress range
$\Delta\sigma_0$	Nominal stress range
$\Delta\sigma_c$	Reference critical fatigue stress range at 2 million cycles
$\Delta\varepsilon$	Total true strain range
$\Delta\varepsilon_e$	True elastic strain range
$\Delta\varepsilon_p$	True plastic strain range
ΔF	Load range
ΔK_I	Stress intensity factor range
ΔK_{th}	Fatigue crack propagation threshold
$\hat{\sigma}$	Standard deviation
ν	Poisson's ratio
ρ	Density
ρ_{water}	Density of water
σ_0	Nominal stress
σ'_f	Fatigue strength coefficient
σ_k	Fatigue strength at the second knee point
σ_{GCF}	Fatigue strength at the gigacycle fatigue region
$\sigma_{max,0}$	Maximum nominal stress
σ_{max}	Maximum stress
σ_{min}	Minimum stress
σ_m	Mean stress

σ_{notch} Stress in the notch root (peak stress)

σ_{rem} Remotely applied stress

ε Strain

ε' Fatigue ductility coefficient

ε_a Total strain amplitude

A Amplitude ratio

a crack length

a_f Critical crack size

a_i Initial crack size

B Number of cycles to failure at the first knee point

b Fatigue strength exponent

c Fatigue ductility exponent

D Dilution

d_{melt} Depth of melt pool below the substrate level

d_{nom} Nominal diameter

d_{spot} Spot diameter of the beam

da/dN Crack growth rate (per cycle)

E Young Modulus

E_d Local energy density

F_p Pre-load

F_{max} Average maximum load acquired by the load cells

F_{min} Average minimum load acquired by the load cells

G_I Strain energy release rate

h Height of material deposited above the substrate level

HB Brinell hardness

I Inertial moment

i High cycle fatigue slope of the S-N curve

j Distance between the support and the load application point

K Stress intensity factor

K' Cyclic strength coefficient

k_a	Surface condition modification factor
k_b	Size modification factor
K_c	Fracture toughness
k_c	Load modification factor
k_d	Temperature modification factor
k_e	Reliability factor
K_f	Fatigue strength reduction factor
k_f	Miscellaneous-effects modification factor
K_t	Stress concentration factor
K_{IC}	Critical value of the stress intensity factor
K_{torque}	Torque coefficient
m_{air}	Weight of the sample in the air
m_{water}	Apparent weight of the sample
n	Side of the square cross-section
n'	Cyclic strain hardening exponent
N_f	Number of cycles to failure by crack propagation
N_i	Number of cycles to crack initiation
N_k	Number of cycles to failure at the second knee point
o	First auxiliary variable for fatigue life prediction
P	Power of the heat source
p	Second auxiliary variable for fatigue life prediction
q	Notch sensitivity
R	Stress ratio
R_a	Arithmetical mean deviation of the surface roughness profile
R_z	Maximum peak to valley height of the surface roughness profile
S'_e	Rotary-beam test specimen endurance limit
S_y	Yield strength
S_e	Fatigue limit
S_{ut}	Ultimate tensile strength
T	Tightening torque
V_{scan}	Scanning velocity
y	Distance to the neutral axis

Chapter 1

Introduction

1.1 Framework and motivation

Metal additive manufacturing (MAM) has been getting more attention over the years as a viable alternative to more usual manufacturing processes, since they provide a unique feature: the ability to produce functional parts with very complex geometries in an automated way. As the need to reduce part weight while maintaining function rises in a never-ending quest for mechanism efficiency and energy consumption reduction, AM becomes a key element in the production industry owing to its flexibility and reliability.

Despite the attractive properties of MAM, the process is not free of limitations. Besides the dimensional imprecision and residual stresses due to successive heat cycles, the low production rate and the feedstock material costs may become an issue for extensive investigation and characterisation of parts produced by these methods.

Some materials with high mechanical properties often find their use limited because it is hard to produce parts with them via conventional manufacturing methods. Inconel 625 is an example of such material that is used in a large number of industries, such as aerospace and marine [1]. Parts utilised in such industries are frequently subjected to repetitive loading cycles, which may lead to fatigue failures.

The usage of finite element methods to predict material behaviour has become an indispensable tool in machine design, preventing design mistakes and reducing extensive testing and prototyping.

This dissertation integrates the Add.Strength project by carrying out a study of characterisation and fatigue behaviour of Inconel 625 produced by Directed Energy Deposition (DED). With this purpose in mind, the complete cycle of life of the material- from the parametrisation study that allowed DED material to be produced, to specimen failure after tensile and fatigue testing, was tackled. Moreover, several characterisation processes were executed, such as surface roughness and hardness measurements, and analysis of microstructure and fracture surfaces. To evaluate fatigue behaviour, four-point bending tests using miniature specimen were performed. For the first time, Inconel 625 specimens were produced by directed energy deposition (DED) at Institute for Science and Innovation in Mechanical and Industrial Engineering (INEGI) with good mechanical properties.

The developed work is incorporated in the ongoing Add.Strength - *Enhanced mechanical properties in additive manufactured components* project, which focus lies on studying and understanding the mechanical behaviour of parts produced through metallic Additive Manufacturing processes. The project is integrated in the Advanced Manufacturing Processes Unit (UTAF), within the INEGI.

1.2 Objectives

The main goal of this dissertation is to characterise Inconel 625 produced by Directed Energy Deposition and to evaluate its fatigue behaviour. To ensure that the main goal is achieved, multiple intermediate objectives were established:

- Theoretical review of additive manufacturing, with special emphasis on metal additive manufacturing and Directed Energy Deposition, Inconel 625 characteristics, properties and applications, fatigue characterisation and testing;
- Development of a gripping system to test miniature specimens in an available fatigue testing machine, changing the type of test from three-point to four-point bending and retrofitting the machine itself;
- Validation of the experimental setup by means of a finite element analysis (FEA) and by strain gauge application, conduction of a convergence study of the numerical model and analysis of its response to different variables;
- Performance of a material characterisation, by doing metallographic and fracture surface analysis as well as hardness, porosity and surface roughness measurements;
- Execution of tensile tests with digital image correlation (DIC) technique to grasp the plastic behaviour of Inconel 625;
- Execution of four-point bending fatigue tests to plot the S-N curve of the material;
- Prediction of fatigue life based on the measured hardness values;
- Comparison of the obtained fatigue life with the reviewed literature.

1.3 Layout

The dissertation is divided into five different chapters:

- Introduction: The framework and motivation of the thesis are detailed as well as the involved institutions in the project. The main goals are described;
- Background Theory: A literature review of the main topics that concern this dissertation is performed: Additive manufacturing, fatigue and Inconel 625;
- Materials and Methods: The description of the performed tests and evaluations are presented. The equipment, materials and standards utilised are referred;
- Results and Discussion: The results of every test detailed in the previous chapter are revealed and their critical discussion takes place;
- Conclusions and Future Work: The conclusions drawn from the tests performed are made, as well as possible future work that would enrich and give sequence to the presented work.

Chapter 2

Background Theory

2.1 Additive manufacturing

Additive manufacturing (AM) is, as the name implies, a method of manufacturing by means of adding material layer by layer aiming at improving an existing piece or creating a new one [2]. Trivially, these methods differ from conventional subtractive machining processes as drilling, boring, milling or electrical discharge machining because the latter remove material until the desired form is created, instead of adding it [3]. Additive processes also differ from metal forming processes, such as stamping, press brake and forging. These methods do not add material, they deform it [2].

However, not all processes that add material can be considered into the additive manufacturing group. There are some processes which require design-specific tooling to produce new parts, such as casting and injection moulding [4, 5]. This property inherent to these processes is what distinguishes non-additive manufacturing processes from the additive manufacturing ones, as the latter do not require design-specific tooling [2].

Taking as an example casting (non-AM process) and DED (AM process), the distinction between them becomes clear. In casting, a mould or tool is required to manufacture a part with a given design. Although this mould can be used to produce several parts; if one wants to change the design of the part, another mould or tool is needed [5]. Alternatively, DED uses a nozzle to deposit material in a certain path. If the design is to be changed, the material can be deposited in a different path, in the same platform, with the same tool, the same equipment. This is the fundamental difference between non-AM additive processes and AM ones [2].

Subtractive processes are currently one of the most used metal shaping processes in the industry and they create parts that have better surface finishing, high dimensional accuracy and, depending on the material and process considered, high mechanical properties. Nonetheless, as well known, geometric freedom is limited and the process generates a lot of material waste [6]. Forming processes, for instance, require an important initial investment in tooling, making it only profitable in high production volume [3].

Additive manufacturing started in the 1980's as a low-production method to produce parts with complex shapes and geometric features, especially prototypes and tooling. These low-cost applications are specially viable for medium and low volumes of production. Nowadays, AM is still mainly used to make prototypes, and also small series of near net shaped parts, in many industries. In fact, part production using more advanced AM processes such as DED or selective laser melting (SLM) can be extremely expensive due to the high feedstock costs, hardware investment and post-processing operations, making it mainly viable for small and medium series, especially because of the low production rates

[3, 7].

The increasingly popular AM processes are sometimes driven by material needs and issues, especially for metal production. DED enables an easy way to produce functionally graded metals, where materials with different compositions are deposited during the build in specific locations, making the material suitable for very specific applications [8]. In the case of AM processes that involve material fusion, the microstructure of the product can be changed by tweaking the process parameters [7].

AM technologies also enable designs conceived by topology optimisation, which is a mathematical framework that, among other uses, may be implemented to optimise material layout for a given set of stresses and loads, supported by a stress analysis software. In these cases, weight can be reduced to a minimum while maintaining functionality. Parts that were optimised often have very complex geometries that would be impossible to manufacture without AM [9]. The ability to create designed lattice/truss and cellular structures in a part is another feature of AM processes [7]. Nonetheless, complex geometric features may require support structures that, sometimes, are not possible to add in some AM processes.

The process chain was also massively affected by these emerging technologies. Usually, prototype part production was held up until late in the process conception cycle. However, with AM methods, it is much easier to create functional prototypes, which can be produced earlier in said cycle [6]. Having a prototype in the early stages of development has great advantages and facilitates the final design [7]. As stated by Isaac Ferreira [3], "AM is a powerful tool which creates a quick bridge from the virtual model to the physical part".

Moreover, AM technologies allow fabrication of traditionally assembled parts as an integral component, which potentially reduces the overall weight and the number of joints between parts [10]. Generally, AM process chain can be divided into five different stages, as seen in Figure 2.1.

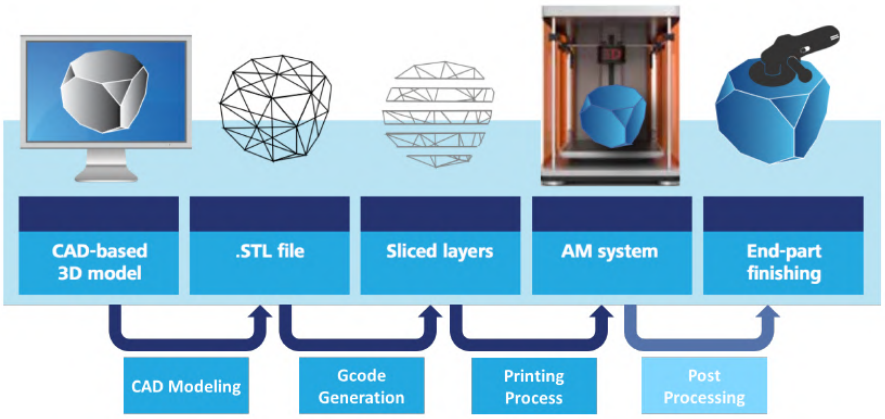

Figure 2.1: AM process chain [3].

The process starts by creating a computer aided design (CAD)-based 3D model of the part. Then, this 3D model is generally turned into a .STL file, which is the 3D model converted into a mesh of triangles. The .STL file is then sliced into layers by a slicing software, in which the layer thickness of the part is defined. The tool path is then determined and a G-code is created, so that the machine can use its tool accordingly and convert the data- which are the virtual layers, into physical, printable layers [11]. At this point, the information about printing routes, velocities, layer thickness, temperatures and energy intensity are defined in the output file that is going to be read by the machine and

the AM system produces the designed part, layer by layer. Post processing can be applied to improve mechanical properties or surface finish, if necessary, to achieve the final part [2, 3].

The parts obtained by AM can be made from several materials, such as metals, polymers, ceramics and even composites or graded materials, like previously mentioned. Additive manufacturing processes can be classified according to the ISO-ASTM 52900 [12], into seven different categories. In Table 2.1, the main categories are presented, coupled some of the main technologies within each category, the typical material and a brief description. Note that there are different names for the same process resulting from distinct manufacturers or patents [2].

Table 2.1: Additive manufacturing main categories and technologies [3, 7].

Category	Technology	Typical Material	Description
Material Extrusion	Fused Filament Fabrication	-Thermoplastic paste; -Ceramic paste; -Metal paste.	Material feedstock is heated and extruded through a nozzle that moves relative to a build platform.
	Contour Crafting		
Vat Polymerisation	Stereolitography DLP	Photopolymers	A photosensitive polymer is exposed to UV light, which cures or hardens the resin.
Material Jetting	Inkjet Printing	-Photopolymers; -Wax.	Material is deposited in the building platform where it solidifies. It is then cured by UV light.
Binder Jetting	3DP	-Polymer powder; -Ceramic powder; -Metallic powder.	An adhesive is sprayed selectively onto the surface of the powder bed.
Powder Bed Fusion	Selective Laser Sintering	Polymer powder	Laser or electron beam melts or sinters selectively a powder bed.
	Direct Metal Laser Sintering	-Atomised metal powder; -Ceramic powder.	
	Selective Laser Melting		
	Electron Beam Melting		
Directed Energy Deposition	Laser Engineered Net Shaping	Metallic powder	Powder or wire is deposited by an extrusion head while being simultaneously melted by a laser or electron beam.
	Electron Beam Welding		
Sheet Lamination	Laminated Object Manufacturing	-Polymeric film; -Metallic sheet; -Ceramic sheet; -Paper sheet.	Stacking and laminating thin sheets of material, by bonding, ultrasonic welding or brazing.

It is important to refer that due to the recent growth of AM industry, there are many additive manufacturing processes that do not find its place in any of the previously defined

categories. Therefore, there are many other ways of classifying AM technologies. For example, organise them on the basis of materials and agents to join them, and form or conveyance of feedstock [2].

2.1.1 Metal additive manufacturing

One of the main purposes of the present dissertation is to explore metal additive manufacturing techniques. Therefore, only these technologies are going to be object of study in the following sections with special emphasis on Directed Energy Deposition, since the specimens used for fatigue testing and characterisation were produced by the said process.

Considering all the categories mentioned in Table 2.1, it can be stated that Vat Photopolymerisation and Material Jetting are used exclusively for the production of non-metallic parts. The remaining additive manufacturing technologies can be used to produce metal parts, although the most common in industry are the Powder Bed Fusion techniques and Directed Energy Deposition ones.

Material extrusion is one of the most common AM techniques when it comes to the production of polymer parts. Nonetheless, nowadays it is possible to print composite and metal parts with very specific systems. For the case of metal part production, those systems can extrude filaments made of a polymeric binder, filled with metal particles ($\approx$ 50 - 60 % volume). After extrusion, the filament is debinded and undergoes subsequent sintering to obtain a fully metal part [13].

Binder Jetting is a powder-bed based AM technology that, coupled with a Inkjet printing technology, can produce "green parts" that need to be densified [14]. These are parts with very low mechanical properties which are often brittle until they are cured, sintered or infiltrated [15]. Using metallic powder, a binder and then a metallic infiltrator, metal parts can be produced. The main steps of Binder Jetting process are [7]:

1. Printing in the metal powder bed;
2. Curing of the green part;
3. Depowdering;
4. Sintering and other post-processing steps.

This process involves selectively spraying the binder into the powder bed, layer by layer, in which each layer consists of the local cross section of the part to be printed. When the printing ends, the binder is still wet and the part is somewhat malleable. Hence, a curing step is required, where the whole build volume is heated to a temperature of around 200 °C. After the part is cured and cooled to a temperature that allows its handling, the depowdering step starts. Here, the individual parts, which are usually 50 % dense and have low mechanical strength, are removed from the powder bed. To solve this issue, the voids can be extinguished by sintering or by infiltrating the part with another metal. Other post processing steps may also be required before the part is ready to be used [7].

Another AM category that allows the production of metallic parts is Sheet Lamination, more specifically the ultrasonic additive manufacturing (UAM) technique. This method takes advantage of the principles of ultrasonic welding, mechanised tape layering and computer numerically controlled (CNC) machining operations to create metallic parts. It involves stacking metallic sheets on top of each other and then bonding them by ultrasonic welding [7]. When two sheets are placed in contact under tangential sliding load, the asperities of their surfaces yield, collapse and form joints with great strength [16]. Every

ten layers, the process stops and a milling operation is performed to trim off the excess material [7]. This process could be considered as a hybrid one, since it couples principles of additive and subtractive processes.

The powder-bed systems are the most used to additively manufacture metallic parts. The ones that are relevant for MAM can be divided in two major groups that differ in the energy source used to melt the powder. On the one hand, the processes that use a laser are referred to as laser powder bed fusion (L-PBF). On the other hand, the technologies that utilise an electron beam can be called electron beam melting (EBM) [17].

In these systems, a powder bed is generated by raking powder across the work area with a roller or blade. The energy source then delivers energy to the surface of the bed, selectively melting, in the case of SLM, or sintering, in the case of selective laser sintering (SLS), the powder into the desired shape, which corresponds to the local cross section of the part. The powder bed platform descends the equivalent distance of a single layer and a new layer of powder is raked across the work area. The process is repeated until the three dimensional component is created. Figure 2.2 provides a graphical description of an AM powder bed system [18].

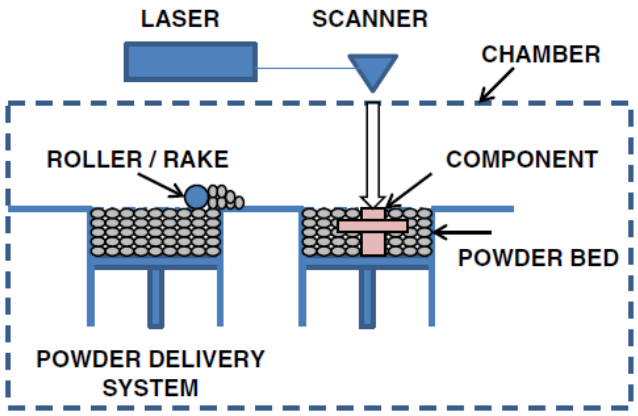

Figure 2.2: Generic AM powder bed system [18].

The powder bed is placed inside a chamber, which allows for the usage of an inert atmosphere, mostly to protect the oxidation of metallic powders at high temperatures [19].

The main advantages of powder bed fusion (PBF) are its ability to produce high resolution features with great dimensional control, utilising a great range of materials and producing parts with near-net shape [18]. However, it also has some limitations, such as the allowed build volume which only allows for the construction of small or medium sized parts. More often than not, SLM built parts need to undergo a post heat treatment such as hot isostatic pressing (HIP) to reduce their porosity levels [20].

The second most used AM method for metallic part manufacturing is Directed Energy Deposition. Due to its importance to the current dissertation, this category of AM is explored in a more detailed way in the following subsections, especially the powder-based DED systems.

2.1.2 Directed energy deposition

Directed Energy Deposition is an additive manufacturing process where metallic material is fed through a nozzle and deposited directly into a melt pool that is created, simultaneously,

by a focused energy source acting on a substrate or previously deposited layer.

A focused energy source, such as a laser beam, collimated with a nozzle acts like a heat source which melts the substrate in the first deposition or previous layer in the subsequent depositions, creating a melt pool. The material feedstock (either powder or wire) is conveyed by a single coaxial nozzle or multiple discrete ones and deposited into the melt pool. Given that the laser beam provides enough thermal energy to melt the blown particles and the substrate, in the case of powder feedstock, they adhere to it, by the creation of a melt pool. This melt pool, coupled with Marangoni convection ensures a good bonding between materials and, once it solidifies, creates a point of solidified metal. By moving the nozzle parallel to a fixed substrate or by moving the substrate parallel to a fixed nozzle, the point of solidified metal becomes a line. Moreover, by moving the nozzle up or the substrate down and repeating the process, a three-dimensional part can be created [2, 7, 10].

In the case of powder DED, the powder is carried by a carrier gas. This carrier gas is ejected with the powder from the lateral cavities of the nozzle and is responsible for the transport of the powder particles. The process utilises another gas, the shielding gas that is ejected through the same nozzle as the laser. The main purpose of the shielding gas is to protect the molten metal from oxidation. The most common inert gases used for this purpose are Argon and Nitrogen [21]. A schematic of the powder and wire process is presented in Figures 2.3 and 2.4, respectively.

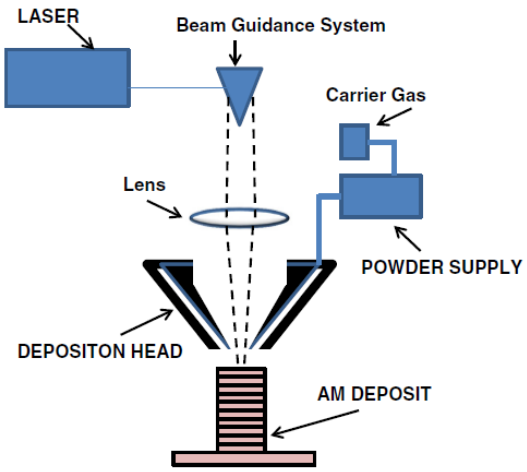

Figure 2.3: Generic powder DED system [18].

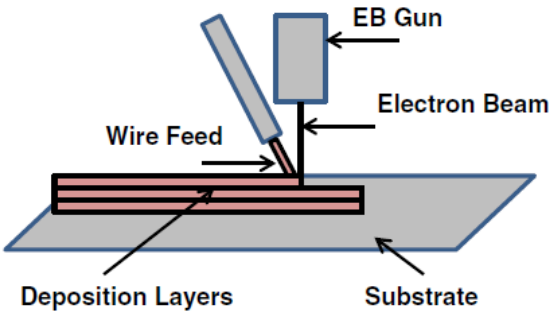

Figure 2.4: Generic wire DED system [18].

In DED, various heat sources and forms of feedstock can be used. Hence, many designations have been given to variations of this process. Some of them include: Laser cladding, direct metal deposition (DMD), laser rapid forming, laser-aided direct metal deposition, direct light fabrication, direct laser deposition, Laser Engineered Net Shaping (laser engineered net shaping (LENS) ®) [10], laser metal deposition (LMD) and wire arc additive manufacturing (WAAM) [17].

The process can be classified on the basis of the type of energy source: melt based DED and kinetic energy based DED. The melt based systems can be further classified according to the energy source: Laser beam, Electron Beam, Plasma and Electric Arc. As already mentioned, the process can also be classified on the basis of form of feedstock: wire or powder [22].

Wire based machines have a higher process efficiency, higher deposition rate and provide better surface quality to the produced parts. However, powder based machines are much more common in the industry. This fact might be due to the fact that blown powder dynamics are easier to control in real-time and its form can be manipulated to produce parts with more complex shapes and geometries. Moreover, non-used powders may be recycled and used again in other depositions. Wire-fed systems are also susceptible to vibrations and disturbances [10].

Generally, wire-based DED uses an electron beam, plasma or electric arc as a heat source. Kinetic energy DED systems, also referred to as Cold Spray, use micron sized particles to coat components. A converging-diverging nozzle is used to accelerate these particles to supersonic velocities. Beyond a certain impact velocity, they adhesively bond to the substrate and build up material [22].

The number of alloys that can be used in AM has increased since the genesis of this process. Some of the most used alloys to produce parts using Directed Energy Deposition are listed in Table 2.2.

Table 2.2: Some of the most common alloys used in DED processing. The superalloys are presented by their commercial names. Adapted from [18].

Titanium	Aluminium	Tool Steels	Superalloys	Stainless Steels
UNS R56400	UNS A96005	DIN 1.2344	IN625	UNS S31600
ASTM F136	UNS A96061	Cermets	IN718	UNS S42000
			Stellite	UNS S34700

A comparison can be established between the Powder Bed Fusion and DED processes to better cope with the differences, advantages and limitations of the two most widely used AM processes for the production of metal parts.

The main aspects that differ between the two processes are the production rate, the source power and the quality of features. Figure 2.5 shows the clear contrast between the three aspects.

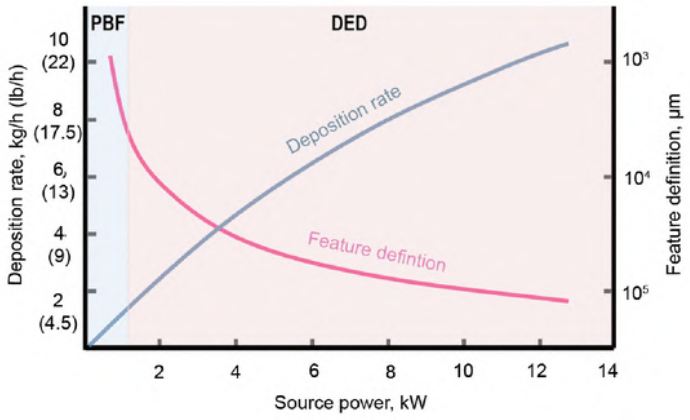

Figure 2.5: Effect of energy source on deposition rate and feature quality for DED and PBF processes [7].

Generally, the lasers utilised for PBF have less power than those used for DED, since there is the presence of a powder stream in the latter, meaning more power is needed to effectively melt the material [10]. The mean laser diameter is also higher in DED, so in order to achieve the same productivity, the laser needs to be more powerful. Moreover, the higher power of the laser allows for a higher deposition rate, characteristic of DED processes. However, the feature quality and definition decreases with increasing laser power. This way, PBF processes can produce parts with finer surface quality. While PBF parts may require a depowdering process and a post processing heat treatment, such as HIP, DED parts usually need a post AM processing procedure, such as machining, to achieve the dimensional requirements. PBF might be more advantageous to the construction of overhanging structures, since the powder bed acts as semi-support structure, reducing the need for supporting structures and, consequently, residual stress formation [7, 10].

While DED requires a substrate to deposit material on, the PBF utilises a powder bed. One of the biggest advantages of the DED process over the PBF is the fact that an existing part can be used as a substrate for deposition, meaning that the reparation or coating of components is easily achieved.

The component size is also more restricted in the PBF process since the build size (powder bed) is limited [23]. Nevertheless, the build size of PBF processes has been object of innovation in the industry. In fact, efforts have been made using mobile building chambers, which allow building bigger parts than the conventional PBF machines [24].

DED versatility makes the process useful in many applications for a wide range of industries. The main applications of DED are [7, 18]:

- Producing distinct features by selectively adding material on wrought products;
- Repairing and refurbishing damaged and worn components, restoring their initial dimensions;
- Adding coatings to components, to improve some characteristics locally, such as wear and corrosion resistance;
- Producing near-net shaped components that usually require machining operations. For this application, DED requires a substrate to deposit the material, which may or may not be part of the final component;

- Producing parts with multiple alloys, as long as they are metallurgically compatible. An example of this are functionally graded materials.

In the following subsections, the DED process components and parameters, thermal phenomena, the common defects that may arise during or post manufacturing, as well as the production of metallic powders are approached. Other relevant topics are also discussed, such as the presence of residual stresses and the post-processing operations required after DED.

2.1.3 DED components

There are many DED machines available commercially, differing slightly from each other. Nonetheless, there are some components that are common to most systems, including [7]:

- Heat source to melt the feedstock material;
- Deposition head to manage the simultaneous delivery of energy and powder to an intended interaction area;
- Powder feeder system for continuous delivery of feedstock to the melt pool;
- Automated system to manipulate the deposition head on a predetermined path by rotating or translating it;
- Adequate processing space, either at room temperature or controlled atmosphere;
- Real-time feedback control, for "closed-loop" processing (Optional) [10].

Heat sources

As already stated, DED utilises several types of heat sources, being the most prominent laser beams, electron beams and electric arcs. These can be continuous wave (CW) lasers or pulsed ones. With a pulsed laser, heat build-up to the substrate during cladding is less pronounced than with a continuous laser, providing a narrower heat affected zone, lower dilution, i.e., a dimensionless parameter that quantifies the level of metallurgical bonding between subsequent layers [22, 25], and a lower tendency to crack. Dilution, D, can be defined as:

$$D = \frac{d_{melt}}{h + d_{melt}} \tag{2.1}$$

where d_{melt} is the depth of the melt pool below the substrate level and h is the height of the material deposited above the substrate level.

However, in pulsed lasers, powder cannot be melted during the laser power-off period, meaning that processes with this type of lasers might have a lower deposition efficiency [26].

When choosing the proper laser to use in a DED system, several factors need to be taken into account: laser power, to ensure the melting of the particles and to achieve the desired deposition rate; adequate wavelength to minimise energy losses due to reflection; beam quality, to guarantee satisfactory energy distribution and, of course, cost of the equipment [7, 27].

Industrially, there are several types of laser available, some of the most notorious include: ytterbium fibre (Yb), neodymium:yttrium-aluminum-garnet (Nd:YAG), CO_2 lasers

and direct diode. All these examples have different wavelength, ranging from 100 nm to 10000 nm. However, the most used ones are those whose wavelength is near 1000 nm. This is due to the fact that some metals have increased absorptivity in the near-infrared portion of the electromagnetic spectrum, which means the energy is used more efficiently to melt the particles. In Figure 2.6, the absorption percentage of some metals is presented as a function of wavelength.

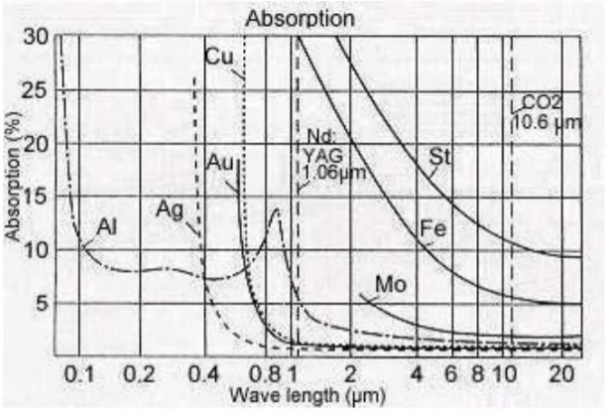

Figure 2.6: Absorption of some metals as a function of wavelength [28].

Moreover, these lasers have a better transmissivity within an optical fibre. Hence, they can be transmitted to the workstation through an optic fibre cable, increasing the consistency of important beam characteristics [7, 27].

In the case of a laser with characteristic wavelength of 1000 nm, the beam is emitted by the laser source and focused onto the fibre optic, which transports it to the deposition head. There, the beam is collimated and re-focused to achieve a certain spot size. A schematic of the explained process is presented in Figure 2.7.

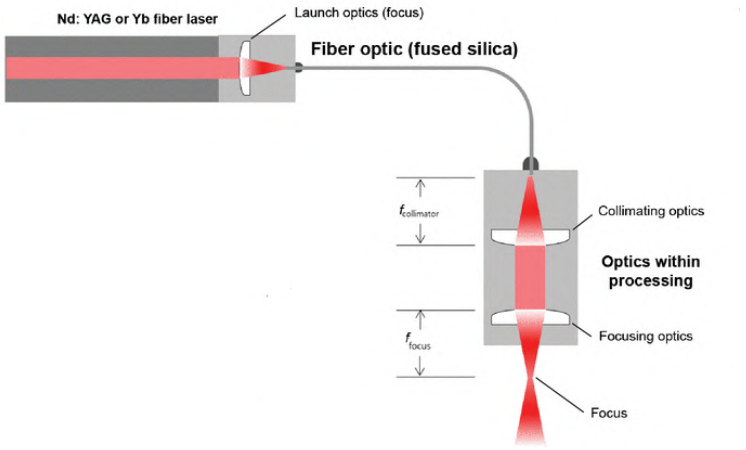

Figure 2.7: Fibre delivery schematic. Adapted from [7].

It is important to note that the focal length is the distance between the last focusing optic and the focus of the laser beam, and it can be regulated by the curvature of said optic. The laser focus point is a function of the magnification, which depends on the collimator and focal length, the radius of the delivery fibre and the characteristics of the laser source [7].

The energy distribution that a certain laser provides is of extreme importance to understand melt pool dynamics and final dimensional properties of the part [10, 22]. Higher power laser that is transmitted through an optic fibre usually uses a multi-mode beam. This causes a superposition of the many modes and originates an output with a "top hat" energy distribution. Lower power lasers, which often have single-mode beams, provide a Gaussian energy distribution [7]. A representation of such energy distributions is shown in Figure 2.8.

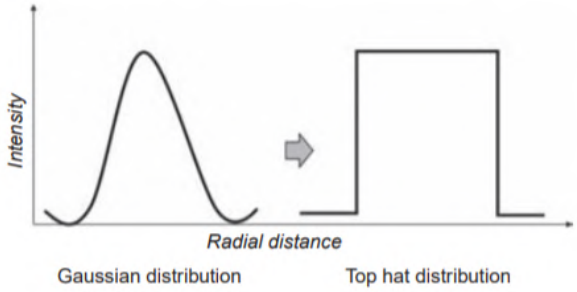

Figure 2.8: Gaussian and "top hat" distribution of energy [29].

Heat source power can also vary depending on the desired deposition rate. It can range from 500 W to 10 000 W for laser beam DED, and up to 30 000 W for electron beam DED. The lasers can be focused to a very small spot diameter. However, laser based DED usually uses a defocused beam at the interaction plane, since a larger laser spot increases the potential deposition area. This is accomplished by positioning the laser at a distance above the focal plane of the beam, by moving the deposition head [7, 10].

Deposition head

The deposition head is one of the most important components of laser-based DED systems. It is responsible for focusing the beam to the substrate, while conducting the feedstock (powder or wire) to be melted for deposition. A schematic of a typical deposition head is shown in Figure 2.9.

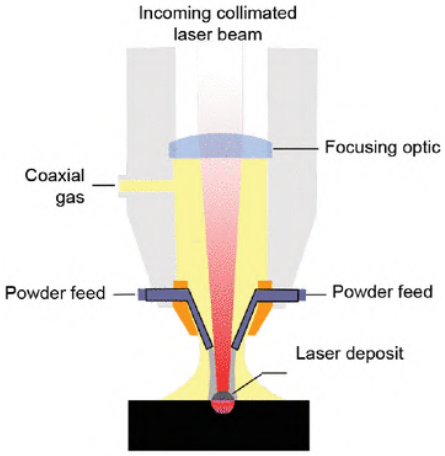

Figure 2.9: Laser-based DED deposition head [7].

The feeding nozzles connect to the deposition head. As already mentioned, there can be various discrete powder-feeding nozzles or an annular coaxial one that blows powder into the melt pool. Inert gas is also used to carry the powder feedstock to minimise contamination of optics due to possible splattering and to protect the molten metal. Inside the deposition head, there is also an optic responsible for focusing the laser beam. Nevertheless, the laser beam can be further manipulated using galvanometer-driven mirrors [7].

Electron beam-based DED uses a different system. It relies on a beam gun to focus, manipulate and direct the electron beam to the substrate and a separate secondary nozzle delivers the wire feedstock [7]. It should be noted that these systems require a vacuum chamber, so that the electron beam is not scattered by residual gas molecules, resulting in a lower process efficiency.

Feedstock system

The feedstock system guarantees a continuum and reliable way to provide material to the deposition head.

In the cases of electron beam-based DED and arc-based DED, wire is the feedstock. If the processing is made in a processing chamber, the feedstock system is also contained within the chamber, to maintain the integrity of the vacuum. The wire is pushed by drive rolls at the spool, conducting it to the feed nozzle [7]. The concept is the same for laser-based DED that uses wire as feedstock.

In most instances, laser-based DED uses metallic powder with a diameter of 50 - 150 μm. In such cases, the powder is stored at a hopper or reservoir and is supplied to the nozzles by a system, for example, a revolving wheel with cavities. These cavities capture the powder from the hopper and feed it to the nozzle. Moreover, the rotational speed of the wheel and the volume of the cavities determine the mass feed rate. A carrier gas may be used to improve the powder flowability through the nozzles [7].

Motion

The motion on a DED system may involve movement of the deposition head, movement of the component or substrate, or even a combination of both. Some of DED applications, such as repairing of pre-existing components, may require complex movement of the system. Hence, articulating systems, for instance robots with several degrees of freedom can be utilised for the motion of the deposition head. An example of a robot where the deposition head can be mounted to is given in Figure 2.10 [7].

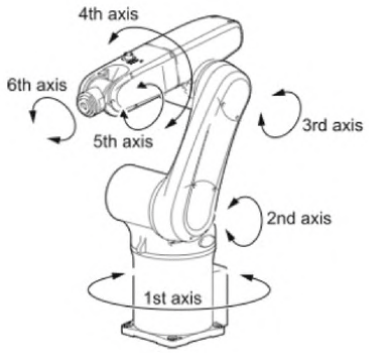

Figure 2.10: Industrial robot system with 6 axis of freedom [7].

For more straightforward applications, simpler rectilinear devices can be used, such as gantry systems. With three axis, these have less geometric freedom, but provide movements with higher accuracy.

Processing chamber

When the material to be processed has propensity to oxidise while in liquid state, absorb gaseous elements in the melt pool or react harmfully with gases at high temperatures, the process needs to be performed in a controlled environment inside a processing chamber. It is expected that by processing the material in vacuum or surrounded by inert gas, the detrimental reactions are minimised or eliminated [7].

Examples of highly detrimental reactions are: oxide formation in the surface of the molten pool for various alloys, hydrogen absorption into the molten pool for aluminum processing, and oxygen and nitrogen absorption for titanium alloys at high temperatures [7].

Control system

The control system of a DED machine must ensure a way of intercommunication between all subsystems, as well as responding to every safety commands [7]. Moreover, several monitoring systems have been developed over the years as a way to provide real-time feedback. Modern systems receive the inputs monitored and can react to them, changing the processing parameters in real time.

This type of monitoring systems make the AM process work in a "closed-loop". The feedback control can be integrated in the machine and is accomplished by having non-destructive monitoring systems that can measure, indirectly, part quality. For instance, localized hot regions of the melt pool, which may later originate extreme residual stresses or warping, can be traced by infrared thermal imaging. This data can be used to adjust the AM process parameters and rectify them automatically, enabling a "hands-off" operation [10].

One example of a closed-loop system is melt pool temperature control. It is possible to measure the melt pool temperature in real time and adjust the laser power to increase or decrease the temperature with the intent of keeping it constant.

2.1.4 DED parameters

Directed Energy Deposition is a very complex manufacturing process, that involves many physical and thermal phenomena. Obviously, the properties and characteristics of a final component produced by DED depends strongly on a wide variety of chosen processing parameters [30]. Understanding their role in the process is a necessary exercise to fully grasp the nature of DED and to overcome or predict possible defects. A fish bone diagram is presented in Figure 2.11, showing most of the DED processing parameters.

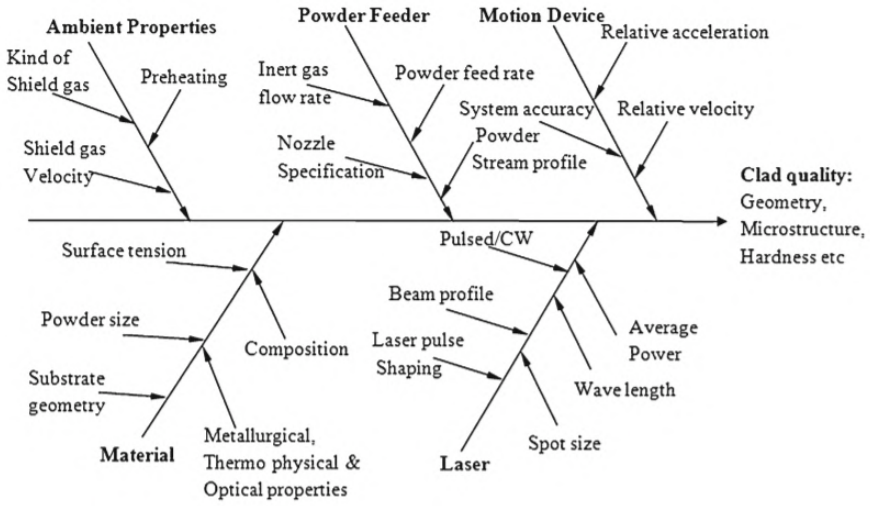

Figure 2.11: Fish bone diagram of the main DED process parameters [31].

Not all the parameters have the same level of influence in the quality of the final part. Some of the most fundamental parameters include [7]:

- Power provided by the energy source;
- Traverse velocity of the moving heat source, or scanning speed;
- Diameter of the energy source, projected onto the substrate, i.e., spot size;
- Mass flow rate of the feedstock, or feed rate;
- Hatch spacing between adjacent deposition beads, or overlap [18];
- Interlayer idle time [10];
- Carrier gas flow rate;
- Shielding gas flow rate;
- Clad angle [22] or feed angle;
- Plate-nozzle distance [32];
- Layer thickness [18, 22].

Most of the aforementioned parameters are self-explanatory. Laser power depends on the type of the utilised laser beam. If the laser power is insufficient, there will be a lot of lack of fusion defects in the final part and dilution problems may arise. If the power is too high, there can be substantial thermal related defects, such as vaporisation of material or extreme residual stresses, due to high thermal gradient during cyclic heating and cooling.

The traverse speed, or scanning speed, is the velocity at which the laser performs its path. The scanning speed is tightly connected with the laser power and mass flow rate, and their combined effects are very notorious. For instance, a low scanning speed needs to be compensated by low mass flow rate. Otherwise, the dimensional accuracy of the part is compromised. Likewise, a high scanning speed accompanied by a low mass flow rate produces a part with insufficient material to fulfil the dimensional requirements. On the

other hand, a low scanning speed connected to a high mass flow rate originates oversized beads.

The laser spot size is the projection of the beam diameter into the substrate. In many cases, the spot diameter of the beam intersects with the powder stream focal spot at the same point [22]. This can be changed in multiple ways, one of them by changing the distance between the nozzle and the substrate [7]. Low distances can result in higher nozzle temperatures and consequent nozzle adhesions, while high nozzle distances do not form proper deposition tracks [32]. Moreover, the nozzle distance must take into account the laser focal point and the zone of convergence of the powder.

The mass flow rate, or powder flow rate, is the rate at which the feedstock is deposited through the deposition head.

The hatch spacing is the distance between two adjacent beads of material. The parameter is sometimes dictated by the overlap ratio, which is the ratio of material that is overlapped to length of one single bead of material [33]. The distance between layers is the layer thickness or Z increment. Some of the already mentioned parameters can be visualised in Figure 2.12, where two adjacent deposits are shown.

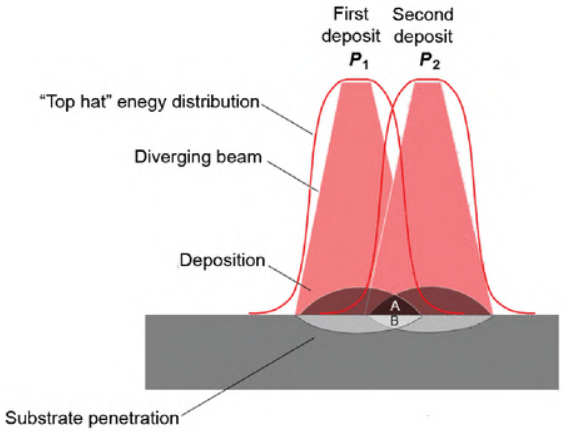

Figure 2.12: Deposition of two adjacent beads. Adapted from [7].

The idle time between layers is also important. It is the amount of time comprised between finishing the deposition of a layer and the deposition of the next layer. In this interval of time, the deposition stops and the part is allowed to cool off before the next layer is deposited, reducing potential residual stresses.

The carrier gas flow rate is the rate at which the carrier gas is blown. The clad or feed angle can be defined as the angle between the centre of the nozzle and the direction of the material feedstock.

Over the years, several relationships between the processing parameters have been developed. One of them is the concept of local energy density (E_d), which defines the energy available for melting the material during DED. It can be given by [7]:

$$E_d = \frac{\beta P}{V_{scan} d_{spot}} \tag{2.2}$$

where β is the bulk absorption coefficient, which represents the fraction of the energy that is absorbed by the melt pool when compared to the total energy provided by the laser

during melting and deposition and depends on many different factors, such as the laser wavelength, the type and physical form of the material, and temperature, among others; P is the power of the heat source, V_{scan} is the scanning velocity and d_{spot} is the spot diameter of the beam. A given material requires a minimum local energy density to fully melt, without having major defects related to lack of fusion [7, 32].

Several studies have been performed, attempting to understand the effects of each parameter in the melt pool characteristics, bead dimensions of single line depositions and geometric and mechanical properties of components produced by DED. Determining the effect of each individual parameter is further complicated by interactions between process parameters themselves [30].

K. Shah et. al [34] studied the effect of carrier gas flow rate, powder mass flow rate and laser operating mode (pulsed or continuous wave) on the melt pool characteristics and surface roughness of a nickel-based superalloy, Inconel 718, deposited in a Ti-6Al-4V thin wall. They found that an increase in the powder mass flow rate, in the carrier gas flow rate and using the laser in pulsed mode, lead to an increase in the mean surface disturbance of the melt pool, which, in its turn, decreases the surface roughness of the final part. This was attributed to the fact that increased melt pool disturbance may reduce the amount of partially assimilated particles, which are one of the main reasons for high surface roughness in parts fabricated by DED. Moreover, an increase in powder mass flow rate led to an increase in the melt pool cross-sectional area. On the other hand, a shorter melt pool was produced with increasing carrier gas flow rate, which was attributed to possible changes in the characteristics of the powder stream, causing less powder to impact on the melt pool.

H. Lee [26] investigated the influence of some cladding parameters on the deposition efficiency. It was found that while the shielding gas type, focal position and laser pulse shape had almost no effect on the efficiency, the powder feed position and angle, powder feed rate and traverse speed were highly influential. The author defined the deposition efficiency as the ratio of weight percentage of deposited power to weight percentage of supplied power. It was found that in order to have the best efficiency, the powder has to be melted by the laser without rebounding away from the surface. If the focal feeding position, which is the position where the powder streams make contact, and the feed angle are high, a lot of material from the powder stream is going to hit the surface at a very inclined angle and far away from the laser action zone, originating a very low efficiency. A situation where the feeding focal point and feeding angle are different is shown in Figure 2.13.

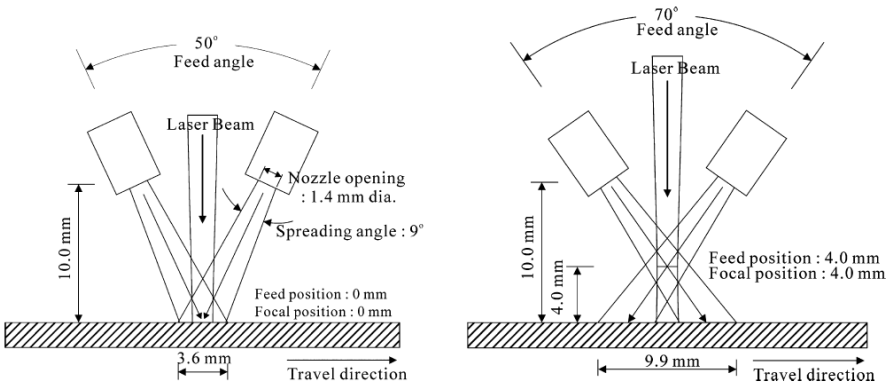

Figure 2.13: Depositions with different feed angle and feed focal position. Adapted from [26].

The deposition efficiency was also increased by increasing the powder feed rate and by lowering the traverse speed. Higher powder feed rate means that the powder blown collides more often and changes direction downward, being exposed to the laser action for longer periods of time. If the traverse speed is lower, the surface temperature increases and so does the deposition efficiency.

D. J. Corbin et. al [35] analysed the influence of laser power, traverse speed working distance and initial substrate temperature on the bead geometry of laser deposited Inconel 718. It was found that bead height and width decreased with an increase in traverse speed. When the travel speed increases, there is a decrease in energy output per unit length (assuming that the power remains constant) and a decrease in the mass of powder flow per unit length (assuming the powder feed rate remains constant), originating a smaller bead geometry. Moreover, with an increase in laser power, larger beads were achieved because the melt pool was larger. The bead height also increased slightly.

The working distance affected the height of beads, since it affects the laser beam spot size and the size of the area of powder distribution and thus the density of powder deposited at the melt pool. Hence, it has great influence on height, but not so much influence on the width. The maximum value for the bead height was found when the focus of the powder stream is coincident with the deposition surface.

The substrate preheating further amplified the effects of laser in bead geometry, since preheating generates the conditions for a wider melt pool, increasing the amount of powder that can be absorbed.

P. A. Kobryn et. al [36] investigated the effects of laser power and traverse speed on build height of laser deposited Ti-6Al-4V. They concluded that the height decreases with increasing travel speed, but the influence of laser power was not conclusive.

J. Choi et. al [30] analysed the influence of powder flow rate in the layer thickness error (difference between actual layer thickness and layer thickness setting) of a H13 tool steel produced by Direct Metal Deposition. They stated that increasing the powder flow rate leads to a decrease in the layer thickness error.

M. J. Kim et. al [23] studied the effect of laser power, mass flow rate and thickness of the substrate on the dimensions of a thin wall deposition of Inconel 625. By increasing the mass flow rate, the width and height of the deposit was found to increase, both for the thin and thick substrates. By increasing the laser power, for the thick substrate, the width and height of the deposit also increased. However, in the case of the thin substrate, the influence of power in the deposit height and width was not conclusive, as the trend was not clear due to excessive melting of the substrate.

One example of a very practical situation where the deposition quality was improved by tweaking the processing parameters is the one portrayed by Y. Woo et. al [21]. When depositing rectangular corners, the scanning speed of a conventional system is decreased near the junction points to change the direction of the scan track. This decrease in velocity can lead to over-depositing near the sharp corners, which can cause loss of geometric tolerance and accuracy. In order to fix this issue, the authors studied the effects of scanning speed, laser power and powder feed rate on the bead deposition, in order to predict bead geometry and be able to guarantee a constant height in sharp corner deposition. The bead dimensions investigated were height, depth and width, as shown in Figure 2.14.

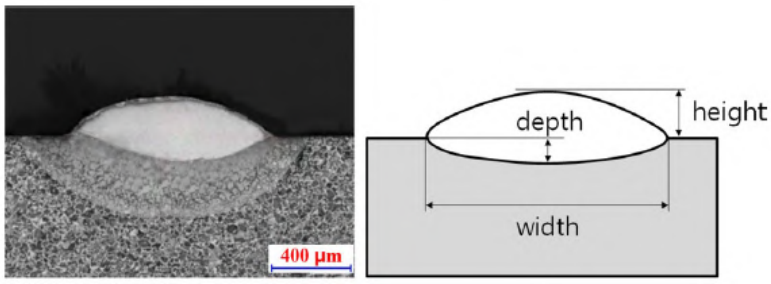

Figure 2.14: Height, width and depth of a deposition bead. Adapted from [21].

They found that an increase in scanning speed led to a decrease in all three bead geometry parameters. An increase in laser power led to an increase in bead width and depth, but had no influence on bead height. Moreover, by increasing the powder feed rate, the bead height and width increased, while the depth decreased.

Furthermore, by adjusting these parameters during scanning of sharp corners, they were able to produce almost equal height squares. Figure 2.15 shows the excessive deposition at the corners with the points used for height measuring and Figure 2.16 shows a big improvement was achieved after parameter tweaking.

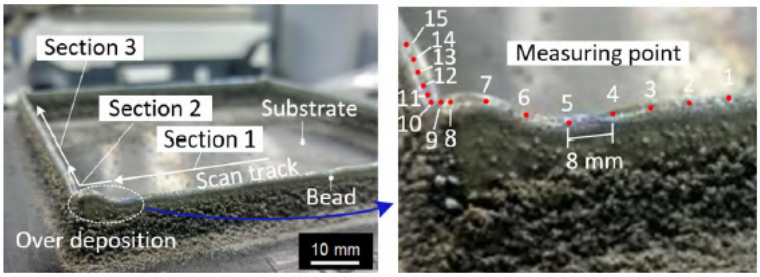

Figure 2.15: Excessive material deposition at the sharp corners [21].

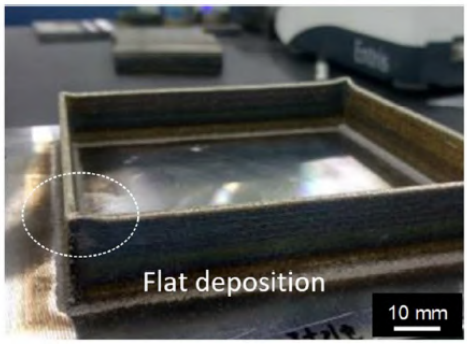

Figure 2.16: Improvement on height deposition at the sharp corners. Adapted from [21].

Several other articles studied the clad geometry variation with different processing parameters [25, 37, 38]. The authors arrived at similar conclusions as the aforementioned studies.

The processing parameters also influence the thermal phenomena of the DED process. A discussion of the melt pool dynamics and thermal energy transfer is addressed in the

following subsection.

2.1.5 Thermal phenomena

An understanding of the thermal phenomena that takes place during DED processes and predicting the thermal gradients, localized solidification phenomena and residual stresses, is essential to optimise the process and ensure consistent and high-quality parts.

DED can be a laser-based AM process, meaning that, in those cases, its driving force is heat transfer. In order to accomplish proper bonding between layers and beads, the thermal energy transfer must be effective and the fluidic behaviour of the melt pool needs to be understood [10].

At a given instant in time, there are several, interconnected, physical events occurring during DED. These events, coupled with proper processing parameters, for a given material and machine, can generate fully dense and structurally sound parts. Some of the physical events and "sub-events" that can occur simultaneously or subsequently are detailed in Figure 2.17.

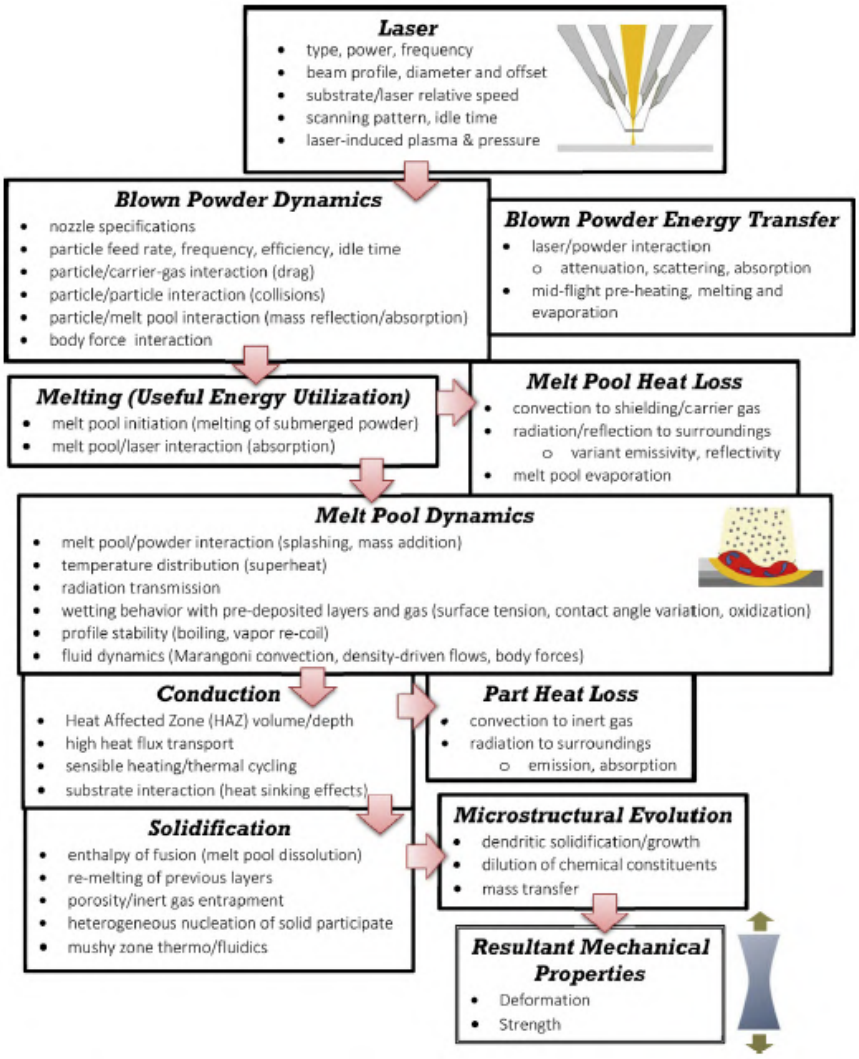

Figure 2.17: Physical phenomena occurring during DED at a given time period [10].

Some of the most prominent phenomena include laser delivery, powder delivery, laser/

powder/carrier gas interactions, melt pool initiation (melting), melt pool energy, stability and morphology, heat losses to the environment due to thermal radiation and convection, solidification of the melt pool, conduction within the part, thermal cycling and conduction from the part to the substrate [10]. All these phenomena have influence on the microstructural evolution of the material and, naturally, on the resultant mechanical properties.

Laser and powder delivery

As already stated, laser-based DED utilises lasers with a wide range of power, varying depending of which material needs to be processed. Most of the laser's spectral intensity is a Gaussian or near-Gaussian wave form, which means that the power intensity is higher near the centre of the beam. However, not all the power provided from the laser gets to the melt pool surface. Instead, laser attenuation occurs, due to the blown powder absorbing and scattering the radiation. Hence, increasing the powder feed rate, leads to an increase in laser attenuation.

Besides the absorptivity of the mid-flight feedstock particles, the absorptivity of the melt pool, which depends primarily on the surface oxygen content and temperatures, also plays a role in efficient laser power delivery. The absorptivity of the melt pool is further affected by Marangoni convection, a convective heat transfer phenomenon, which indirectly contributes towards porosity. Marangoni forces are generated due to differences in surface tension and temperatures along the melt pool that can lead to more splattering and circulation within the liquid of the melt pool. Primarily, the movement is from regions of low surface tension to high surface tension, since the regions with high surface tension tend to pull more strongly the adjacent fluid, leading to variable melt pool penetration [10, 22, 39]. Because of these laser attenuation phenomenon, the laser power that actually reaches the melt pool is much lower than the original laser power.

Due to mid-flight power absorption of the particles, sensible heating of the powder occurs. In extreme cases, some particles evaporate, leading to an increase in gas entrapment and, therefore, an increase in porosity. Note that the main cooling mechanism for mid-flight particles is forced convection with the shielding gas. Mid-flight collision of particles when using discrete nozzles, also comprises a problem of powder waste, since the collisions drive the powder away from the melting pool. To avoid inefficient laser and powder delivery, several processing parameters need to be adjusted, taking into account the just discussed phenomenon [10].

The melt pool

The melt pool is the region of the laser/material interface of superheated molten metal that moves at the transverse speed. The melt pool is extremely thermodynamically unstable since it adjusts its shape and internal energy with time, exchanging heat with its surroundings constantly. The molten pool is situated on top of a "mushy" zone, a region with a two-phase mixture- with remains of solid particles and molten metal. After solidification, the melt pool leaves behind a heat affected zone (HAZ), which is represented as the "Re-melted zone" in Figure 2.18.

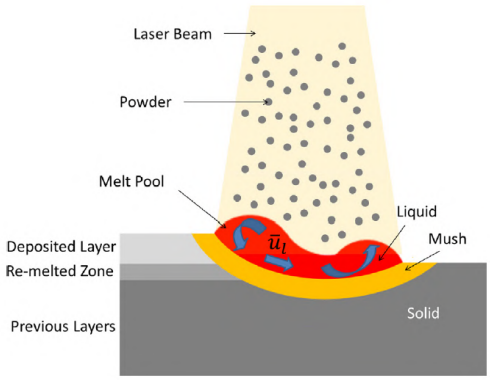

Figure 2.18: Melt pool creation on top of HAZ and intrinsic instability [10].

As explained before, only a portion of laser power hits the melt pool surface. Then, it either gets transferred to the environment via radiation or convection, or sensibly to the HAZ and melt pool region. Newtonian convection, radiation, vapour recoil or boiling in the melt pool, and conduction to previously deposited layers or substrate, all take its toll in the melt pool topology deformation, making it very unstable and in constant motion, as it can be seen in Figure 2.18 [10].

Smaller particles may result in a more stable melt pool. Larger particles have higher momentum, providing larger melt pool motion, which is undesirable. The instability of the melt pool is associated to worse dimensional tolerances, microstructural features and more noticeable residual stresses.

The temperature distribution within the melt pool can be significant, with gradients ranging between 100 and 1000 K/mm due to the laser's Gaussian distribution. The average temperature of a melt pool increases as the number of tracks or layers increases even if the laser power remains constant, because of bulk heating effects. In an extreme case, the initial temperature of a new layer approaches the final temperature of the last deposited layer, which means there is going to be a heat accumulation during the process [10]. Figure 2.19 presents the increase of peak temperature with increasing number of layers due to heat accumulation.

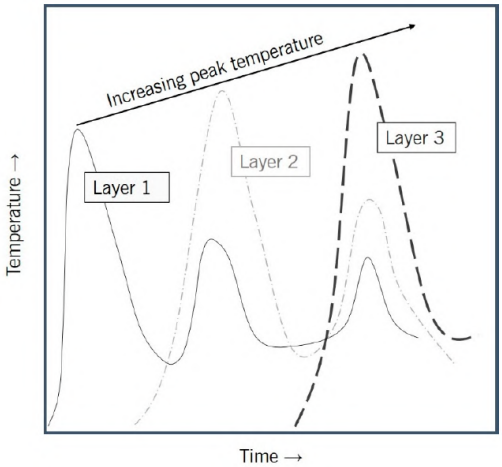

Figure 2.19: Consecutive thermal cycles with increasing peak temperature due to heat accumulation [22].

Bulk heating of the layers while the substrate's temperature increases at a slower rate leads to more significant thermal gradients and, consequently, more pronounced residual stress formation and thermal warping defects.

One way to prevent this bulk heating effect is to utilise idle time between depositions. Another way is to implement "closed-loop" process monitoring, i.e. a way of monitoring temperature and adjusting laser power delivery to maintain a constant temperature across deposited layers. Marangoni convection can also be of use, since the motion it induces increases the convection with the surroundings, providing a way of transportation of thermal energy from the centre of the melt pool to its periphery [10].

The morphology of the melt pool can be affected by the same Marangoni forces. In Figure 2.20 two different situations are presented, where the dissimilar temperatures and surface tensions generate different-sized melt pools.

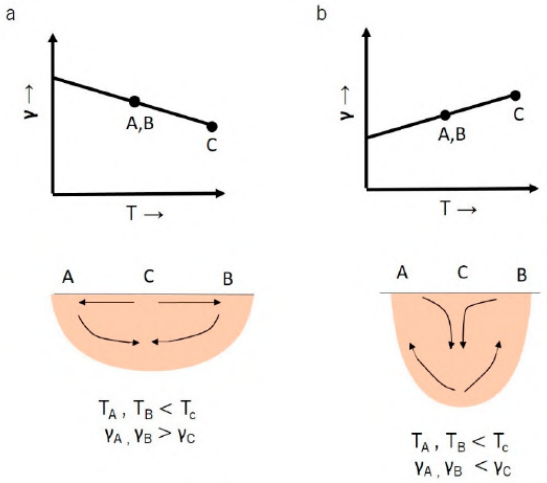

Figure 2.20: Marangoni forces influence on the melt pool geometry. (a) Melt pool geometry when the surface tension gradient is negative; (b) Melt pool geometry when the surface tension gradient is positive. Temperature on the x-axis and surface tension on the y-axis. Adapted from [22].

The slope of the graph is the surface tension gradient and it governs the melt pool movement. For most pure metals, the surface tension decreases with increasing temperature, which results in a negative surface tension gradient, such as the one presented in Figure 2.20 a). In this case, the surface tension is greater in the cooler regions at the boundary of the melt pool, inducing a radially outward surface flow, carrying molten metal from the centre to the edge of the melt pool, originating a shallow weld. In opposition, Fe-based melts will have a positive surface tension gradient, such as the one in Figure 2.20 b). In this case, the surface tension is higher in the high temperature region (centre of the pool), which produces a radially inward flow, which consequently induces a downward flow in the centre of the melt pool, generating a deep and narrow pool that re-melts and induces more thermal cycles to previously deposited layers[39].

Moreover, due to bulk heating, the top layers may have more hydrophilic melt pools, meaning that these layers can be wider than the previously deposited layers. This is called the "mushroom effect" and also affects the geometric precision achieved by DED [10].

Bulk heating and thermal cycling

The temperature of the substrate and melt pool are different. Hence, conduction heat transfer through the part thickness occurs. Moreover, due to the difference of temperature between the part and the surrounding environment, convection and radiation also take place. This heat loss results in cooling that, coupled with laser passing that induces heating, subject the part to repetitive heating and cooling cycles which in its turn, can result in heat treatment and microstructural evolution. Hence, top layers are subjected to less thermal cycles than lower layers. This fact can originate parts with different properties along its height [10].

Bulk heating, as already explained, is nothing but a heat accumulation that occurs incrementally, if no idle time is used, as new layers are deposited. It can adversely affect residual stresses due to excessive thermal gradients, when the substrate's temperature does not rise at the same rate. It can also alter the melt pool geometry, since a higher bulk temperature originates a hotter HAZ and, consequently, a bigger melt pool. Moreover, with each new layer deposited, the part will start to get thicker and wider, giving rise to a larger HAZ and a more pronounced "mushrooming effect" [35].

Another issue related to bulk heating is the fact that with extreme temperatures vaporisation of the melt pool may occur, leading to loss of alloying elements. Oxidation of the previously deposited layers may also occur.

The partial remelting of previously deposited layers or substrate guarantees a good bonding connection between layers. The amount of layers that are remelted depends on the penetration depth of the melt pool and HAZ. Low penetration may originate parts with bad adhesion between layers, while high penetration may cause excessive thermal cycles in previously deposited layers, originating more residual stresses. Approximately, 1.5 layers are melted for each pass in a DED process. The amount of remelted layers can be tweaked by increasing laser power or decreasing traverse speed, for instance [35].

Effect of substrate and idle time

The thermal history of a part can be significantly influenced by the size, thermal capacitance and initial temperature of the substrate used. The difference in temperature between the melt pool and the substrate allows for conduction heat transfer between them, where the substrate acts as a heat sink, especially in the first few layers, where the conduction heat transfer to the substrate is more significant. Usually, larger substrates have a greater heat extraction capacity than thinner ones, assuming they are made of the same material. Hence, thinner substrates, with lower idle time, promote heat build-up.

Pre-heating of the substrate is a common practise in DED processes, since it originates lower thermal gradients. It can reduce residual stresses and the risk of cracking and thermal distortions. Nonetheless, increasing the substrate initial temperature also originates lower cooling rates, which may contribute to heat build-up, and limits the grain refinement.

The idle time is the amount of time that DED stops and allows the part to cool before the next deposition begins. Since the part is allowed to cool down, build up heat can be reduced.

2.1.6 Metallic powder

The feedstock for metal additive manufacturing processes is metallic powder. Hence, it is important to understand how the powders are produced, how they can be characterised and how their properties may affect the process.

Although it is essential to additive manufacturing, metallic powders are also used for other applications, such as Metal Injection Moulding (MIM), Brazing, or to produce components parts of materials that would be very hard to make by conventional processes [40]. One example of this are Tungsten Carbide tools. They are very hard and difficult to machine, so they can be produced by sintering of metallic powders.

Metal powder production

There are many ways of producing metallic powder, especially designed to fulfil the requirements of their many applications. They can be produced by either mechanical methods or chemical methods and the proper selection of production method depends on the required production rates, powder properties and the physical and chemical properties of the material [7]. The most used mechanical methods are milling, atomisation and mechanical alloying. Moreover, the chemical methods are associated with physical and chemical transformations, whereas the chemical composition and structure of the final metal powder may differ from the raw materials.

Atomisation is the most used method for metallic powder production for metal additive manufacturing processes, owing to its versatility. It can produce feedstock over a wide range of production rates and a wide variety of powder average diameters (from 10 μm to 1000 μm) due to the many variants of the method [7]. It is surely the dominant method for producing pre-alloyed powders from aluminium, brass, iron, stainless steels, titanium alloys and superalloys [40].

By definition, atomisation is the change of a liquid into small droplets [41]. Theoretically, any material available in liquid form can be atomised. In the case of high-melting materials, the result is a powder. Most atomisation processes generate powders with less than 150 μm of diameter. Nonetheless, bigger particles can be produced, in which case the atomisation process can be called shotting or granulation. The main types of atomisation are the following [40]:

- Two-fluid atomisation;
- Centrifugal atomisation;
- Vacuum or soluble-gas atomisation;
- Ultrasonic atomisation.

Only the first two types are going to be covered for the purpose of this dissertation, since they are the most common.

The main principle of atomisation procedures is the dispersion of a thin stream of molten metal by forcing it with impact of gas, high pressured water, plasma, rotating forces, and so on. Due to this impact, the molten metal is divided into small droplets, which crystallise in flight before they reach the atomiser walls [42].

In two-fluid atomisation, the liquid metal is broken up into droplets by impingement of high pressure jets of a second fluid, which can be gas, water, oil or plasma. This type of atomisation is the most used worldwide, comprising about 95% of the industrial powder metallurgy capacity. A schematic of a water atomisation process with its key variables is presented in Figure 2.21.

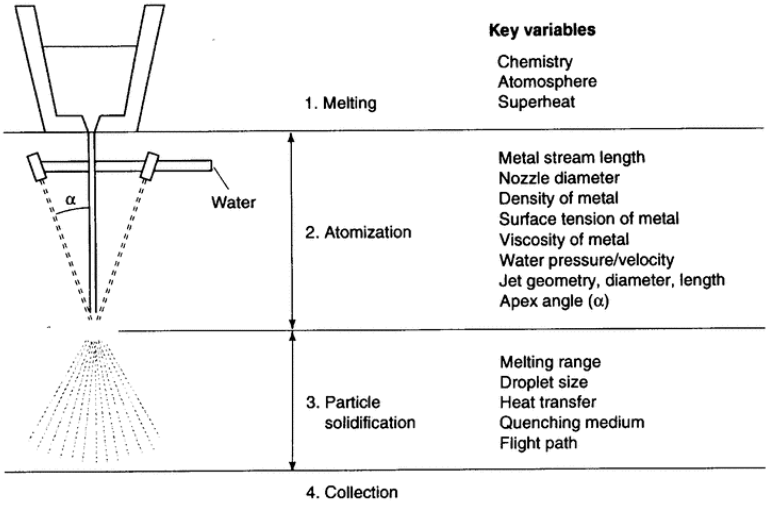

Figure 2.21: Schematic of a water atomisation system. Adapted from [40].

The main processing steps involved can be verified: melting, atomising and solidifying of the respective metals and alloys. Water atomisation is mainly used for the production of powders of non-reactive materials. Although it is cheaper than the other methods of atomisation, the high cooling rates originate particles with irregular shapes and sizes [40, 42]. It is important to note that the average particle size is controlled by the pressure of the water jets, the melt temperature and the apex angle, α, which is the angle between the water and the metal stream [40].

Gas atomisation is the main process for producing metal powders for additive manufacturing, where the liquid metal is disrupted by a high velocity gas, such as air, nitrogen, argon or helium. Hence, the atomisation occurs by kinetic energy transfer from the gas to the metal [40]. Using an inert gas allows for the production of powders from reactive metals, without oxidation problems. This process is expensive, but the particles produced have a fine spherical shape, high cleanliness and homogeneous microstructure. If compressed air is to be used, the particle shapes can have several defects, like particle satellites and internal porosity [42].

Plasma atomisation was developed to produce powders of reactive materials with high purity. The main materials used are alloys with high melting point, such as titanium, zirconium and tantalum. The initial material for this kind of atomisation is a metal wire and the resulting particles are highly spherical and have a low oxygen content [42].

The rotating electrode process (REP) is a type of centrifugal atomisation where the metal is spinned before melting. The material, in the form of a consumable electrode is rotated at about 1500 rpm while it is being melted by an arc. The molten metal is centrifugally ejected in the form of molten metal droplets that solidify. A schematic of this process is presented in Figure 2.22.

This process can have some advantages over the aforementioned methods. In fact, many high-duty materials to be processed into powder may benefit not being in contact with a liquid container made out of a refractory ceramic. This ensures that no ceramic particles are added into the powder mix, resulting in cleaner particles, with less impurities [40]. REP is mainly utilised in high volumes of production due to its high costs and machine size.

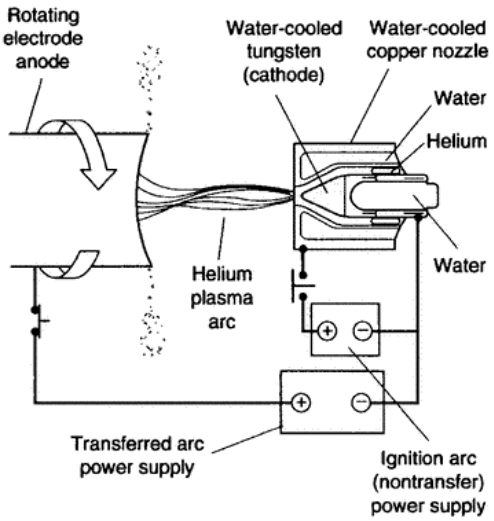

Figure 2.22: Schematic of a plasma rotating electrode process [40].

Metal powder characterisation

Selection of the proper powder metallurgy method ensures that the feedstock is adequate for additive manufacturing. To guarantee process repeatability and ability to produce consistent and uniform parts, the bulk properties of powders must be characterised and labelled.

One of the most important properties of metal powder for AM is the particle size distribution, since it contributes to the particle packing behaviour, which is known to influence the final density and porosity levels of a part. The packing behaviour of the particles is much more important to PBF processes than DED ones, since in the former, the particles are placed together inside the powder bed, and having powder with different sizes arranged together reduces the porosity. The particle size distribution is often represented in a histogram, in which the x-axis corresponds to the particle diameter and the y-axis denotes the number of particles within a certain range of diameters. It has an inherent probabilistic nature [7, 40, 42].

This characteristic of the powder is usually provided by the powder supplier and can be obtained by several methods, such as Sieving, Laser Diffraction and Image Analysis Methods [7].

The powder morphology represents the shape of the powder. It also determines the packing behaviour of the particles, i.e. how well the particles lie together and form an interlocking pattern, and influences the density, powder flow and, ultimately, the surface roughness. Moreover, the particles have different levels of sphericity and this property is primarily given by the type of metal powder formation method. Usually, with increasing level of sphericity, higher the cost and better the final part quality [40].

The powder flow is important to determine the flowability of the powder. The type of feedstock delivery systems of DED was already discussed and the powder flow characteristics influence how easily the powder flows from the reservoir and fills empty spaces, contributing to a constant and uniform feedstock delivery [40]. Spherical powder flows better than irregular powder, since the particles do not interlock in each other [42].

The cohesive strength is the capacity of the powder to stick together. Many metal powders can behave like liquids when poured from a reservoir, which means they have very little to no cohesive strength. On the other hand, other powders stick together

when lightly pressed, meaning they have a certain cohesive strength. This property may influence how the feedstock is delivered by a deposit. If the powder has enough cohesive strength, a small "rat hole" can form in the smallest cross section of the deposit, preventing feedstock delivery until an external force is applied. This undesirable occurrence is shown in Figure 2.23.

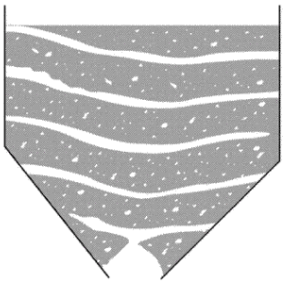

Figure 2.23: Example of a "rat hole" formation and consequent no-flow situation. Adapted from [40].

The internal and external friction coefficients are associated with the cohesive strength and the powder flowability. While internal friction is caused by the solid particles flowing against each other, the external friction occurs between the powder and the deposit walls. It is important to know this powder property prior to the design of the feedstock delivery system, to ensure that the flow of the powder is not interrupted.

The bulk apparent density is another very important parameter of the powder. It defines the actual volume occupied by a mass of loose powder [40]. The particle size distribution and the shape of particles have a clear influence in apparent density [42]. Generally, apparent density decreases with decreasing particle size and decreases as the particles get more irregular [40].

Powder recycling

Powder recycling is becoming a widely accepted practise in metallic AM industries, owing to the high costs of the material feedstock. This thematic is even more relevant for PBF processes, since a powder bed is used, as it would be impossible to discard the remaining powder after a part production [43]. Generally, in the case of DED, less powder is wasted during the process, but powder recycling can always be an option. Therefore, it is important to understand the dangers and consequences of powder recycling if not performed correctly and with adequate criteria.

After an AM process and the removal of the produced part, the remaining powder consists of partially melted or sintered particles in the vicinity of the laser beam and loose powder away and unexposed to the laser beam. The latter can be recycled and used in further processes. However, the former should be discarded, since its properties can be substantially different from the virgin powder properties, as it was already somewhat affected by the heat source [7].

A. Saboori et. al [44] investigated the effect of powder recycling on the microstructure and mechanical properties of AISI 316L fabricated by DED. They found that both the virgin and recycled powder had some particles with satellites, a common defect originated by the gas atomisation process that produced the powders. Besides these defects, the recycled powder showed the presence of splats, which are small amounts of material that were

melted and then re-solidified, adhering to other particles, and surface oxides. In Figure 2.24 the scanning electron microscopy (SEM) images of their investigation is presented.

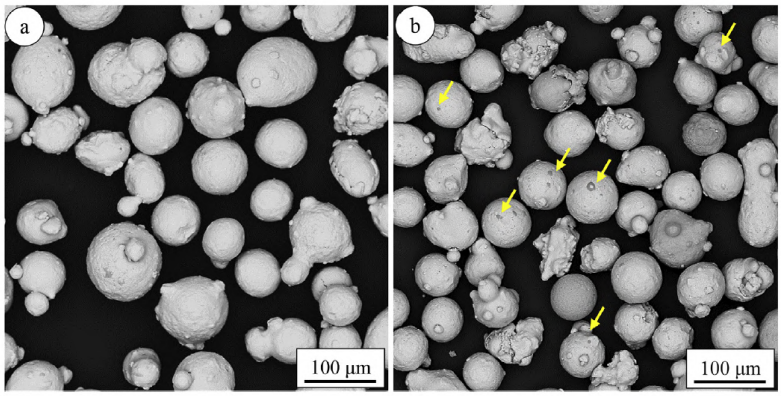

Figure 2.24: Images of: (a) fresh and (b) recycled powder. Yellow arrows point to the surface oxides [44].

The authors concluded that the recycling of powder had almost no influence on the porosity, inclusion levels and on the microstructure of the powder, as the recycled powders showed the same microstructural features as the virgin powder. Nevertheless, some spherical oxide inclusions were found [44].

The main difference between recycled and virgin powders was found in the stress-strain curve shape, especially in the elongation to fracture. In fact, samples produced with fresh powder has an elongation to fracture 50% higher than the samples produced with re-used powder. Moreover, the latter samples exhibit a sudden drop in the stress-strain curve just after reaching the ultimate tensile strength, as it can be observed in Figure 2.25. Both these aspects were attributed to the formation and clustering of the inclusion particles, which drastically reduce the capacity of plastic deformation of the AISI 316L matrix [44].

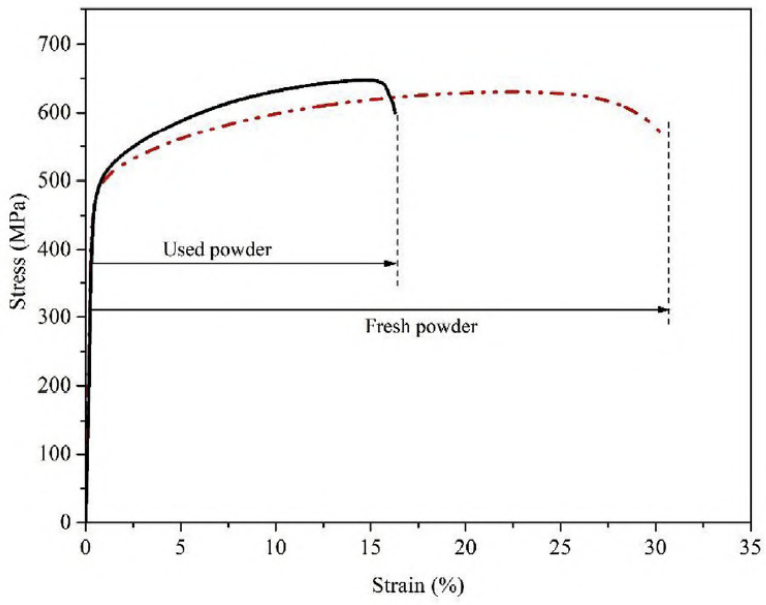

Figure 2.25: Stress-strain curves of samples produced by fresh and recycled powders [44].

The fracture surface of the samples was also object of study. The fracture surface of a

sample produced by virgin powder and recycled powder is shown in Figure 2.26.

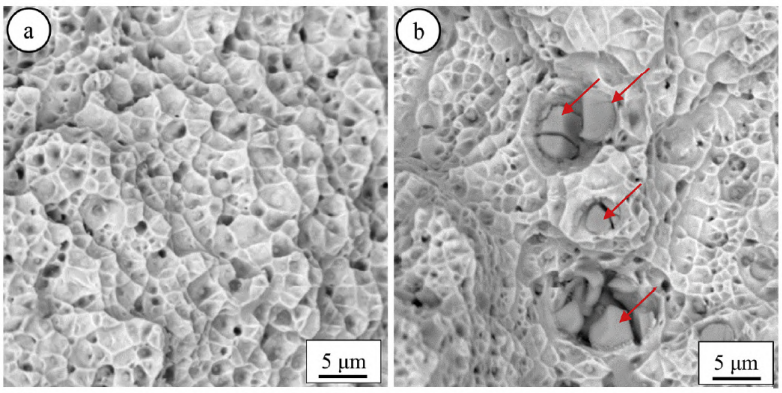

Figure 2.26: Tensile test fracture surface of a sample produced by: (a) fresh powder and (b) recycled powder. Red arrows point to fractured coarse oxides [44].

As it can be observed, larger dimples are present around coarse oxides which are fractured as a consequence of crack propagation, further supporting the theory that those oxides indeed limit the elongation of the matrix [44].

However, contrary conclusions were drawn from other authors. P. Carrion et. al [45] studied the powder recycling effects on the tensile behaviour of additively manufactured Ti-6Al-4V parts and concluded that powder recycling did not have significant effects on the tensile behaviour of the specimens.

L. C. Ardila et. al [43] studied the effect of powder recycling in the production of Inconel 718 parts by SLM, using a self-developed recycling method. After 14 iterations of powder usage, the particle size distribution changed slightly, having more coarse particles and less fine ones. The powder remained mostly spherical, without an increase in satellite or crater numbers, or other defects, such as porosity or oxidation. The particle distributions after 1, 7 and 14 iterations are shown in Figure 2.27.

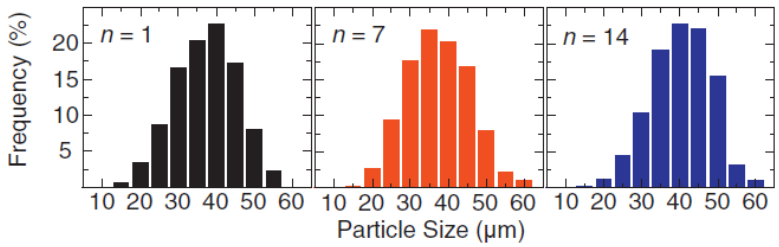

Figure 2.27: Powder size distributions after 1, 7 and 14 iterations of powder usage. Adapted from [43].

The samples were also subjected to Charpy V impact tests and showed very similar toughness properties. The authors concluded that powder recycling had no significant harmful effects in terms of powder quality and toughness of the part up to 14 iterations, meaning that, in this case, the advantages of cost saving largely outweigh the small risks of powder recycling [43].

The topic of powder recycling is still controversial, as contrary conclusions are being drawn from different investigators. The procedure of powder recycling as well as the material at hands may play an important role in whether or not powder recycling has an effect on material properties.

Safety

The handling of metallic powders must be performed with extreme care due to their hazardous nature. During DED, powder is blown out of a nozzle onto a molten pool. However, as already mentioned, not all the powder gets deposited into the pool. In fact, there is always powder waste and dust. This dust is released into the atmosphere of the DED chamber and workers can be exposed to it after depositions [7, 40].

The high surface-area-to-volume ratio of the powders and their very small particle size may increase their chemical reactivity in biological exposures, such as inhalation or ingestion, and increase the risk of flash fires and explosions.

These materials may pose real toxicological and ecological risks due to their sizes. For example, inhalation of powder dust is possible without any filtering to the lungs, causing adverse health effects, which may range from minor impairment to irreversible diseases and life-threatening conditions, such as pneumoconiosis, cancer, systemic poisoning, and irritation and inflammatory lung diseases [7, 40].

Hence, it is extremely recommended that personal protective equipment is utilised to prevent diseases. The equipment includes a proper mask, clothing and gloves. A good reference to personal protective equipment required for DED is the "Standard for Combustible Metals" [46].

2.1.7 Defects

Defects are a common consequence of an inadequate definition of process parameters. These may arise during powder production or during part manufacturing. Knowing how the most common defects are formed, it is of upmost importance to be able to reduce or avoid them. Some of the most frequent defects are discussed in this subsection.

Chemical composition changes

Changes in the chemical composition of printed parts can happen due to two main occurrences: solute segregation and loss of alloying elements.

The layered aspect of AM, coupled with the fact that the composition of the substrate and the deposit are quite different, promote the redistribution of solute particles, leading to the segregation and formation of different microstructural bands. Moreover, a higher solidification rate ensures a higher probability of solute trapping [22].

Loss of alloying elements is a problem that can be originated by having elements in the alloy with distinct boiling points, meaning that a preferential vaporisation of a few elements might take place. Ultimately, this phenomenon promotes the loss of alloying elements and gives rise to compositional unhomogeneity along the printed material [22, 47].

Porosity

Porosity is one of the most common defects that can arise during metal AM processes. They can be of three different types: lack of fusion, keyhole porosity or gas porosity.

Lack of fusion is an interlayer type of porosity, which occurs due to a lack of sufficient energy input to melt the feedstock material, leading to un-melted regions. Usually, it can be found near the substrate or between layers or tracks, when the laser power is insufficient, when the traverse speed is too high for the selected laser power or when the overlap between tracks is too little. These defects are easily spotted under light microscopy, due to their irregular and elongated shapes [7, 22].

Keyhole formation is mainly due to high energy density input that originates a narrow and deep melt pool with a V shape by vaporising the metal underneath it. These keyholes are extremely unstable, forming and collapsing on a regular basis, leading to voids inside the deposit that consist of entrapped vapour [7]. A keyhole type of melt pool is presented in Figure 2.28.

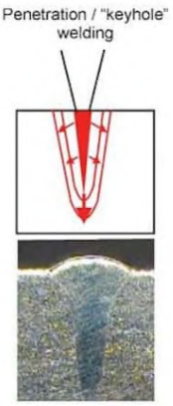

Figure 2.28: Keyhole formation. Adapted from [48].

Gas porosity or intralayer porosity is linked to the usage of carrier gas and its entrapment (if the process utilises it), supersaturation of dissolved gases, chemical reactions that produce gases within the melt pool, low solidification rates or vaporisation of volatile alloying elements [7, 22]. These pores are usually spherical in shape, which means they can be easily distinguished from the lack of fusion pores.

It is important to note that gas porosity could be formed during the metal powder atomisation process. The gas may be trapped during that process and remains in the structure of the part after additive manufacturing, meaning that sometimes this kind of porosity does not depend on the AM process itself or its properties. A schematic of lack of fusion and gas porosity is presented in Figure 2.29.

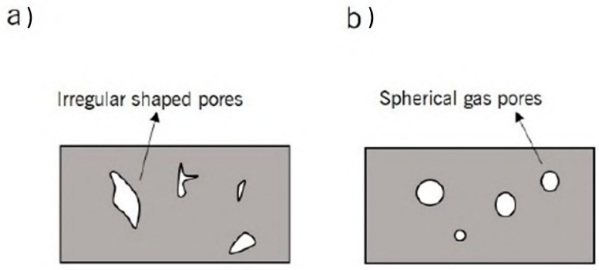

Figure 2.29: Porosity due to: (a) lack of fusion and (b) gas entrapment. Adapted from [22].

P. A. Kobryn et. al [36] investigated the effect of laser power, traverse speed and substrate thickness of the porosity levels of a laser deposited Ti-6Al-4V. They found that, in general, porosity tended to decrease when the laser power and traverse speed increased. The authors stated that the effect of the laser power was expected, since a higher laser power provides more energy to melt the same amount of powder. However, the decrease of porosity with increasing traverse speed was unexpected. Nevertheless, it was attributed to

a decrease in powder delivery, meaning that the same laser power now melts less particles, each of them receiving more energy. Regarding the substrate thickness, porosity was found to have higher levels in thin substrate deposits [36].

J. Choi et. al [30] studied the influence of powder feed rate and laser powder on porosity levels of a laser aided direct metal deposition H13 tool steel. It was experimentally verified that a higher powder feed rate originates a part with more pores. They also stated that a higher laser power also provided parts with less pores, although high laser power results in low porosity levels regardless of powder mass flow rate. The authors suggested that by designing a deposition tool-path with higher overlap, one can produce parts with less porosity levels, since the power density is increased.

M. J. Kim et. al [23] analysed the porosity levels of Inconel 625 produced by DED with laser power and powder mass flow rate variations. The effect of mass flow rate was similar to the previously mentioned studies, but the effect of laser power was not conclusive. Regarding the effect of powder feed rate on porosity, many other studies were performed, all reaching the same conclusions [25, 49].

Surface roughness

Surface roughness is a major defect in DED parts, since it does not allow them to be ready for use right after the process. Due to its intrinsic characteristics, DED parts always need to undergo some type of machining operation to reduce surface roughness and to get them into the desired dimensions.

It is influenced by the precision and resolution of the process, the powder quality and size, the part's design and the processing parameters. The resolution can be divided into two: the xy plane resolution and the z-axis (direction of build) resolution. The former is given by the laser diameter and focal point while the latter is determined by the layer thickness [47]. Moreover, the "staircase" characteristic of AM built parts, shown in Figure 2.30, also takes its toll on z-axis resolution [50].

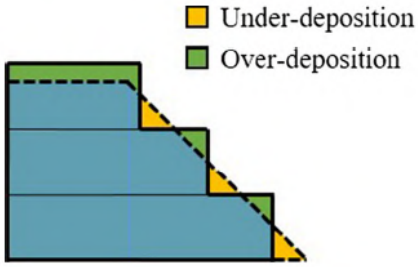

Figure 2.30: "Staircase" error of AM builds [50].

The melt pool disturbance and several process parameters can also dictate the surface roughness of a part. For instance, a high surface disturbance of the melt pool can enhance the mixing of the powder particles in the melt pool, preventing partially assimilated powder particles, which are a common cause of high surface roughness [34].

K. Shah et. al [34] studied the influence of melt pool variables and process parameters in the surface roughness of Laser Direct Metal Deposition of Inconel 718 powder on a Ti-6Al-4V thin wall. The authors found that the mean surface roughness decreases with an increase in powder flow rate and with an increase in the velocity of the carrier gas. Moreover, the overall lower mean surface roughness was achieved using a pulsed wave laser. As already mentioned, a high surface disturbance of the melt pool originates parts

with lower surface roughness, by reducing the amount of partially assimilated particles, such as the ones presented in Figure 2.31.

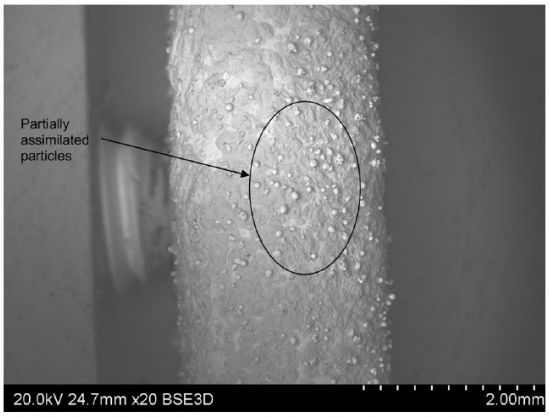

Figure 2.31: Partially assimilated powder particles on one of the produced samples [34].

The authors also noted that a higher velocity of carrier gas flow rate originates increased surface agitation, further decreasing the mean surface roughness.

An explanation of partially assimilated particle formation was given by P. Y. Lin et. al [25]. They claimed that when the cladding width was greater than the laser spot size, the powder particles would not stick to the sides of the build section. As the cladding diameter was smaller than the laser spot size, however, powder particles at the melt pool's edge melted and dripped down the side wall, where they solidified and adhered. A schematic of the given explanation is presented in Figure 2.32.

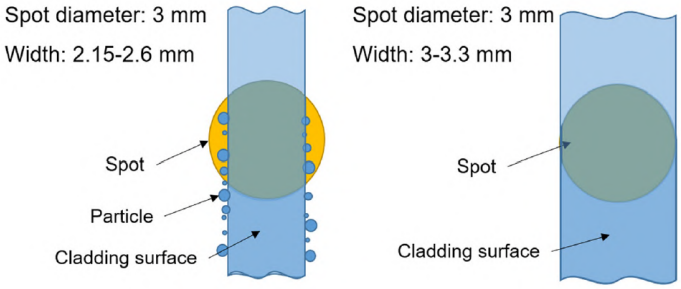

Figure 2.32: Partially assimilated particles formation mechanism [49].

A. Angelastro et. al [49] investigated the impact of powder flow rate, laser power and scanning speed on the surface roughness of nickel-based alloy samples obtained by Direct Laser Metal Deposition. They experimentally concluded that an increase in both powder flow rate and laser power originated a higher surface roughness, while an increase in scanning speed reduced the surface roughness. No explanation was given by the authors to potentially explain this behaviour.

Solid state cracking

Solid state cracking mainly results from the continuous heating and cooling cycles of additive manufacturing, insufficient temperature or excessive one. It presents itself as one of five types, differing by the cracking mechanism and preferred crack location:

- Ductility-dip cracking;
- Reheat and post heat treatment cracking;
- Strain age cracking;
- Lamellar or delamination cracking;
- Copper contamination cracking.

The first type, ductility-dip cracking, occurs when a reduction in ductility is verified during the process and takes place preferentially intergranular, along the grain boundaries [7]. It is more frequent in copper, nickel, titanium, aluminium and austenitic stainless steels.

Reheat cracking is related to post-processing heat treatments which are used to reduce residual stresses. Although it is not very frequent, it can occur in low-alloy steels due to their secondary carbide producers contained within the melt, such as chromium, molybdenum or vanadium. Moreover, materials with high chance of precipitation may experience this type of solid state cracking [7].

Strain age cracking can be formed in precipitation-strengthened nickel based alloys, such as Inconel 625 or 718, and appears mostly intergranularly. Alloying elements that retard the formation of precipitates are useful to prevent this type of cracking [7].

The last two solid state cracking types are both observed in the HAZ and present detrimental effects on the mechanical properties of parts produced by AM [7].

Residual stresses

The very distinctive thermal cycle that an AM produced part undergoes can be characterised by the rapid heating, high cooling rates and simultaneous melting of the top material layer and the re-melting of previously deposited or solidified layers. The excessive thermal gradients and fast solidification of the material frequently causes the formation of residual stresses in the part. Residual stresses may lead to part distortion and, as will be discussed in further sections, may be responsible for crack nucleation, which can affect the fatigue performance of a part [19, 51].

Residual stress formation in AM can be explained by two different models: the Temperature Gradient Mechanism (TGM) and the cool-sown phase model. In the former, during the heating phase, the energy source promotes heating of the bulk material which then tends to expand. This expansion of the heated material is restrained by the surrounding cooler material. This way, a compressive stress state is formed near the heated zone. When the heating source is removed, the heated material begins to solidify and tends to shrink, but then again the shrinkage is partially constrained by the plastic strain formed earlier. Besides, a tensile stress zone is formed, being balanced by the previously mentioned compressive zone. A visual description of this process can be seen in Figure 2.33 [51].

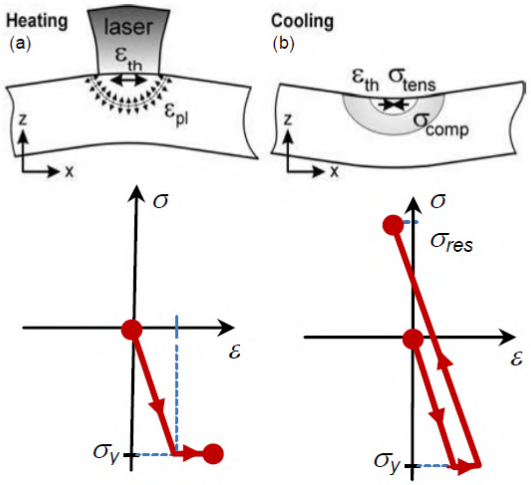

Figure 2.33: Residual stress formation model during: (a) heating phase and (b) cooling phase [51].

The cool-down phase model uses the layer build-up characteristic of AM to explain the residual stress formation. As already explained, some of the previously deposited material will be remelted and then re-solidified. The re-solidification leads to a contraction of the material, which is restrained by the previous layers, leading to a tensile stress zone formation in the newly deposited material [51].

Extensive research led to the conclusion that residual stresses near the centre of the part tends to be compressive, whereas they tend to be tensile near the surfaces. Each new deposited layer is under tensile stresses, while the previously deposited layer is under compressive stresses. The deposition of additional layers leads to a decrease in the level of stress and reduces the adjacent tensile stresses, eventually leading to compressive ones [51–53]. A typical residual stress distribution of a part produced by SLM is shown in Figure 2.34.

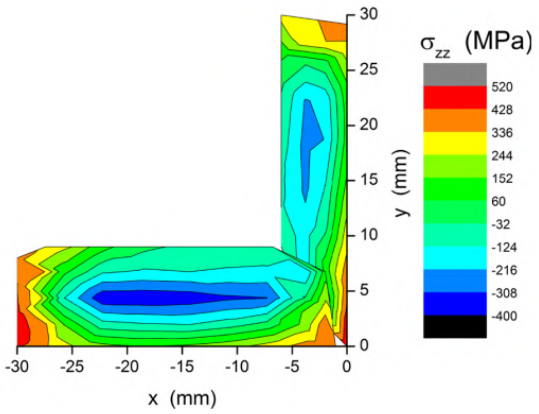

Figure 2.34: Residual stresses distribution in a SLM produced part. Adapted from [54].

Generally, compressive residual stresses are beneficial since they prevent crack growth. On the other hand, tensile residual stresses promote crack nucleation and growth [55].

By reducing the thermal gradient in the process, it is possible to reduce residual stresses formation. Hence, preheating of the substrate or building plate is a common practise.

Nonetheless, it has been shown that the scanning strategy influences residual stress formation. In fact, it was discovered that a "chessboard" pattern would cause less distortion than other scanning methods for PBF processes [51].

Metal AM processes are usually performed on top of a building plate. This plate represents a restrain to material movement, therefore the formation of residual stresses may be inevitable. When the part is separated from this plate, the relieving of stresses may originate part distortions. Hence, in many cases, a stress relief heat treatment is performed prior to part-plate separation in order to limit part distortion [51].

L. Li et. al [53] investigated residual stress distribution in parts produced by DED. The novelty of the author's study was the deposition of material in a substrate of similar and very distinct material from the deposited one. It was found that when the deposited material is very different from the substrate material, an unusually high temperature gradient is formed in the interface between the part and the substrate. This temperature gradient then originates very high residual stresses, leading to large part distortions after the removal from the substrate. However, this might not always be the case, as it depends on the properties of the considered materials.

2.1.8 Post-processing

Additive manufacturing has appeared as an alternative to traditional manufacturing techniques such as machining. The latter shapes the part by removing material from unwanted zones from a metal block. Although AM can be used to achieve complex parts in near net shape, with minimal operator interaction, it still requires some post processing.

Powder removal

In DED, several types of powder are used. While these powders are blown to the molten pool, not all particles get deposited and used for layer building. Some of them are deposited near the workpiece and are not melted in the process. After the deposition process, this excess, unused powder needs to be removed, usually by brushing, since they are loosely adhered to the surfaces. After, this powder can be thrown off or recycled [7].

In the case of Powder Bed Fusion processes, the part is completely surrounded by un-melted powder. The part needs to be removed and the excess, loosely adhered powder is to be brushed off.

Part removal

Both in Powder Bed Fusion and in DED, the first layers are built on top of a platform or substrate. Removing the part from this platform is the next post processing step. After this, the substrate can be rehabilitated and used again. The most common methods for separating the part and the substrate are sawing and electrical discharge machining (EDM). The latter is especially applied to conductive materials and does not depend on material hardness. In fact, EDM creates a small field of residual stresses with up to 100 μm of depth, making it an almost ideal candidate for the part removal [7].

Machining operations

Most parts built by DED need to undergo machining operations to guarantee that the geometric tolerances are fulfilled, since AM cannot guarantee them directly. The surface roughness of the as built part may also be higher than required, which means machining or grinding is necessary [7].

Heat treatment

The rapid and repetitive thermal cycles in PBF and DED may originate various defects. Major issues with these technologies include [7]:

- Porosity;
- Anisotropy: The building direction affects the properties of the material;
- Inferior properties: Mechanical properties of AM parts might be inferior to those produced by traditional methods;
- Residual stresses: Non-uniform and rapid cooling originates high residual stresses and part distortion.

Most of these issues with AM can be smoothened by applying a specific thermal treatment, such as: stress relieving, annealing, quenching, solution heat treatment, ageing, HIP, among others.

2.2 Fatigue

The classical monotonic stress-strain curve is one of the most common ways to represent some of the most important mechanical properties of a material. In order to obtain such curve, the load is uniaxially gradually applied to allow the strain to develop, until the destruction of the specimen. In these static conditions, each stress is only applied once [56]. However, in real life service conditions, mechanical failures imply a complex interaction between load, time and service environment. The loads applied may be monotonic, constant, variable, uniaxial, multiaxial and their application times can range from milliseconds to centuries. Temperatures can vary between cryogenic and 1000 °C, remaining constant or changing during service [57].

Fatigue is the progressive accumulation of damage in a material, originated by fluctuating, cyclic stresses or strains. One of the main characteristics of fatigue, is that the stresses the material is subjected to are below the ultimate strength and, quite frequently, below the yield strength of the material. Hence, one application of the load is not enough to cause failure. Instead, the stress is applied a very large number of times [56].

Trivially, two major types of failure can occur: ductile fracture and brittle fracture. When ductile mechanical parts fail under static load, they frequently develop a visible deflection, based on the material's ductility, because the stress exceeds the yield strength. Therefore, this deformation can be seen as a warning sign and the part can be replaced before failure [56]. This type of fracture involves high plastic deformation and is associated with high energy absorption. Moreover, the fracture occurs mainly by microvoid coalescence formed at inclusions and secondary phase particles.

On the other hand, brittle fracture is undesirable since there are fewer warning signs. It is almost sudden, total and dangerous. This kind of fracture contains almost no plasticity and involves low-energy absorption. It is also characterised by a very high crack growth velocity during fracture [56, 57].

Fatigue fracture is very similar to brittle fracture, in the sense that there can be no warning signs. Its appearance is also alike the brittle one, as the fracture surfaces are flat and perpendicular to the stress axis, with no presence of necking. However, the features of the fracture are quite different since they arise from different phenomena. There are three main stages of fatigue fracture development [56]:

- Stage I: Fatigue crack nucleation;
- Stage II: Fatigue crack propagation
- Stage III: Fatigue fracture.

In Stage I, one or more microcracks can initiate due to cyclic plastic deformation and then undergo a small crystallographic propagation, from 2 up to 5 grains about the origin. Most of the times, fatigue cracks originate in discontinuities in the material, where the cyclic stress is a maximum, forming a stress concentration location. Usually, Stage I cracks are not visible to the naked eye. In Stage II, cracks transform from microcracks to macrocraks, forming parallel plateau-like surfaces separated by longitudinal ridges. These features, generally referred to as "beachmarks", are smooth and normal to the direction of maximum tensile stress. They appear as a result of opening and closing of the cracked surfaces, as they rub together. In Stage III, the sudden final fracture occurs when the remaining material cannot support the loads applied. The fracture can be brittle, ductile or a combination of both [56, 57]. A fatigue fracture surface of hot rolled Inconel 625 is presented in Figure 2.35, where the three main stages of fatigue are clearly visible.

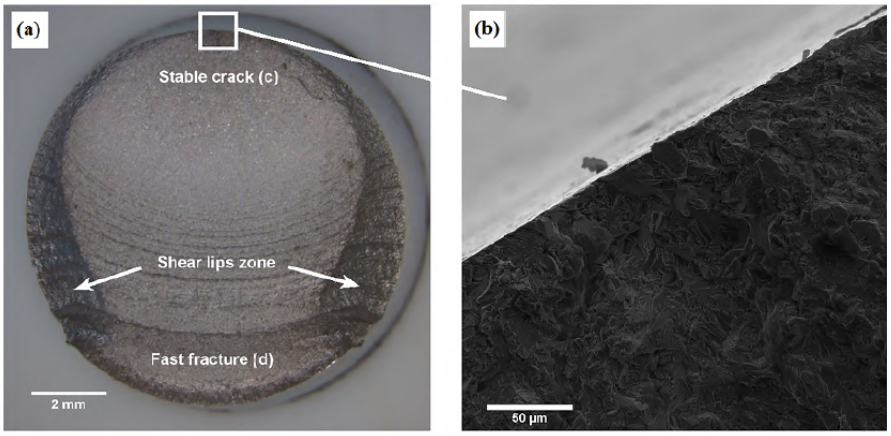

Figure 2.35: Inconel 625 fracture surface, showing the three main stages of fatigue: Nucleation of cracks in the upper region of the specimen, followed by crack propagation and "beachmarks" formation, ending with fast, sudden fracture of the specimen [58].

It is simple to design a component against a static failure, because the knowledge on the matter is extensive and the behaviour of the material is foreseeable. However, fatigue is only partially understood, due to its intrinsic somewhat unpredictable nature. There are three major approaches used to roughly predict when, if ever, a cyclically loaded component will fail by fatigue over a period of time, i.e. the fatigue life of a component [56]:

1. Stress-Life Methods;
2. Strain-Life Methods;
3. Linear-Elastic Fracture Mechanics Methods.

Fatigue life can be defined as the number of cycles of strain or stress variations, N, under a specific amplitude, that a part can be subjected to before failure. Most references divide fatigue life in two ranges: Low-cycle fatigue, from 1 cycle up to 10^5 cycles and

High-cycle fatigue, when $N > 10^5$ cycles [56]. However, if one takes into account the damage mechanisms that take place during cyclic loading, four different ranges of fatigue life can be specified:

- Ultra low-cycle fatigue: number of cycles is lower than 10^2 [59];
- Low-cycle fatigue: number of cycles between 10^2 and 10^5;
- High-cycle fatigue: number of cycles between 10^5 and 10^7;
- Ultra high-cycle fatigue or gigacycle fatigue: number of cycles is higher than 10^7 [60].

The stress-life approach is, as the name specifies, based on stress cycles. It is the least accurate approach, especially for low-cycle applications, since a lot of plastic deformation occurs. Yet, it is the most common method used to predict fatigue life since it is the easiest to implement and represents high-cycle fatigue well enough.

The strain-life approach is especially accurate for low-cycle applications, since it provides a more detailed analysis of the plastic deformation that takes place in localized regions where the stresses and strains are considered.

The fracture mechanics approach presupposes that a crack is already present. Hence, it is used to predict crack growth, based on stress intensity factors and can help to understand the mechanics of crack propagation.

These enumerated methods are explained in detail in the following subsections.

2.2.1 The stress-life method

In order to determine the fatigue life of a material using the stress-life method, or S-N approach, specimens are subjected to repeated or varying loads of predefined magnitudes while the cycles or stress reversals to failure are counted. Fluctuating stresses often take the form of a sinusoidal pattern, such as the one shown in Figure 2.36 [56, 57].

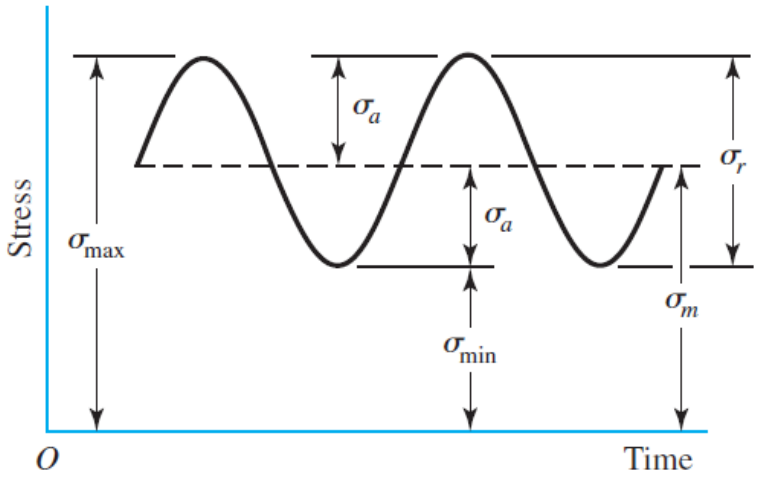

Figure 2.36: Constant amplitude sinusoidal [56].

In fatigue testing, the loads applied are defined either by a constant stress range ($\Delta\sigma$) or a constant stress amplitude (σ_a). The stress range is the difference between the maximum stress (σ_{max}) and the minimum (σ_{min}) in a cycle [56]:

$$\Delta\sigma = \sigma_{max} - \sigma_{min} \tag{2.3}$$

The stress amplitude is half of the stress range:

$$\sigma_a = \frac{\Delta\sigma}{2} = \frac{\sigma_{max} - \sigma_{min}}{2} \tag{2.4}$$

The stress ratio, R, is an important parameter to characterise the fluctuating stress. Conventionally, tensile stresses are considered to be positive, while compressive ones are regarded as negative. The stress ratio is given by the ratio of σ_{min} to σ_{max}:

$$R = \frac{\sigma_{min}}{\sigma_{max}} \tag{2.5}$$

Stress ratios of -1 and 0 are two of the main test condition references for fatigue testing. $R = -1$ is commonly referred to as "fully reversed condition" since σ_{min} is equal to $-\sigma_{max}$. Thus, the loading is alternating between a zero mean. The mean stress, σ_m, is given by:

$$\sigma_m = \frac{\sigma_{max} + \sigma_{min}}{2} \tag{2.6}$$

$R = 0$ is called "pulsating tension", since the tension fluctuates between zero and σ_{max}. Consequently, $\sigma_{min} = 0$.

Another stress parameter that is frequently used in literature is the amplitude ratio, A, defined by:

$$A = \frac{\sigma_a}{\sigma_m} \tag{2.7}$$

Although the definition of cycle is relatively controversial [57], in fatigue testing, one cycle ($N = 1$) usually constitutes two reversals of the load, i.e., a single application and removal of the load and then another application and removal of the load in the opposite direction. Logically, $N = \frac{1}{2}$ means the load is applied once and then removed, which is the case of the simple tension test [56].

It is important to note that these fluctuating loads can be axial, flexural, torsional, of shear or a combination of them.

In order to determine the fatigue strength of the material, it is required to perform a considerable number of tests, because of the statistical nature of fatigue. In fact, several specimens are tested at different stress amplitudes and the number of cycles until fracture is recorded. Afterwards, this fatigue testing data is plotted on semi-log (being the number of cycles in log) or log-log coordinates, resulting in the classical S-N diagram or curve [56]. The ordinate of the S-N curve may be the stress range, $\Delta\sigma$, or the stress amplitude, σ_a and is always accompanied by a statement of the number of cycles to failure, N_f, or to crack initiation, N_i. In many cases, the ordinate in S-N curves goes by the name of fatigue strength, S_f. A typical S-N curve of UNS G41300 steel is presented in Figure 2.37 [56]:

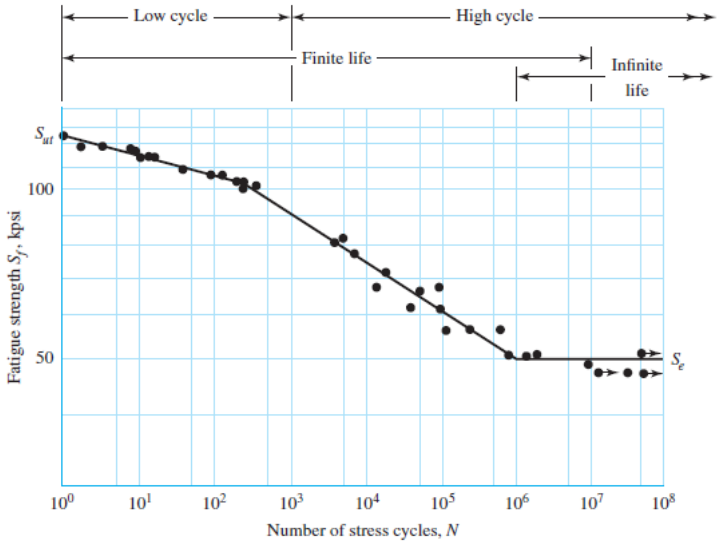

Figure 2.37: S-N curve for a material that presents a fatigue limit [56].

As it can be observed, the number of cycles until fracture increases with the decrease of the stress range that is applied. Nevertheless, there are two types of behaviour that can be observed, depending on the material analysed. One of the behaviour is the one shown in Figure 2.37, commonly observed in ferrous alloys. After the initial decrease in stress range that leads to an increase of fatigue life, further improvement on the fatigue life does not prompt a decrease in load capacity. This limit is named endurance limit S_e or fatigue limit, which is the stress range below which fatigue failure will not occur, no matter how great the number of cycles are [56]. Hence, the material is considered to have an infinite life in terms of fatigue. Recently, the concept of infinite life is being questioned, as gigacycle fatigue tests are showing fatigue failure after the conventional 5×10^6 cycles.

The boundary between finite and infinite life is not well defined, as it depends on the considered material. However, it usually ranges between 10^6 and 10^7 cycles for steels. When the fatigue test ends without fracture, i.e., the number of cycles reaches the infinite life and the specimen did not fracture, the testing stops and the trial is represented with an arrow in the S-N curve, meaning that a "runout" occurred [56].

On the other hand, common in non-ferrous alloys such as aluminium, do not present a fatigue limit, which means fatigue failure will always occur once a certain number of cycles is reached. In Figure 2.38, a S-N curve for a material that does not have an endurance limit is presented [57].

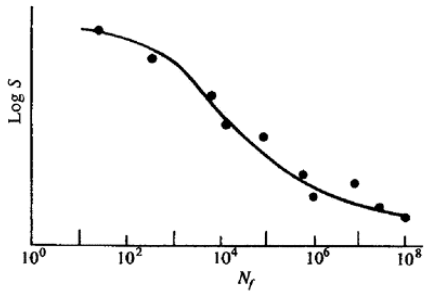

Figure 2.38: S-N curve for a material that does not present a fatigue limit [57].

Mean stress effect on S-N behaviour

As previously mentioned, the S-N curves are usually built based on the applied stress range or stress amplitude. However, the mean stress can have a notorious influence on fatigue behaviour, as it can be seen in Figure 2.39 [57]. Note that alternating stress and stress amplitude is the same parameter.

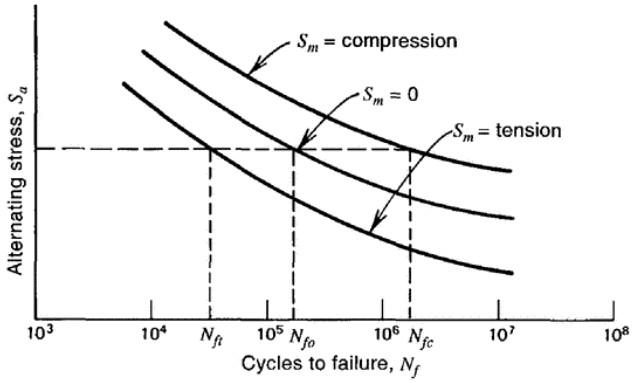

Figure 2.39: Effect of mean stress in fatigue life [57].

Moreover, by the analysis of Figure 2.39 it can be verified that, in general, tensile mean stresses are detrimental and compressive mean stresses are beneficial to fatigue life. This effect is even more pronounced in high cycle fatigue, since the mean stresses are responsible for the opening and closing of microcracks, in the case of tensile and compressive mean stresses, respectively [56, 57, 61].

Over the years, a few models were proposed based on experimental data, that relate the stress amplitude with the mean stress or mid-range stress. Some of the proposed models are presented in Figure 2.40 [56].

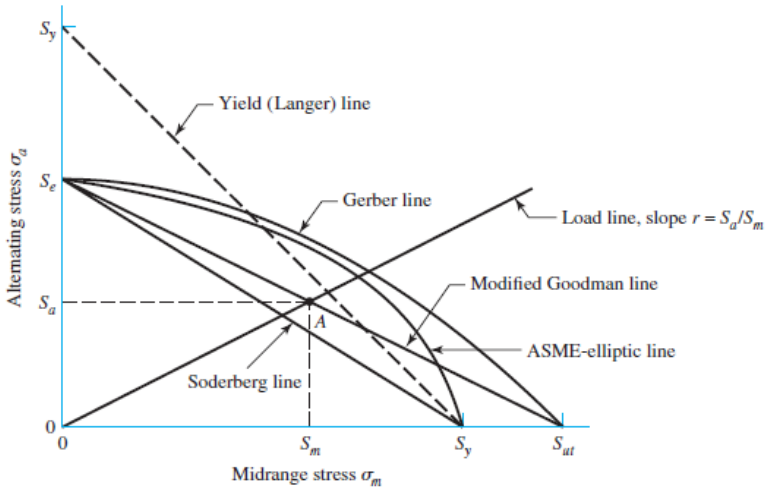

Figure 2.40: Fatigue diagram showing various criteria of failure [56].

For each criterion, points on or above the respective line indicate failure. It is important to note that the model proposed by Soderberg is the most conservative one, since it does not allow stresses higher than the yield strength [56].

The equations of the criteria presented in Figure 2.40 are shown forthwith:

$$\textbf{Soderberg} \quad \frac{\sigma_a}{S_e} + \frac{\sigma_m}{S_y} = 1 \tag{2.8}$$

$$\textbf{Modified Goodman} \quad \frac{\sigma_a}{S_e} + \frac{\sigma_m}{S_{ut}} = 1 \tag{2.9}$$

$$\textbf{Gerber} \quad \frac{\sigma_a}{S_e} + \left(\frac{\sigma_m}{S_{ut}}\right)^2 = 1 \tag{2.10}$$

$$\textbf{ASME-elliptic} \quad \frac{\sigma_a}{S_e} + \left(\frac{\sigma_m}{S_y}\right)^2 = 1 \tag{2.11}$$

$$\textbf{Langer} \quad \sigma_a + \sigma_m = S_y \tag{2.12}$$

where S_y is the yield strength and S_{ut} is the ultimate tensile strength. These criteria allow the comparison of fatigue test data with different load ratios, as long as they are performed on the same material.

2.2.2 The strain-life method

The strain-life approach utilises the concept of total strain to predict the fatigue life of a component. As previously mentioned, fatigue failure frequently arises from a local discontinuity, such as a notch, crack, pore or other stress concentration feature. When the stress at a discontinuity exceeds the elastic limit, plastic strain is known to occur. So, cyclic plastic strains precede any fatigue fracture, which means the behaviour of materials under cyclic deformation is of extreme importance [56, 57, 61].

Bauschinger found out that the stress-strain behaviour of a material obtained by a monotonic tension or compression test is different from the one obtained under cyclic loading. During his experiments, Bauschinger verified that the yield strength in tension or compression was modified after applying a load of the opposite sign that caused inelastic deformation [57].

In 1910, Bairstow confirmed via experiment the theory first proposed by Bauschinger that the elastic limit of iron and steels can be changed, either upwards or downwards, by cyclic variations of stress: the elastic limit of annealed steals is likely to increase after cycles of stress reversals, while cold-drawn steels display a decrease [56].

Later, R. W. Landgraf investigated the low-cycle fatigue behaviour of many high strength steels and made several stress-strain hysteresis loops, like the one shown in Figure 2.41.

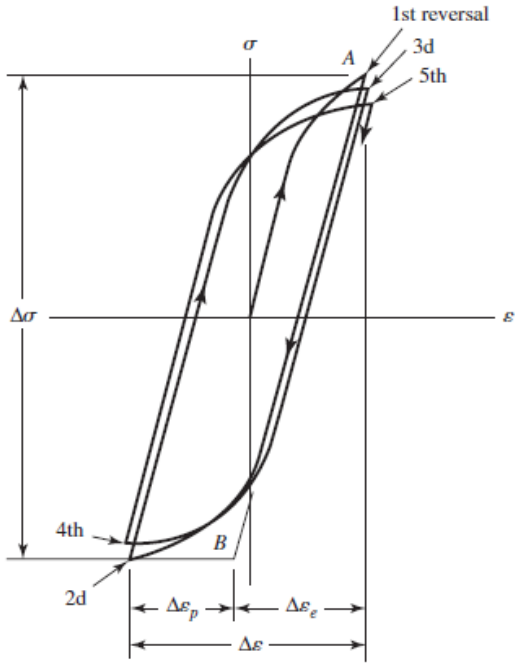

Figure 2.41: True stress-true strain hysteresis loops of a cyclic softening material [56].

In Figure 2.41, only the first few cycles have been plotted and the graph is slightly exaggerated to clearly show the aforementioned behaviour. In this case, the strength decreases with stress reversals, as demonstrated by the fact that the successive reversals occur at decreasing stress. This means the material shows a cyclic softening, i.e., the material becomes less resistant to the applied strain. Instead, other materials may be strengthened, which means the material shows a cyclic hardening behaviour [56, 57].

The material softening/hardening behaviour is tightly related to the density and arrangement of the dislocation structure and substructure of the metal. Inelastic deformation and dislocation can be related by "slip", which is a shear deformation of the material. Slip commonly occurs in metals within individual grains by dislocations moving along crystallographic planes. In the case of materials that are initially soft, the dislocation density is low. So, as inelastic deformation occurs under stress/strain cycling, the density of dislocations increases promptly, which means the dislocation's mobility is going to be damaged. In conclusion, if dislocations are constrained to move and slip is minimised, the material is said to cyclic harden. When the material is initially hard, the inelastic strain may reconfigure the dislocation structure into one that offers less resistance to deformation. This way, the material cyclic softens [57].

It is to be noted that the changes in cyclic deformation are more pronounced at the beginning of cyclic loading. The material usually stabilises progressively with prolonged cycling [57]. Moreover, as mentioned earlier, plasticity is more impactful in low-cycle fatigue [56, 57].

Physically, the area within a hysteresis loop is energy dissipated per unit volume during a cycle. This energy is usually in the form of heating. Additionally, this energy represents the plastic work that results from the loading cycle [57].

Mathematically, the cyclic stress-strain equation can be represented by the Ramberg-Osgood equation:

$$\varepsilon_a = \frac{\Delta\varepsilon}{2} = \frac{\Delta\sigma}{2E} + \left(\frac{\Delta\sigma}{2K'}\right)^{1/n'} = \frac{\sigma_a}{E} + \left(\frac{\sigma_a}{K'}\right)^{1/n'} \tag{2.13}$$

where ε_a is the total strain amplitude, $\Delta\varepsilon$ is the total true strain range, $\Delta\sigma$ is the true stress range, E is the Young Modulus of the material, σ_a is the true stress amplitude, K' is the cyclic strength coefficient and n' is the cyclic strain hardening exponent [57].

Strain-life fatigue curves can be plotted on log-log coordinates. An example of such curve is presented in Figure 2.42.

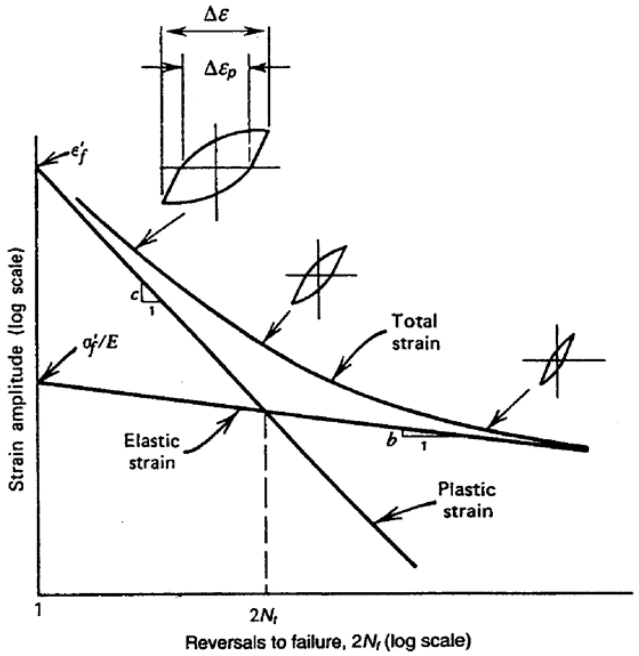

Figure 2.42: Strain-life curves showing total, elastic and plastic strain components [57].

The total strain amplitude can be resolved into two components: elastic and plastic strain from the steady-state hysteresis loops. These two components summed up give the total strain at a given life, N_f, and can be approximated as straight lines.

The total strain amplitude is half of the total strain range. Hence:

$$\frac{\Delta\varepsilon}{2} = \frac{\Delta\varepsilon_e}{2} + \frac{\Delta\varepsilon_p}{2} \tag{2.14}$$

where $\Delta\varepsilon_e$ is the true elastic strain range and $\Delta\varepsilon_p$ is the true plastic strain range. As it can be observed in Figure 2.42, at short lives or large strains, the plastic component is predominant. At longer lives or smaller strains, the elastic strain component is predominant [57]. The elastic strain straight line can be transformed into Basquin's equation [57]:

$$\frac{\Delta\varepsilon_e}{2} = \frac{\sigma_a}{E} = \frac{\sigma'_f}{E}(2N_f)^b \tag{2.15}$$

where σ'_f is the fatigue strength coefficient: the true stress corresponding to fracture in one reversal and b is the fatigue strength exponent: the slope of the elastic-strain line [56].

The relation between plastic strain and life is given by the Manson-Coffin relationship [57]:

$$\frac{\Delta\varepsilon_p}{2} = \varepsilon'_f(2N_f)^c \tag{2.16}$$

where ε'_f is the fatigue ductility coefficient: the true strain corresponding to fracture in one reversal and c is the fatigue ductility exponent: slope of the plastic-strain line [56]. Therefore, from Equation (2.14), the total strain amplitude can be written as:

$$\frac{\Delta\varepsilon}{2} = \frac{\sigma'_f}{E}(2N_f)^b + \varepsilon'_f(2N_f)^c \tag{2.17}$$

Equation (2.17) expresses the relation between fatigue life and total strain, and can be used to estimate the fatigue life of a part when strain or other cyclic characteristics are given [56].

2.2.3 Fracture mechanics approach

The fracture mechanics method deals with the inevitability of cracks and their growth during service of components, which led to the "damage-tolerant" design. In this approach, it is presumed that cracks exist even before service begins and that its growth is acceptable until it becomes critical. At this point, the part must be removed from service. Hence, it predicts the growth of cracks in a given material to estimate its fatigue life, using linear elastic fracture mechanics (LEFM) as the main tool [56, 57].

Cracks can form due to fatigue or they can appear as a consequence of the manufacturing process, such as voids or metallurgical discontinuities like particle inclusions or second phase precipitates. In order to make predictions on fatigue life based on fatigue crack growth, several pieces of information are often needed, including the following [57]:

- The stress intensity factor, K;
- The fracture toughness, K_c;
- The crack growth rate expression, da/dN;
- The initial crack size, a_i or a_0;
- The critical crack size, a_f or a_c.

These parameters are addressed thereafter.

Loading modes

Cracks can propagate in three different modes, as shown in Figure 2.43. Mode I, generally called as the opening mode, is the most common in fatigue, primarily because cracks tend to grow on the plane of maximum tensile stress. It is originated by a tensile stress field. Mode II is the sliding mode, which is due to in-plane shear. Mode III is called the tearing mode and it is created by out-of-plane shear. Nevertheless, mixed-mode crack propagation, i.e., when more than one loading mode is present, is also common.

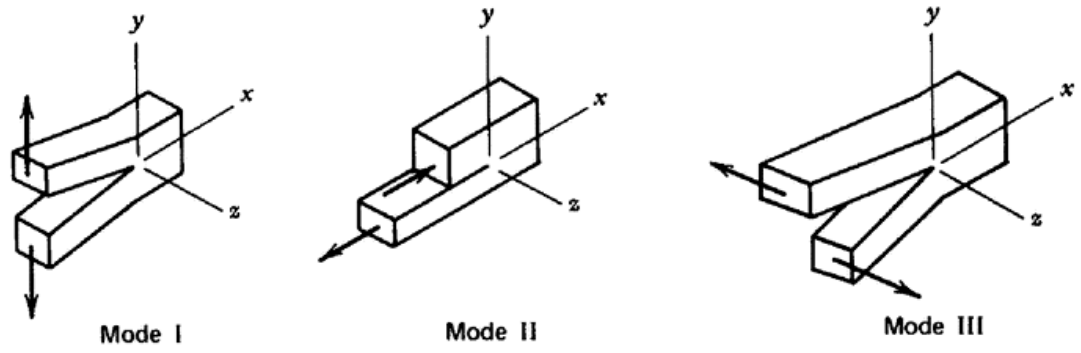

Figure 2.43: Loading modes of crack propagation [57].

Since mode I is the most common mode of failure, only this loading mode will be covered. By applying subscript "I" to the parameters mentioned further, the mode I loading is the one being referred to.

Stress intensity factor

The foundation for the development of the stress intensity factor, K was laid by Griffith. He understood that crack propagation in brittle materials, such as glass, was governed by the stress field, the crack length and the material properties. Taking that into account, Griffith proposed Equation 2.18, that would be the basis of LEFM [57]:

$$G_I = \frac{\pi a \, \sigma_{rem}^2}{E} \tag{2.18}$$

where G_I is the strain energy release rate, which represents the elastic energy per unit crack surface area required for crack propagation, a is the crack length and σ_{rem} is the remotely applied stress [57]. Note that Griffith's work was only on brittle materials.

Later on, Irwin applied the previous theory to metals with small plastic deformation at the crack tip. He introduced the stress intensity factor, K_I (of mode I), to quantify the severity of the stress surrounding a crack tip [56]. The stress intensity factor is a function of geometry and size of the crack, loading mode and, in some cases, a modification factor, β_m, as well. It is given by:

$$K_I = \beta_m \sigma_{rem} \sqrt{\pi a} \tag{2.19}$$

Using Griffith's energy approach, Irwin showed that for plane stress and for $\beta_m = 1$ [57, 61]:

$$G_I = \frac{K_I^2}{E} \tag{2.20}$$

and for plane strain:

$$G_I = \frac{K_I^2}{E}(1 - \nu^2) \tag{2.21}$$

where ν is the Poisson's ratio. For these contributions, Griffith and Irwin are known as the "early father" and "modern father" of Fracture Mechanics [57].

Fracture toughness

When the stress intensity factor reaches a certain critical value, K_{IC}, the crack propagates in an unstable and unpredictable way, without the increase in load. The critical stress intensity factor is a property of a material that depends on the material itself, the crack propagation mode, environment conditions such as temperature, strain rate and a function of width of the specimen and crack length [57]. It is given by:

$$K_{IC} = \sigma_c \sqrt{\pi a_c}\, f\left(\frac{a_c}{w}\right) \tag{2.22}$$

where σ_c is the applied nominal stress at crack instability, a_c is the crack length at instability and w is the width of the specimen. This critical factor is also named the fracture toughness of the material.

Moreover, K_{IC} is the critical value of the stress intensity factor, K for a given load, geometry and crack length necessary to cause fracture. Furthermore, it also represents the stress intensity factor at the last cycle of fatigue fracture [57].

Crack growth

Crack nucleation and subsequent growth is due to variations of stress and to the presence of tension in each stress cycle. If stresses fluctuate between the limits of σ_{min} and σ_{max}, the stress intensity factor, presented in Equation (2.19), can be expressed in terms of stress range, $\Delta\sigma$. Hence, the stress intensity range per cycle is:

$$\Delta K_I = \beta_m(\sigma_{max} - \sigma_{min})\sqrt{\pi a} = \beta \Delta\sigma \sqrt{\pi a} \tag{2.23}$$

In order to develop useful fatigue strength data, a reasonable number of specimens of the same material are tested at various levels of $\Delta\sigma$. If one assumes the presence of an initial crack with a length of a_i, the crack growth as a function of number of stress cycles, N, will naturally depend on the stress range, $\Delta\sigma$, or, as shown by Equation (2.23), depend on ΔK_I. The value of K_I below which the fatigue crack won't propagate is called the fatigue crack threshold, ΔK_{th} [56].

The crack length as a function of the number of cycles can be plotted in graphs such as the one in Figure 2.44.

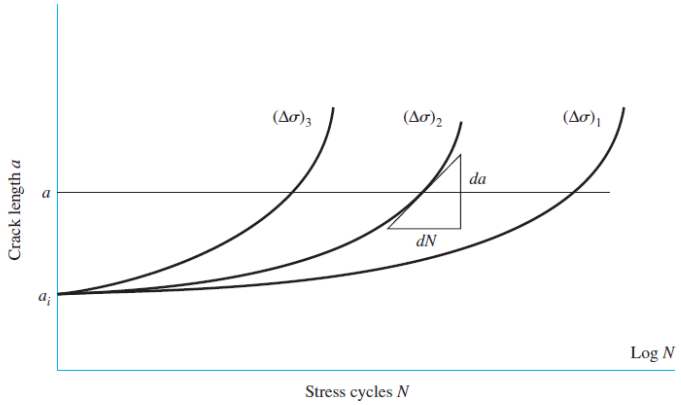

Figure 2.44: Increase of crack length as a function of number of cycles [56].

In Figure 2.44, three stress range levels are presented, $(\Delta\sigma)_3 > (\Delta\sigma)_2 > (\Delta\sigma)_1$. It can be said that a higher stress range leads to a faster crack growth rate per cycle, da/dN, since for the same number of cycles, $(\Delta\sigma)_3$ originated a lengthier crack than the other two stress ranges [56].

The crack growth per cycle can also be plotted in a graph versus ΔK in log-log coordinates. An example of such plot is presented in Figure 2.45.

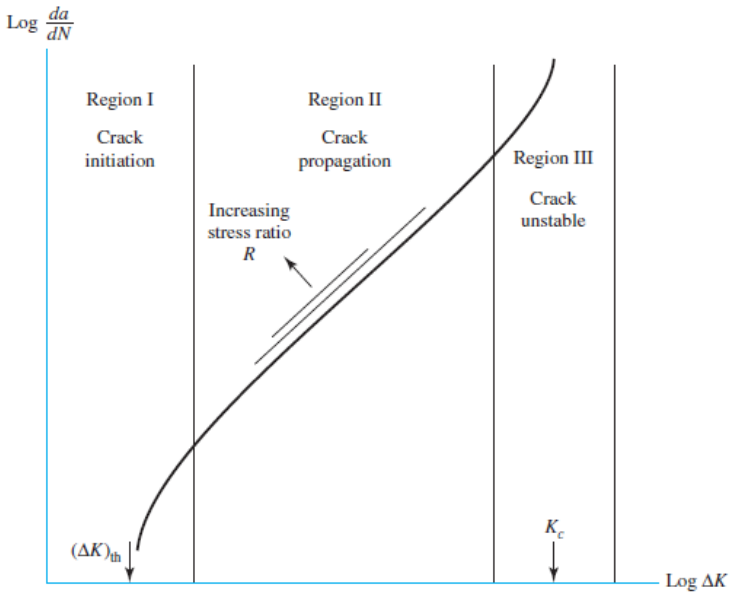

Figure 2.45: Crack growth per cycle as a function of the stress intensity range [56].

The three main stages of fatigue cracks can be visualised in Figure 2.45. Although it can vary between materials, from threshold to rupture, a given material in high cycle fatigue regime will spend approximately 85-90 % of life in region I, 5-8 % in region II and 1-2% in region III [56].

One important particularity to note is that the stage II (crack propagation) data is linear in log-log coordinates. This fact allows for an estimation of the remaining life of a cyclically stresses part after discovery of a crack, since the crack growth in stage II is stable and can be predicted, as long as K_c is known [56].

Assuming that the crack is found early in stage II, the crack growth in region II can be approximated by the Paris equation, which is of the form:

$$\frac{da}{dN} = C(\Delta K_I)^m \tag{2.24}$$

where C and m are empirical material constants. Integrating both sides of Equation (2.24):

$$\int_0^{N_f} dN = N_f = \frac{1}{C}\int_{a_i}^{a_f} \frac{da}{(\beta_m \Delta\sigma\sqrt{\pi a})^m} \tag{2.25}$$

where a_i is the initial crack length, a_f is the final crack length (that corresponds to failure) and N_f is the estimated number of cycles to failure after the initial crack is formed.

2.2.4 Endurance limit modifying factors

The fatigue life curves are obtained by curve-fitting several results obtained by experimentation. The scatter in data is inevitable, which means fatigue design has a probabilistic characteristic and is influenced by external factors. Furthermore, the endurance limit of a mechanical member is expected to be somewhat different from the results obtained in laboratory [56].

Marin proposed a series of factors that quantified the effects of surface condition, size, loading type, temperature of the environment and miscellaneous items and modified the endurance limit to better represent reality. Marin's equation can be written as [56]:

$$S_e = k_a k_b k_c k_d k_e k_f S'_e \tag{2.26}$$

where k_a is the surface condition modification factor, k_b is the size modification factor, k_c is the load modification factor, k_d is the temperature modification factor, k_e is the reliability factor, k_f is the miscellaneous-effects modification factor, S'_e is the rotary-beam test specimen endurance limit and S_e is the endurance limit at the critical location of a machine part in the exact conditions of use.

2.2.5 Stress concentration and notch sensitivity

It was previously briefly discussed that the presence of discontinuities or irregularities, such as holes, grooves or notches in a part increases the theoretical stresses in the immediate surroundings of the discontinuity [56].

Notches cannot be avoided in many cases. For instance, if a bolted connection is required, there is going to exist a discontinuity at the joint. Therefore, significant effort needs to be made to understand notch influence in the mechanical properties, so that the mechanical design of such components can be performed in a conscientious way [57].

Notches concentrate stresses and strains. The maximum resulting stress due to the presence of an irregularity or discontinuity is represented by the stress-concentration factor, K_t, given by the ratio of the maximum stress, σ, at the notch to the nominal stress, σ_0:

$$K_t = \frac{\sigma}{\sigma_0} \tag{2.27}$$

The nominal stress can be obtained by the elementary stress equations. The stress concentration factor depends on the geometry of the part and the type of loading, while being independent on the type of material. The analysis of geometric shapes to determine K_t are complex. Therefore, experimental and numerical techniques are employed.

When dealing with cyclic loading, as in fatigue, a reduced value of K_t can be used and the effective maximum stress in fatigue is [56]:

$$\sigma_{max} = K_f \sigma_0 \tag{2.28}$$

where K_f is the reduced value of K_t, commonly named as fatigue stress-concentration factor. The usage of this factor instead of K_t is more conservative and, for the same fatigue life, it can be defined by [56]:

$$K_f = \frac{\text{maximum stress in notched specimen}}{\text{stress in notch-free specimen}} \tag{2.29}$$

Some materials are not fully sensitive to the presence of notches during cyclic loads. Hence, the notch sensitivity, q, is the relation between K_t and K_f:

$$q = \frac{K_f - 1}{K_t - 1} \tag{2.30}$$

The notch sensitivity can range between zero and unity. If $q = 0$, then the material has no sensitivity to notches. On the other hand, if $q = 1$, then $K_f = K_t$ and the material has full notch sensitivity. Notch sensitivity for specific materials can be obtained experimentally [56].

2.2.6 Cumulative fatigue damage

Frequently, a mechanical component is subjected to cyclic loads with variable amplitudes. Take a car as an example. When travelling in the asphalt of the highway, the amplitude of the cyclic load on the suspension system might be approximately constant. However, when riding in square stones or other irregular pavement, the amplitude of the load is very uneven, such as the one presented in Figure 2.46.

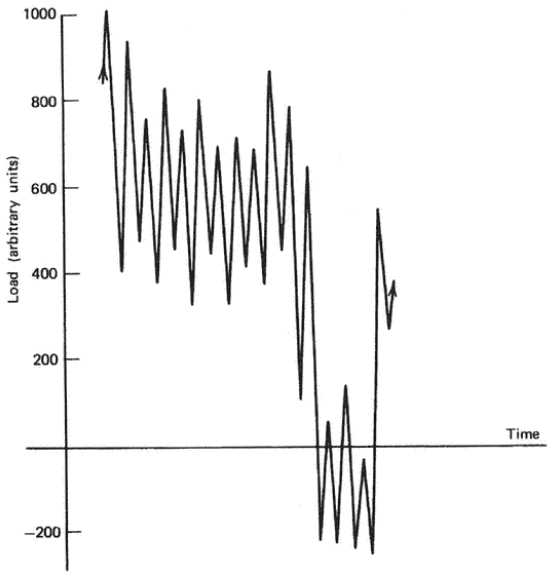

Figure 2.46: Variable amplitude load spectrum [57].

The term "cumulative damage" refers to the effects of loading cycles that are not of constant amplitude. One way of accounting for the fatigue damage of such variable amplitude load is dividing the loading spectrum in smaller blocks of load with constant amplitude. The individual blocks fatigue damage can then be summed linearly and the cumulative fatigue damage of the variable amplitude spectrum can be calculated [57].

One of the most common cumulative damage law is the Palmgren-Miner cycle-ratio summation rule, also referred to as Miner's rule. It can be written as [56]:

$$\sum \frac{n_i}{N_i} = c \tag{2.31}$$

where n_i is the number of cycles at stress level σ_i and N_i is the number of cycles to failure at the same stress level. Trivially, when $c = 1$, failure occurs [56].

2.2.7 Fatigue testing

Fatigue life assessment relies heavily in experimental testing. Systematic, constant amplitude fatigue testing was first started off by Wöhler, the author of S-N curves, on railway axles in the 1850s [57]. There are two main types of testing machines regarding the load/displacement control. One type is known as "force-controlled constant amplitude machines", while the other type is referred to as "displacement-controlled machines". Other types of devices, such as the "strain-controlled machines" are getting more and more common.

In "load-controlled" tests, the load amplitudes do not change, despite the changes in material properties or crack growth. On the other hand, in "displacement-controlled" machines, the displacement amplitude is constant, which means the load amplitude changes with the specimen cyclic hardening or softening, decreasing as the cracks in the specimen arise and propagate. Hence, for a given initial stress amplitude, constant displacement machines may provide longer fatigue life than load-controlled machines, since the load amplitude decreases during testing [57].

Nevertheless, the functioning principle includes generating an input signal of load, displacement or strain and applying it through an hydraulic actuator or electric motor. In the most recent machines, the specimen response is measured via load cell, clip gage or other displacement transducers and compared with the input. The difference between them drives the system. The test frequency is also of interest, ranging between mHz to kHz, since it gives the speed of the test (which may last for days) [57].

To ensure repeatability across multiple fatigue tests, ASTM Standards provide guidelines for specimen preparation, methods and procedures. Some of the most pertinent standards are given in Table 2.3.

Table 2.3: ASTM Standard practices related to fatigue testing of metals [57].

E466	Conducting Force Controlled Constant Amplitude Axial Fatigue Tests of Metallic Materials
E467	Verification of Constant Amplitude Dynamic Forces in an Axial Fatigue Testing System
E468	Presentation of Constant Amplitude Fatigue Test Results for Metallic Materials
E606	Strain-Controlled Fatigue Testing
E647	Measurement of Fatigue Crack Growth Rates

In terms of fatigue specimens, there are a few which can be categorised according to their mode of loading. These include direct axial stress, plane bending, rotating beam, alternating torsion and combined stress [62]. They can be used to evaluate total fatigue life, including crack nucleation and crack growth until failure and even fatigue crack propagation. They are usually polished in order to minimise the effect of surface roughness [19]. Some of the most common fatigue testing specimens are presented in Figure 2.47.

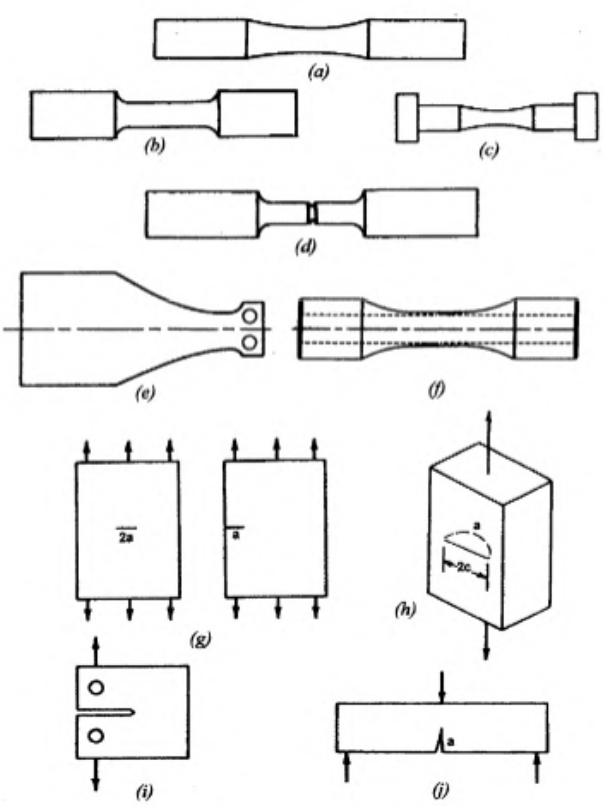

Figure 2.47: Fatigue testing specimens: (a) Rotating bending; (b) Axial uniform; (c) Axial hourglass; (d) Axial or bending with circumferential groove; (e) Cantilever flat sheet/plate; (f) Tubular combined axial/torsion with or without internal/external pressure; (g) Axial cracked sheet/plate; (h) part-through crack; (i) Compact tension; (j) Three-point bending [57].

Recently, some other specimens were created as an answer for the new challenges that arise from the most recent technologies and techniques.

2.2.8 Nicoletto specimens

As briefly mentioned before, the feedstock material for metal AM processes such as PBF and DED is quite costly, even more so than the feedstock used for conventional production methods. Hence, specimen production for extensive investigation and characterisation of parts produced by AM methods or to study their process parameters may require substantial capital investment, which make testing nonviable for many companies. This issue is even more relevant when trying to characterise fatigue behaviour, since normally more than a dozen specimens are needed in order to build a S-N curve.

In an attempt to solve these issues, G. Nicoletto [63] developed an original test methodology using a miniature specimen especially designed for fatigue testing. The proposed miniature specimen, presented in Figure 2.48 with one euro coin for scale, shares the nominal cross-sectional area (5 x 5 mm^2) with the specimen geometry used in a Schenk-Erlinger type machine, having a sectional modulus of $W = 20.8$ mm^3. Moreover, the value of the miniature specimen's sectional modulus is almost the same of the common rotating bending specimen geometry with 6 mm diameter, i.e. $W = 21$ mm^3.

Figure 2.48: Fatigue testing miniature specimen proposed by Nicoletto, with a size of (7 x 5 x 22 mm^3). One euro coin as size reference [63].

The material and money saving of this geometry is clearly perceivable, as shown in Figure 2.49. The volume of the miniature specimen is about 1/6 of the standard specimen [63].

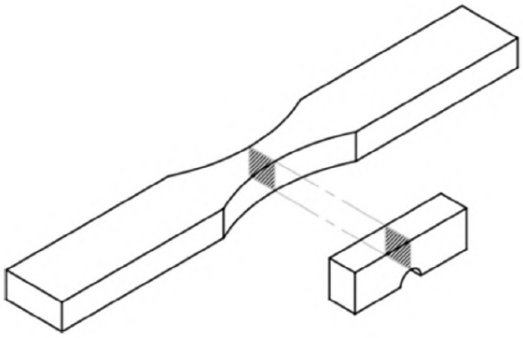

Figure 2.49: Fatigue testing miniature specimen proposed by Nicoletto [63].

Conventional fatigue testing machines are not prepared to hold tight this kind of specimens. Hence, Nicoletto [63] had to adapt the grips to securely hold the specimen end and apply a pure bending load in 4-point bending tests, ensuring a mode I type of failure would take place. In the present dissertation, the miniature specimens were also tested, in 4-point bending tests. Furthermore, new testing grips were built in order to accurately perform the fatigue tests. This topic is going to be detailed in a further section.

Nicoletto proposed terminating the test when the initially applied bending load showed a 10% reduction. This way, the test method is dependent on the number of cycles to crack initiation and not on the number of cycles to failure. The evolution of bending force measured by the load cells during one of the tests and the definition of test end are presented in Figure 2.50 [63].

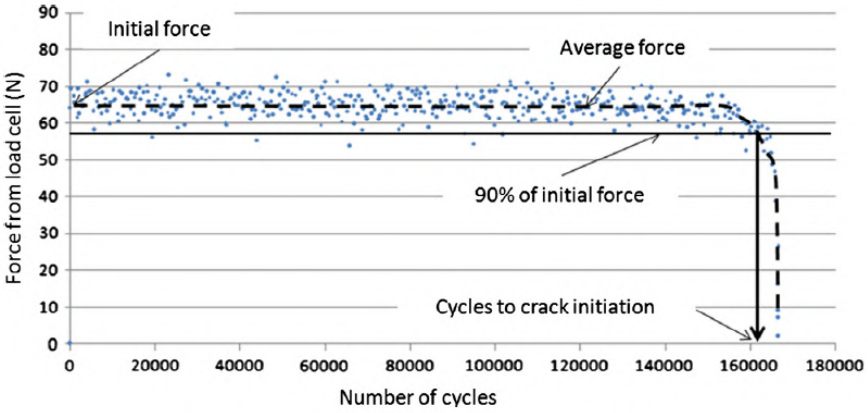

Figure 2.50: Bending force measured vs. number of cycles and definition of test end [63].

Nicoletto projected the specimen to localise the crack initiation at the centre of the smooth top surface plane. Hence, a notch with 2 mm diameter was built in the opposite side. During the fatigue tests, the top flat surface is meant to be subjected with tensile load, while the smooth notch is subjected with compressive loads. This way, crack initiation is promoted in the top flat surface, as tensile stresses promote crack initiation. A FE analysis was performed by the author to optimise the geometry of the miniature specimen, as shown in Figure 2.51 [63].

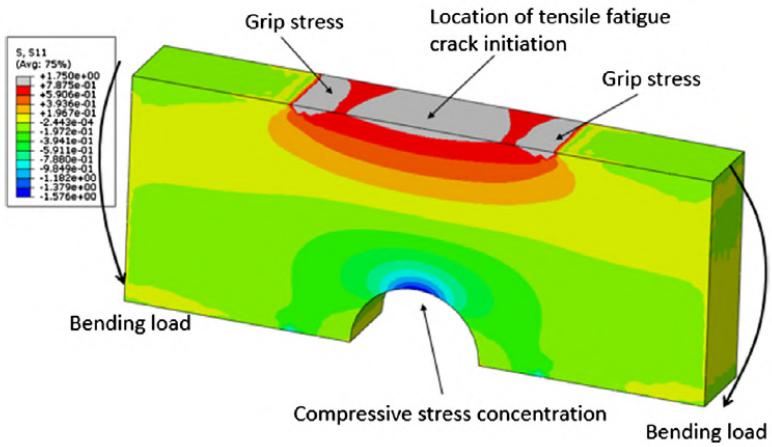

Figure 2.51: FE analysis of the fatigue test, showing the stress distribution in the XX direction (S11) [63].

By thorough investigation, Nicoletto proposed an effective stress factor of 0.92 to allow comparison between stress results obtained by the miniature specimen and conventional ones. A bridge between conventional and miniature specimens was now established. Although testing with such specimen has great advantages, it is always recommended that a few of the tests should be performed with standard specimens to obtain more reliable data.

2.3 Nickel-based superalloys

Superalloys are high performance alloys that are able to operate at very high temperatures, sometimes up to 1200 °C, and close to their melting point, while maintaining high mechanical properties. These materials are usually endowed with excellent mechanical strength, good surface stability, resistance to thermal creep deformation and to corrosion and oxidation. Due to this outstanding combination of properties, they are frequently used in the aerospace, petrochemical and marine industries. These alloys can be based on nickel, cobalt or iron with considerable additions of alloying elements in order to provide strength, toughness and durability at high temperatures [64].

Inconel® is a family of more than 20 high performance nickel-based alloys developed by Special Metals Corporation [65]. Each Inconel has different chemical composition, which allows for a wide range of properties for specific applications and needs. Some of the most used alloys are Inconel 600, 625, 690 and 718. Their chemical composition in weight percentage (wt%) is presented in Table 2.4 [1].

Table 2.4: Chemical composition of some of the most common Inconel alloys [1].

Alloy	Ni	Cr	Mo	Nb	Fe	C	Si	Al	Ti	Mn	Other
600	72.0 min.	14.0-17.0	-	-	6.0 10.0	0.15 max.	0.5 max.	-	-	1.0 max.	0.515 max.
625	58.0 min.	20.0-23.0	8.0-10.0	3.15-4.15	5.0 max.	0.10 max.	1.0 max.	0.4 max.	0.4 max.	0.5 max.	0.015 max.
690	58.0 min.	27.0-31.0	-	-	7.0-11.0	0.05 max.	0.5 max.	-	-	0.5 max.	0.515 max.
718	50.0 55.0.	17.0-21.0	2.80-3.30	4.75-5.50	Balance	0.08 max.	0.35 max.	0.2-0.8	0.65-1.15	0.35 max.	0.336 max.

2.3.1 Inconel 625

Inconel 625 (UNS N06625) or Alloy 625 is a highly alloyed nickel-based alloy that possesses high strength, creep resistance and exceptional corrosion resistance in various environments, while providing good weldability. Moreover, it has great thermal stability, which means it can be used from cryogenic temperatures up to ultra-hot environments over 1000 °C. This combination of alluring properties makes it a very demanded alloy in a large number of industries, varying from widespread applications in aeronautic, aerospace, marine, chemical and petrochemical industries, to really specific uses, such as reactor-core and control-rod components in pressurised water reactors or heat exchanger tubes in ammonia cracker plants for heavy water production [66, 67].

This superalloy is generally considered to be a solid solution alloy that gets its strength from the high levels of chromium, molybdenum, niobium[1] and, to a lesser extent, from the iron content. The titanium and aluminium contents are present mainly for refining purposes and are kept low, when comparing to other similar alloys such as Inconel 718, to improve the material weldability. However, if sufficient content of Nb, Ti and Al are present in the alloy, precipitation hardening is possible, as discussed below [66].

[1] At all times throughout the dissertation, the percent niobium is intended to be interpreted as niobium + tantalum, with the tantalum comprising less than 10% of the niobium + tantalum content.

The excellent corrosion resistance is primarily given by the high levels of Cr and Mo [66].

Early work

The genesis of the Alloy 625 dates back to the 1950s. Initially, it was developed to be used as replacement for 316 stainless steel in super critical steam power plants, where it would be used as a main steam-line material with service temperatures up to 650 °C. With this application in mind, the main product goals were good weldability, high creep resistance and non-age hardening behaviour, i.e. the non precipitation of phases that provide strength while taking away ductility when subjected to high temperatures for several hours. Being easily fabricable into tubing was also an important feature [68].

Since the metallurgical stability was of extreme importance, tensile samples of alloys with slightly different composition were given a simple ageing treatment (700 °C for 16 hours) and room-temperature tested. These experiments were meant to evaluate the strengthening effects of the major alloying elements after heat treatment. The results were not expected, as they showed the material did, in fact, age. The results of this experiment are presented in Figure 2.52 [68].

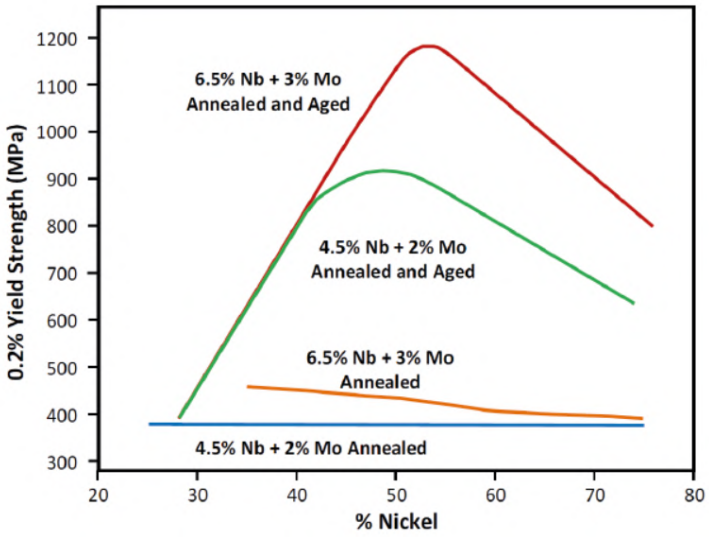

Figure 2.52: The effect of Ni, Nb an Mo content on the room temperature yield strength of annealed and aged variations of Alloy 625. Annealed at 1038 °C for 1 hour, water quenched then aged at 677-732 °C for 16 hours and air cooled. Annealed at 1038 °C for 1 hour and water quenched with no ageing [69].

This discovery led to the delay of development of Alloy 625, as attention shifted to the development of a different alloy, namely Alloy 718. The approximate composition of Inconel 625, at the time, is presented in Table 2.5

Table 2.5: Initial approximate composition (wt%) of Inconel 625 [68].

Ni	Cr	Mo	Nb	Fe	C	Si	Al	Ti	Mn	S
60	15	2	3	19	-	-	0.5	0.5	-	-

Later on, when the development of this alloy was resumed, there was no longer a market

for super critical steam plants. Therefore, in order to become more attractive, it had its content levels of Cr and Mo raised to the current ones. This change not only improved the room temperature properties of the material, but also greatly increased its corrosion resistance, while not impairing the weldability, increasing its marketing opportunities [68]. The current composition of Alloy 625 is shown in Table 2.6.

Table 2.6: Present composition (wt%) of Inconel 625 [66].

Ni	Cr	Mo	Nb	Fe	C	Si	Al	Ti	Mn	S
58.0 min.	20.0-23.0	8.0-10.0	3.15-4.15	5.0 max.	0.10 max.	1.0 max.	0.4 max.	0.4 max.	0.5 max.	0.015 max.

The main properties of Inconel 625, at room temperature in the annealed state are presented in Table 2.7.

Table 2.7: Some properties of wrought Inconel 625, at room temperature in the annealed state [1].

Density (g/cm^3)	Melting range (°C)	Specific heat (J/kg°C)	Modulus of elasticity (GPa)	Poisson's ratio
8.44	1290 - 1350	410	207.5	0.278
Tensile strength (MPa)	**Yield strength (MPa)**	**Elongation (%)**	**Hardness (HB)**	**Impact strength (Charpy V, J)**
965.3	479.2	54	145 - 220	65 - 68

Effect of elements on strength

Although Alloy's 625 purpose was slightly deviated from the original one, it was still meant to be used in high temperature environment. The effect of nickel on the stress rupture strength at 649 °C of annealed Inconel 625 is shown in Figure 2.53. As it can be observed, the strength has a peak between 55 and 60% of nickel content.

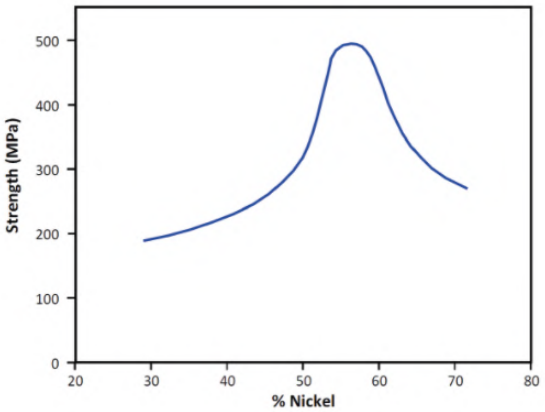

Figure 2.53: The effect of Ni on the material's rupture strength at 649 °C. The material was annealed at 1038°C for 1 hour [69].

The effect of niobium on the stiffness of the matrix is presented in Figure 2.54. It can be verified that the content of Nb has little effect over the stiffness of the matrix in an annealed state. The same observation can be made for the annealed and aged state if the content of Nb is lower than 2%. However, once the Nb level exceeds about 3%, the effect becomes clearly significant. This effect appears to coincide with the observation that the solubility of niobium in the alloy was found to be around 2.5 % [69]. Above this content, the element in no longer soluble and, with proper temperature and time (ageing treatment), the Nb precipitates, improving the yield strength of the material.

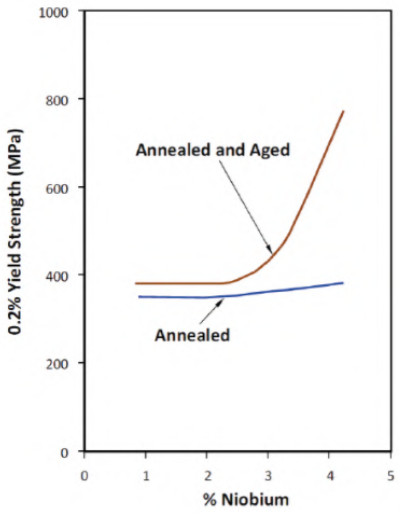

Figure 2.54: The effect of Nb on 0.2% yield strength of Alloy 625 [69].

Molybdenum is known to increase the strength of the matrix through solid solution. In the case of Alloy 625, Mo also increases the age-hardening response of the material, as previously noted in Figure 2.52, although it was still not investigated whether solely or through some interaction with Nb. One aspect that might be relevant to this behaviour is the fact that the solubility of Nb in the alloy decreases with the increasing Cr + Mo content [68]. Chromium also increases the strength of the solid solution, but has no known influence on the age-hardening response of the alloy [69].

The creep strength of the alloy is primarily influenced by the Mo, Cr and Nb content [68]. Their effects are shown in Figure 2.55 and 2.56.

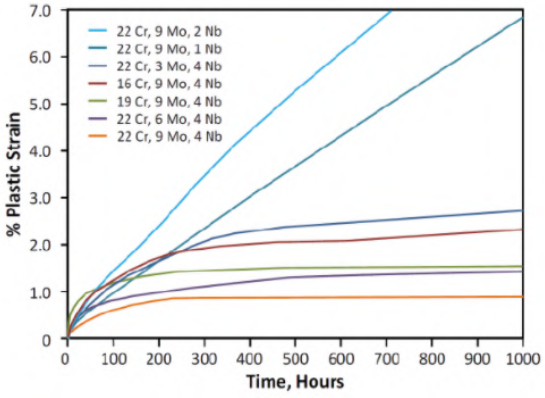

Figure 2.55: Creep tests at 816 °C and 52 MPa [69].

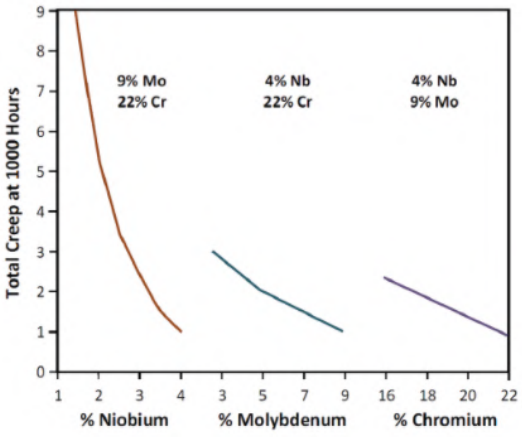

Figure 2.56: The effect of Nb, Mo and Cr content on the total creep (%) of alloy 625 at 816 °C [69].

By observation of Figure 2.55 and 2.56 one can conclude that Nb is the element which influences creep strength the most.

The content level of aluminium and titanium is generally kept low (below 0.5%) to minimise the age-hardenability of the alloy. As previously stated, if sufficient content of these elements is present, precipitation hardening is possible. Nevertheless, creep tests at 649 °C showed a slight benefit in retaining 0.2% of these alloys instead of 0%. Moreover, a low level of Al + Ti showed improved welding properties [68].

In fact, through tight control of Al and Ti levels, Inconel 625 does not precipitate γ', like most nickel-based superalloys with higher content of Al and Ti. It rather precipitates a metastable γ" and a stable orthorhombic Ni_3Nb or δ phase. The first one, is the phase of most use in age hardening, conferring the alloy with high strength. On the other hand, the Ni_3Nb phase is not coherent with the matrix, contributing to hardening only as a dispersant [68]. Additionally, Laves phases can also be precipitated.

Effects of elements on corrosion resistance

The outstanding corrosion resistance of Alloy 625 is due to the resistance of the different alloying elements to various corrosive environments.

For instance, nickel offers great resistance to many corrosive media, such as neutral salt solutions, alkalies, reducing environments and plays an important part in preventing stress-corrosion cracking. On the other hand, chromium has superb resistance to oxidising solutions, while offering little resistance to non-oxidising media. The element provides its protection through the formation of an adherent chromium oxide surface layer, Cr_2O_3 [68, 70].

Molybdenum contributes greatly to corrosion resistance in reducing media and by furnishing the alloy with pitting resistance [68, 71].

As expected, an alloy with such characteristics has found success in a broad range of industries and numerous applications, such as the ones of aerospace, naval and marine, where, for example, resistance to pitting and stress-corrosion cracking is of extreme importance [68].

Solidification behaviour

The solidification behaviour of Alloy 625 has been thoroughly investigated over the years. The reaction begins with the formation of austenitic FCC γ phase in dendritic form [72]. This fact can be supported by the liquidus projection of the Ni-Cr-Mo ternary phase diagram present in Figure 2.57, where the red-shaded area represents the approximate Ni, Cr and Mo content levels present in Inconel 625.

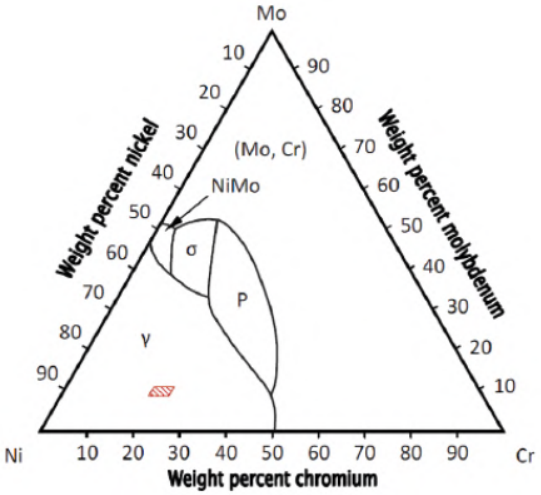

Figure 2.57: Ni-Cr-Mo liquidus projection [70].

The austenitic matrix is enriched with Ni, Cr, Mo and Fe in solid solution. As it forms, elements such as Nb and Mo segregate in the interdendritic region [72–74].

In fact, S. Floreen et. al [66] found that the dominant reaction is the enrichment of Nb in the interdendritic liquid, which consequently originates niobium-rich Laves phase and/or niobium carbide during the final stages of solidification. These Laves phases in Inconel 625 follow a A_2B hexagonal close packed (HCP) crystal structure, where the "A" atoms can be Fe, Ni or Cr and the "B" atoms can be Mo, Nb or Si [69]. They are reportedly hard and brittle phases which may cause deterioration in ductility and stress-rupture properties, especially when the material is subjected to elevated temperatures for long times [75].

M. J. Cieslak [76] used analytical electron microscopy (AEM) analysis to measure the Laves phase composition (wt%) of three variations of Alloy 625. The results are listed in Table 2.8.

Table 2.8: Phase compositions (wt%) of Laves phase from AEM analysis [76].

	C	Ni	Fe	Cr	Nb	Mo	Si
Alloy 1	-	45.6	1.4	15.6	19.2	18.2	<0.1
Alloy 2	-	48.2	1.0	13.9	18.2	17.6	1.2
Alloy 3	-	46.7	0.9	13.6	16.8	19.8	2.2

It can be seen that the Laves phase was significantly enriched in Nb, Mo and Si, while the Fe, Cr and Ni levels were not manifestly enriched versus the nominal Alloy 625 composition.

It was the high content levels of Nb present in the Laves phase that led to believe

that this element dominates the solidification behaviour. In a similar study, M.J. Cieslak [77] confirmed that alloys similar to Inconel 625 which were Nb-free, did not form Laves-containing solidification constituents.

The solidification path and the resultant microstructures can be represented in a pseudo ternary equilibrium diagram, like the one shown in Figure 2.58, proposed by S. Floreen et. al [66].

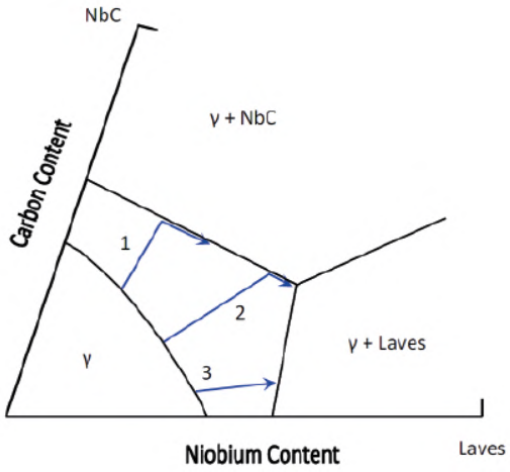

Figure 2.58: Schematic view of solidification paths and resulting microstructure of Alloy 625 [70].

The authors claim that the C/Nb ratio dictates the solidification behaviour. Therefore, three different paths can be taken. For path 1, where the C/Nb ratio is high, austenitic phase γ transforms into γ + NbC. In the second path, for intermediate ratios of C/Nb, γ + NbC is formed first, while the Laves phase is formed at the end of solidification. At very low ratios, Laves phase forms without the formation of NbC. The formation of Laves phase without the NbC phase (path 3) is very uncommon in Inconel 625, but has been reported to occur in the alloy containing less than 0.01% C [66].

Nevertheless, Nb and C are not the only elements that influence the solidification behaviour and resulting phases. Reducing the iron and silicon contents in Alloy 625 welding filler wire has been observed to increase the ductility in weldments because the formation of Laves phase is minimised [66, 76].

The NbC elements were found as blocky carbides and with a dendritic Chinese script morphology at the grain boundaries, with eutectic-type constituents [66]. These carbides provide strengthening by stabilising the grain boundaries against shear stress. Although it is beneficial to have such carbides, their concentration should be tightly controlled to avoid excessive number of localised concentrations, in order to improve the ductility of the alloy [74].

Cieslak [76] proved experimentally that lowering the solidification or melting range minimised the tendency for hot cracking during welding. It was explained that reducing this range should minimise the amount of segregation of elements that would occur during solidification and consequently improve hot workability, making the material more suitable for welding, casting and, more recently, to metal additive manufacturing. This behaviour was also explored and confirmed by J. N. DuPont [73].

The solidification range during cooling versus the carbon content of a number of different Alloy 625 variations, within the material composition ranges for each element, is presented in Figure 2.59.

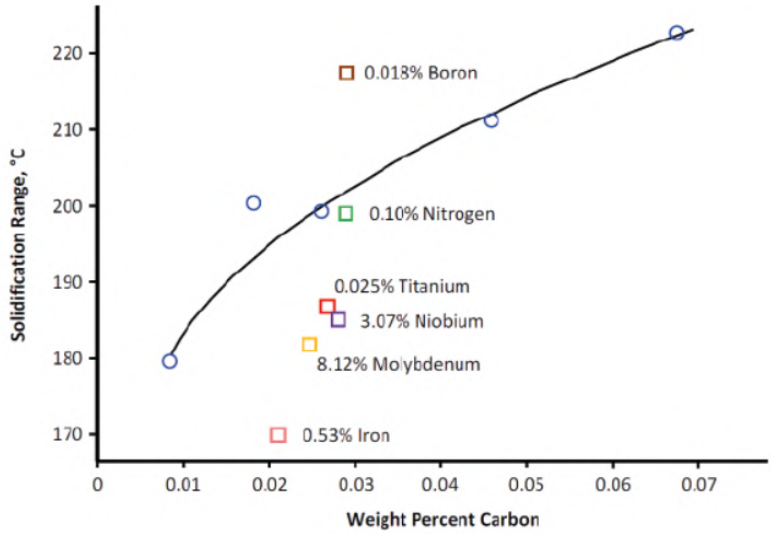

Figure 2.59: Solidification range during cooling of different alloy variations [70].

By observation of Figure 2.59, the reduction of Fe, Mo, Nb and C content in the alloy, close to their lower limits of Table 2.6, can significantly reduce the solidification range [70]. It was also found that by reducing the Si content, the same behaviour was observed [76]. However, an increase in Boron content can broaden the solidification range of the alloy.

Laves phase can be eliminated by solution annealing at high temperatures. However, NbC particles are much more stable and once formed are much more difficult to eliminate. V. Shankar et. al [67] reported the presence of continuous thick film of niobium carbides along the grain boundaries in a service-exposed ($\sim$ 60000h/600 °C) ammonia cracker tube made of Inconel 625. These carbides were not dissolved during the solution treatment given to the alloy, prior to service-exposure. Moreover, the same alloy was given a re-solution annealing treatment at 1150 °C for 0.5h, which caused the dissolution of most of the pre-existing NbC particles. However, a few large primary NbC were found to remain undissolved.

Phase transformations

Although it was initially materialised to be a solid solution material, various phase changes can occur in Inconel 625, as a function of time and temperature. In order to fully comprehend these transformations, a time-temperature-transformation (T-T-T) diagram of wrought Alloy 625 is presented in Figure 2.60. The starting material is assumed to be solution annealed so that all phases, except the NbC particles previously discussed, have been put in solid solution [66].

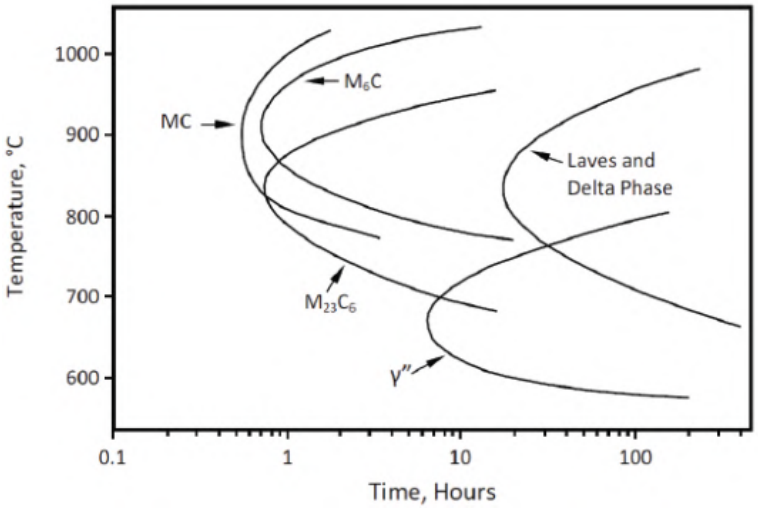

Figure 2.60: T-T-T diagram for Inconel 625 [78].

As shown in Figure 2.60, different carbides and intermetallic phases can precipitate after thermal exposures from around 0.5 up to 100 hours. Prolonged exposures are also object of study.

According to the T-T-T diagram, three different carbides can precipitate in the alloy grain boundaries, depending on the temperature employed during thermal treatment. The first carbides start precipitating at around 10 minutes, so their formation can easily be suppressed even when air cooling is used after the solution annealing treatment.

At higher temperatures, approximately from 870 to 1038 °C, the carbides are both MC as thin grain boundary films (mainly NbC) and M_6C, where M is mostly Ni, Cr and Mo. Between 700 and 870 °C, the carbides formed are principally $M_{23}C_6$, where M is Cr most of the times. At intermediate temperatures, all three carbides can often be found. These M_6C and $M_{23}C_6$ carbides usually have blocky, irregular shapes and form as series of discrete grain boundary particles [66, 79].

Li Jiang et. al [80] studied the high content of Si in the M_6C carbides, concluding that this element promoted the nucleation of these precipitates.

S. Floreen et. al [66] concluded that the aforementioned carbides increased the tensile strength and hardness of the alloy, while contributing to the loss of ductility, even though the fracture in all cases were ductile.

With longer exposures to temperatures within the 700-980 °C, both Laves phase and a δ-Ni_3Nb phase will start to precipitate. This precipitation initiates in the grain boundary regions that already have carbide particles [66].

The Laves particles morphology was already discussed, having a very similar blocky and irregular shape to the M_6C and $M_{23}C_6$ carbides, making them easy to be overlooked when performing a metallographic examination. On the other hand, δ particles have an acicular morphology and an orthorhombic DO_a structure [66, 81], like the one shown in Figure 2.61.

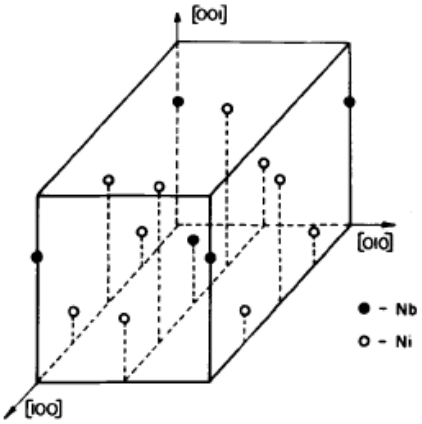

Figure 2.61: Unit cell of the δ-Ni_3Nb phase [81].

At lower temperatures in the mentioned range, δ phase nucleates at grain boundaries as well as coherent and incoherent twin boundaries. Contrarily, at higher temperatures, it precipitates intragranularly [67, 81].

M. Sundararaman et. al [81] explored the precipitation of δ-Ni_3Nb phase in Inconel 625 and 718 and concluded that it can occur in two manners:

1. At temperatures below 800 °C, preceded by the γ'' precipitation;
2. At temperatures higher than 800 °C, directly from the austenite.

Although a controlled precipitation of δ phase may be beneficial towards grain stabilisation, the formation of these two intermetallic phases is known to negatively impact the ductility and toughness of Inconel 625. Moreover, formation of γ phase depletes Nb from the matrix, which can affect the strength of the alloy. However, δ phase does not usually form under the as-deposited condition, rather after heat treatment [66, 82].

The δ and Laves phase can be put back into solution by annealing at around 1093 °C [67, 81].

At temperatures in the 600-760 °C range, the precipitation of gamma double-prime, γ'', is the dominant reaction due to the presence of sufficient Nb, Ti and Al in the composition. Therefore, this phase precipitates as fine Ni_3(Nb + Ti + Al) dispersoid, plate or disc shaped, with a body-centered tetragonal (BCT) structure [66].

The processing history influences the formation of γ'' particles. In fact, if NbC, Laves or δ particles are present around the grain boundaries, the zones adjacent to these particles will be depleted of niobium. In this case, the formation of γ''-phase may be retarded, resulting in zones denuded of this phase. The presence of such zones has been associated with a degradation in mechanical properties or corrosion resistance in similar superalloys, resulting in early failure of nickel-based alloys components [66].

Nonetheless, the precipitation of face centered cubic (FCC) γ' (Ni_3(Nb,Al,Ti)) has been reported to occur after high temperature exposure in Inconel 625 alloys with high Al and Ti content [83].

2.3.2 Inconel 625 in additive manufacturing

The production of Inconel 625 parts by means of additive manufacturing is growing by the day. Owing to its high strength, poor machinability and low thermal conductivity, it

is very difficult to shape by traditional, subtractive methods. This fact, coupled with the inevitable increase in demand for complex and efficient part geometries, as an ever-growing number of industries strive to improve performance and productivity through topology optimisation methods, make Inconel 625 an ideal candidate for additive manufacturing [84–86].

Moreover, the excellent welding properties reported in the early days of the alloy, ensured a smooth transition from the wrought methods to metal additive manufacturing. This way, expensive and extensive machining is minimised.

In AM processing of superalloys, cooling rates during solidification are in the range of 10^3 - 10^6 °C/s, much higher than in traditional cast and wrought processes. Additionally, the material undergoes repetitive heating and cooling cycles. Therefore, the resultant microstructure, phases and, consequently, mechanical properties are quite different than those of their conventionally produced counterparts [83, 85].

Microstructure characteristics

The wrought alloy in the as-built condition has a typical equiaxed microstructure. However, due to the rapid melting followed by the rapid cooling in several metal AM processes, Inconel 625 in the post-build condition exhibits fine dendritic structures oriented in the build direction and the formation of non-equilibrium phases [74, 85].

Dinda et. al [87] investigated the microstructure of Laser aided direct metal deposition of Inconel 625 superalloy. They were able to produce defect-free thin wall samples using a wide range of process parameters, showing that the material is suited for AM processes. The authors pointed out that the resulting microstructure mostly consisted of columnar dendrites, which grew epitaxially from the substrate. Figure 2.62 shows the microstructure of the transverse section of one of the produced samples.

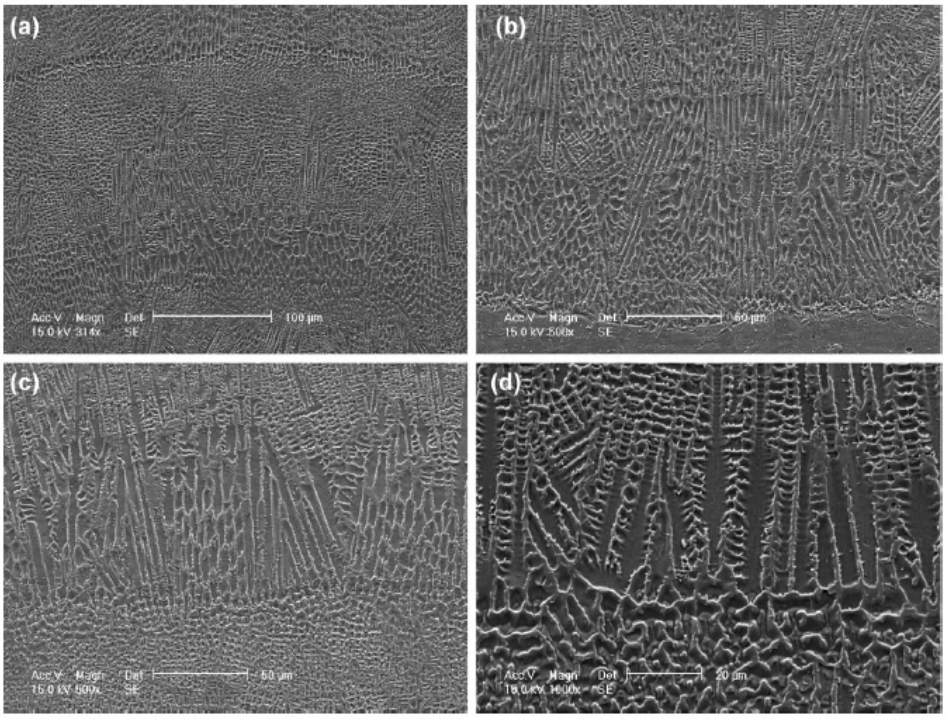

Figure 2.62: Transverse-section microstructures at different locations of the sample [87].

As it can be observed in Figure 2.62, the microstructure of each layer is composed of two regions. The bottom part, near the melt pool limit, is mostly columnar (primary dendrites), showing very little amount of secondary dendrites associated with it, while the top part of the layer shows typical fine dendritic structure with secondary dendrite arms. They stated that this behaviour was a result of different cooling rates within the layer. In laser deposition processes, the cooling rate of the melt pool is very high at the bottom part of the layer. On the other hand, the top part of each layer cools down slowly compared to the bottom part. Owing to the very high solidification velocity of the bottom part of the melt pool, secondary dendrites did not have time to grow. Therefore, because of the progressive decrease of cooling rate from the bottom to the top of the melt pool, a gradual transition of microstructure from fully columnar to dendritic is observed [87].

A similar behaviour of Inconel 625 produced by Selective Laser Melting was reported by J. Nguejio [88]. Other authors [89–91] also investigated the microstructure of the alloy having obtained similar results.

Dinda et. al [87] also observed the microstructure of the horizontal section (perpendicular to the build direction). The morphology of the section is the typically equiaxed cellular structure, as presented in Figure 2.63.

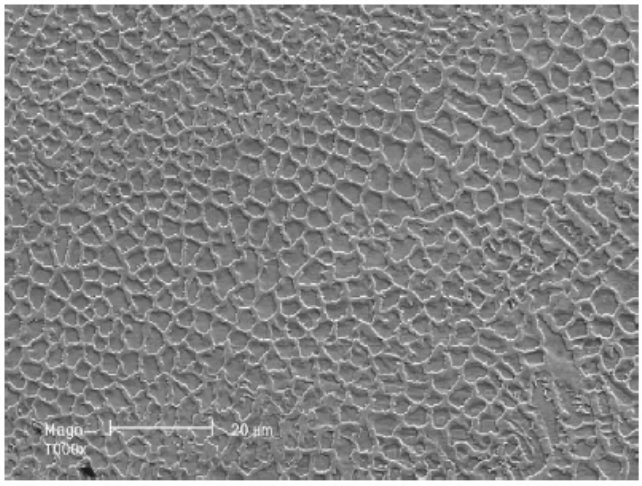

Figure 2.63: Microstructure of the horizontal section [87].

Given that the as-deposited microstructure is close to vertical in orientation, in the section perpendicular to the build it appears as an equiaxed structure [87]. Moreover, the authors presented a detailed isometric view of microstructure at three different locations at the deposit: a) first layer, (b) middle of the sample, and (c) top layer. The three-dimensional view of the mentioned layers is shown in Figure 2.64.

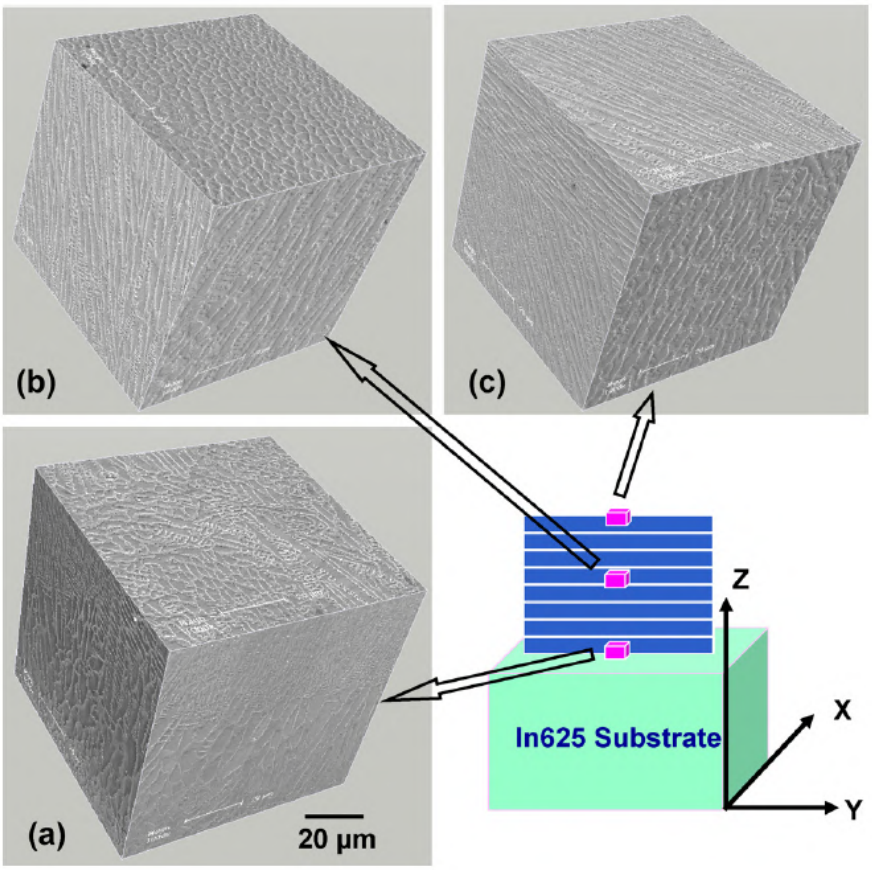

Figure 2.64: Three-dimensional view of microstructure at three locations of the deposit: (a) first layer, (b) middle of the sample, and (c) top layer [87].

It was observed an orientation transition from vertical dendrites to horizontal dendrites in the upper part of the top layer, which the authors attributed to changes in the heat flux direction. At the top surface of the melt pool, the magnitude of heat flux to the back of the melt pool is higher compared to the substrate, due to hemispherical shape of the melt pool. As a result, the very top part of each layer, dendrite grew from the back of the laser melt pool which appears as horizontal grains. This effect is only verified in the top layer, since the deposition of a new layer partially remelts the upper part of the previously deposited layer, changing the grain orientation [87].

Even though the rapid solidification is a common feature to all metal AM methods, there are still some microstructural differences between Inconel obtained by DED or by SLM, for instance.

J. Nguejio et. al [88] established a comparison of microstructural features of alloy 625 produced by SLM and LMD. The authors reported that although the samples showed identical columnar and cellular dendritic structure, the direction of growth of the columnar dendrites was not the same. In the SLM specimen, the primary dendrites show a growth with an angle of about 90°with the substrate, while in the LMD specimen the columnar dendrites were not perpendicular to the substrate. The SEM images of the specimens are shown in Figure 2.65 and 2.66.

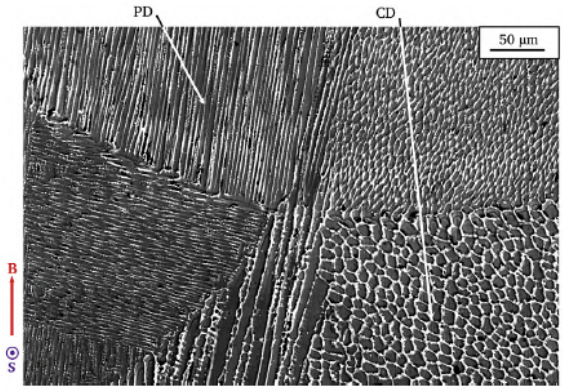

Figure 2.65: SEM images of Inconel processed by SLM; PD = primary dendrites; CD = cellular dendrites; B stands for building direction and S for laser scan direction [88].

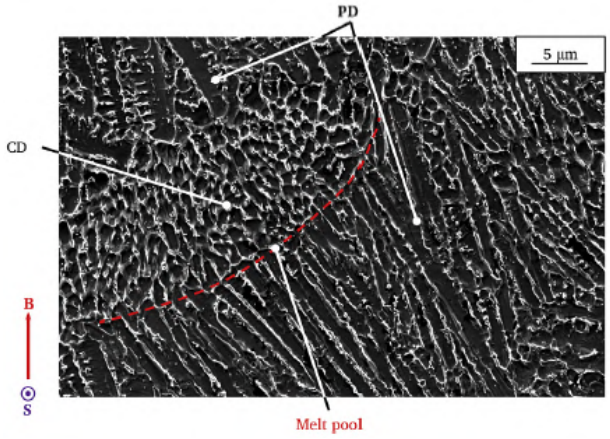

Figure 2.66: SEM images of Inconel processed by LMD; PD = primary dendrites; CD = cellular dendrites; B stands for building direction and S for laser scan direction [88].

The authors provided an in-depth explanation for this behaviour. They stated that the growth direction of dendrites is opposite to the resultant heat flux direction, which also explains the elongation of the primary dendrites. SLM parts are in direct contact with the supporting plate and with the powder bed, reducing significantly the cooling rate, since the latter acts as a thermal insulator. Therefore, there is an obvious vertical cooling towards this supporting plate, making the dendrites grow perpendicular to it. On the other hand, for LMD specimens, the same vertical cooling towards the plate occurs, but also heat exchanges with surrounding ambient air and extra cooling coming from the last solidified layers beyond the melting bath. This shared cooling between the substrate and the adjacent solidified layers causes a grain growth at an angle of about 60° compared to the substrate, which means that the vertical heat flux via the substrate was twice intense than the horizontal heat flux via the deposit. This value was also reported by other authors [82, 87, 90].

Nevertheless, an angle of about 45° was recorded [87], which depended on the process parameters. In this case, both heat flux via substrate and deposit play an equal role.

A. Tanvir et. al [82] characterised the microstructure of Inconel 625 components fabricated by WAAM. The authors declared that the direction of the columnar primary dendrites can vary along the thickness of a sample, as presented in Figure 2.67.

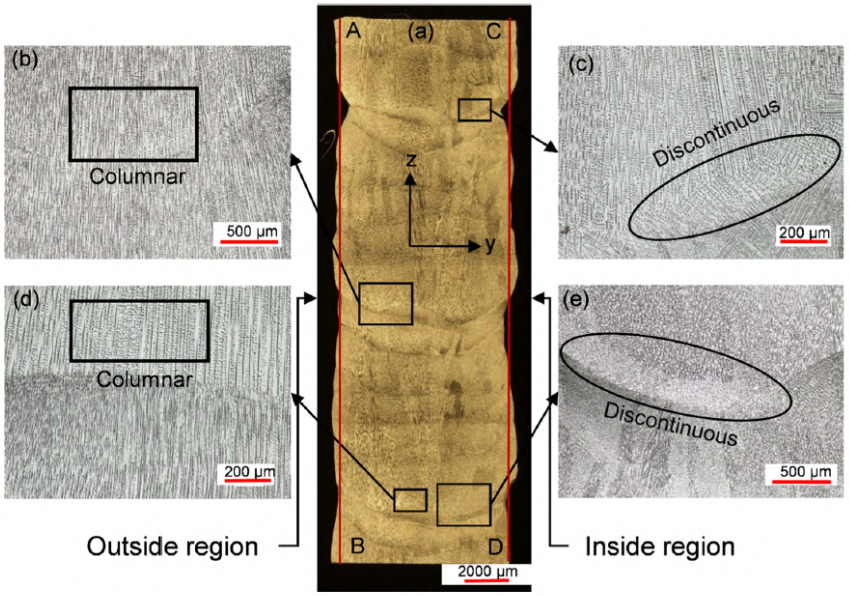

Figure 2.67: As-deposited sample microstructure under optical microstructure with important areas highly magnified [82].

The inside and outside of the sample differ from the middle region. This behaviour was attributed to the differences in cooling rate. On the one hand, the side regions were formed during solidification using two forms of cooling: conduction by the previously deposited layer and atmospheric convection, which promote a diagonal growth (Figure 2.67 c) and e)). On the other hand, the solidification of the middle region occurred through conduction only by the previously deposited layer, developing a vertical growth (Figure 2.67 b) and d)) [82].

The processing parameters can also influence the microstructure of Inconel 625. Dinda et. al [87] studied the effect of two different scanning strategies on the direction of the primary dendrites. The obtained result is shown in Figure 2.68.

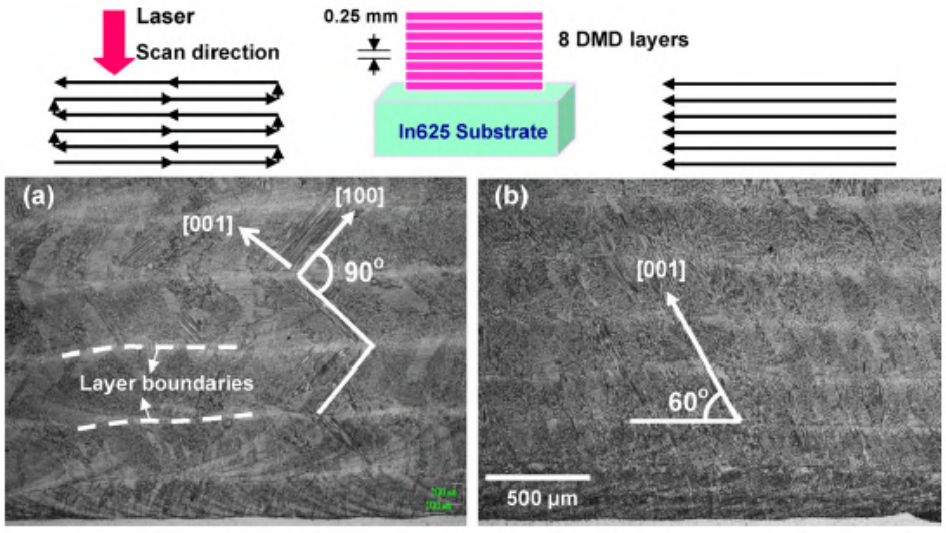

Figure 2.68: Optical micrographs of the longitudinal section of as-deposited samples [87].

If the scanning direction changes in every layer, like presented in Figure 2.68 a), the growth direction of the columnar dendrites changes by 90° in each layer, with a 45° angle with the substrate. In fact, the partially remelted grains of the previously deposited layer acts as pre-nuclei for directional growth of crystal in the newly melted layer [87], changing 45° each time a new layer is deposited. If a single scan direction is used, like in Figure 2.68 b), the growth of these dendrites forms an angle of about 60°with the substrate.

Phases and thermal treatments

Inconel 625 is classified as a solid solution strengthened superalloy, although additional strengthening can be derived by precipitation of carbides and/or intermetallic phases [85]. In fact, as previously mentioned, Nb segregates strongly to the liquid phase during solidification. Therefore, Nb-rich MC carbides and the Laves phase precipitates can be formed through two eutectic reactions:

$$\mathrm{L} \longrightarrow \gamma + \mathrm{NbC} \text{ and } \mathrm{L} \longrightarrow \gamma + \mathrm{Laves}$$

According to the T-T-T diagram presented in Figure 2.60, various other carbides and intermetallic phases can precipitate in the alloy, such as γ'', δ, $M_{23}C_6$ and M_6C if a proper heat treatment is applied. However, in AM processes, this behaviour can be quite different.

In additive manufacturing, the material is deposited layer by layer. When depositing a new layer of material, the deposits of the previous layers are somewhat heat treated, resulting in the appearance of different phases in the as-built condition, when compared to the wrought as-built where, without thermal treatment, these elements tend to stay in solid solution. Moreover, different metal AM processes compel the material undergo different heating/cooling cycles. Hence, it is understandable that different phases may arise from different phases.

It is important to note that it is still not well established whether and which precipitates are present in the as-built condition, because of the similarities in chemical composition and small differences of lattice parameters between some of the phases [83, 85].

B. Dubiel et. al [85] investigated the microstructure and precipitates in laser based directed energy deposition (L-DED) manufactured Inconel 625 in the as-build condition, by means of light microscopy and transmission electron microscopy. The authors found precipitates in the interdendritic areas and identified them as Nb-rich MC, Cr-rich $M_{23}C_6$ carbides and as Nb-, Cr-, and Mo-rich Laves phase. The unexpected precipitation of $M_{23}C_6$ carbides was attributed to local variations in chemical composition of the L-DED processed material that may favour such phases.

F. Xu et. al [86] studied the microstructural evolution of Inconel 625 produced by Pulsed Plasma Arc Deposition process. They reported the precipitation of Laves phase, MC carbides and δ-Ni_3Nb phases in the as-deposited state, as shown in Figure 2.69.

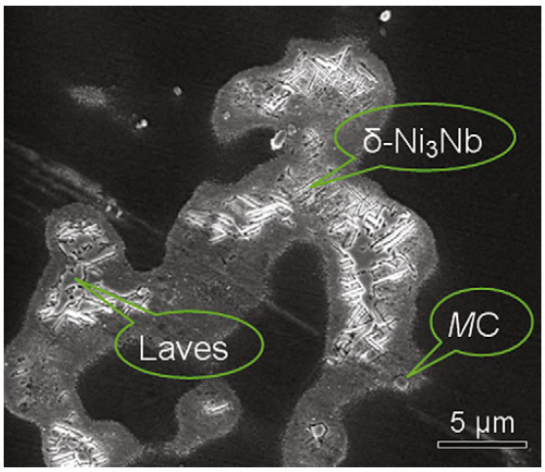

Figure 2.69: SEM image of the major phases appearing in the as-deposited microstructure [86].

The formation of the δ phase might be due to solidification conditions and the complex thermal cycling of the process. During solidification, the residual liquid after the eutectic reaction is rich in Ni and Nb elements, which is beneficial to the nucleation and growth of δ-Ni_3Nb phase. When depositing a new layer of material, the previous layer is partially heat-treated, resulting in the dissolution of Laves phases. Thus, the released niobium elements can be used for the formation of δ-Ni_3Nb. This statement was then supported by the small amount of Laves particles in the as-deposited microstructure of the upper part [86].

A. Tanvir et. al [82] reported the presence of MC carbides and Laves phases in specimens produced by WAAM, while other authors [90] reported solely the presence of Nb-rich MC carbides.

As previously discussed, MC carbides tend to precipitate thin grain boundary films. However, in AM the high cooling rates promote solute trapping [90, 92]. Hence, the amount of solute atoms such as Nb and Mo that remain entrapped in the dendritic core increases. G. Marchese et. al [90] disclosed the presence of Nb-rich MC carbides in the dendritic core in specimens produced by SLM. The aforementioned high Nb content trapped inside the cores, may promote eutectic reactions involving the formation of NbC carbides in dendritic cores. These precipitates were found to be coherent with the matrix.

It was already shown that the as-deposited microstructure is not the same for all the AM methods. The building orientation and geometry can also influence the microstructure. M. Rombouts et. al [83] studied the influence of building orientation of specimens in the microstructure and phases of Alloy 625 produced by Laser Metal Deposition. For that purpose, the authors build two samples: one in a "standing orientation" and another in a "lying orientation". They found that the cellular and dendritic structure in the samples built in the standing orientation was coarser than those built in the lying orientation. This particularity was attributed to the locally higher heat accumulation and to the lower cooling rate in the central part of the standing specimens, during the LMD process. Moreover, it was found that the specimens built in standing orientation had more carbides present, and especially at higher distances from the baseplate.

One of the main limitations of AM processes is the high thermal residual stresses induced by the extremely fast solidification rates. These residual stresses are detrimental

to the mechanical properties and undesirable for high thermal applications. In order to reduce these residual stresses, a heat treatment is frequently applied to the parts, having other beneficial side-effects, such as eliminating segregation of elements and unwelcome phases, promoting grain growth and advantageous phase precipitation, thus obtaining specific microstructure and mechanical properties suitable for different conditions. Moreover, performing a solution heat treatment followed by an ageing treatment ensures that there is a more homogeneous precipitation of carbides and intermetallic phases [90, 93].

A meticulous study of heat treatments at different temperatures is a necessary exercise to understand when and which phases form, allowing to avoid the most detrimental precipitates. As previously mentioned, the rapid solidification of the material in AM processes may originate different phases when compared to the T-T-T diagram of the wrought alloy.

J. Nguejio et. al [88] made a very detailed analysis of the influence of different heat treatments in the microstructure, phases and tensile properties of wrought and LMD and SLM additively manufactured Inconel 625. Their results are presented as follows.

For reference, the wrought Inconel 625 is taken as example. To that purpose, it was heated at 700 °C, 900 °C and 1100 °C in a furnace for 1 hour, then cooled in air. At 700 °C, δ hardening precipitates in globular and acicular form are observed. These same precipitates gradually decrease at 900 °C until they fully disappear at 1100 °C. The SEM images of wrought Inconel 625 samples with the different annealing times are presented in Figure 2.70.

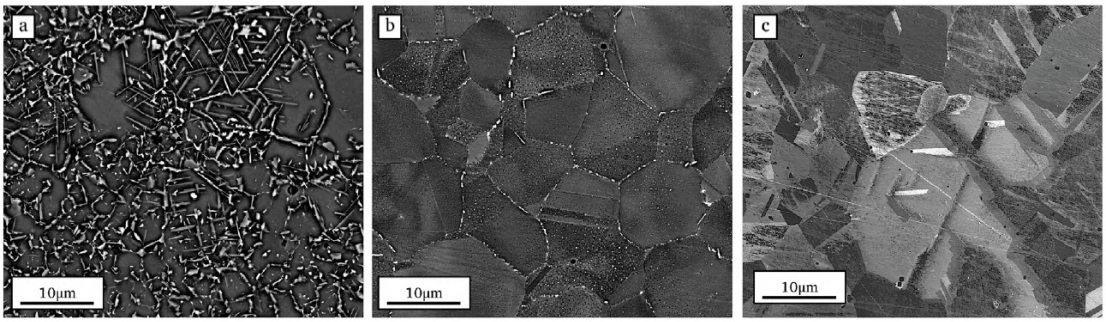

Figure 2.70: SEM images of wrought Inconel 625 samples annealed 1 hour at: a) 700 °C; b) 900 °C; c) 1100 °C [88].

In the case of SLM and LMD specimens, their observations revealed that the dendritic microstructure was stable after annealing from 700 °C up to 900 °C, at which point the first steps of grain recrystallisation take place, with a widening of the dendrite grains. When the samples where annealed at 1100 °C, the SLM and LMD microstructures start to differ. In SLM, the recrystallisation process was complete, as there are no dendritic grains in the structure, revealing a microstructure which is similar to the one obtained for wrought samples using the same treatment. The appearance of annealing twins is also to be noted. These twinning highlight the release of the stored residual stresses in the as-built SLM sample [87, 88].

The LMD sample heated at 1100 °C, has a microstructure that consists in a mixture of elongated and equiaxed grains, evidencing that the recrystallisation process was not completed. The SEM images that support these statements are shown in Figure 2.71.

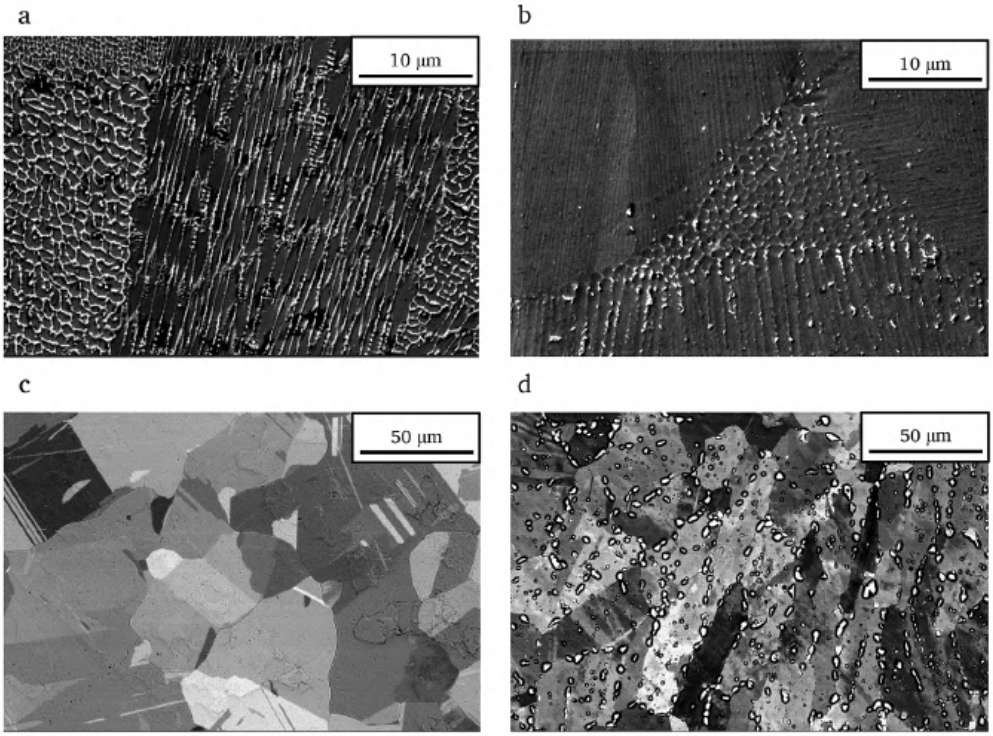

Figure 2.71: SEM images additively manufactured samples annealed 1 hour: a) SLM at 700 °C; b) SLM at 900 °C; c) SLM at 1100 °C; d) LMD at 1100 °C [88].

The tensile properties of the wrought Inconel 625 at different annealing temperatures are presented in Figure 2.72.

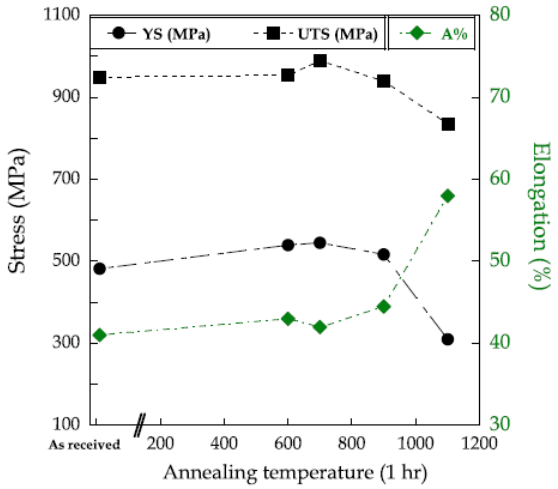

Figure 2.72: Tensile properties of the wrought Inconel 625 at different annealing temperatures [88].

As it can be observed in Figure 2.72, the heat treatment at 700 °C does not change significantly the yield stress (YS), the ultimate tensile strength (UTS) and the elongation to failure (A). These good tensile properties might be due to the precipitation of the strengthening γ'' phases after exposures at temperatures between 600 and 700 °C. Tensile

strength characteristics (YS and UTS) then decrease as the heat treatment temperature increases. For specimens heated at 900 °C, this decrease is due to the progressive dissolution of the precipitates in the matrix. On the other hand, the ductility of the specimens heat-treated at 900 °C and 1100 °C increases moderately.

The tensile curves for as-received wrought Inconel 625 and as-built AM Inconel 625 are presented in Figure 2.73.

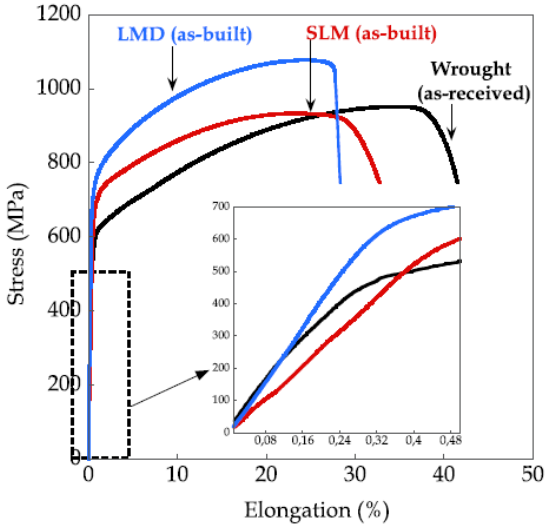

Figure 2.73: Comparison between the tensile curves of the conventional and the additive manufactured material [88].

It can be seen that the highest strength characteristics were obtained for the LMD specimens, with a YS approximately 50% higher and an UTS 12% higher than those of the wrought specimens. The SLM specimens present lower YS and UTS than the LMD ones, but still with a YS higher than the wrought specimens. The UTS of SLM and wrought samples were similar. In terms of elongation to failure, the SLM samples show lower ductility than wrought material, but still higher than the LMD specimens. The tensile properties of conventional and additively manufactured Inconel 625, in the as-deposited and with heat treatment are resumed in Table 2.9.

Table 2.9: Tensile properties of conventional and additively manufactured Inconel 625 [88].

Inconel 625	Young Modulus (GPa)	Yield Stress (MPa)	Ultimate tensile strength (MPa)	Elongation (%)
Wrought samples	184 ± 16	482 ± 42	955 ± 6	41 ± 1
SLM samples				
As-built	145 ± 4	652 ± 10	925 ± 13	32 ± 3
As-built + 900°C/ 1h	142 ± 11	567 ± 15	869 ± 7	38 ± 1
As-built + 1100°C/ 1h	114 ± 8	409 ± 14	886 ± 11	56 ± 5
LMD samples				
As-built	223 ± 24	723 ± 23	1073 ± 5	26 ± 2
As-built + 900°C/ 1h	224 ± 19	654 ± 15	1084 ± 2	27 ± 2
As-built + 1100°C/ 1h	213 ± 22	532 ± 22	991 ± 13	43 ± 1

The effect of heat treatment on the tensile properties of Inconel 625 for the LMD samples is shown in Figure 2.74.

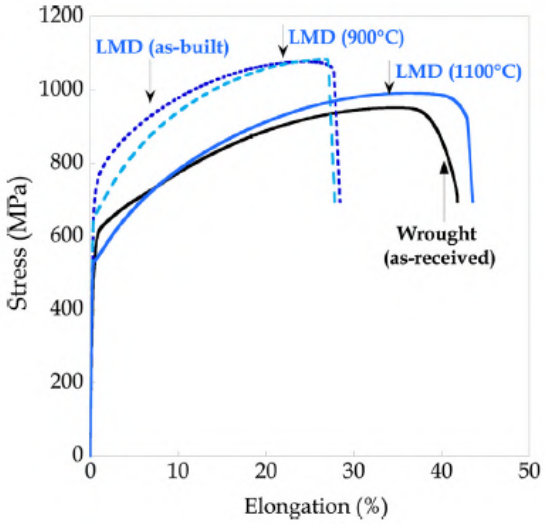

Figure 2.74: Effect of heat treatments on the tensile properties of the LMD samples [88].

After the chosen heat treatments, the YS and UTS are still higher than those of the wrought sample. Compared to the as-built samples, there is no significant change on the ultimate strength and the elongation to failure after annealing at 900 °C. Nonetheless, YS decreases slightly probably due to a small level of residual stresses relaxation. After annealing at 1100 °C, the samples show a decrease in the mechanical strength, while presenting an increase in elongation to failure, which might be attributed to the dissolution of some of the hardening phases [67, 90]. These properties are closer to the ones of the wrought specimen [88].

One of the most detrimental phases that can precipitate in Inconel 625 is the δ-phase. While some literature suggests that this phase enhances the tensile strength [67, 88, 93], it is generally considered to be undesirable since it decreases the ductility, the fracture toughness and the corrosion resistance of the alloy. S. Floreen et. al [66] indicated that δ-phase is not expected to appear until after about 20 hours at around 870 °C in wrought Inconel 625. However, due to the repetitive thermal cycles and faster cooling rates, the precipitation kinetics of this phase is expected to be different in AM processes [93, 94].

M. R. Stoudt et. al [93] performed a series of post-build stress-relief heat treatments at different temperatures and duration in SLM produced specimens of Alloy 625. The purpose of the study was to create a T-T-T diagram comparing the presence of δ-phase in additively-manufactured Inconel 625 to the wrought material. The resulting T-T-T diagram is presented in Figure 2.75.

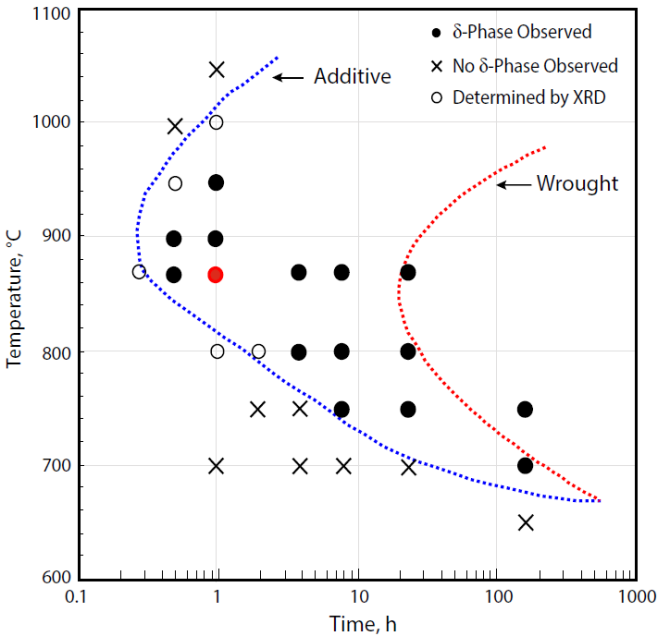

Figure 2.75: Time-Temperature-Transformation diagram comparing the presence of δ-phase in additively-manufactured Inconel 625 to the wrought material. The red dot represents an industry recommended stress-relief treatment [93].

The authors concluded that the transformation of γ-phase occurred at least two orders of magnitude faster in the AM specimen. In fact, an anneal at 870 °C for five minutes is enough to precipitate these unwanted phases. The faster kinetic was attributed to the large local composition gradients produced during the repetitive thermal transients and ensuing micro-segregation in the additive manufactured specimen [93].

As previously mentioned, slight changes in the chemical composition of Inconel 625 can produce notorious changes in microstructure, phases and thermal treatment behaviour. Since the material does not have a rigid composition- the chemical elements can vary within the standard, it is very likely that different Inconel 625 producers supply materials with slightly different chemical compositions.

With this statement in mind, M. D. Fullen et. al [95] analysed the effect of several heat treatments in four Inconel 625 specimens provided from four different vendors. As expected, the four specimens had distinct elemental compositions and reacted differently to the thermal treatments. One of the main conclusion of the authors was that the presence of N greatly affects the degree of recrystallisation and the temperature at which it occurs. They found that the alloy with the highest N content (0.191 wt.%) displayed no evidence of recrystallisation at any of the heat treatment temperatures investigated (900, 1100, 1125 and 1150 °C). The samples were produced using the Blown Powder process and the microstructure after stress relief and homogenisation heat treatment for the four vendors is presented in Figure 2.76.

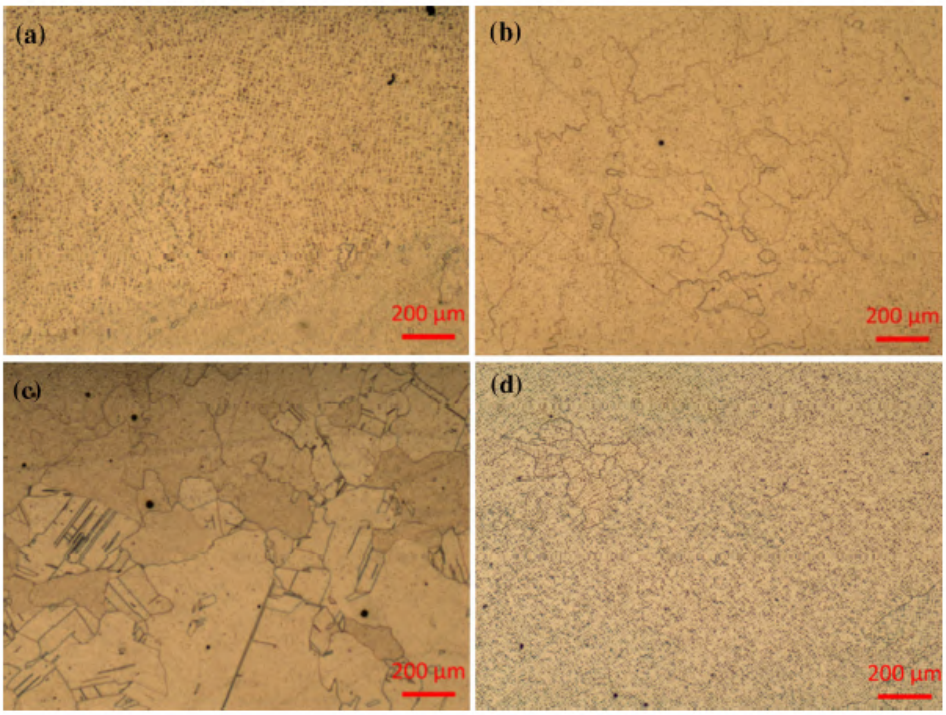

Figure 2.76: Comparison of microstructure after stress relief and 1150 °C homogenisation heat treatment for specimens from the four different vendors [95].

Fatigue behaviour

Additive manufactured parts may carry several different defects, such as lack of fusion regions between adjacent clad tracks, inclusions due to the entrapment of oxidised powder particles, gas porosities, delamination and severe segregation at interdendritic/grain boundaries. The rapid solidification inherent to these processes may result in orientation dependent properties, high level of residual stresses and cracking in susceptible, brittle phases. The presence of such defects may reduce substantially the fatigue life of Inconel 625 parts [96].

Carbides and other precipitates strengthen grain and interdendritic boundaries, retarding boundary migration, pinning dislocations, i.e. retarding them and consequently, hardening the matrix. However, their interface with the matrix becomes the initiation sites for fracture, due to being considered a local stress raiser [83]. In fact, fracture has been known to occur in regions with discontinuities and localised deformations, which are associated with the distribution of MC and $M_{23}C_6$ carbides and Laves phase, in the case of Inconel 625 [58]. Moreover, the non-uniform distribution of the precipitates, which typically occurs in AM as-deposited specimens, lead to local stress concentrations, originating more microscopic holes or cracks than in the case of the wrought material, where the precipitates are distributed in a more homogeneous fashion [97].

K. Kim et. al [98] studied the high-temperature high cycle fatigue properties of Inconel 625 alloy manufactured by L-PBF and compared them to those of the wrought alloy. The L-PBF material underwent a stress-relieving heat treatment (800 °C for 1 hour) and then a hot isostatic pressing (1175 °C, 150 MPa for 3 hours). On the other hand, the wrought alloy underwent solution annealing heat treatment (1100 °C for 1 hour). These treatments were meant to change the initial cellular/columnar structure to an equiaxed one. Moreover, according to the T-T-T diagram present in Figure 2.60, most precipitates

and intermetallics were expected to be dissolved. The authors found that L-PBF alloy showed the presence of Al_2O_3 and TiN phases. The presence of the oxides was considered to be a consequence of in-situ reactions with the controlled atmosphere. The wrought alloy showed the presence of (Nb, Mo, Ti)-type MC carbides.

Figure 2.77 shows the S-N curves that resulted from the author's experimental work. The results show that L-PBF alloy has better fatigue properties in the low-cycle region than the wrought alloy. In the high-cycle region, the opposite is verified. In this case, the fatigue life of the wrought alloy was 550 MPa, while the fatigue life of AM alloy was 500 MPa.

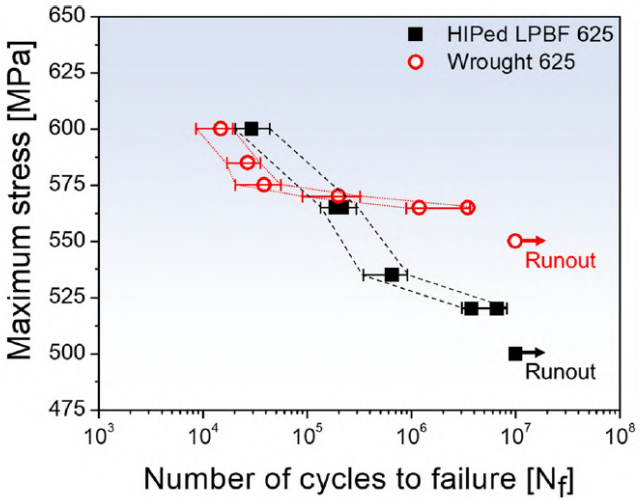

Figure 2.77: S-N curves of L-PBF and wrought Inconel 625 at 650 °C [98].

Generally, high-cycle fatigue life and fatigue limit are known to be greater in a material with higher yield strength. On the other hand, in low-cycle fatigue region, materials with greater elongation are known to have higher fatigue life. However, the results obtained by the authors are unusual. L-PBF Inconel 625 had lower elongation at fracture at 650 °C (38.7 ± 4.6 %) than the wrought alloy (77.0 ± 3.4 %). Hence, it was expected that the wrought material would have better low-cycle fatigue properties. Moreover, the yield strength of both materials was similar, so in the high-cycle fatigue region, fatigue life was expected to be almost the same [98]. Nevertheless, this result could be explained if the L-PBF material had high levels of porosity, since these voids can act as pre-existing cracks, being detrimental to high cycle fatigue.

After analysing the fracture surfaces of both specimens, they found that while a single point crack was verified in the L-PBF sample, in the wrought one multiple crack initiations were observed. Hence, they assumed that the difference in crack initiations could have led to the reversed fatigue behaviour [98].

No cracks that initiated by secondary phases were observed in the L-PBF material. However, in the case of wrought Inconel 625, fatigue cracks were identified to initiate from carbides near the sample's surface. It was confirmed that carbides easily undergo premature fracturing in the high stress/low-cycle regime, which promotes fatigue crack initiation [98].

D. Z. Avery et. al [99] investigated the fatigue behaviour of Inconel 625 produced by hybrid solid-state additive manufacturing, a process that is commercially known as MELD. By inspection of the fracture surface of one of the specimens, the authors found that a fractured particle was responsible for the initiation of the fatigue crack. Moreover,

they stated that brittle, irregular shaped carbides were observed cracked and debonded from the nickel matrix, originating stress risers that may reduce the expected fatigue life of the considered material. In one of the samples, inter-layer delamination was observed and, as a consequence, the number of cycles required to nucleate the fatigue crack was reduced.

Pereira et. al [58] performed fatigue tests of hot rolled and annealed Inconel 625 and analysed the fracture surface. They observed that the crack growth was a stable one, with shear lip and fast fracture. They realised the presence of dimples in the fast fracture region, which is a characteristic of the fracture mode by microvoid coalescence (MVC), indicating that the final fracture stage occurred by plastic collapse. Moreover, these microvoids coalesce, i.e. merge, continuing until the fracture occurs from regions with discontinuities and localized deformations, which are related with the distribution of MC and M_23C_6 carbides. This process can occur because the Inconel 625 matrix is ductile and the carbides are inherently hard. Thus, the matrix deforms plastically around the carbides, resulting in microcavities.

Beachmarks were observed in the fracture surface, which is a typical feature of the fatigue process in materials with good ductility [58]. These beachmarks are shown in Figure 2.78.

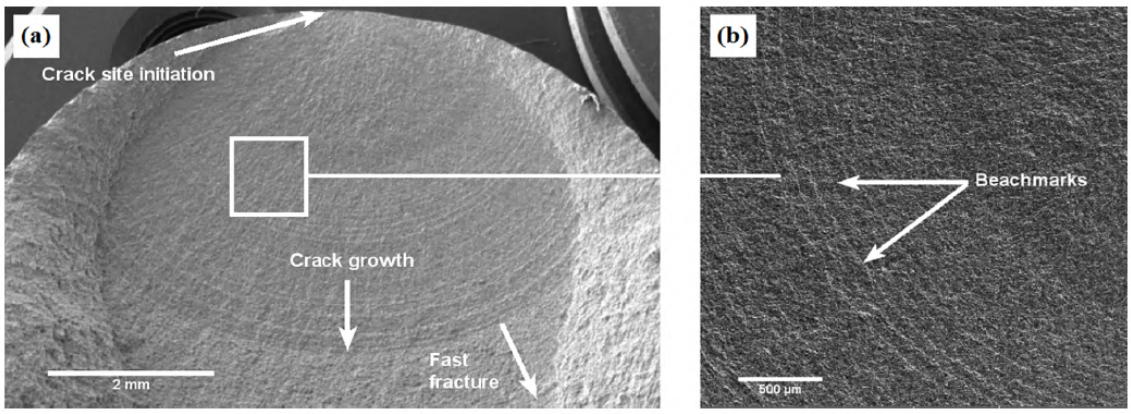

Figure 2.78: Fracture surface of annealed Inconel 625 showing stable crack growth region by fatigue and the presence of beachmarks [58].

Moreover, fatigue striations could also be verified. The presence of these elements further demonstrates that Inconel 625 has a unique combination of mechanical properties. In fact, even when it goes through hardening processes and has a high resistance limit, it has the necessary ductility to form fatigue striations [58].

S. Sui et. al [97] investigated the influence of the Laves and δ phases on the high-cycle fatigue behaviour of laser additive manufactured Inconel 718 and compared it to the wrought material. Despite being a different material than the one analysed in the present dissertation, the materials have similarities in composition and most of strengthening elements are the same. Hence, the effects Laves and δ phases has on Inconel 718 can be extrapolated to Inconel 625.

As previously mentioned, a heat treatment administered to the material can be used to remove these intermetallics. However, it is frequently not suitable for components repaired by a laser, because the high temperature can deteriorate the wrought substrate. In such cases, the Laves and δ phases can remain in the microstructure [97].

In relation to the δ phases, no such phase broke up in the cracking initiation region, although some of them fragmented in the fatigue crack propagation region. Moreover,

the authors found bent δ phases in this mentioned region, which means these phases have a certain capacity to plastically deform. When under loading, these phases possess the ability to deform with the austenitic matrix and keep the local stress concentration at a low level. Some of these phases were observed to hinder crack propagation, improving fatigue life [97].

On the other hand, Laves phase showed a different behaviour. These phases are brittle and exhibit poor plastic deformation capability compared to the austenitic matrix. Therefore, uncoordinated deformation will occur at the interface of the Laves phases and the austenitic matrix during loading processes, leading to the formation and concentration of local stresses. Hence, under plastic deformation, the separation between Laves phases and the matrix is likely to occur, leading to an easy path for cracks to propagate. Nevertheless, these phases behaved differently in the low-cycle and high-cycle fatigue [97].

In crack initiation region, the stress concentration was relatively small, so the Laves phases kept their original morphologies, independently of the stress range. In crack propagation region, their morphology was dependent on the stress amplitude. At low stress levels, fragmentation did not occur because the stress was not high enough. However, at high stress levels, most Laves phases broke up and separated with the austenitic matrix, originating microscopic holes or cracks at the interface. So, the authors concluded that Laves phases have a higher influence in fatigue life in the high stress region [97].

Chapter 3

Materials and Methods

The production of parts by Metal Additive Manufacturing is growing by the day. Most materials that are eligible to be produced by these processes are utilised in many technological fields, such as the aerospace, aeronautics and mould/tooling industries. These parts are frequently loaded under cyclic loading, which means that the fatigue characterisation of such components is of upmost importance in order to make MAM a viable option for part production.

To achieve the established goals for this dissertation, four point bending tests under displacement control are performed to evaluate the fatigue behaviour of Inconel 625. The price of feedstock is too expensive to allow extensive testing and material characterisation. Hence, miniature specimens [63] were utilised instead of specimens with standard dimensions.

In this chapter, the experimental procedures, preparation of numerical simulations and parameters are exposed, so that the reader may replicate the obtained results. This chapter is divided into five main parts:

1. Specimen production - Sections 3.1-3.2 - In these sections, the production process of the specimen is detailed: from the DED machine used, to the process parametrisation that led to the final specimens being ready for testing;

2. Material characterisation - Section 3.3 - The material that is used for fatigue testing is described and characterised;

3. Tensile testing - Section 3.4 - The experimental details of the tensile tests are presented;

4. Fatigue gripping system and respective numerical model - Section 3.5 - The gripping system that was built to hold the miniature specimen is presented. Moreover, the numerical model is outlined, as well as the made assumptions;

5. Fatigue Testing - Section 3.6 - The experimental details of the fatigue tests are presented; a fatigue life prediction based on material hardness is done and the usage of strain gauges for experimental calibration is explained.

3.1 DED machine

Every metal deposition and specimen production was performed at INEGI, where a DED setup is mounted and fully functional.

The main component of the DED unit is a COAX12 Laser Cladding Head provided by Fraunhofer IWS, Germany, specially designed for metallic components repair, deposition of coatings, and for additive manufacturing. Instead of being annular, like in many existing deposition heads, the powder delivery is guaranteed by four discrete nozzles, built in the deposition head, that are directed to the working point. Despite having separate nozzles, the system assures an homogeneous powder spot, making the powder supply independent from the deposition direction and the inclination of the cladding head [100]. Moreover, the cladding head is movable since it is mounted on a 6-axis KUKA robotic arm. In Figure 3.1, the Laser Cladding Head and the robotic arm are presented.

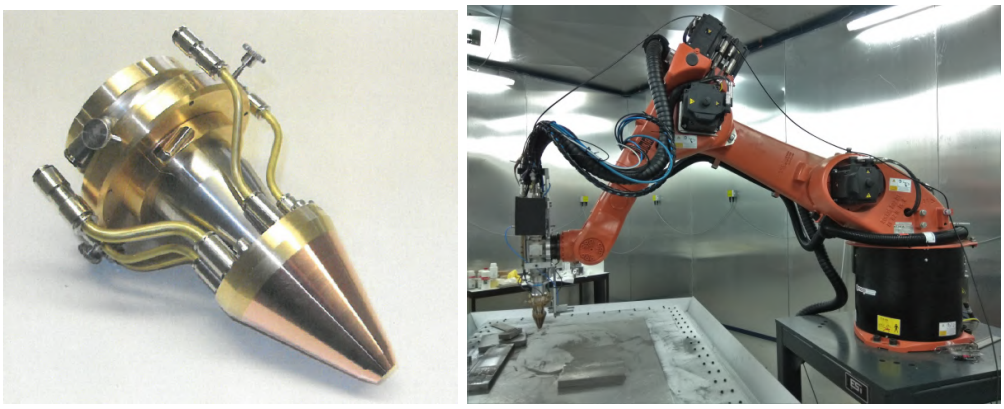

(a) (b)

Figure 3.1: Laser cladding head (a) and DED setup (b) [101].

The nozzles are water cooled, allowing continuous operation at up to 6 kW of laser power, while still being compatible with diode and solid-state lasers [102]. The deposition track width can range between 2 and 6 mm, while the powder feed rate between 10 and 75 g/min. Moreover, the focus length can be defined up to 70 mm [100]. Argon was the chosen carrier gas.

When it comes to the laser system, it was used a CoherentHighLight FL 3000, a fiber laser capable of delivering up to 3 kW and achieving an accuracy of $\pm$ 1 % with a wavelength of 1070 $\pm$ 10 nm [101].

Two independent Medicoat AG Disk Feeder systems were used as the powder feed system and are shown in Figure 3.2. They offer stable and pulsation free powder flow varying from 0.5 to 100 g/min [101]. For the experiments performed, only one of these was used. Nevertheless, they are suited for multimaterial depositions, if two different materials are placed inside each feeder system.

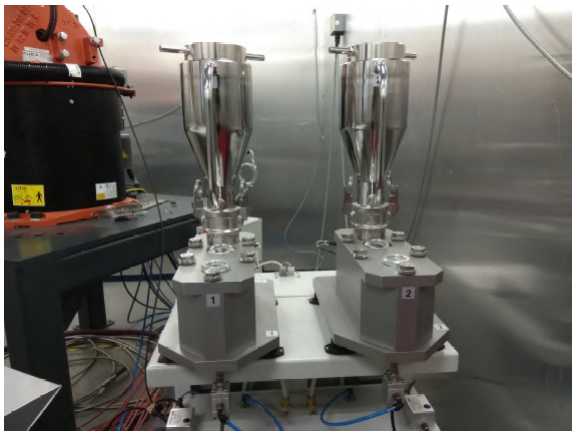

Figure 3.2: Utilised powder feeders [101].

The process was controlled in a closed-loop fashion by an E-MAqS temperature measuring system built in the cladding head and by the LompocPro 8 control software. A thermal sensing camera is used by the E-MAqS system to measure the melt pool temperature distribution. These values are then transferred to the control software, which is capable of reading them and then adjusting the laser power accordingly, in order to maintain a certain melt pool temperature distribution. Certain parameters are used to regulate the adjustment of the LompocPro 8 software, such as the target temperature of the melt pool, the minimum and maximum power delivery (the lower and upper thresholds for the acceptable power modification) and the starting power, which is the initial power value for every deposition step. The interface of the LompocPro 8 software is presented in Figure 3.3.

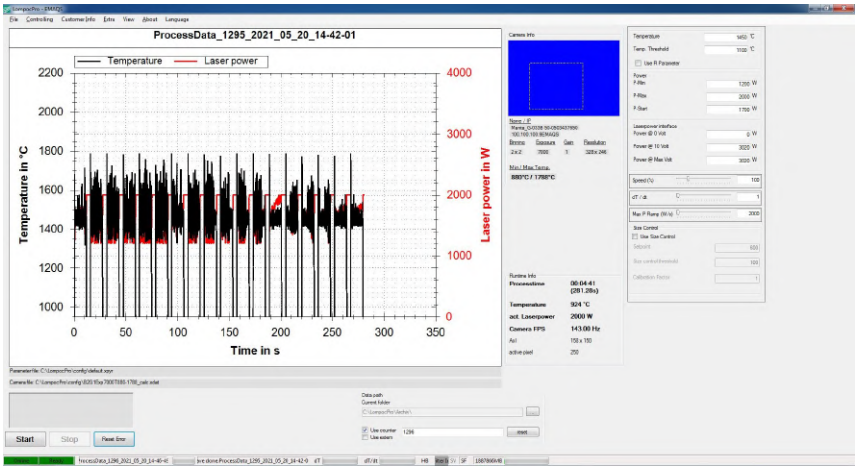

Figure 3.3: LompocPro software interface.

3.1.1 Optimisation of parameters

When a novel material is used to produce parts by a given process, extensive research as well as meticulous testing must be done. Optimal process parameters are often unknown and although literature review might provide a good starting point, every AM system is different and parameters tweaking might be necessary to guarantee defect-free parts.

With this in mind, the workflow chart presented in Figure 3.4 was idealised, in order to understand the influence of parameters on deposition quality.

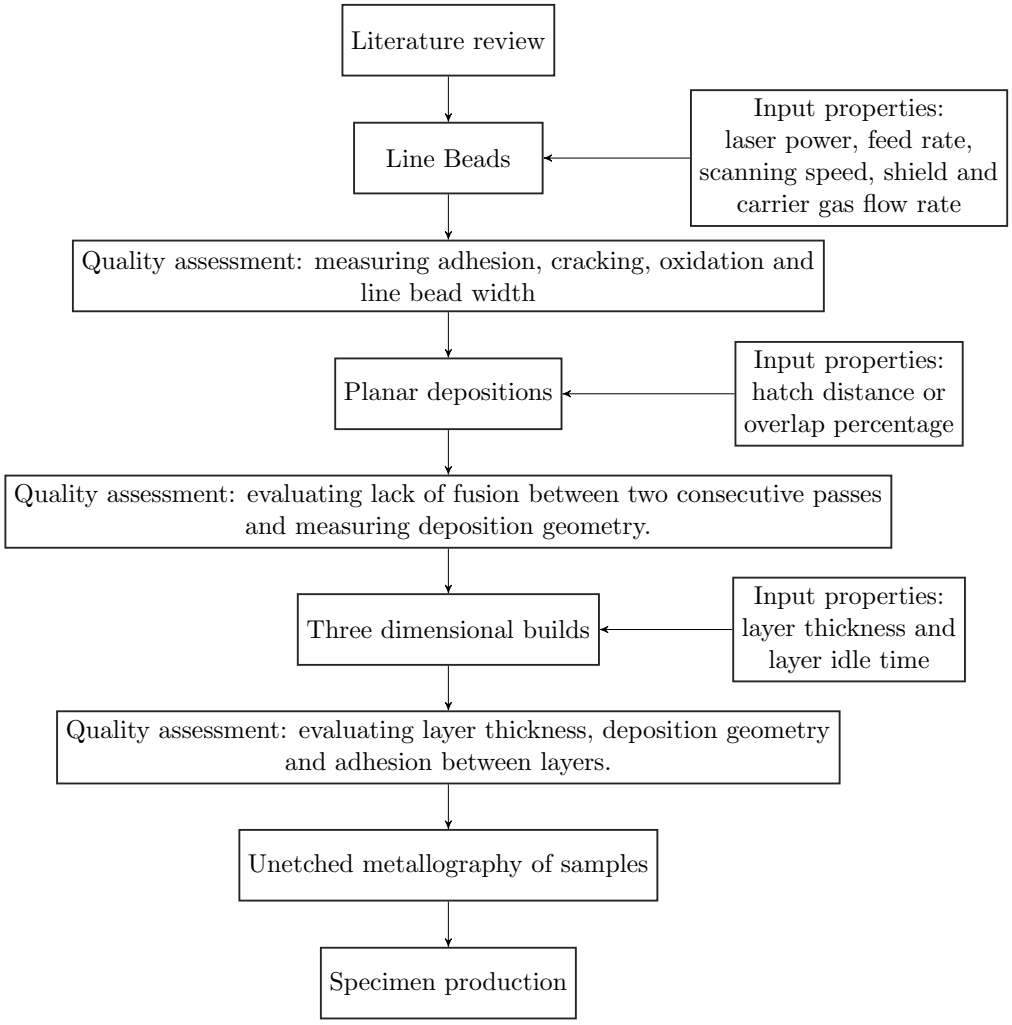

Figure 3.4: Process parametrisation workflow.

It is important to note that the parametrisation process is iterative, which means each step must be repeated until good results are obtained.

The first step was to review the available literature. This initial assessment was useful to define a good starting point for the process parameters. After the initial parameters were defined, single line beads were deposited. By measuring adhesion, cracking, oxidation and line bead width, it was possible to check if the laser power, feed rate, scanning speed, shield and carrier gas flow utilised were adequate. If these properties were not satisfactory, a parameter would be changed and another line bead deposited. The process was repeated until no defect visible to the naked eye was observed.

The next step was to make 2D or planar depositions. Here, the main parameter to be analysed was hatching distance, which can be evaluated by the lack of fusion between two consecutive beads and outside geometry. Once again, if no defects were detected, the next step could be considered. If not, the parameters would be changed and a new deposition made.

Afterwards, three dimensional builds were made, by introducing the desired layer thickness and idle time. At this step, the quality assessment could be performed by measuring

the produced layer thickness and outside geometry.

Besides visual inspection, the parametrisation of the process should take into account variables such as energy density and other dimensionless properties that quantify the energy and powder efficiency that, ultimately, provide information about the efficiency of the process itself.

Some of the carried out depositions are shown in Figure 3.5, where examples of the three aforementioned types of builds can be seen. Note that the substrate utilised for every deposition was DIN 40CrMnMo7, a structural steel.

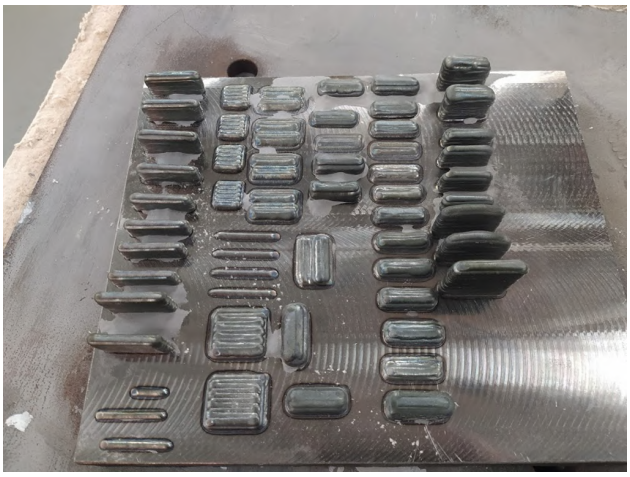

Figure 3.5: Single beads, planar and three dimensional depositions.

When reliable and consistent three dimensional depositions were achieved, like the ones in Figure 3.6, an unetched metallography was executed. The main goal of this was to verify if the inside of the samples had any major defects, such as porosity or lack of fusion between layers or consecutive passes of the laser.

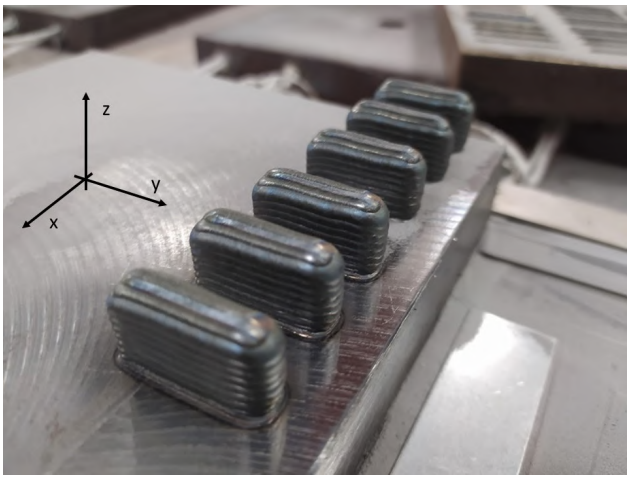

Figure 3.6: Three dimensional depositions. Z-axis is parallel to the build direction.

The initial parametrisation efforts established optimised parameters as the ones presented in Table 3.1. The EMAqS temperature measuring system was utilised and the defined parameters within that control system are listed in Table 3.2.

Table 3.1: First set of parameters: DED system parameters.

Hatch Spacing [mm]	Layer thickness [mm]	Layer idle time [s]	Laser power [W]	Feed rate [g/min]	Scanning speed [mm/s]	Shield gas flow rate [l/min]	Carrier gas flow rate [l/min]
1.52	1.45	30	Variable	12	6	26	4

Table 3.2: First set of parameters: EMAqS parameters.

Temperature setpoint [°C]	Minimum power [W]	Maximum power [W]
1350	650	1900

The properties of Table 3.1 were already explored in the Background Theory chapter, section 2.1.4. However, the properties set in the EMAqS control system should be further explained. The temperature setpoint is the target temperature of the melt pool. The system provides closed-loop control and, by calculating the real time temperature of the melt pool, is able to adjust the power of the laser, either to increase the temperature (by increasing the power) or to decrease it (by decreasing the power), in order to match the desired temperature setpoint. By defining the maximum and minimum power, the user is setting the upper and lower limits of power regulation.

After this first set of parameters, the samples were separated and then cut from the substrate using a mechanical saw located at INEGI. Afterwards, they were cut in two different planes: build (XZ plane) and transverse (XY plane), to be analysed. Note that Z-axis is the building direction. They were then polished and placed under a microscope. Some images taken to the samples cut in the build plane are presented in Figure 3.7.

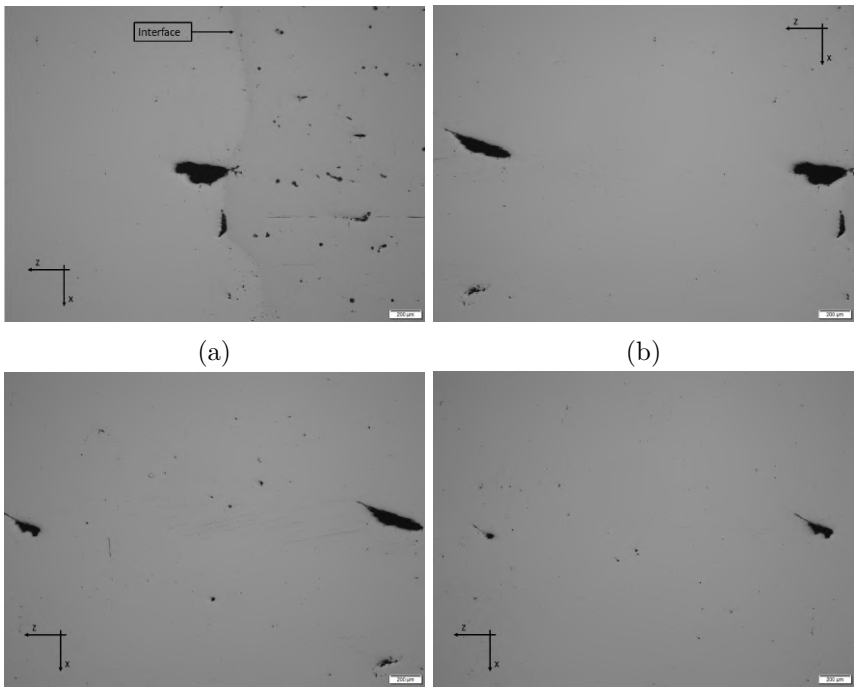

Figure 3.7: Images taken in the build plane, XZ, in different locations.

Note that these images were taken in the middle of the sample section by only changing one coordinate between each other, which means they can be mounted next to each other, establishing a horizontally aligned profile.

The four images presented in Figure 3.7 show an alarming fact. The parameters resulting from the first iteration led to some lack-of-fusion defects in the middle section of the sample. The one near the interface between Inconel 625 and the 40CrMnMo7 substrate has a considerable size (around 250 μm), as visible in Figure 3.7a. These defects tend to get smaller as the image is taken farther away from the interface. The defects near the interface are not much of a concern, since the interface is going to be cut off during the machining of the samples.

However, the other defects further away from the interface are not acceptable, specially since the main purpose of the current dissertation is to characterise the material's fatigue behaviour. As already stated, lack-of-fusion porosity represents an ideal candidate for crack nucleation, degrading the fatigue life of the component. Due to this finding, a re-parametrisation of the process was required.

Some of the images taken to the samples cut in the transverse plane are presented in Figure 3.8.

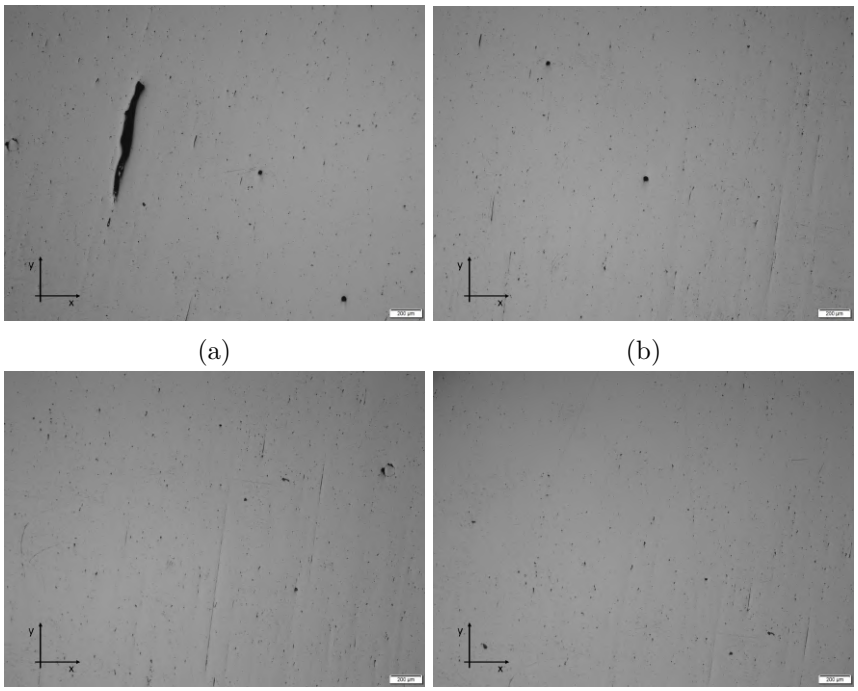

(a) (b)

(c) (d)

Figure 3.8: Images taken in the transverse plane, XY.

Although the lack-of-fusion defects are a clear deal-breaker, the samples show promising results, since no other visible defect or major porosity can be found. Other straight "marks" can be found in the material, but are most likely scratches produced by the polishing of the samples.

By analysing the defects present on the samples, it was hypothesised that not enough thermal energy was being delivered to the workpiece, specially in the first few layers, where the substrate is able to quickly dissipate heat. The fact that the defects grow in size when getting closer to the interface seems to backup this hypothesis. Therefore, the goal was to increase energy density, at first by increasing settings in the EMAqS system, and

then by imposing one layer with constant power. Hence, in the second set of parameters, the EMAqS system was only activated after the first layer, which was deposited with a constant power of 1800 W. Moreover, the hatching distance was also increased slightly.

The second parametrisation established parameters as the ones presented in Table 3.3 for the DED system, and in Table 3.4, for the EMAqS system.

Table 3.3: Second set of parameters: DED system parameters.

Hatch Spacing [mm]	Layer thickness [mm]	Layer idle time [s]	Laser power [W]	Feed rate [g/min]	Scanning speed [mm/s]	Shield gas flow rate [l/min]	Carrier gas flow rate [l/min]
1.8	1.7	30	Variable	12	6	26	4

Table 3.4: Second set of parameters: EMAqS parameters.

Temperature setpoint [°C]	Minimum power [W]	Maximum power [W]
1500	900	2200

Using this set of parameters, the miniature specimen were manufactured. After unetched metallography of the samples, the lack-of-fusion defects had disappeared and no additional defects were present.

At this point in parameter optimisation, unknown singularities started appearing in the melt pool, as shown in Figure 3.9, that would skew the temperature measurements, forcing a decrease in power. In fact, after the high temperature singularity is detected, the EMAqS system decreases the laser power to lower the melt pool temperature. After this, the system detects a low temperature and increases the power to compensate it. When the temperature starts to stabilise, a new singularity emerges and this error loop restarts.

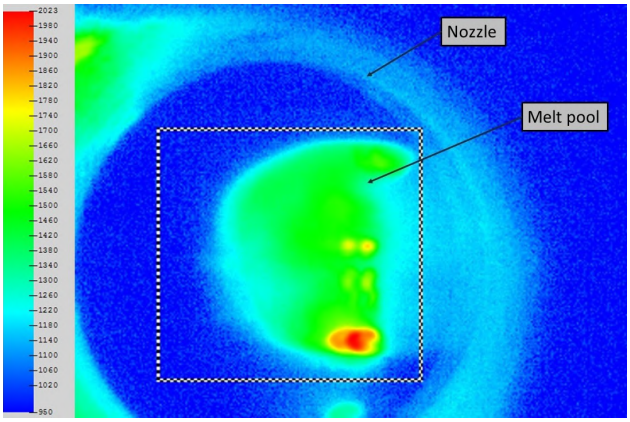

Figure 3.9: Singularities that would appear in the melt pool. Temperature [°C] scale. Picture taken from the LompocPro 8 software.

Often, the power setting would not converge, creating line beads with uneven thickness throughout. Facing these problems, it was decided to stop using the EMAqS system and instead rely on a constant power setting. The idle time was also changed resulting from the fact that the control system was no longer activated. Hence, a variable idle time between layers was used: 10s for the first layer, 15s for the second, 20s for the third and

25s from the fourth to the final layer. The idle time was increased with each deposited layer because as the build height increases, the sample takes longer to dissipate the heat. The third and final parametrisation led to the parameters shown in Table 3.5.

Table 3.5: Final optimisation of parameters: DED system parameters.

Hatch Spacing [mm]	Layer thickness [mm]	Layer idle time [s]	Laser power [W]	Feed rate [g/min]	Scanning speed [mm/s]	Shield gas flow rate [l/min]	Carrier gas flow rate [l/min]
1.8	1.7	Variable	1800	12	6	26	2.5

Although the Nicoletto specimen were produced with the second set of parameters, the tensile specimen were built with this last set of parameters. Note that the substrate was never preheated for any material deposition. Some of the images taken in multiple locations of the unetched samples are gathered in Figure 3.10.

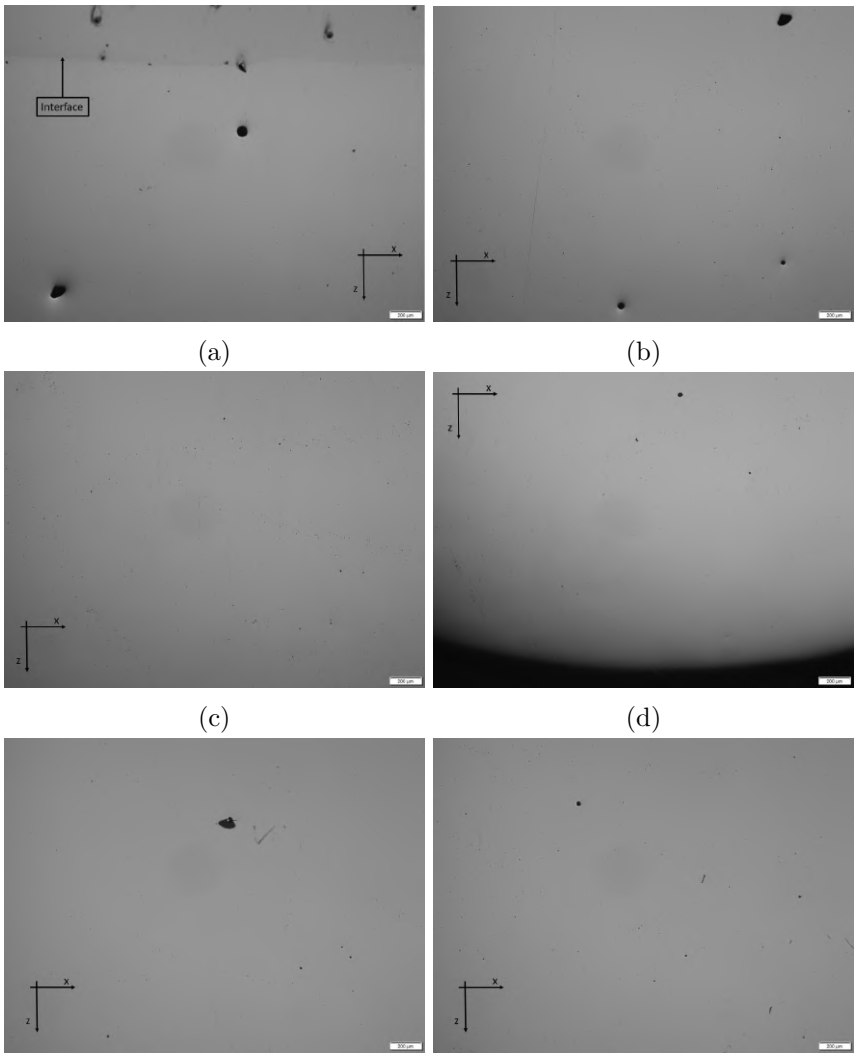

(a) (b) (c) (d) (e) (f)

Figure 3.10: Images taken in the build plane with samples produced with the last set of parameters.

As it can be observed in Figure 3.10, no major defects can be detected. Only a few entrapped gas and lack-of-fusion porosity that can be found in almost all AM parts without any post thermal treatment. These defects are mostly located near the interface between the Inconel 625 and the substrate. After production, the region near the interface is going to machined and will not be featured in the specimen, so the defects near the interface are not troublesome. Note that the overlap percentage of every deposition was kept at 30%.

3.2 Specimen production

The production of specimen, from the CAD idealisation to the finished specimen ready to be tested, is a long process that can be divided into many different steps. The specimen production workflow followed during the present dissertation is presented in Figure 3.11.

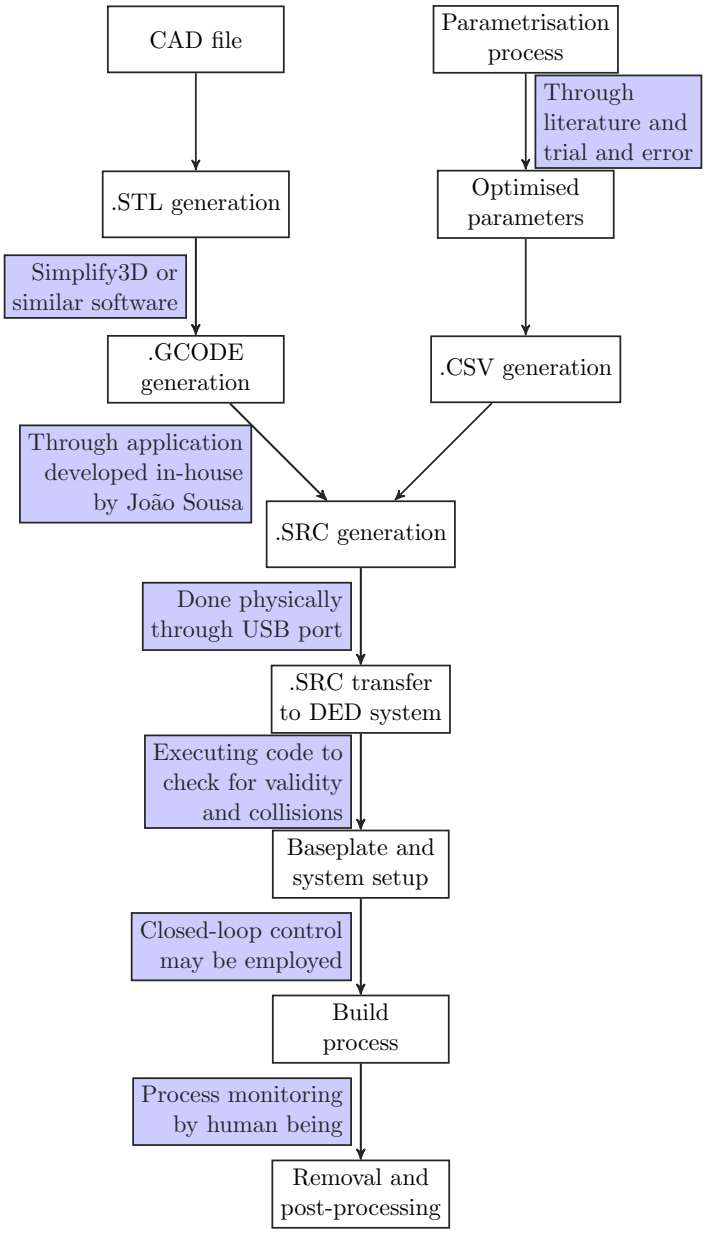

Figure 3.11: Specimen production workflow.

The first step is to design the specimen to be produced. For that purpose, a CAD file is created based on a model with the required geometry. This file should then be converted to an .STL file, dividing the model in a mesh of triangles.

The next step is to create a GCODE based on the .STL file, to determine the tool path that is going to allow the printing of the part. This process can be done manually, but is a tedious and time-consuming process. As an alternative, a software such as Simplify3D reads the .STL file and automatically generates the GCODE. During this generation, it is possible to define the hatch and printing pattern, as well as the oversize that is going to be given to the part.

The part is not directly printed with the desired geometry. DED is a near net shape process, which means the material would not be deposited in its final shape, since it is almost always going to need a post-process operation, such as machining. Hence, a block of material that embodies the specimen is printed, and the excess material is removed through machining. To avoid geometric and tolerancing defects, an oversize of material is estimated and the block is larger in every direction than the specimen to be produced. An example of a block of material used to print two miniature specimens is shown in Figure 3.12. In the same figure, the interface of the Simplify 3D software can be observed.

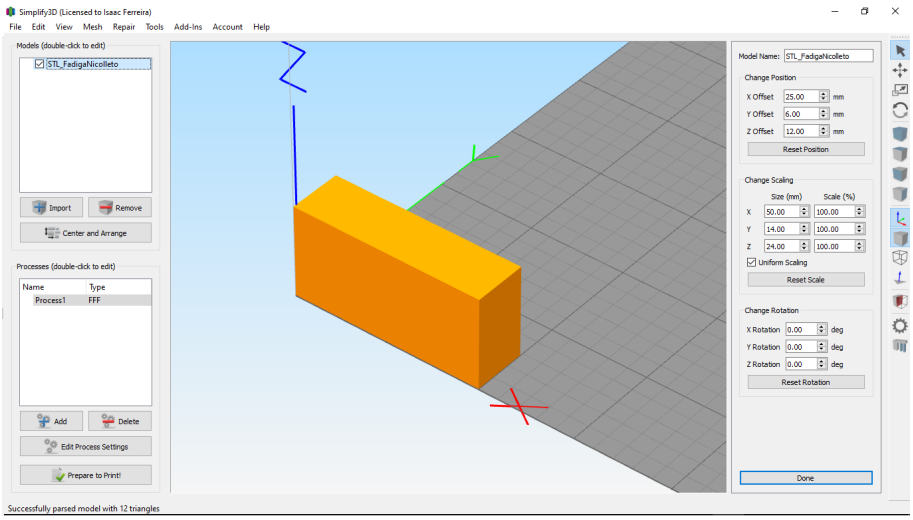

Figure 3.12: A GCODE is generated for a block of material with bigger dimensions than the desired specimen, using Simplify3D software.

The created block has 25 x 9 x 12 mm^3 and, since two miniature specimen are obtained from each block, it means that the block has 2 mm of extra material on the Y-axis, 2 mm on the Z-axis and 3 mm on the X-axis. The block is placed in the zero of the Cartesian referential to avoid unnecessary movements by the DED machine. The next step is to determine the printing pattern. In the present case, for each layer, the outside contours of the block is made first and only then the resulting rectangle would be filled. To avoid excess heat in a certain zone, each layer, the deposition starts at a random location. A step-by-step representation of the printing pattern is presented in Figure 3.13.

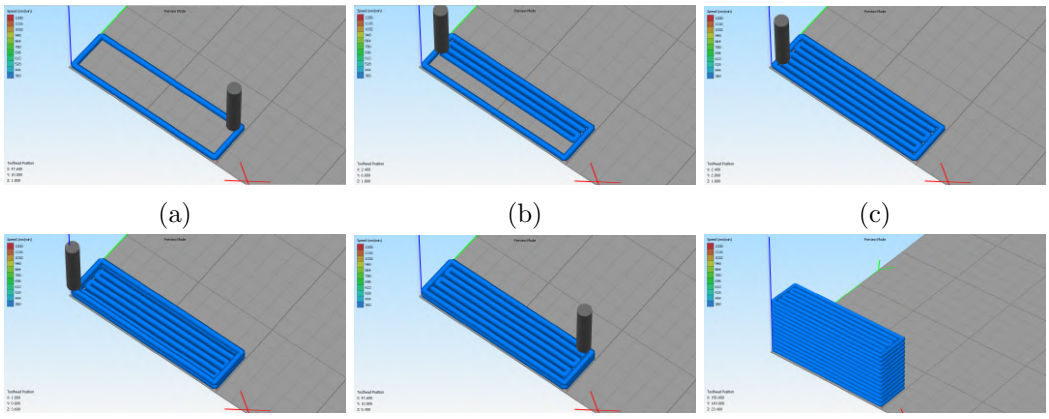

(a) (b) (c)

(d) (e) (f)

Figure 3.13: Defined printing pattern.

In parallel, the parametrisation process, through trial and error, is performed to achieve optimised parameters, as explained in section 3.1.1.

Having these parameters, their values are introduced in a .CSV file that, together with the GCODE (which has information about the part geometry), allow the machine to print the part as planned. The information of these two files can be coupled through an in-house python application developed by Eng. João Sousa, resulting in a .SRC type file. The application can be ran in a software such as RoboDK, where a simulation of the process can be performed. In Figure 3.14, the interface of the software with the DED setup can be seen.

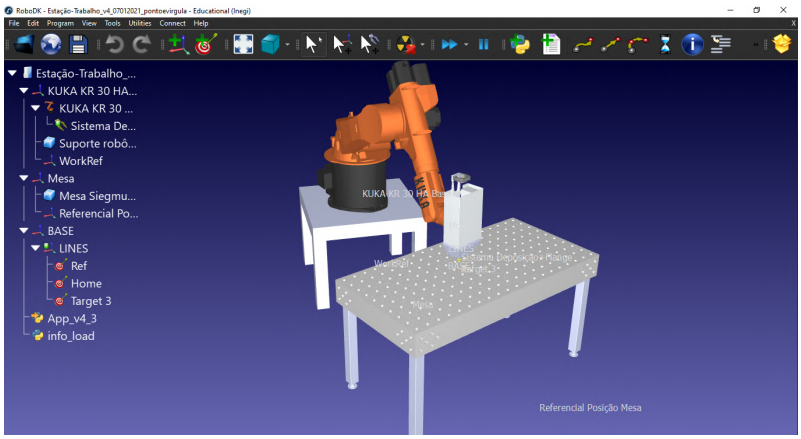

Figure 3.14: Interface of RoboDK software with the DED setup.

The generated .SRC file can be transferred to the DED system through an universal serial bus (USB) port. It is recommended to run the code in “offline” mode, i.e. without the laser and powder feeder turned on, to verify if there are any errors or collisions between the deposition head and other parts or depositions.

After all the security procedures are performed, the building process can be started, with or without closed-loop controls, such as EMAqS. During the building process, an user should be supervising and monitoring it at all times. After the building of the part is done, the DED chamber can be opened and the user, properly equipped with security gear, may enter and grab the baseplate with the deposition.

In Figure 3.15, the building direction and orientation of the specimens that are going to be machined is presented. Note that, in each material deposition seen in Figure 3.15a, two miniature specimens were obtained. For the tensile specimen, only one was machined from each deposition in a standing orientation, as shown in Figure 3.15b. In addition, the first one or two layers in the interface between materials were machined and were not part of the specimen.

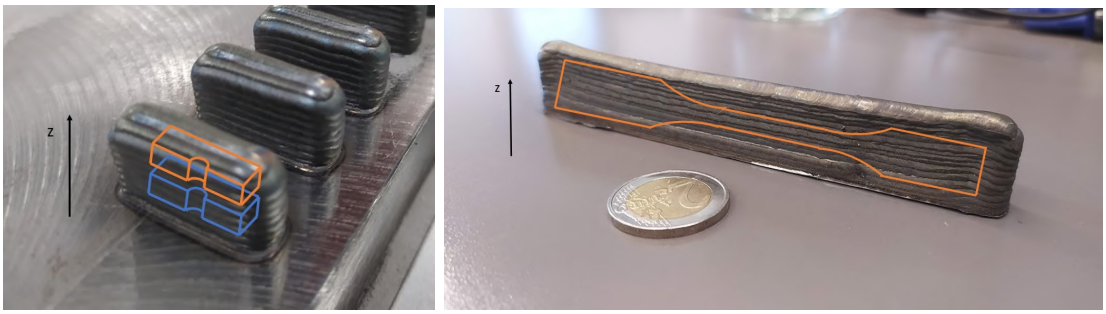

(a) (b)

Figure 3.15: (a) Material deposition of the miniature specimens; (b) Material deposition of the tensile specimens. Z-axis represents the building direction.

A mechanical saw, such as the one in Figure 3.16a, was used to separate the substrate that had depositions from the substrate that could still be used for further printing. The next step is the separation of the specimens from the pieces of substrate. In the present case, that separation was made using an abrasive saw disc that can be seen in Figure 3.16b.

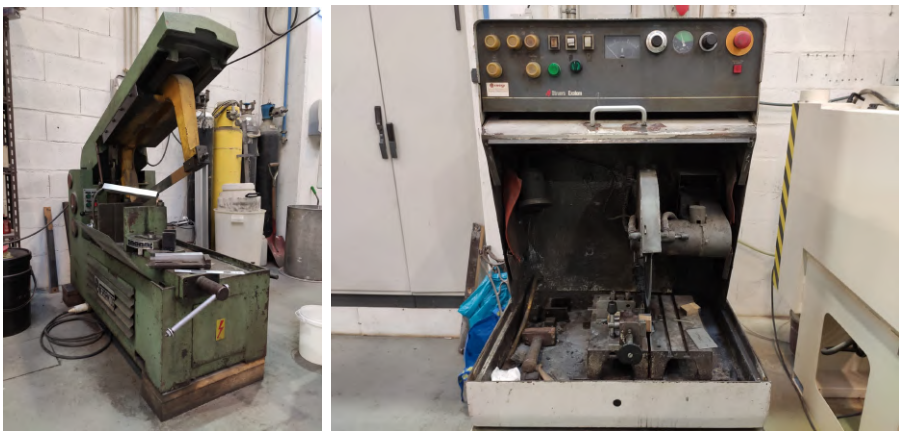

(a) (b)

Figure 3.16: (a) Mechanical saw used to cut the substrate; (b) Saw disc used to separate the sample from the substrate.

After the separation, the sample is ready to be machined to obtain the desired geometry and tolerances. At this point, the specimen is ready to be tested. In Figure 3.17a, the specimen numbered from 1 to 17 are presented. The technical drawing of the miniature specimen is presented in Appendix A and its main dimensions in Figure 3.17b.

(a) (b)

Figure 3.17: Nicoletto specimens and their general dimensions.

3.3 Material description and characterisation

In this sub-chapter, the material that is going to be tested is properly described and characterised, so that its condition is well understood.

3.3.1 Chemical composition

As already mentioned, some problems regarding the DED machine were faced and steadily solved, which lead to the production of specimens with two different sets of processing parameters. At the same time, all the powder had been used after the miniature specimens were manufactured, so a new batch of the same powder was used. The Nicoletto specimens were produced using the first batch, while the tensile ones were manufactured using the second. Moreover, the chemical characterisation of samples was made twice, one for each batch.

The utilised method for these measurements was optical emission spectroscopy (OES), a widely used method for finding the chemical composition of various metals.

In this process, an electrical source is used to excite atoms at the surface of the sample, to make them emit their characteristic light. This is guaranteed by the potential difference between an electrode and the sample of the metal, which produces a discharge channel, either a spark or an arc, that heats and vaporises the elements in the sample surface [103, 104].

At this point, the emitted light passes through a spectrometer where a diffraction rating separates the incoming light into element specific wavelengths that are sensed by specific detectors that measure the intensity of light in each wavelength. The intensity of each emission spectrum is proportional to the concentration of each element in the sample. In the final step, a computerised system gathers the intensities and provide the element percentages of the sample [103, 104].

The measurements were taken at the metallography laboratory at INEGI, using the SPECTROMAXx from Spectro as presented in Figure 3.18.

Figure 3.18: Machine used for the chemical composition measurements.

3.3.2 Density measurement

Two Nicoletto samples cut in two different directions, transverse and longitudinal, were used to measure the density of the material.

The density measurement was performed based on the Archimedes's principle. Firstly, the mass of the "dry" sample was measured using a scale. After, the sample was placed inside a recipient with water and the sample's mass was measured. Since the recipient was placed on top of a platform which was not in contact with the scale, the mass of the recipient and the water was not accounted by it. Hence, in this second measurement, only the apparent mass of the sample was calculated, as shown in Figure 3.19.

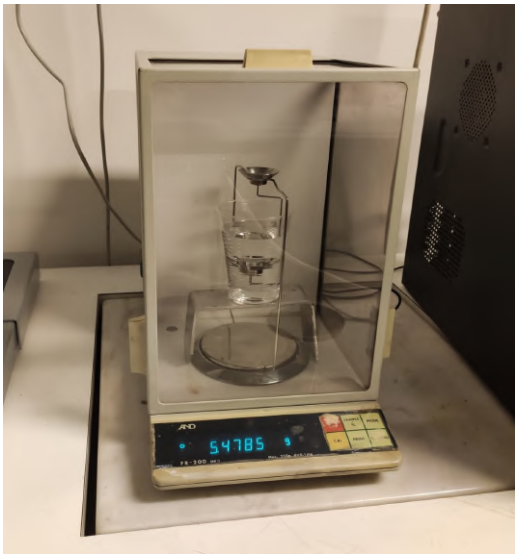

Figure 3.19: Measurement of density using Archimedes's principle.

The buoyant force that is exerted in a submerse body is equal to the difference between the weight of the body measured in the air and the apparent weight of the body (measured in the water). The same force is equal to the weight of the displaced liquid. In its turn, the weight of the displaced liquid can be given as a function of the density of the liquid and volume displaced. The volume of displaced liquid is equal to the volume of the submersed

solid. Hence, the density of the sample could be calculated by the following formula:

$$\rho = \frac{m_{air}}{m_{air} - m_{water}} \times \rho_{water} \tag{3.1}$$

where ρ is the density of the sample, m_{air} is the weight of the sample in the air, m_{water} is the apparent weight of the sample, and ρ_{water} is the density of water, which is known and equal to 1 g/cm^3.

Each measurement was taken three times and the sample was dried between each test. The samples were cut in a direction parallel to the build direction, hence the optical images were taken in the same direction.

3.3.3 Etching

Etching is a widely used technique to reveal the microstructure of materials through selective chemical attack. After the chemical attack, the sample might disclose information about grain size and geometry, distribution of inclusions and, particularly for AM produced samples, details about shape and size of the melt pool and features of the laser scanning tracks.

Many particularities of the sample may also be detected by unetched specimen, such as porosity and cracks. More about this topic can be found in section 3.3.4.

The etching of Inconel 625 sample was performed by electrolysis using Oxalic Acid Dihydrate. The sample is placed on a eletrolysis cell where direct current (DC) is applied. The sample was cut in three different directions, so all three Cartesian planes would be analysed. All the optical observations were made in INEGI's metallographic laboratory using a PMG3 optical microscope produced by OLYMPUS. The etched planes as well as their designation (frontal, horizontal and lateral) are presented in Figure 3.20. Note that the Z-axis represents the building direction.

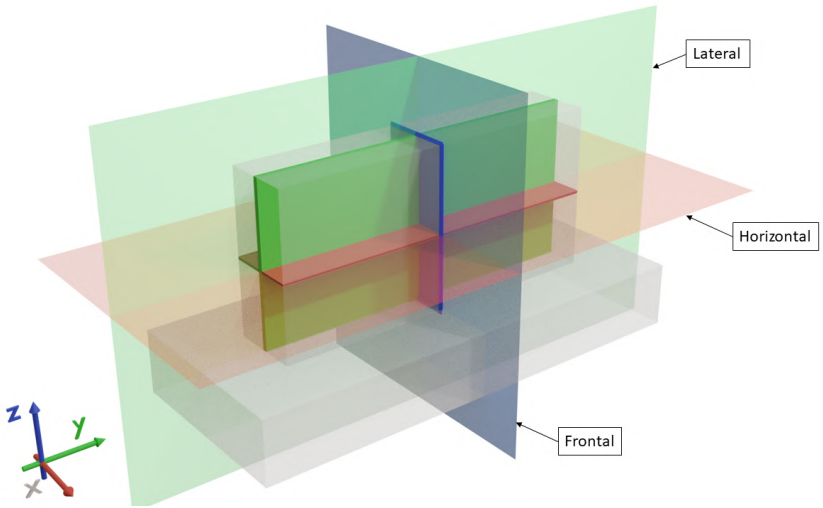

Figure 3.20: The three considered planes for the etching analysis. Z-axis represents the building direction.

3.3.4 Porosity analysis

Porosity is a well known defect in AM produced parts. The presence of porosity in parts affects mechanical behaviour, specially when it comes to fatigue resistance, as voids in the

material are ideal spots for crack nucleation. This subject is particularly relevant for AM parts, since the carrier gas may become entrapped in the melt pool during the successive remelting of the layers and cannot be removed unless a thermal treatment, such as HIP, is utilised. Moreover, if inadequate laser power is used, the presence of lack-of-fusion porosity may occur. Hence, the level of porosity of a few AM samples were analysed using ImageJ [105], an image analysis software.

The mentioned software is capable of measuring, in a certain image, the area where there is no material, proving to be resourceful to measure porosity levels.

Three samples were analysed. For each sample, two different images had their porosity levels measured, since the porosity is not expected to be homogeneous throughout the whole sample. With this approach, a better representation of the porosity of the sample is hoped to be achieved.

3.3.5 Hardness measurements

Hardness measurements were performed in samples of two different specimens. The two tested specimen were carefully chosen, as they have different heights and widths. Every measurement was done in Laboratório de Ensaios Tecnológicos (LET) at Faculty of Engineering, University of Porto (FEUP).

Since a variation of hardness with height is a possibility due to different cooling rates along the height of the specimen, several measurements were taken. The first measurement was taken 1.2 mm below the top of the specimen and the rest of them were taken below the first one, distancing 2 mm between measurements. However, the results will be presented in relation to the interface.

Moreover, in one of the samples, six other measurements were taken, in two different heights, to guarantee that the first method of measurement was accurate and representative of the hardness of the samples.

The samples were put inside an acrylic resin. The mixing was a manual process and the purpose of using the resin was to achieve better surface evenness. The samples were then polished. For the macrohardness measurements, a Vickers Otto Wolpert-Werke hardness testing machine of the "Dia Testor 2 Rc" type was used. The used identer had a penetrator made out of diamond and the macrohardness obtained was in Vickers scale. In Figure 3.21 the machine is presented, as well as one of the performed measurements. Every test was made using 196 N.

(a) Machine used for the hardness measurements

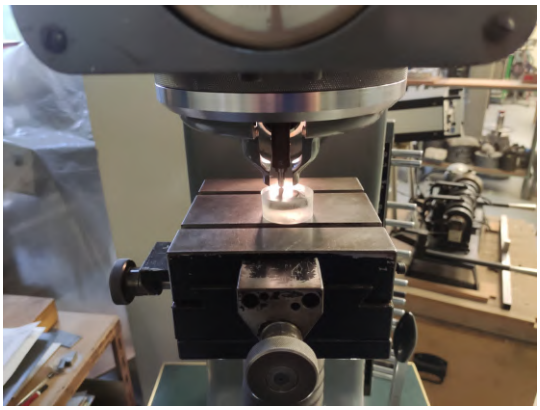

(b) Example of measurement

Figure 3.21: Macrohardness testing.

For the microhardness tests, a digital microhardness tester from Matsuzawa, model MXT70, was utilised. The meausurements were made in Vickers scale.

3.3.6 Surface roughness measurement

The surface condition of the miniature specimens was also object of study. As already explored, cracks tend to nucleate in regions with high stress concentration. The asperities that form the surface roughness are ideal candidates for crack formation. Hence, specimen were grinded in order to enhance the material's fatigue life and the surface roughness of two specimen- specimen 5 and 6, was measured.

Two different surfaces in each specimen were analysed- the flat bottom surface and a lateral one, as seen in Figure 3.22. For the former, two different directions were considered-

longitudinal (along the longest dimension) and transverse (along the shortest direction), while for the latter only the longitudinal direction was analysed.

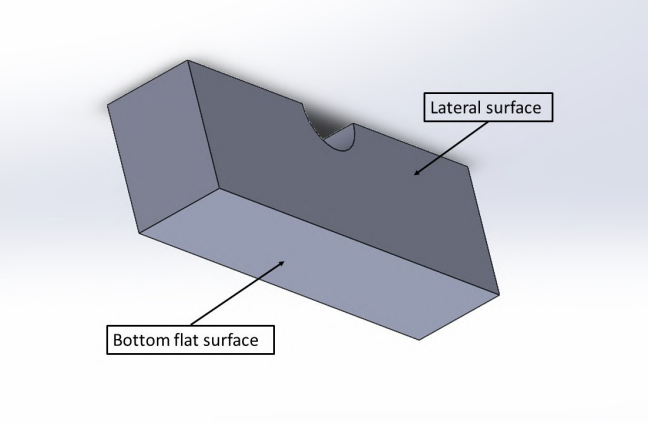

Figure 3.22: Surfaces of the miniature specimen analysed.

The bottom surface is relevant to analyse, since it is the surface that undergoes tensile stresses and where the crack is expected to nucleate. The lateral one was analysed because the crack could also initiate from the edge formed by the intersection of these two surfaces.

For each measurement, R_a and R_z were recorded. The R_a is the arithmetical mean deviation of the measured profile, while the R_z is the maximum peak to valley height of the profile, both being good examples of representation of the analysed surface. The measurements were carried out using a Mitutoyo surftest SJ-910 profilometer. The measurement speed was 0.5 mm/s and the measured length was 4.8 mm. An example of measurement of the R_a in a lateral surface is presented in Figure 3.23.

Figure 3.23: Measurement of the surface roughness.

3.4 Tensile testing

The tensile tests were performed in the mechanical testing laboratory of INEGI, utilising an Instron 5900R universal testing system, presented in Figure 3.24.

Figure 3.24: Machine used for tensile testing.

Two specimen were tested, which were designed according to the American Society for Testing and Materials (ASTM) E-8 [106] recommendations. The dimensions of the tensile specimen are presented in Figure 3.25, while the complete technical drawing can be found in Appendix B. These tests ran under displacement control, using a displacement rate of 2.5 mm/min. The acquisition of data was made at 5 Hz.

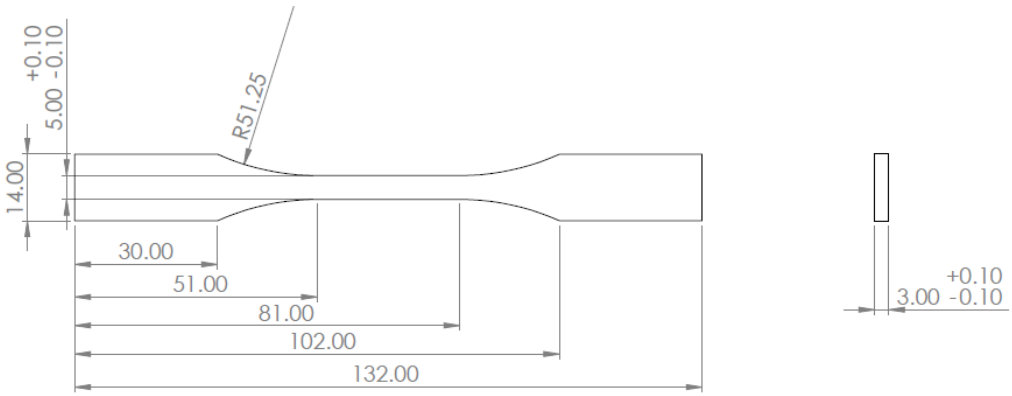

Figure 3.25: Dimensions of the tensile specimen utilised.

The two specimen were measured, before the tests, in three different locations within the testing length, using a micrometer. The different measurements and their locations can be observed in Figure 3.26.

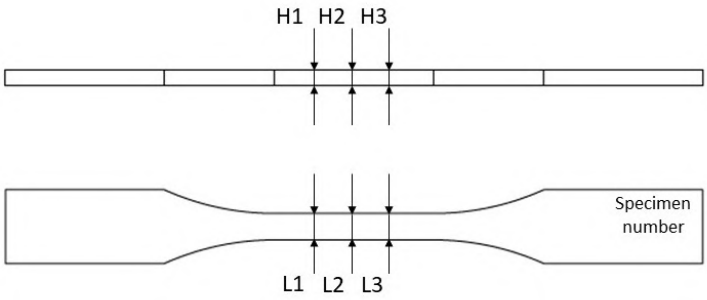

Figure 3.26: Measurements performed in each specimen.

One face of the specimen was painted with the intent of using DIC technique to measure the strain of the specimen during testing. DIC is a non-contact strain measurement technique, as opposed to contact measurement techniques, such as strain gauges. Its basic concept is to compare images taken at various stages of the test and correlating the position of pixels from one to another picture, in order to measure the deformation. Normally, the correlation is based on contrast, so the surface is painted with contrasting colours, prior to testing, in a speckle pattern [107]. The final experimental setup was ready for testing, as presented in Figure 3.27.

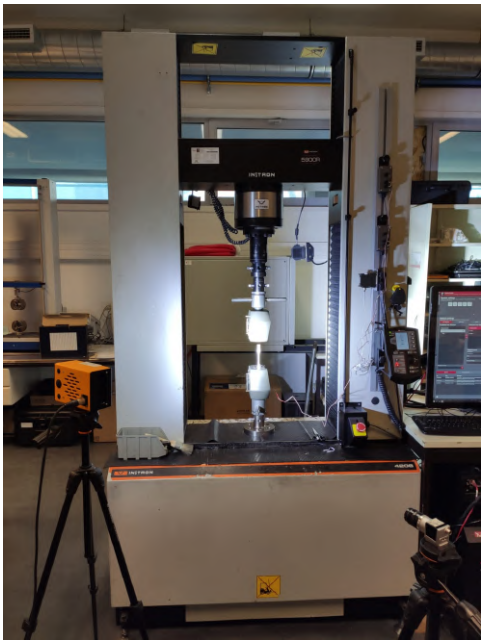

Figure 3.27: Final experimental setup ready for tensile testing.

3.5 Nicoletto specimen test machine

The machine used for fatigue testing of the miniature specimen is located at the Department of Mechanical Engineering, in LET, at FEUP. The machine, shown in Figure 3.28, is an electromechanical three-point bending machine with a three-phase electric motor from EFACEC. It has a rotational speed of 575 rpm, which can be converted to a test frequency of approximately 9.6 Hz.

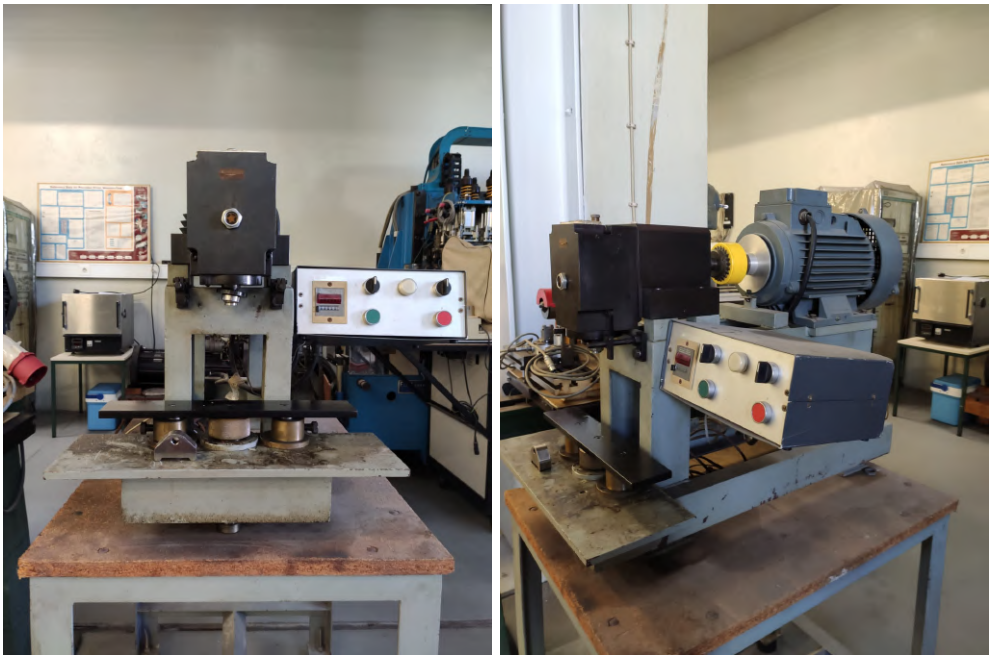

(a) (b)

Figure 3.28: Machine used for miniature fatigue testing.

The machine runs tests on displacement control, having its displacement range defined by an eccentric that can be regulated manually. The machine was not prepared to grip miniature specimen, which led to the development of a new gripping system.

The two load cells that were assembled to the machine were broken. Therefore, new load cells had to be ordered. For this purpose, two U3 HBM force transducers with maximum nominal capacity of 10 kN were used. The signals produced by these load cells are registered periodically by a data acquisition system, Spyder 8, equipped with an acquisiton software, Catman.

3.5.1 Development of the gripping system

The already mentioned machine was not prepared to test miniature specimen. Hence, it was necessary to design and develop a new gripping system that had to fulfil a few fundamental requirements to ensure reliable fatigue data:

1. The gripping system needed to be adjustable to the already existing machine, without making any major changes;
2. The whole system should remain in the same place during testing;
3. The tightening torque transmitted to the specimen as a compressive pre-load had to be easily calculated;

4. Allow for a 4-point bending test;
5. The cylindrical pins should be removable;
6. The maximum stress should be felt in the middle section of the specimen.

With these requirements in mind, a gripping mechanism was designed with SolidWorks software. The final sketch is presented in Figure 3.29 and the major overall dimensions are shown in Figure 3.30.

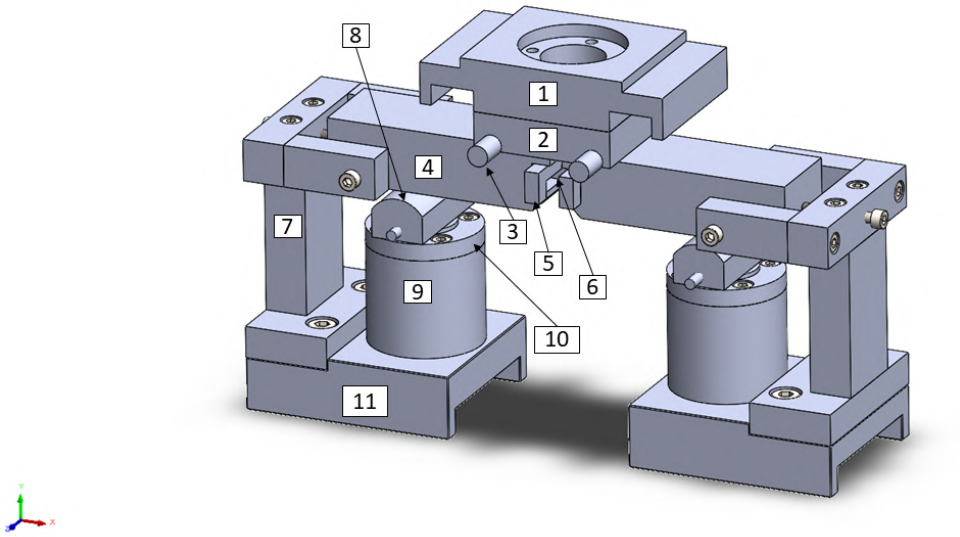

Figure 3.29: Assembly of the designed gripping mechanism.

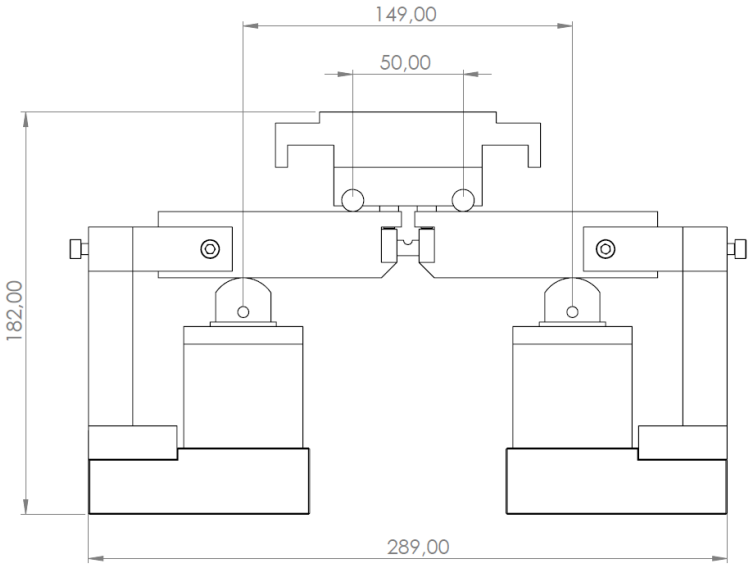

Figure 3.30: Assembly of the designed gripping mechanism. Units in mm.

The part numbered "1" in Figure 3.29 is an already existing part that was refurbished. It is connected to the machine through a ball joint that allowed the rotation of the plat-

form, enabling slight adjustments to the distribution of load. Originally, the machine was designed to perform 3-point bending tests, so the actuator that was bolted to part “1” was changed to one that allowed 4-point bending testing, such as part “2”. The new displacement actuator has two cylindrical pins with transition fit, allowing them to be assembled and disassembled easily, meaning that they can be replaced if they start to become flat at the contact points. The pins ensure the displacement is applied in two symmetric points from the centre of the specimen, with 50 mm between them. Part “1” and “2” are connected by four bolts and the cylindrical pins can be placed afterwards.

The main advantage of 4-point bending over 3-point bending is that the bending moment applied between the actuator contact points is constant. Moreover, in 4-point bending, there is also no shear stress between those points. This way, in four-point bending, fatigue will be happening in Mode 1, while in 3-point a mixed mode fatigue would occur (Mode 1 and Mode 2). In Figure 3.31 a simple example of a beam with one pin and one roller support, sustaining two loads distancing 50 mm, is provided [108].

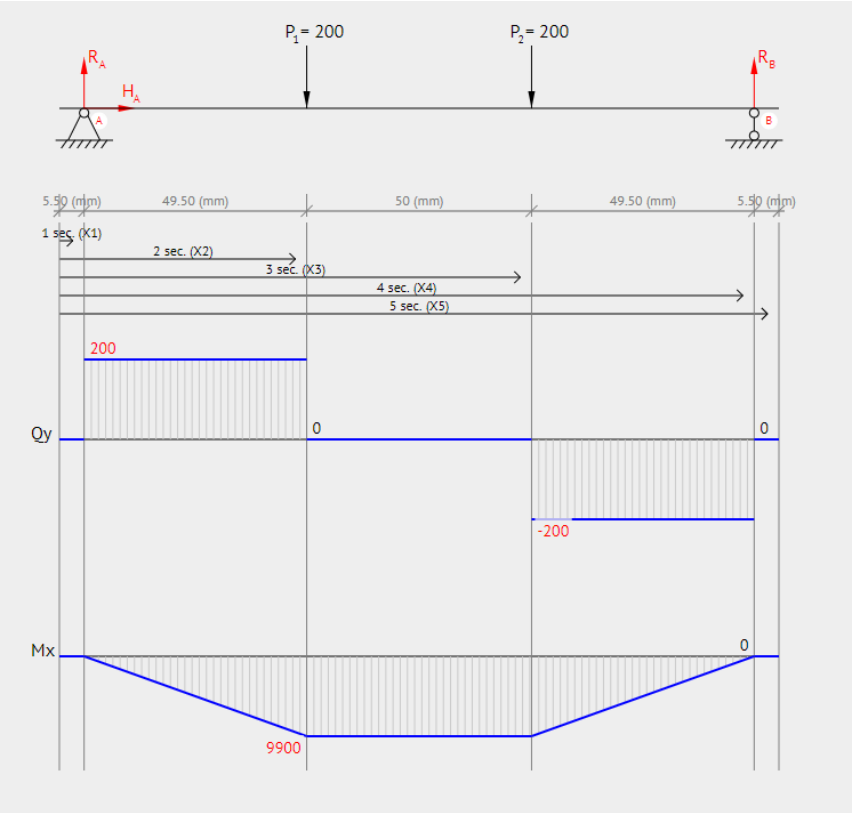

Figure 3.31: Moment and shear stress diagram of a 4-point loaded beam [108].

The main part of the gripping system can be considered the sub-assembly consisting of part “4”,“5” and “6”. Half of that system is presented in Figure 3.32, showing two different views.

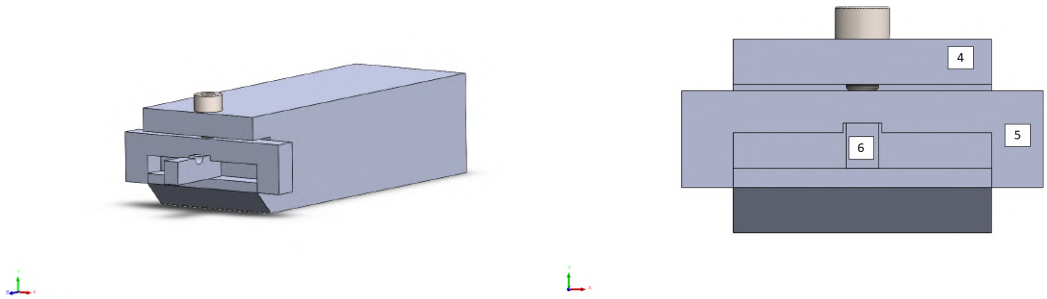

(a) Pseudo-isometric view (b) Front view

Figure 3.32: Gripping system sub-assembly.

As it can be observed, torque can be applied to tighten the screw. The normal load resulting from this torque is applied to part "5", which in turn transmits that load to the Nicoletto specimen, represented by the number "6". This way, the specimen is pressed against the bottom of part "4", or specimen holder, providing a secure and tight grip. This apparatus guarantees that all the load applied by the screw is going to be transmitted to the specimen, which proves to be useful when calibrating the finite element method (FEM) model.

The side wings of part "5" were designed to help the alignment of the specimen with its support. Moreover, a gap between the lateral face of the specimen and part "5" was kept to cover up for dimensional variations of the many tested specimens.

More importantly, the back of the specimen must not be in contact with part "4", to allow deformation of the specimen owing to Poisson's ratio. Otherwise, if the deformation on that direction was restricted, the overall stress on the specimen would, undesirably, increase. This detail is shown in Figure 3.33.

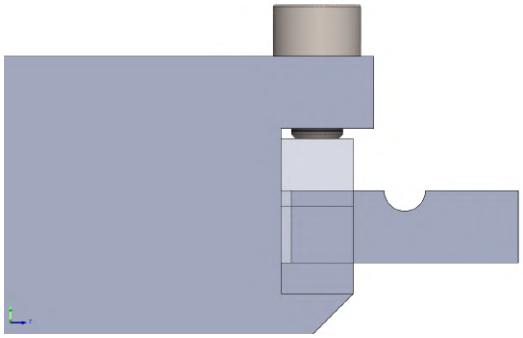

Figure 3.33: Detail showing the back of the specimen is not in contact with part "4".

The correct positioning and calibration of the gripping sub-assembly is guaranteed by part "7". This part has three bolts that can regulate the position of the back and lateral faces of part "4", ensuring that the middle section of the specimen is in the middle of the whole system. A top view of the assembly is presented in Figure 3.34, where it can be observed how the calibration is performed.

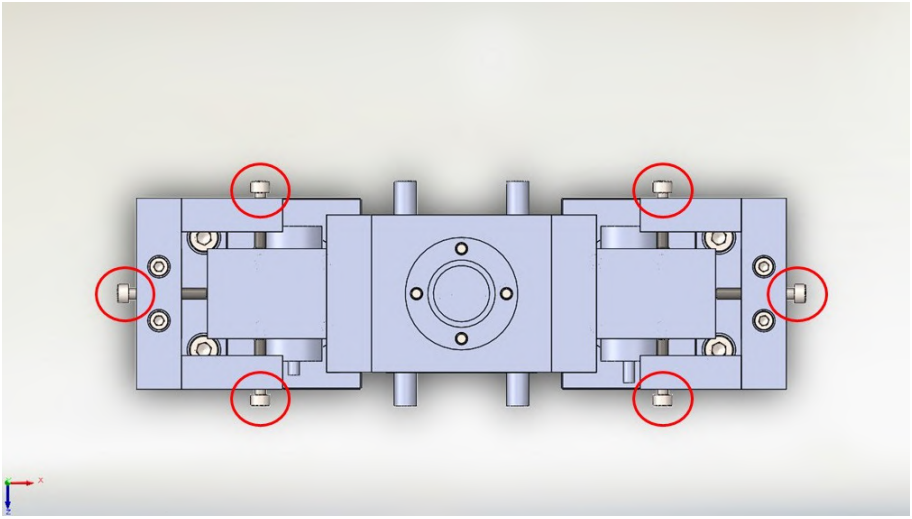

Figure 3.34: Top view of the assembly. Calibrating screws are marked in red.

This calibration system is bolted to part “11”, which is another refurbished part. This one enables sliding laterally on top of the base of the machine. This movement is of extreme importance, since it allows to place and remove the gripping system and the specimen, before and after testing, respectively. It also allows to change the bending moment diagram by changing the distance between supports. On top of part “11” is part “9”, a simplistic representation of the acquired load cells. These load cells are responsible for measuring the reaction forces.

On top of the load cells are the supports, represented by number “8”. These transmit the reaction forces to the load cells and are connected to them through part “10”. The connection is done by a hexagon socket set screw, as it can be seen in Figure 3.35

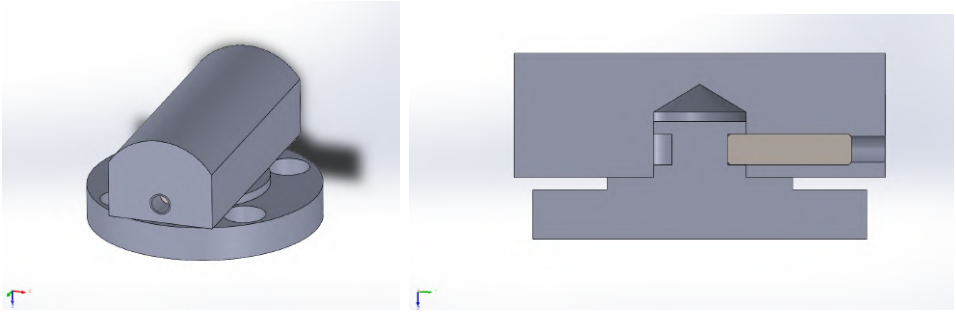

(a) Pseudo-isometric view (b) Section view

Figure 3.35: Connection between part “8” and “10” guaranteed by a hexagon socket set screw.

The designed gripping system, mounted on top of the existing machine, is presented in Figure 3.36. Below the gripping system, there is a movable platform that can translate the whole gripping system vertically. This mechanism allows the gripping system to be removed by lowering the platform and can also adjust the reaction forces by being raised or lowered.

Figure 3.36: Miniature specimen testing machine with adequate gripping system.

A FEM model was prepared in Abaqus software, to verify if the developed gripping system was adequately functioning. The model particularities will be discussed in the following section.

3.5.2 FEM analysis

In order to understand the behaviour of the specimen when tested in the designed gripping system, a FEM numerical analysis was modelled using the software Abaqus. Hence, a 3D model was built, taking into account two symmetry conditions of the problem: planes Y-X and Y-Z, allowing a shorter computational time. With that goal in mind, the threaded screw was not modelled in the software. Instead, a block of material with a tie contact constrain with the surrounding body and the pre-load imposed by the screw tightening torque were considered. The assembly of the created model is presented in Figure 3.37.

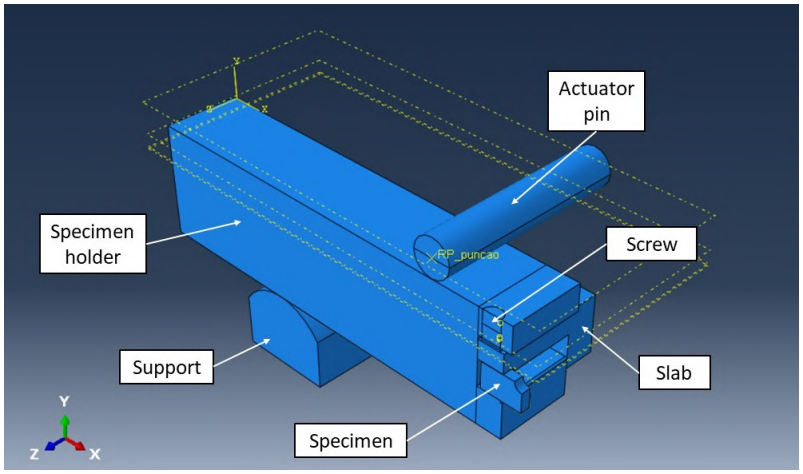

Figure 3.37: Assembly of the model in Abaqus.

It is important to note that the specimen holder used in the numerical simulations is slightly different that its final version. For these simulations, the holder had no chamfer in the bottom part. More on this topic is discussed further ahead.

Every part of the assembly was modelled as a deformable. As expected, the Nicoletto specimen was assigned the Inconel 625 material properties, while the rest of the components were assigned PM300 metal properties. Only the elastic behaviour was considered for both materials, since, initially, the plastic behaviour of Inconel 625 was unknown. After the tensile tests results were obtained, the plastic behaviour was modelled. The defined properties for both materials are presented in Table 3.6.

Table 3.6: Material properties applied in the numerical model.

Material	Young Modulus [GPa]	Poisson's ratio
Inconel 625 [1]	207.5	0.278
PM300 [109]	205	0.3

Later on, strain gauges were placed in the specimen. To replicate their location, a partition with one fourth the dimensions of the strain gauge grid was made in the specimen, taking advantage of the two symmetry conditions. This way, when the part was meshed, there would be one node in each vertex of the gauge grid. The partition can be observed in Figure 3.38.

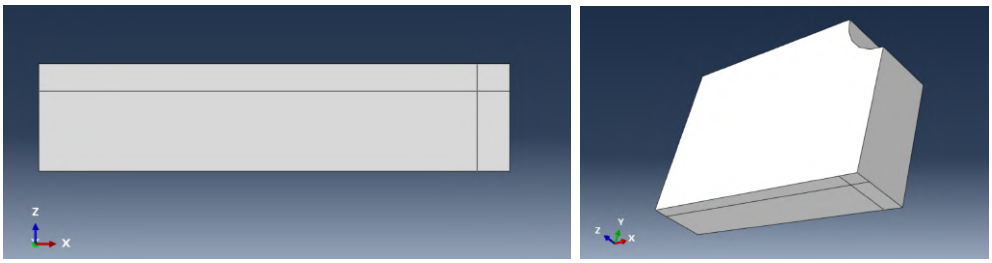

(a) Partition location (b) Psuedo-isometric view

Figure 3.38: Partition made in the specimen.

The simulation was preformed using two different steps. The first one where the screw would be tightened by applying a certain pre-load, and the specimen secured, and the second step where the displacement would be applied by the actuator. While the time period for the pre-load step was 1, the time period for the displacement step was 3. This will be explained ahead.

At this point, the interaction between components had to be introduced. As already mentioned, instead of modelling the thread of the screw, a tie contact was created between the outer surface of the screw and the inner surface of the specimen holder (the real surface where the screw actually screws), which means that during the simulation the two selected surfaces will keep forming a contact pair together, as shown in Figure 3.39. Note that, he PM300 properties were also attributed to the screw.

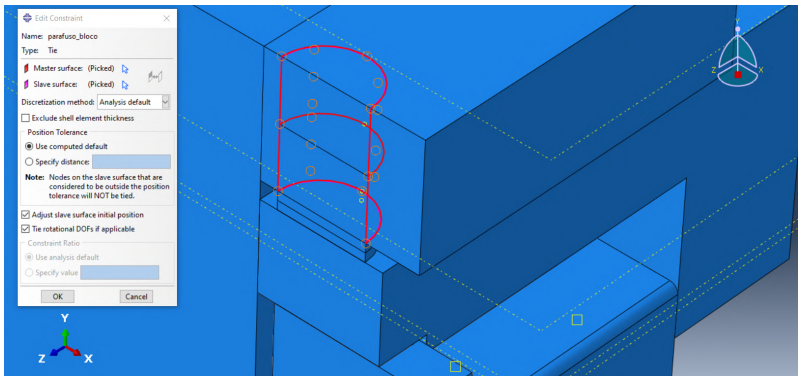

Figure 3.39: Tie contact established between the two contact surfaces.

Two kinds of interaction properties were established, both with a coefficient of friction of 0.15. One of them allowed separation after contact, while the other did not, to guarantee that once the parts made contact, they would stay that way during the simulation. The latter was attributed to the interaction between part specimen holder and the support, to further restrict the model. The former was attributed to every other contact in the model, them being: the contact between the screw and inner surface of the specimen holder where it would screw, top surface of the specimen and bottom surface of the slab, specimen holder and bottom surface of the specimen, and between the actuator pin and the top surface of the specimen holder.

Every aforementioned contact was created in the initial step and propagated until the last, with the exception of the contact between the actuator and the specimen holder, which was created only in the displacement step. By creating this interaction in the last step, one allows the specimen holder to deform at will during pre-load application, without being limited by the actuator, i.e. without adding extra stress.

Moreover, for the results to be as accurate as possible, the simulation must be performed twice. In the first simulation, ran until the end of the step 1, one can measure the displacement of the specimen holder resulting from the pre-load application. With this displacement, it is possible to know where the actuator will first contact with the specimen holder. Hence, prior to the second simulation, the cylindrical actuator must be translated upwards the previously mentioned displacement in the assembly. Only then the second simulation can be ran until the last step and the results recorded.

By taking this approach, the numerical model is closer to what happens in reality. The gripping system will first secure the specimen by tightening a screw and only then the displacement is transmitted by the actuator.

The boundary conditions were also specified. First, an encastre in the bottom surface of the support was added, since these supports are placed on top of the load cells. Secondly, both symmetries (x and z) were included, as shown in Figures 3.40a and 3.40b

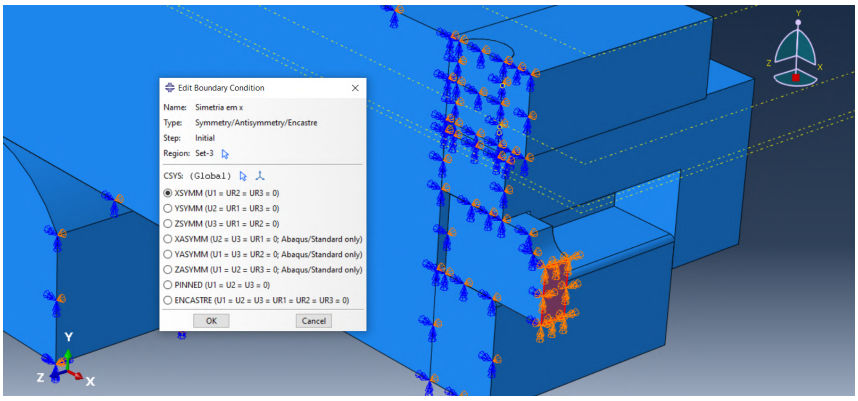

(a) Symmetry regarding x-axis

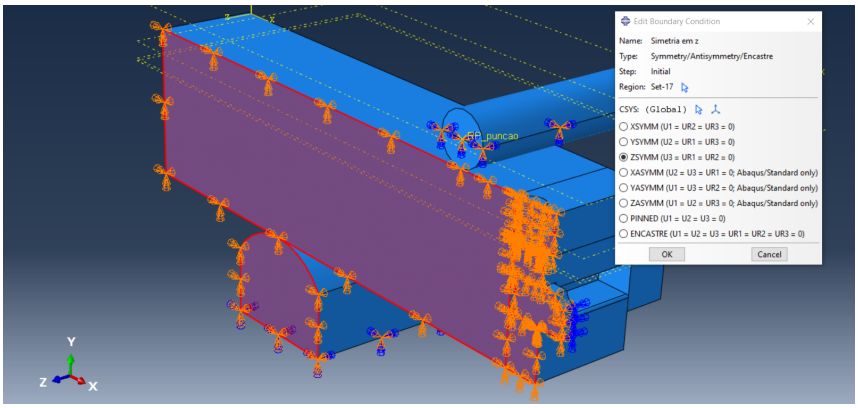

(b) Symmetry regrading z-axis

Figure 3.40: Symmetry boundary condition.

Note that the actuator did not need the symmetry condition, since it was restricted in another way which provides the same results as a symmetry condition. In fact, the actuator had two boundary conditions. In the initial and pre-load step, the actuator was given an encastre so that it could not move. In the last step, the actuator was restricted in every direction except in the Y-axis, i.e. in the same direction that the displacement is to be imposed.

The last boundary condition was the maximum displacement imposed by the machine through the actuator. In this case, it was used 0.1 mm as the maximum applied displacement, although in other analyses in further sections different displacements were considered. Since the analysis objective was to simulate an application of displacement, subsequent removal and one more application, an amplitude had to be created and applied to this boundary condition. This condition, shown in Figure 3.41, would be initiated at the displacement step, hence the step period being 3.

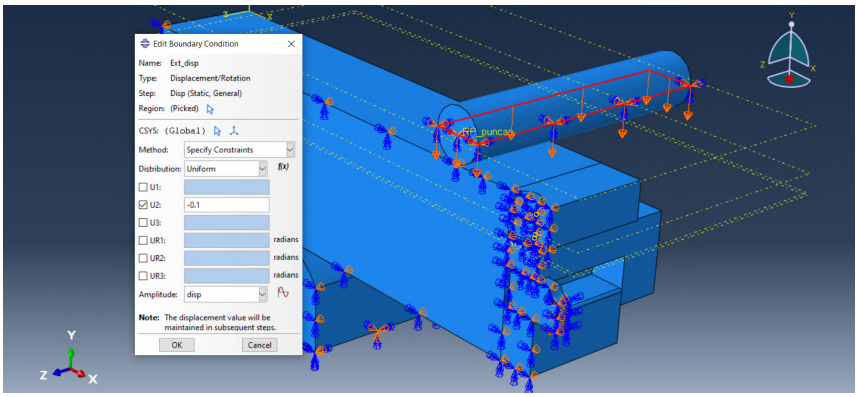

Figure 3.41: Applied displacement to the actuator.

To further demonstrate and explain the amplitude of the boundary condition, in Figure 3.42 the amplitude definition and the originated results is presented.

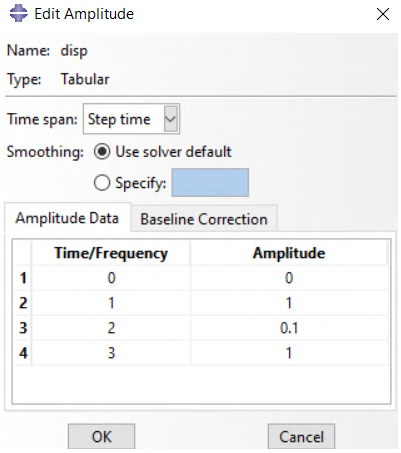

(a) Displacement amplitude definition

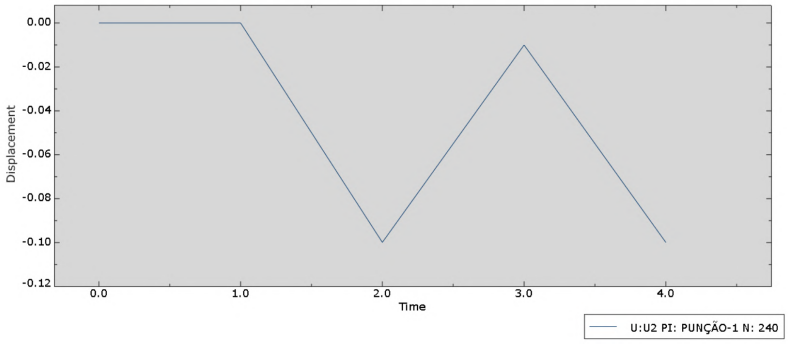

(b) Y-axis displacement, in mm, of a node from the actuator

Figure 3.42: Displacement of the actuator.

As it can be observed by Figure 3.42a, the amplitude ranges between 0.1 and 1 of the considered displacement, i.e., the minimum displacement is $0.1 \times 0.1 = 0.01$, while the maximum displacement is $0.1 \times 1 = 0.1$. Hence, $\Delta\delta = 0.1 - 0.01 = 0.09$ mm.

After the boundary conditions were applied, the pre-load of the screw needed to be

modelled. The maximum recommended tightening torque for a 12.9 class M5 screw is 10 N.m [110]. The pre-load that corresponds to that torque can be calculating using the following equation [111]:

$$T = F_p \times K_{torque} \times d_{nom} \tag{3.2}$$

where T is the tightening torque, K_{torque} is a torque coefficient based on the friction between threaded surfaces, the materials in contact and shape of the thread, which may range from 0.12 to 0.3 [111], F_p is the pre-load, and d_{nom} the nominal diameter of the bolt or screw. By assuming a K_{nom} equal to 0.2, the pre-load obtained for a M5 screw tightened with the recommended torque is around 10602 N. This value was considered for the first analysis.

Finally, the mesh was defined. The part was seeded locally, giving a more refined mesh to the most important parts of the model, meaning that the specimen had the most refined mesh. A convergence study was performed to understand the relation between mesh refinement and computational time. Those results are presented in a further section.

The mesh given to the model is shown in Figure 3.43a. Moreover, a zoom-in in the most important parts is given in Figure 3.43b, revealing a much more refined mesh in Nicoletto specimen.

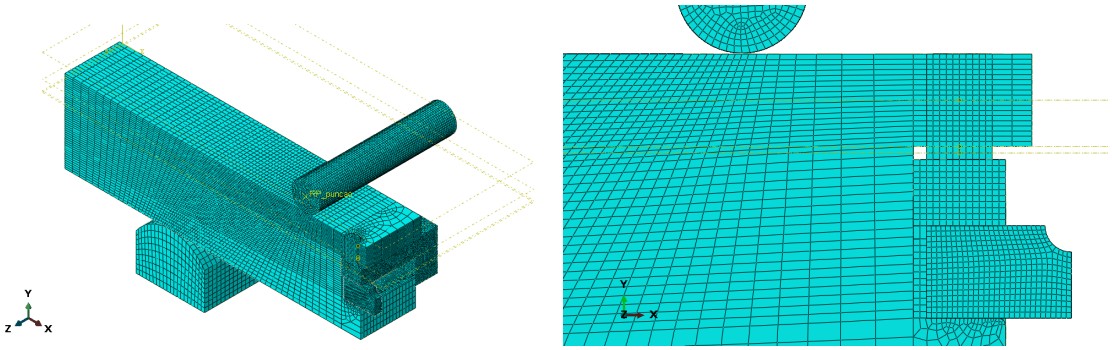

(a) (b)

Figure 3.43: Mesh of the model.

The mesh controls varied from part to part. When it was possible, an "Hex" element shape was given and the type of element would be C3D8, an 8-node linear brick. In other occasions, the elements were "Hex-dominated", and C3D8R, an 8-node linear brick with reduced integration was used. These elements are part of the 3D Stress family and have a linear geometric order, meaning that linear integrations are performed between each node of the model.

3.6 Fatigue testing

The Catman software is the tool selected to monitor the reaction forces registered by the load cells. So, a few parameters must be defined to ensure proper acquisition of values.

Instead of the usual 5×10^6 cycles as the stopping criterion of infinite life, for the current study a criterion of 3×10^6 cycles was adopted. As already mentioned, the machine had a rotational speed of 575 rpm, meaning that it is able to make around 10 cycles per second. If the stopping criterion was 5×10^6 cycles, the tests with specimen performed until the infinite life regime would take about five days and a half. Due to time restrictions, this procedure was not feasible, making 3×10^6 cycles much more practical.

Continuous tracking of reaction forces during the whole test would generate an enormous file. This way, the number of samples per period was defined as 1200 and the number of periods of 2700. This means that a maximum number of 3.24×10^6 cycles could be acquired. The sample rate was set to 1200 Hz and the acquisition interval between readings to 120 seconds. These settings imply that every 120 seconds, the data acquisition software collects 1200 samples at a frequency of 1200 Hz, which is equivalent to approximately 10 cycles of the fatigue test- around 120 samples per cycle.

The tests were carried out using a load ratio (R) between 0.1 and 0, due to small variations during testing. At the beginning of testing, the ratio was slightly higher than zero, guaranteeing that the minimum reaction was not null. By having a minimum reaction higher than zero, one can guarantee that the actuator is always in contact with the specimen holder, not allowing separation between them during trials.

The data acquisition system plots the load measured in each load cell over time. However, this type of plot disclosed little information. So, the time measured must be converted into the number of cycles (N), diving it by the period, as shown in the following equation:

$$N = \frac{t}{T} \tag{3.3}$$

where t is the time given by the data acquisition system and T is the period. In Figure 3.44, a regular plot of the acquired raw data, for a single load cell, is presented.

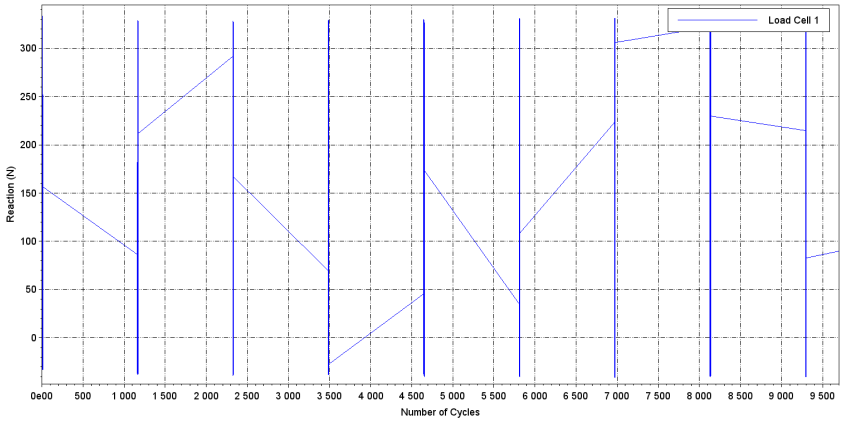

Figure 3.44: Data obtained by one of the load cells, comprising 10000 cycles.

In plots like this one, it is possible to analyse the evolution of the maximum force (F_{max}) and the minimum force (F_{min}) acquired by the load cells. With this information, one can adopt a criterion for the number of cycles to crack initiation (N_i). For these tests, N_i corresponds to the moment when a reduction of 10% of the maximum load is verified, as presented in Figure 3.45.

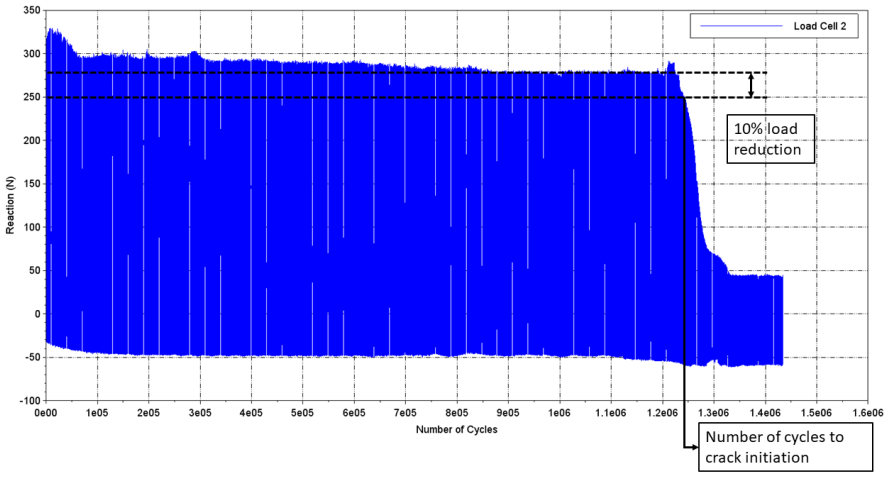

Figure 3.45: The number of cycles to crack initiation corresponds to a maximum load reduction of 10%.

By zooming one of the acquisitions in Figure 3.44, it is possible to observe the cyclic nature of fatigue testing, as shown in Figure 3.46.

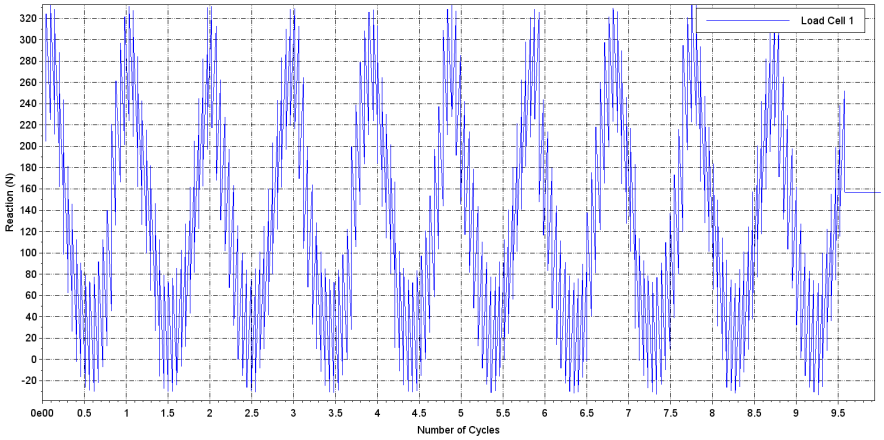

Figure 3.46: A single acquisition records the values of around 10 cycles.

The signal acquired by the load cells had some noise that would difficult the reading of values, so a low-pass, second order, Butterworth filter was applied using a Python script, with a 1.67 Hz frequency. The filter allowed a more clear visualisation of the load acquisition, as it can be observed in Figure 3.47. This procedure was not necessary for every fatigue test, since the noise issue was solved by directly applying a low-pass Butterworth 40 Hz filter on the Catman software.

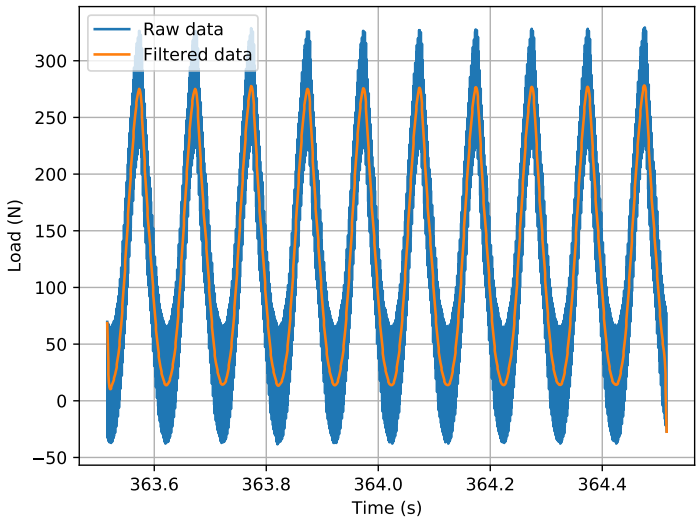

Figure 3.47: Raw and filtered data, obtained by applying a Butterworth filter.

In order to obtain a S-N curve, it is necessary to convert the force vs. time plot into stress vs. number of cycles. The nominal stress in a point, σ_0, which distances c from the neutral axis can be calculated by recurring to the following equation:

$$\sigma_0 = \frac{M \times y}{I} \tag{3.4}$$

where M is the bending moment given by $M = F \times j$, where j is the distance between the round support and the load application point, which is equal to 49.5 mm, and F is the reaction force measured by the load cells, y is the distance to the neutral axis and I is the inertial moment. For the present work, a simplification was performed: the miniature specimen was considered to be a beam with a 5 x 5 mm^2 cross-section, based on the cross section of the middle of the specimen, as seen in Figure 3.48 marked by black and white.

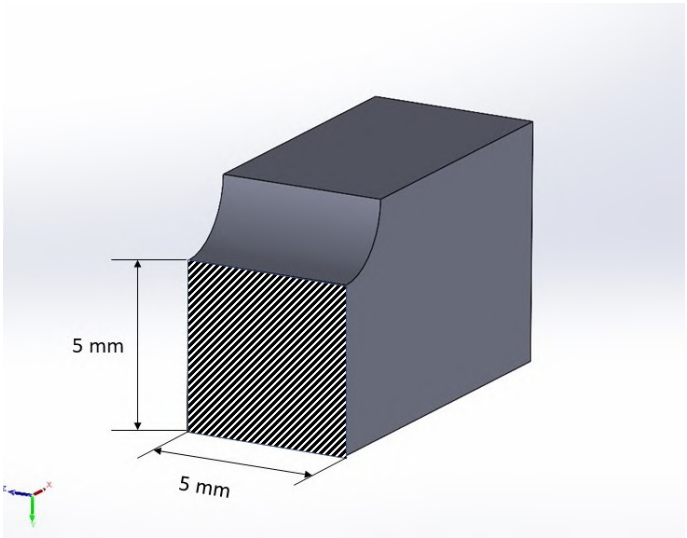

Figure 3.48: Cross sectional area of the miniature specimen.

In case of a beam with a square cross-section, y is given by half the height of the beam, which is 2.5 mm. Moreover, I is given by:

$$I = \frac{n^4}{12} \tag{3.5}$$

where n is the side of the square and equal to 5 mm. It should be reminded that the bending moment, M, is constant is the central area, as this is a four-point bending test, and that the load measured by the load cells changes from trial to trial. In addition, the nominal stress calculation is an approximation, since it does not take into account the complex geometry variations of the specimen and especially of the notch during testing.

Utilising Equation 3.4, a plot can be made featuring the stresses as a function of distance to the neutral axis of the specimen, which is considered to be a beam, for a load of 150 N. This plot is shown in Figure 3.49. Note that the axis are the same as those in Figure 3.48. As expected, near the notch, compressive stresses are felt, while near the bottom flat surface tensile stresses occur. Moreover, in the neutral line there are no stresses.

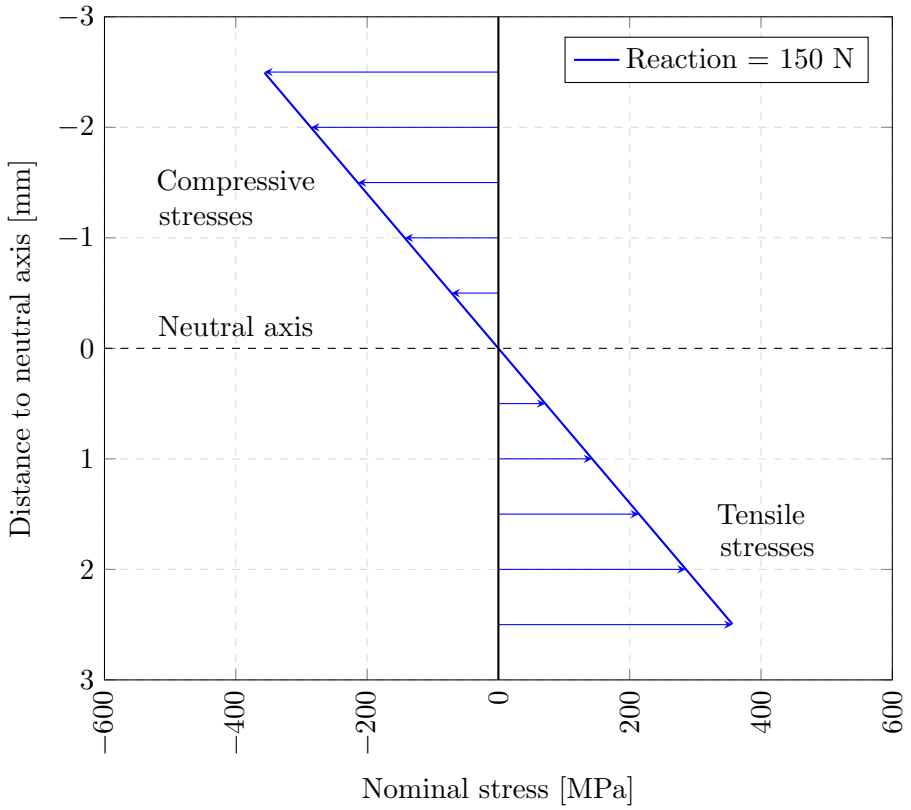

Figure 3.49: Nominal stress as a function of distance to neutral axis.

To obtain the S-N curve, it is necessary to perform tests in different ranges, of either displacement or load. Although the fatigue tests run in displacement control, levels of reaction forces were defined, since these values were the only ones measured during testing. For this reason, for a given trial, the displacement range remained constant throughout and the maximum load would be slightly adjusted during the trial to ensure it also remained constant.

When testing a new material, especially when the stress-strain curve for the material produced by DED is unknown, the first few samples are a wild guess- the number of cycles

might be too high or too low.

The first level of reaction force tested was one that corresponded to 90% of the Yield Strength of the same material, but produced by another process- 432 MPa [58]. This value is very common in the reviewed literature for high cycle fatigue, as the deformation is primarily elastic. By using Equation 3.4, a reaction of around 180 N was obtained and used in the first trial.

The movement of the actuator is regulated by an eccentric and a displacement range of 0.24 mm was utilised. The value of displacement is not of upmost importance, since the reaction forces measured by the load cells are the ones that allow the building of a S-N curve. As they get higher, the displacement range needs to increase, to ensure a permanent contact between the actuator and the gripping system. Note that the reaction forces can be adjusted by raising/lowering the movable platform that supports the grippers.

The utilised machine is hard to calibrate and to achieve the desired range of values with precision. This way, a load ratio between 0 and 0.1 was the aim.

However, at 3 million cycles, the above referred specimen achieved run-out, which meant the stresses had to be higher and the local plastic regime needed to be considered. To increase the stress, the height of the gripping system and load cells needs to increase, which can be done by raising the movable platform below them. Inconel 625 is a very special material, in which its Ultimate Tensile Strength is almost the double of its Yield Strength, showing incredible amounts of elongation to failure.

The fatigue testing plan finally adopted is presented in Table 3.7, in chronological order.

Table 3.7: Fatigue testing plan.

Specimen	Displacement range [mm]	Planned maximum load [N]	Torque [N.m]
1	0.25	180	5
2	0.44	250	5
3	0.44	250	5
4	0.44	300	5
5	0.55	300	5
6	0.55	300	5
14	0.55	350	10
7	0.55	350	10
8	0.55	430	10
9	0.55	430	10
10	0.55	300	10
11	0.34	430	10
12	0.34	250	10

Some of the specimen were tested with a tightening torque of the screw of 5 N.m while others with the recommended torque for a 12.9 class M5 screw- 10 N.m. More on this topic can be found in section 4.4.4.

3.6.1 Fracture surface

The analysis of the fatigue fracture surface of some specimen was performed in the metallography laboratory at INEGI, utilising an Olympus SZH stereo microscope, which is shown in Figure 3.50.

Figure 3.50: Stereo microscope used for fracture surface analysis.

The goal of this experiment was to observe the fatigue fracture surface of Inconel 625 and, perhaps, identify some defects that could have originated crack initiation or aided crack propagation. For that purpose, three different samples were selected, sample 3, 6 and 9. These were fatigue tested with different loads and lasted a different number of cycles.

Observation of the fracture surface utilising a stereo microscope is not the best option. Alternatively, a better choice would be analysing the surface with SEM, since it allows to obtain high magnification images of the sample's surface topography. Moreover, it would contribute to the possible identification of particles or even the cause of failure [112]. However, the SEM analysis was not available during the course of this work.

3.6.2 Fatigue life prediction

In this sub-chapter, an analytical method of predicting the fatigue life using more common mechanical properties is utilised. The method employed is strictly based on the hardness of the material as hardness testing is one of the most widely used nondestructive testing methods to obtain strength properties of materials [113].

Several authors proposed ways of estimating fatigue life based on other known material properties. For instance, A. Fatemi et. al [114, 115] suggested a model to estimate the strain-life curve of steels only requiring hardness and modulus of elasticity values. Although more adequate for steels, the authors utilised it to predict the fatigue life of Inconel 718, a material of the same family as Inconel 625, with satisfactory results.

Using the Roessle-Fatemi hardness-based method, uniaxial fatigue behaviour of some materials can be estimated from their Brinell hardness (HB) using the following formula [114, 115]:

$$\frac{\Delta\varepsilon}{2} = \frac{4.25(HB) + 225}{E}(N_f)^{-0.09} + \frac{0.32(HB)^2 - 478(HB) + 191000}{E}(N_f)^{-0.56} \tag{3.6}$$

where $\Delta\varepsilon$ is the deformation range, E is the Young Modulus and N_f the number of cycles to failure. This formula has two components, the elastic and the plastic one. If one disregards the plastic component of the formula, from Equation 3.6, Equation 3.7 is obtained:

$$\frac{\Delta\varepsilon}{2} \approx \frac{4.25(HB) + 225}{E}(N_f)^{-0.09} \tag{3.7}$$

Multiplying $\Delta\varepsilon$ by E, according to Hooke's law, $\Delta\sigma$ is obtained:

$$\frac{\Delta\sigma}{2} \approx (4.25(HB) + 225)(N_f)^{-0.09} \tag{3.8}$$

where $\Delta\sigma$ is the stress range. As already mentioned, $\Delta\sigma/2$ is equal to the stress amplitude, σ_a. The equation can be plotted as a S-N curve, only considering the elastic component of the model.

J. Li et. al [116] came up with a modified Mitchell's method to estimate the strain-life curve of wrought Aluminium alloys. As it is only appropriate for Aluminium alloys, this model was not considered.

C. Bandara et. al [113] proposed a method that only used hardness to predict the full range S-N curves of steels, directly using the Stress-Life approach. Unlike the Roessle-Fatemi model, this one could be used for the elastic and plastic regime, since it uses the Stress-Life approach.

H. Xin et. al [117] applied the C. Bandara method to butt-welded joints made of high strength steels, considering the method overestimates fatigue life because residual stress effects are not considered. Nevertheless, it proved to be useful to estimate residual stress effects, as they can be calculated as the difference between predicted and experimental stresses.

P. Strzelecki et. al [118] reviewed the same method proposed by Bandara. The authors concluded that the model's estimated cycles were much lower than the experimental ones, specially in the plastic region of the S-N curve. The S-N curve proposed by Bandara for a load ratio of -1 can be defined using four coordinate points and some basic assumptions, as follows:

1. The starting coordinate is $(1, \sigma_u)$, assuming that 1/4 cycles can be approximated to 1 cycle in the ordinate axis;

2. The second coordinate is the first knee point (B, σ_u), assuming that the S-N curve is horizontal until B cycles;

3. The third coordinate is the second knee point (N_k, σ_k), where σ_k is approximately $0.5\sigma_u$;

4. The final coordinate is the fatigue strength at number of cycles to failure in the gigacycle fatigue region, $N_{GCF} = 10^9$, $(10^9, \sigma_{GCF})$.

where σ_u is the ultimate tensile strength, B is the number of cycles to failure at the first knee point, σ_k is the fatigue strength at the second knee point, N_k is the number of cycles to failure at the second knee point and σ_{GCF} is the fatigue strength at gigacycle fatigue region.

An illustration of the four coordinate points and originated S-N curve can be observed in Figure 3.51. It should be noted that B is determined by the high cycle fatigue slope, i, of the S-N curve (Represented as b in Figure 3.51). Experimental data suggest that i value can range between -0.12 to -0.21 for steels. For the sake of simplicity and, as suggested by the author, a value of -0.2 was used.

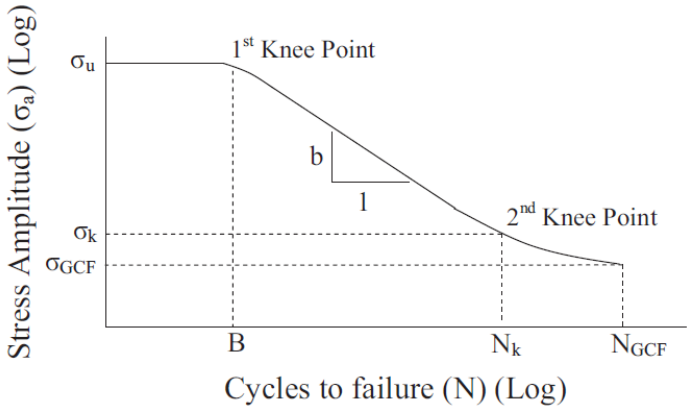

Figure 3.51: Prediction of the S-N curve as modelled by C. Bandara et. al [113].

The formulae necessary to determine such coordinates are [113]:

$$\sigma_k = 1.7 \cdot HB \tag{3.9}$$

$$N_k = 10^{\left(\frac{0.223(HB+120)\cdot(HB)^{1/3}-1.7\cdot HB}{0.0105(HB+120)\cdot(HB)^{1/3}}\right)} \tag{3.10}$$

$$\sigma_{GCF} = 0.138 \cdot (HB)^{1/3}(HB + 120) \tag{3.11}$$

$$B = \left(\frac{3.4HB - p}{o}\right)^{1/i} \tag{3.12}$$

where $o = \left(\frac{\sigma_{GCF}-\sigma_k}{N^i_{GCF}-N^i_k}\right)$ and $p = \left(\frac{\sigma_k N^i_{GCF}-\sigma_{GCF}N^i_k}{N^i_{GCF}-N^i_k}\right)$.

Based on the research done, no specific method of fatigue life prediction based on hardness for superalloys was found. Despite this fact, the models proposed by A. Fatemi et. al [114] and by C. Bandara et. al [113] were employed to Inconel 625 produced by DED.

3.6.3 Experimental and numerical calibration of the test setup

In order to better comprehend the behaviour of the material during the fatigue tests and to further calibrate the numerical model, strain gauges were applied on two specimens and a few measurements were made, using the Spyder acquisition system. The strain gauges utilised were manufactured by Micro-Measurements, a Division of Vishay Precision Group,

with item number MMF307385. Their overall dimensions were 6.4 x 3.6 mm, while the grid dimensions were 1.27 x 1.52 mm. They were glued on the middle of the opposite face to the one that had the notch, as shown in Figure 3.52, which is the one where the crack is expected to nucleate, since it is subjected to tensile loading.

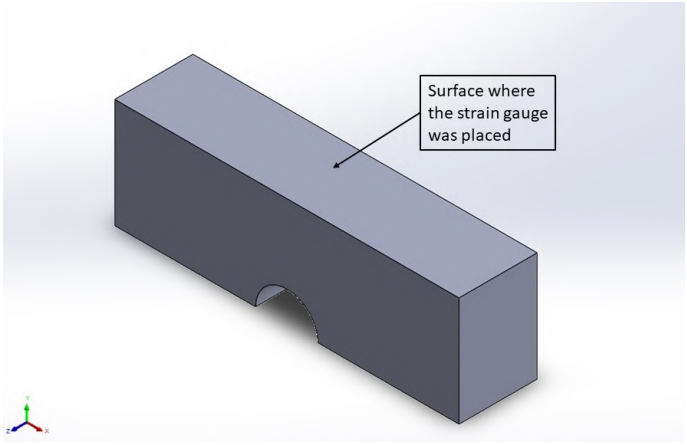

Figure 3.52: Face where the strain gauges were placed.

Influence of the tightening torque

The first test was meant to analyse the influence of the tightening torque of the screw on the deformation of the sample. For that purpose, the gripping system and strain gauge were placed on bench clamps. Firstly, the bench clamps were tightened, then the torque was applied on both screws, one at a time- the first torque was 5 N.m and the second was 10 N.m. After this, the clamps would be loose and the strain gauges could be used to measure the influence of the torque on the deformation of the specimen.

Relation between deformation and reaction force

The second test was meant to discover the relation between measured reaction force and specimen deformation. This relationship would allow a more comprehensive understanding of the material's behaviour during the fatigue test, being easily determined if the specimen is being tested in the elastic or plastic regime. Note that, with the deformation measured, one can calculate the stress on the specimen, either by using Hooke's Law for the elastic region, or a constitutive curve for the plastic region.

These measurements were made on the fatigue testing machine, with a displacement range of 0.55 mm, by manually rotating the electric motor shaft. The reaction force could be raised by moving the platform upwards. With increments of 25N, the originated strain would be measured. From time to time, the shaft would be rotated to the actuator's higher position, where the reaction force would be zero, to verify if there was any residual strain measured at zero load- if there was, the material must have been plastified.

Chapter 4

Results and Discussion

This Chapter presents all the results regarding the description and characterisation of the material, the tensile tests results, the FEM analysis, the fatigue life prediction and actual fatigue life results, as well as the numerical model validation. The discussion of the obtained data is also performed.

4.1 Material description and characterisation

In this sub-chapter, the results of the description and characterisation of the material is presented. As the results are revealed, meaningful discussion takes place.

4.1.1 Chemical composition and density

The chemical composition results of both batches are presented in Tables 4.1 and 4.2.

Table 4.1: Chemical composition (wt.%) of the parts produced by the first batch powder.

Element	C	Si	Mn	P	S	Cr	Fe	Mo
Average (%)	0.0558	0.213	0.0915	0.0210	0.0290	21.15	0.286	8.22
Element	V	Cu	W	Co	Nb	Al	Ti	Zr
Average (%)	0.0635	0.0148	0.0955	0.0727	3.20	0.0482	0.0304	0.0226
Element	Sn	B	Mg	Pb	Ta	Ni		
Average (%)	0.701	0.0021	0.0273	0.0334	0.0335	65.6		

Table 4.2: Chemical composition (wt.%) of the parts produced by the second batch powder.

Element	C	Si	Mn	P	S	Cr	Fe	Mo
Average (%)	0.0538	0.161	0.0536	0.0179	0.0239	21.49	0.286	8.27
Element	V	Cu	W	Co	Nb	Al	Ti	Zr
Average (%)	0.0658	0.0115	0.0855	0.0662	3.25	0.0400	0.0307	0.0202
Element	Sn	B	Mg	Pb	Ta	Ni		
Average (%)	0.620	0.0012	0.0257	0.0332	0.0302	65.4		

In Table 4.3, the chemical composition of the gas atomised powder provided by Oerlikon Metco used for specimen production is shown.

Table 4.3: Chemical composition (wt.%) of the powder provided by Oerlikon Metco, MetcoClad 625.

Element	Ni	Cr	Mo	Nb	Fe	Other
Composition (%)	58.0 - 63.0	20.0 - 23.0	8.0 - 10.0	3.0 - 5.0	< 5.0	< 2.0

The chemical compositions of both material samples produced with different powder batches are quite similar. By comparing the chemical compositions of the powders and the compositions of the materials themselves, it is possible to confirm that all the elements are within the ranges of the supplier, with the exception of Ni, which is 2.6 % and 2.4 % higher in materials of batch 1 and 2, respectively, than the powders supplied.

However, this does not mean that the supplier gave inaccurate value ranges. In fact, as explored in section 2.1.7, during AM processes it is common to lose alloying elements, because of the presence of elements with distinct boiling points. Due to this reality, a preferential vaporisation of elements with low boiling points may occur, and the final part might present a different composition than the powders that produced it.

Therefore, the high percentage of Nickel in the parts comes at the expense of losing some of the other volatile elements.

On another note, the principles of OES imply that only the surface elements are vaporised and measured, meaning that the test results are the composition of the surface of the sample, which may not be an accurate representation of the composition of the sample as a whole if the part is not homogeneous. Nevertheless, the results of this tests are not too distant of the expected composition.

The results of the density tests are presented in Table 4.4. These are the average of the three measurements for each of the cutting orientations. The measured density in both orientations is similar to the one presented by literature.

Table 4.4: Density of the samples cut in two different orientations.

Orientation	Density [g/cm^3]
Transverse	8.4452
Longitudinal	8.4196

4.1.2 Etching

The sample were observed after being etched through electrochemical etching. This process allows to observe microstructural and processing parameter features that would not be highlighted without the etching. It is important to refer that the chemical attack to Inconel 625 was not easy, since the material is well known for its chemical resistance. Moreover, in each optical image presented, more than one layer might be shown, since it is almost impossible to cut a sample parallel to the plane of a single layer. Hence, the dimensions analysed further ahead might not be the real ones, but the result of layer and melt pool projections.

The first set of analysed images are from the frontal plane, which is the one shown in Figure 4.1.

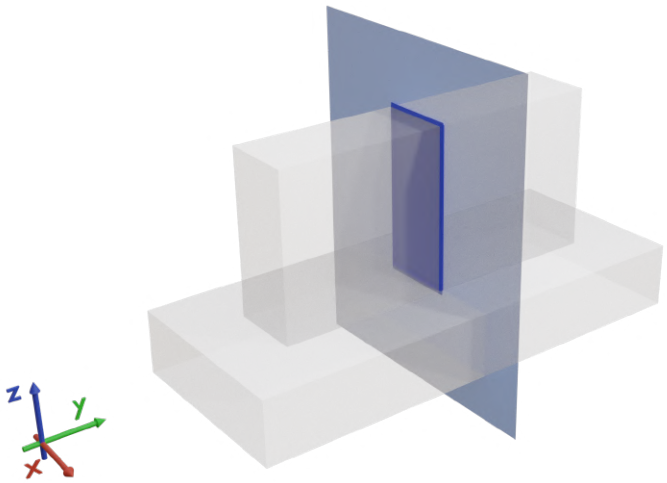

Figure 4.1: Frontal plane.

With only a 23x amplification, the melt pool outlines can be visualised, as presented in Figure 4.2.

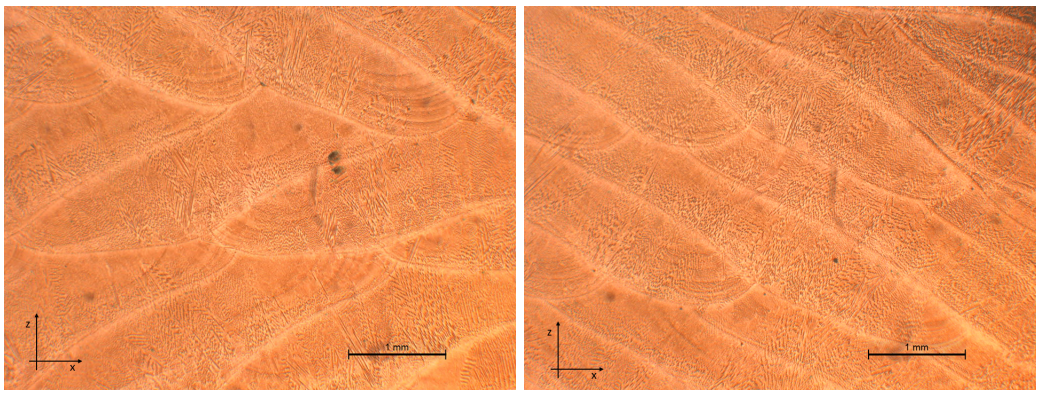

(a) (b)

Figure 4.2: Melt pool outlines in different regions of the sample.

The melt pool has a nearly half-ellipse geometry due to the Gaussian type of energy distribution. If the laser had a "top-hat" energy distribution, for instance, the shape of the melt pool would be narrower and deeper. The shape of the melt pool is not a perfect half-ellipse because, as already stated, the cutting of the sample is not perfectly perpendicular to the laser tracks. Hence, the melt pools seem slightly distorted. As it can be observed in Figure 4.2, the melt pools are slightly overlapped horizontally, due to the adopted processing parameters (around 30%). Moreover, in each layer, the laser remelts part of the layer below to achieve better bonding, originating a vertical overlap.

The melt pool geometry can be compared to some of the dimensions inserted in the .CSV file, such as the hatch spacing and the layer thickness, to verify if the process is being performed according to expectations. In Figure 4.3, the hatch spacing and the layer thickness is roughly measured for comparison purposes. Note that since the melt pools can be slightly distorted due to the cutting plane and because there was an overlap between tracks, these measurements are an approximation.

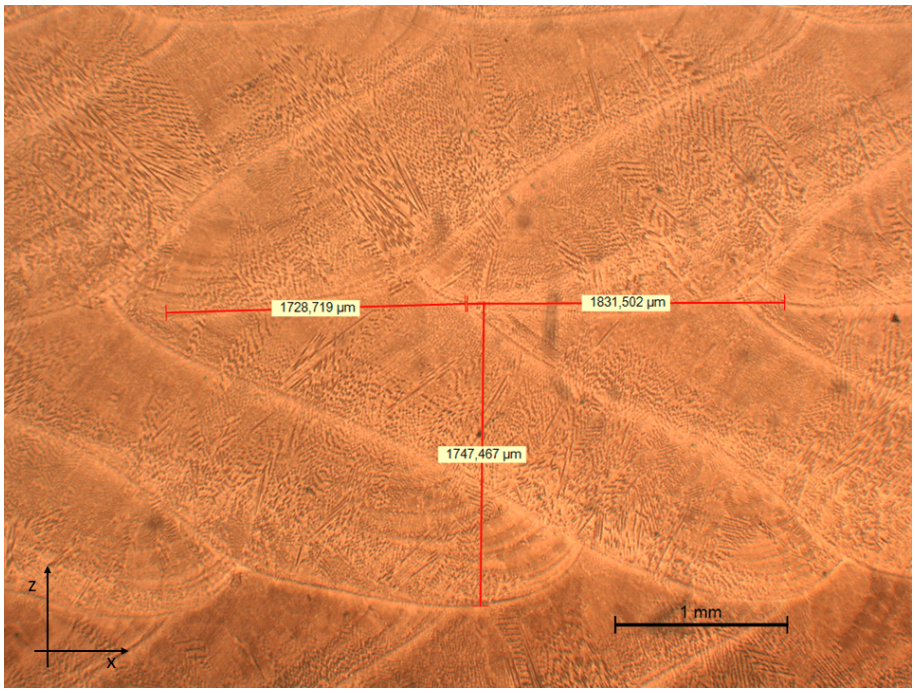

Figure 4.3: Hatch spacing and layer thickness measurements.

The hatch spacing, in mm, programmed into the DED system was of 1.8. The resulting hatch spacing is around the same value. Similarly, the inputed layer thickness was of 1.7 mm, which is in line with the values presented in Figure 4.3. The measurements were made in two other images. The dimensions are shown in Figure 4.4.

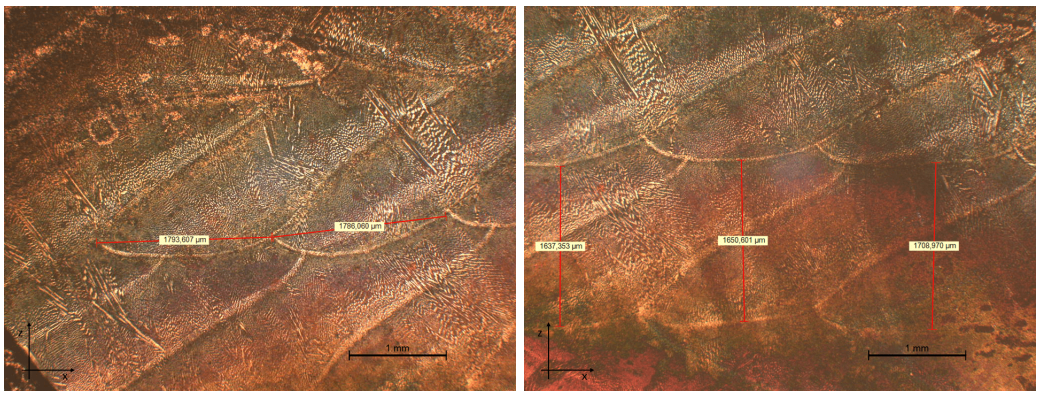

(a) (b)

Figure 4.4: Measurements of: (a) hatch spacing; (b) layer thickness.

The measured dimensions are very close to the intended ones, meaning that the desired parameters were respected and no visible defects rose from that.

Even with a relatively low amplification, columnar primary dendrites can be observed. These grow in different orientations according to the direction of the main heat flux. In fact, in Figure 4.5, it can be seen that the columnar dendrites may change direction each layer. Measuring the angle between the dendrites that change direction, using ImageJ software, an angle of around 90° is obtained. This value is related to the scanning strategy used. Each layer, the deposition starts at a random location. If the location is one that

changes the laser scan direction in 180° compared to the previous layer, the main heat flux direction also changes. As a consequence, the growth direction of the columnar dendrites change 90°. On the other hand, if the location is one that maintains the laser scan direction as the last deposited layer, the main heat flux direction stays the same and the columnar dendrites grow in the same direction as the ones in the previous layer. This behaviour was also observed by Dinda et. al [87].

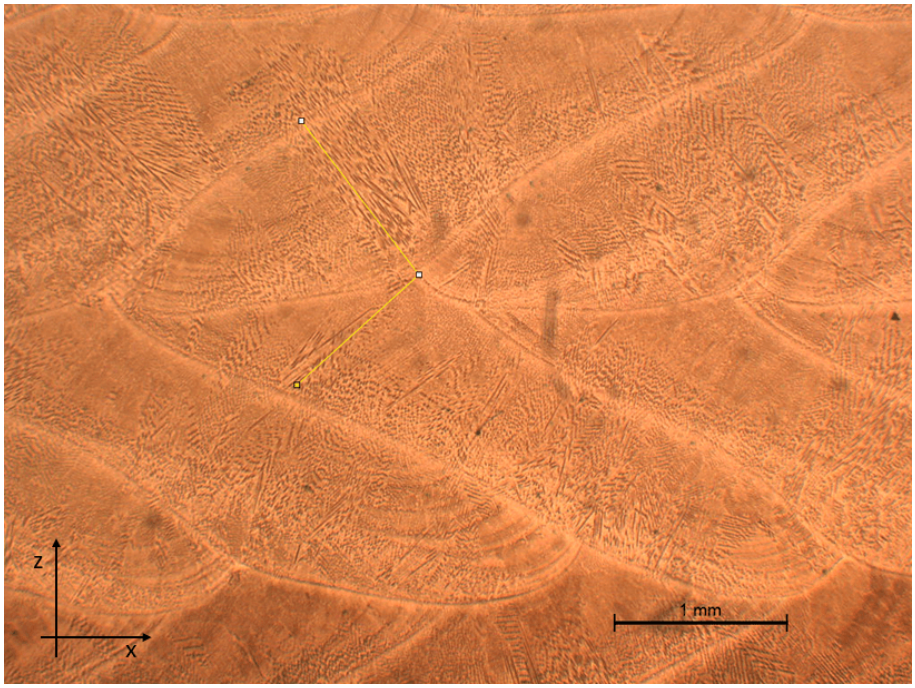

Figure 4.5: Columnar dendrites growth changes between layers.

By further analysis of Figure 4.5, it can be verified that the microstructure can vary within the melt pool, meaning that different cooling rates are present inside a single melt pool. The partial remelting of the upper boundary of the pool also contributes for this heterogeneous microstructure. Moreover, their boundaries are more pronounced by the presence of a HAZ.

Taking a closer look, it can be seen that the microstructure of DED produced Inconel 625 appears to be made up of two kinds of structures: a cell-like equiaxed structure (or cellular) and columnar dendritic shapes. In Figure 4.6, the structure is shown. There are other structures that resemble equiaxed dendrites. However, due to microstructural observation of other planes of the sample, it is hypothesised that these are columnar grains that grow into the observed cutting plane with secondary arms.

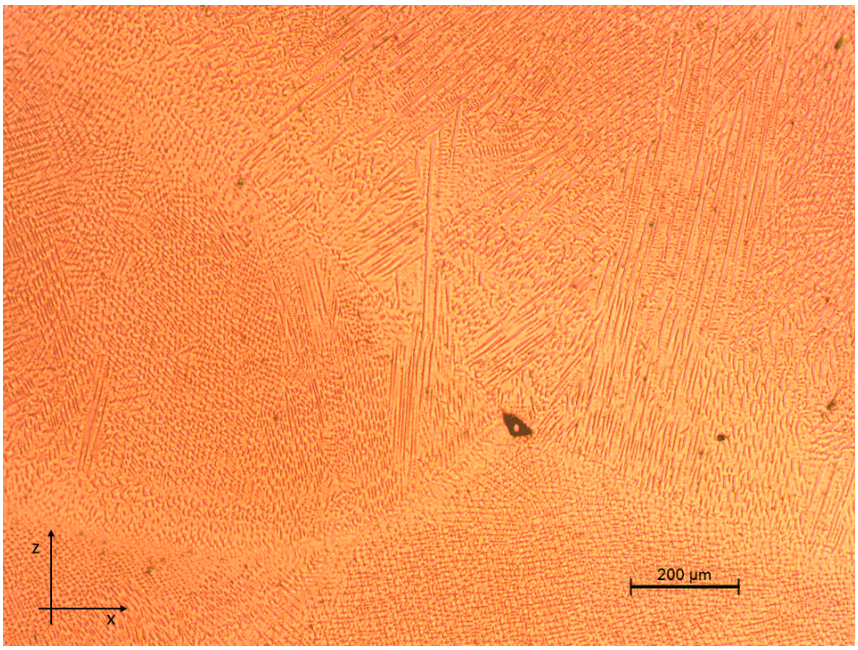

Figure 4.6: Columnar and cellular dendrites.

It seems that the columnar dendrites are mainly present in the lower region of the melt pool, while the cellular structures and columnar dendrites with other orientations (that grow into the plane of observation), are mainly present in the upper regions. This may have to do with the different cooling rates within the melt pool: the dendritic columnar shapes are mostly originated in regions of high cooling rates, while the cellular ones are a product of lower cooling rates. Obviously, the overall cooling rate is very high, hence the structure is fine.

Moreover, the cellular microstructure near the interface might be the result of the partial remelting of the layer and consequent HAZ. A lack of fusion pore can also be verified in the interface between two melt pools, which may degrade the bonding between adjacent tracks.

The same kind of microstructure can be observed in Figure 4.7, which were taken in two other regions of the sample.

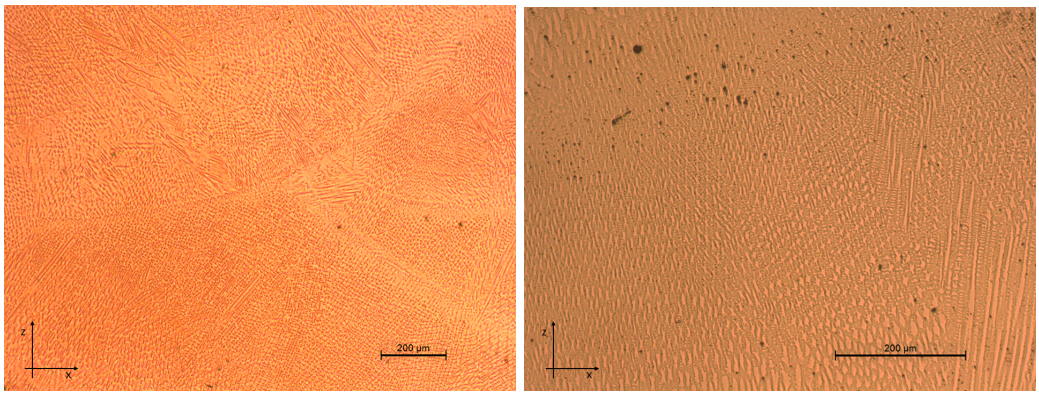

(a) (b)

Figure 4.7: Main structure of the sample: (a) columnar dendrites and cellular structures; (b) columnar dendrites and cellular structures with higher amplification.

In Figure 4.8, dendrites on both sides of the interface have nearly identical crystallographic orientations, which indicates a good consistency in crystal growth across various laser tracks and layers. Moreover, some dendrites propagate across interfaces, indicating that a strong bonding was achieved.

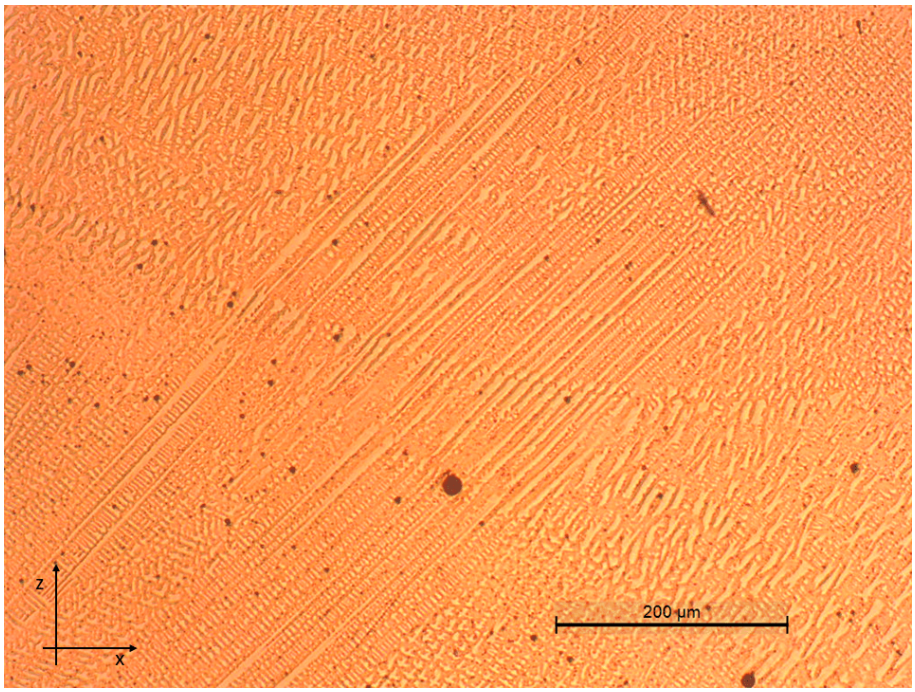

Figure 4.8: Columnar dendrites propagating through laser tracks interfaces.

A few round pores with different dimensions can also be observed. The etching of the sample allowed visualisation to the naked eye, as shown in Figure 4.9, where the overall melt pools can be noticed with ease.

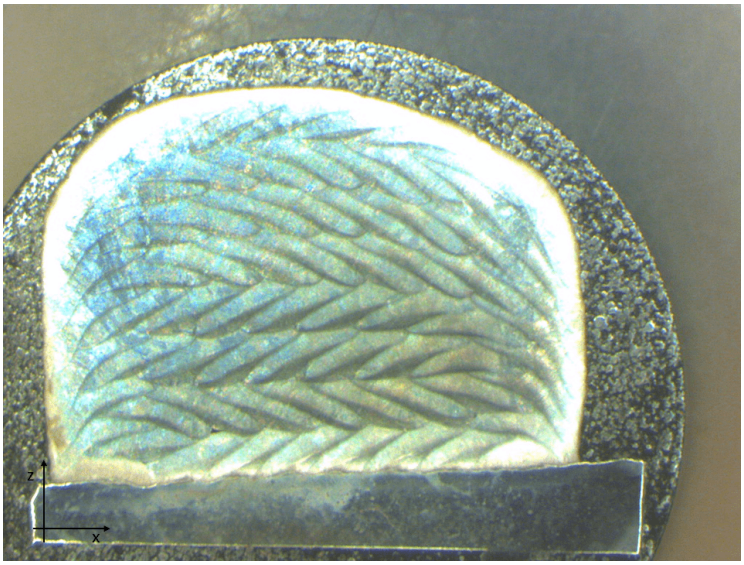

Figure 4.9: Etching made naked eye observation possible.

In the same figure, a very common defect of DED produced parts can be seen- lateral slippage. In the lateral extremities of the sample, the melt pool begins to sag due to

remelting and gravity. As already said, the outside borders of the sample are built first. After them, the contour gets filled, partially remelting the outside borders, which makes them slip laterally. Moreover, in the centre part of the specimen, there is more material to conduct the heat. In opposition, in the lateral zones, there is less conduction of heat, making the cooling longer. However, this defect is not meaningful to fatigue testing. As already mentioned, the samples were built with extra material that is to be machined. Hence, this sagged part of the sample gets removed and will not be present in the final specimen.

The analysis on the horizontal plane of the sample, presented in Figure 4.10, enables the visualisation of the laser tracks. In Figure 4.11, a few of them are presented.

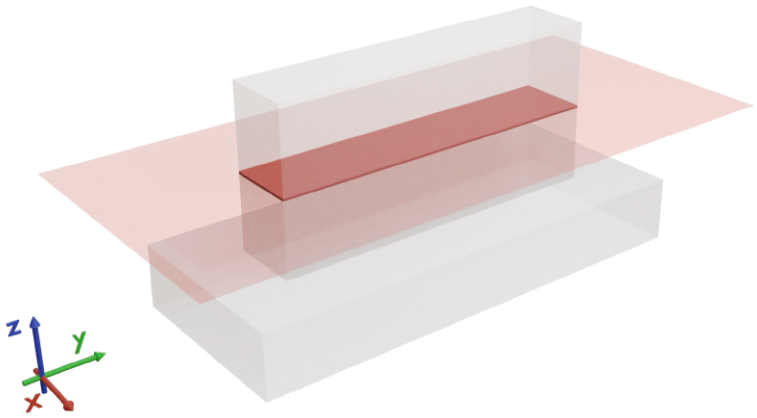

Figure 4.10: Horizontal plane.

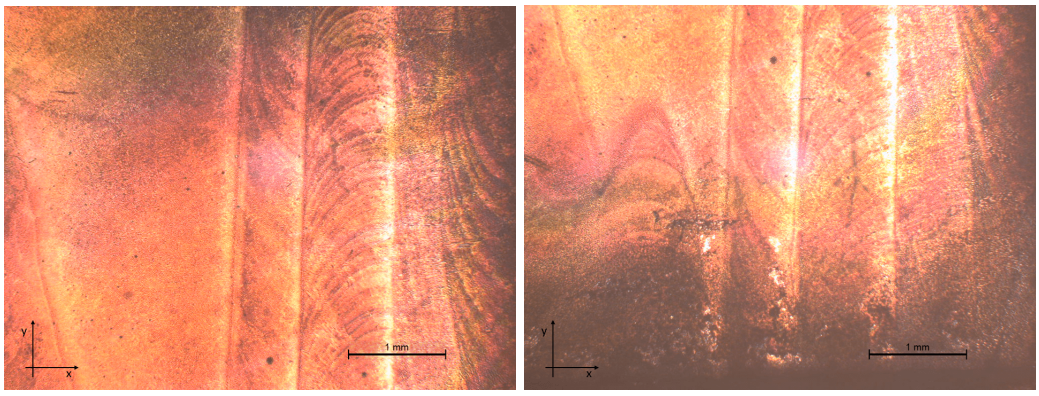

(a) (b)

Figure 4.11: Visualisation of laser tracks: (a) two laser tracks; (b) three laser tracks.

By zooming in, the microstructure of the sample in the horizontal plane is revealed. In Figure 4.12a, the focus is on a laser track, where two HAZ are clearly identified. In Figure 4.12b, an amplification of the previous one, a mixture of microstructure can be seen.

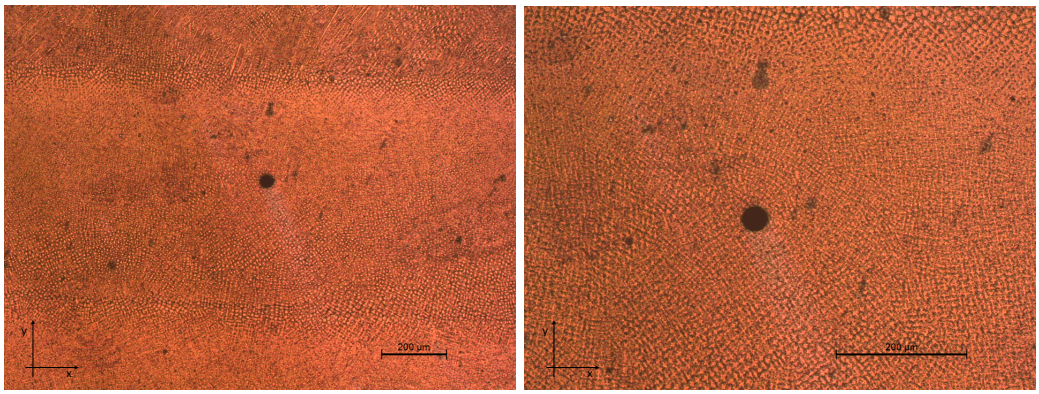

(a) (b)

Figure 4.12: Microstructure on the horizontal plane: (a) two HAZ in the interface of laser tracks can be observed; (b) cellular structures and columnar grains that grow into the observed plane.

Cellular equiaxed structures are mostly present near the laser tracks interfaces, while dendrites with a "star" shape are more prominent in the central zone of the track. These structures are most likely columnar dendrites that go into the XY plane, as hypothesised earlier. Hence, columnar structures observed in the frontal plane (XZ) present themselves as these equiaxed structures in the horizontal plane. Moreover, the "star" shape is due to secondary dendrite arms of the columnar structures. On another note, a round pore with around 50 μm can be observed.

The same microstructure can be seen in Figure 4.13, in the same plane, but on other regions of the sample.

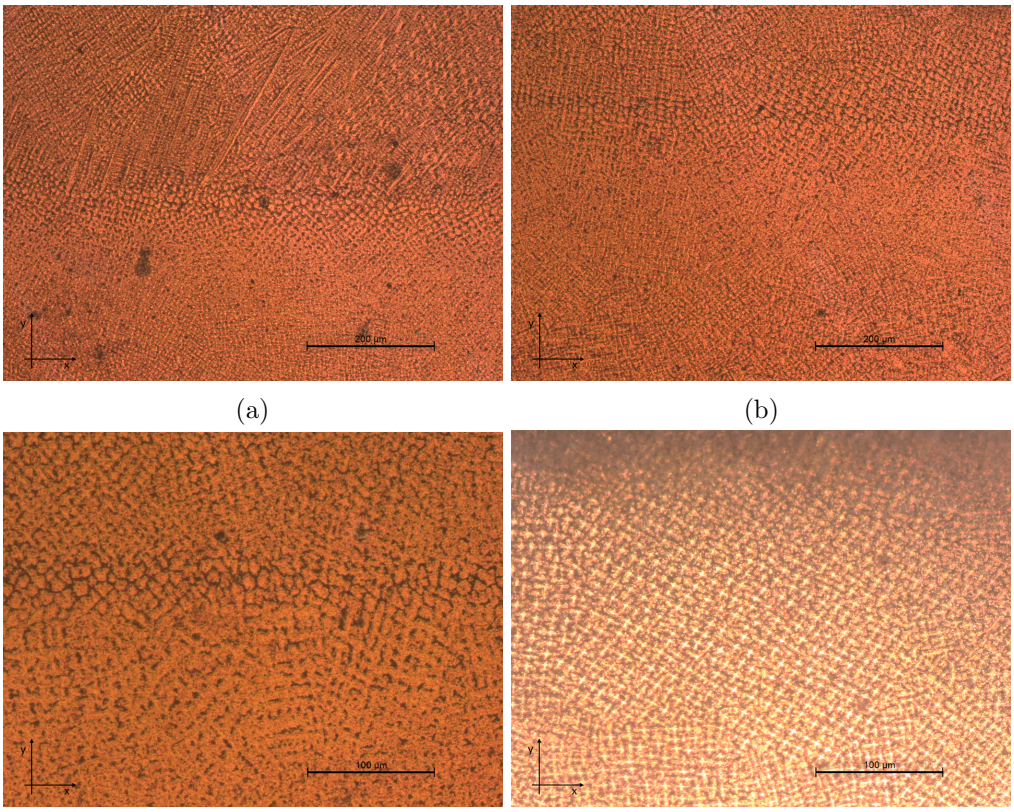

(a) (b)

(c) (d)

Figure 4.13: Different microstructure observed: (a) cellular structures, a few columnar dendrites and dendrites that grow into the plane; (b) mostly cellular structures and columnar dendrites that grow into the plane; (c) cellular structures; (d) columnar dendrites that grow into the plane.

In the same figure, a few columnar dendrites with secondary arms can be found. These arms are small due to the rapid cooling rates of the sample. By analysing the lateral cutting plane, which is the one shown in Figure 4.14, a similar microstructure as the one found in the frontal plane is seen.

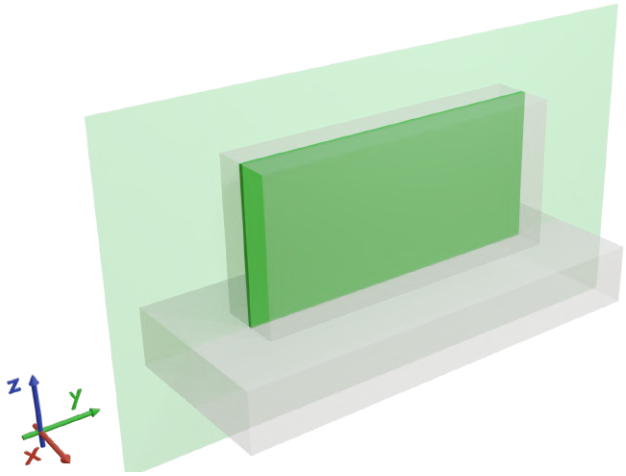

Figure 4.14: Lateral plane.

In Figure 4.15, an image of the plane is presented. Note that the chemical attack was stronger on this plane, slightly burning the sample.

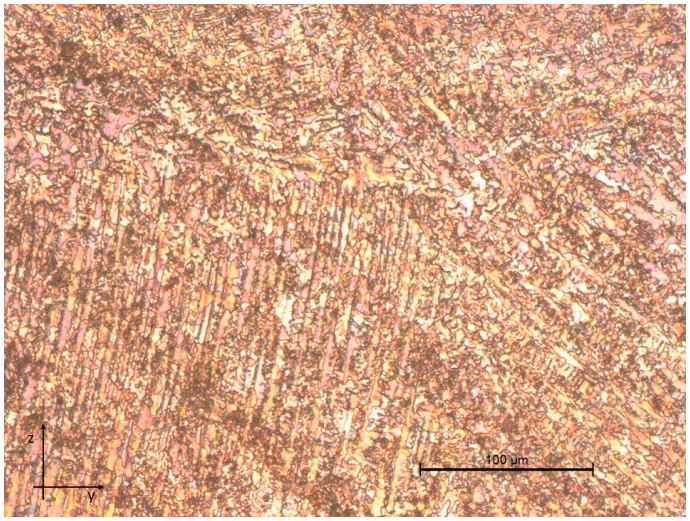

Figure 4.15: Microstructure found in the lateral cutting plane.

For better visualisation of the overall microstructure of the analysed sample, Figure 4.16 was built using optical images of the three cutting planes.

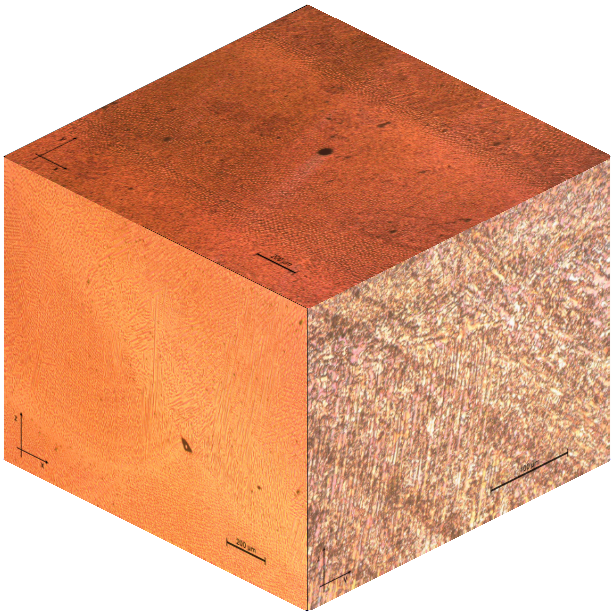

Figure 4.16: Three dimensional representation of the overall microstructure of the Inconel 625 sample.

4.1.3 Porosity

As briefly mentioned, two different samples were tested. It should be noted that, despite not being utilised for the current work, several other types of specimen were manufactured, such as axial fatigue, compact tension (CT) and gigacycle fatigue specimens. The analysed

optical images from sample 1 (CT specimen) are presented in Figure 4.17, while the inspected optical images from sample 2 (Axial fatigue specimen) are presented in Figure 4.18. The optical images from sample 3 (Gigacycle fatigue specimen) can be found in Figure 4.19.

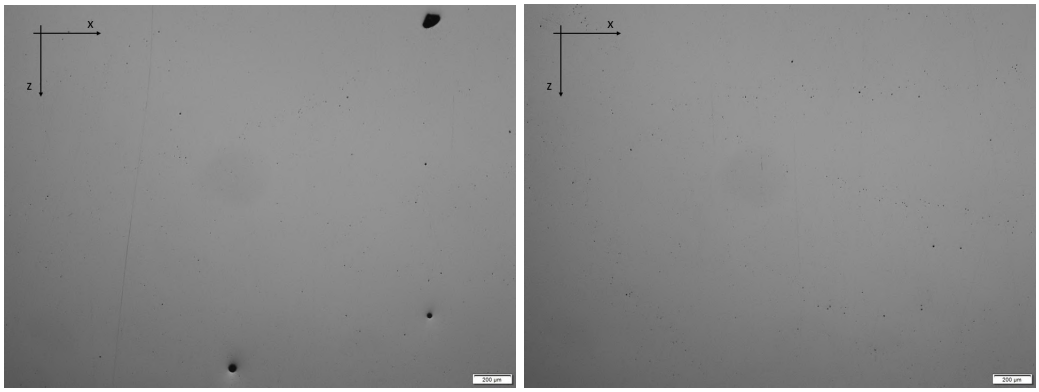

(a) Optical Image 1 (b) Optical Image 2

Figure 4.17: Optical images of sample 1.

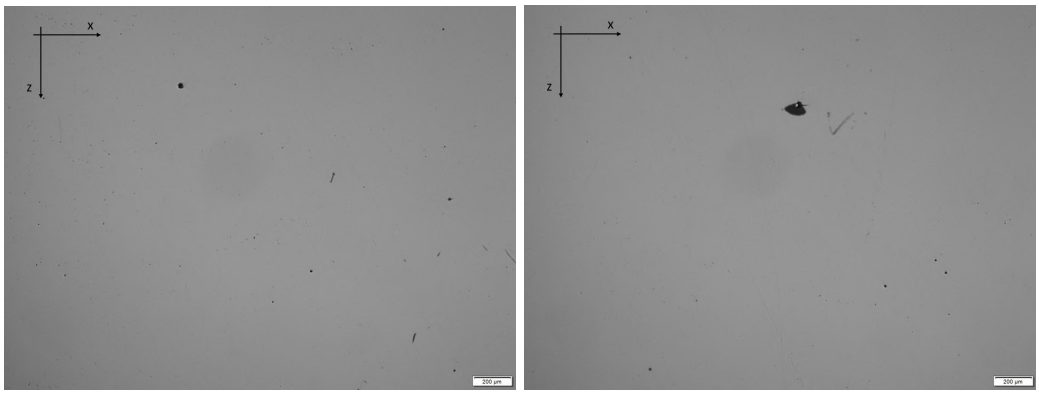

(a) Optical Image 1 (b) Optical Image 2

Figure 4.18: Optical images of sample 2.

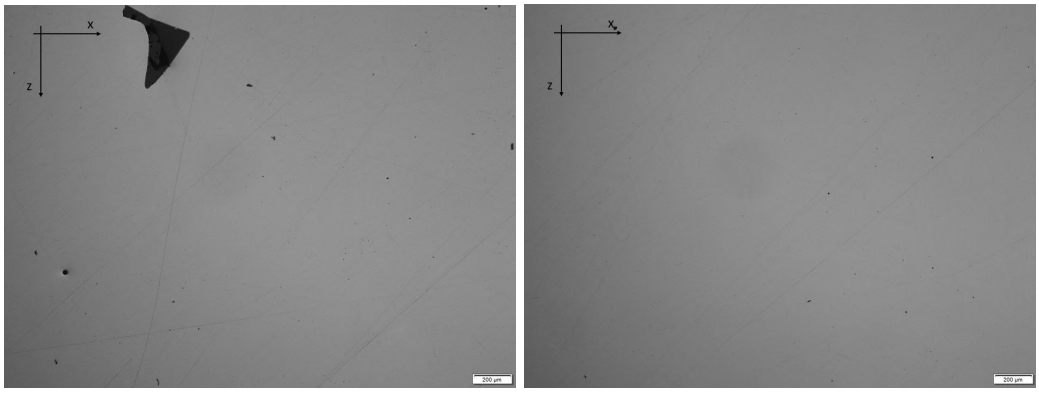

(a) Optical Image 1 (b) Optical Image 2

Figure 4.19: Optical images of sample 3.

The measured levels of porosity, as well as their average for each sample, are listed in Table 4.5.

Table 4.5: Porosity levels of sample 1, 2 and 3.

Sample 1	Porosity level (%)
Optical Image 1	0.154
Optical Image 2	0.075
Average	0.1145
Sample 2	Porosity level (%)
Optical Image 1	0.103
Optical Image 2	0.149
Average	0.126
Sample 3	Porosity level (%)
Optical Image 1	1.053
Optical Image 2	0.039
Average	0.546

In Figures 4.17, 4.18 and 4.19, different types of pores can be observed. For instance, round pores such as the ones in the bottom part of Figure 4.17a are the result of entrapped gas during the process. On the other hand, irregular pores, like the one shown in Figure 4.19a, is the outcome of lack-of-fusion in the process, most likely due to insufficient energy density.

Overall, taking into account sample 1 and 2, it can be said that the level of porosity is very low and in line with the values obtained by some of the reviewed literature. M. Fujishima et. al [119] disclosed values of porosity at around 0.05% for Inconel 625 produced by DED, while C. Pleass et. al [84] presented values between 0.05% and 0.3% for Inconel produced by SLM. Moreover, for the same material and process, P. Wang et. al [120] revealed values of porosity ranging from 0.1% to 0.2%.

Despite having a few irregular and round pores, their quantity is not alarming, as it is almost impossible to produce a porosity-free sample in the as-deposited state.

Regarding sample 3, the existence of a large irregular pore can be observed. The presence of a pore with a length of about 200 μm indicates that some problem with the process might have taken place. Nevertheless, this defect is near the interface with the substrate, which means it will not be featured in the specimen that is going to be tested and certainly not in the testing zone. After production of a specimen, the part needs to be separated from the substrate, therefore a slight chunk of material near the interface will be discarded and not utilised in the fatigue tests. With that being said, despite the existence of a large lack-of-fusion defect, the fatigue life should not be impacted negatively.

4.1.4 Hardness

The two analysed samples are shown in Figure 4.20. As already mentioned, the results are presented in relation to the position of the interface ($z = 0$) between the Inconel 625

and the substrate made out of DIN 40 CrMnMo 7 steel. Note that z is, once again, the building direction.

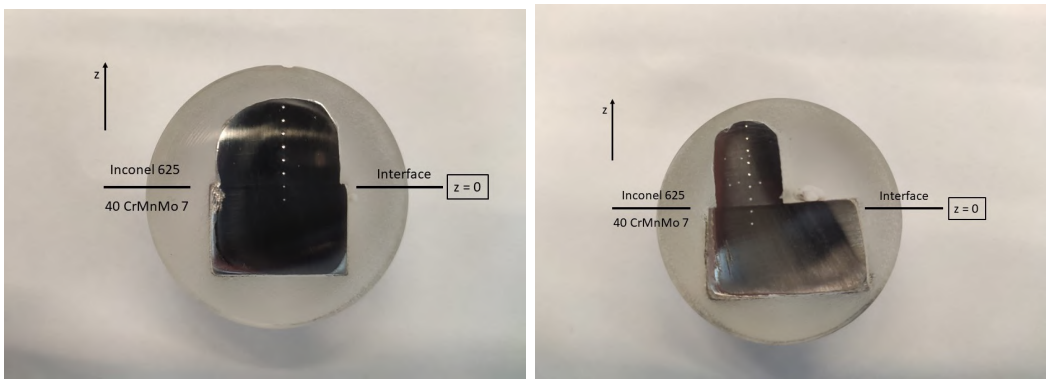

(a) Sample 1 (b) Sample 2

Figure 4.20: Samples used for hardness measurements.

The hardness test measurement results are presented in Table 4.6 and 4.7 and plotted in Figure 4.21. It is important to note that the dimensions of the two samples are different, hence a different amount of points, in distinct positions were measured between the samples. Sample 1 had a height of 13.2 mm and sample 2 had 14.2 mm.

Table 4.6: Hardness measurements of sample 1 in relation to the interface.

z Position [mm]	-2	0	2	4	6	8	10	12
Hardness (HV)	303	412	244	250	244	232	232	238

Table 4.7: Hardness measurements of sample 2 in relation to the interface.

z Position [mm]	-3	-1	1	3	5	7	9	11	13
Hardness (HV)	303	278	244	232	244	238	226	221	221

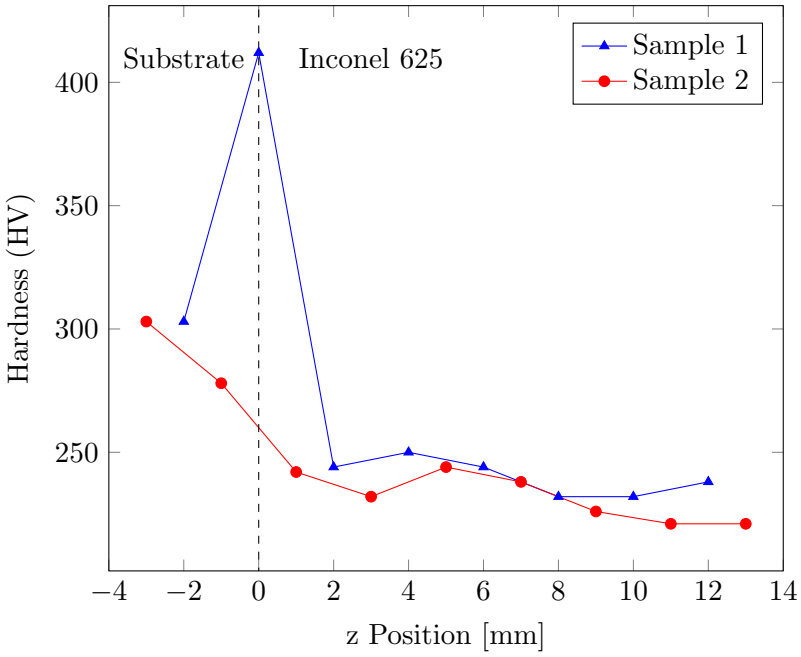

Figure 4.21: Hardness measurements.

The measured values of hardness are generally higher than the ones presented in the background theory for the wrought alloy- between 146 HV and 222 HV. Moreover, there is a clear decrease in hardness as the measurements are taken further away from the interface, with only a few exceptions. This result presents itself as really interesting and in line with the research done. In this first few layers of the sample, the cooling rates are higher than in the intermediate and last layers, because there is heat dissipation to the substrate and to the surrounding environment. In opposition, the intermediate layers are deposited when the previous layers are still hot and heat dissipation through conduction needs to follow a longer path, making the cooling slower and resulting in coarser grains. Higher cooling rates originate smaller grains, which are known to have higher hardness than their coarser counterparts. In sample 2, for instance, the difference between hardness in the interface and top of the specimen is around 20 HV.

The bonding process between the deposited material and the substrate is guaranteed by melting part of the substrate. Due to the Marangoni forces, there is interchange of chemical elements between the two materials in the melt pool. This way, some of the elements that provide hardness to the substrate might segregate to the Inconel and strengthen the bottom part of the sample, further justifying the hardness variation withing the height of the sample.

The last measure taken in sample 1 ($z = 12$ mm) has a higher value than the measure taken in a previous position. This exception to the aforementioned trend may have two explanations. In the last few layers, the cooling rates are once again higher, since less layers are going to be built on top of them. Hence, the grains might be finer and, consequently, provide higher hardness. On the other hand, the exception might be due to uncertainty in the measurement system or due to material heterogeneity. For instance, a measurement taken in the middle of a melt pool might be different from one taken in the interface between melt pools.

One interesting aspect found in the interface of sample 1 is worth of mention. The hardness obtained in the interface- 412 HV, is higher than the hardness of both materials

that form such interface, which is a good omen for future studies and development of multi-material depositions using DED or both these materials- Inconel 625 and DIN 40 CrMnMo 7.

To validate these results and discard trial errors, two measurements of microhardness in the interface, but on the side of the substrate, were taken in each sample. The average values of microhardness were 470 HV and 460 HV in samples 1 and 2, respectively.

The high hardness result of the samples in the interface might be the result of a HAZ of the steel. In fact, as the first depositions are made, a very small part of the substrate is melted to form a good bonding with the material being deposited. Due to high initial temperatures and rapid cooling, the material can behave as if it was subjected to a high energy quench, resulting in small microstructure and, most importantly, in the formation of martensite or other hard crystalline structures. This phenomenon leaves a HAZ around the interface. In Figure 4.22, a continuous cooling transformation (CCT) diagram of the 40 CrMnMo 7 or AISI P20 is presented.

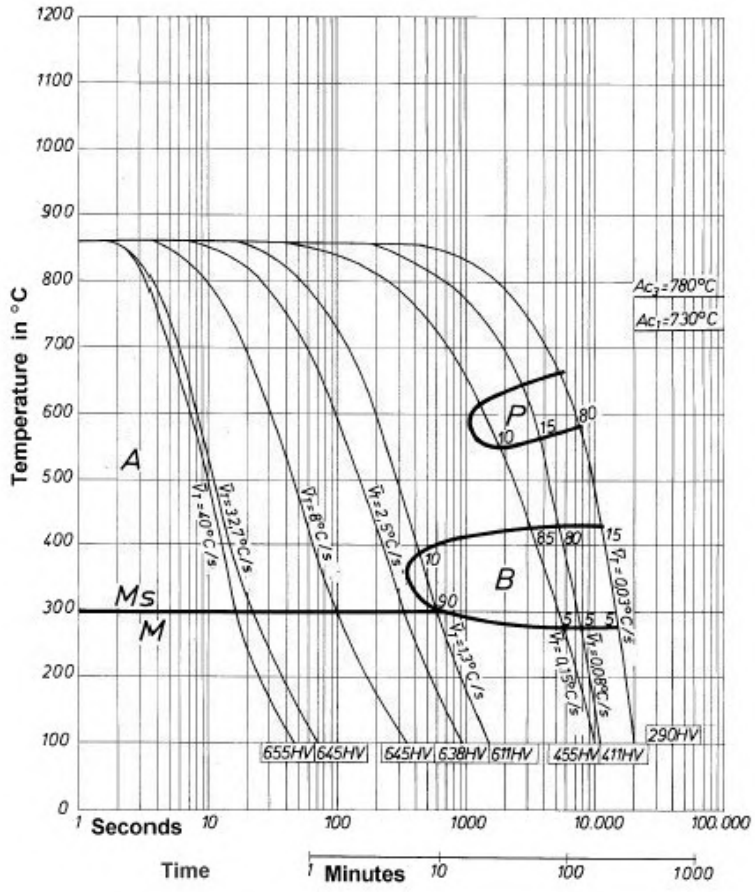

Figure 4.22: Continuous Cooling Transformation Diagram of 40 CrMnMo 7 steel [121].

The CCT diagram can provide an understanding of the approximate microstructure of the steel after the repeated cooling cycles. For the sake of simplicity, it can be observed that the cooling curve with the cooling speed of 0.15 °C/s originates a material with 455 HV, the approximate value obtained in the microhardness measurements. For that specific curve, the approximate structure is composed by 10% Perlite, 85% Bainite and 5% Martensite.

The substrate material was provided by Ramada Aços [122] in the tempered and

quenched state. In the first deposition of material, a small region of the substrate interface was heated to around 1200 °C and, in that region, the initial microstructure disappeared and coarse Austenitic grains developed. After the cooling, these austenitic grains were transformed into other structures, such as Perlite, Bainite and Martensite, leaving a HAZ in the material, where the properties should be different from the rest of the substrate.

Note that the diagram presented in Figure 4.22 has an initial temperature of 850 °C. In the present case, the initial temperature is much higher, meaning that the whole diagram is shifted to the right. Hence, the final microstructure composition might be different from the aforementioned one. For instance, no Perlite was formed, and more Bainite or Martensite was present. Note that this is only a possibility, since through optical observation it was not possible to verify the microstructure. In addition, the cooling rates are much higher than the presented in the CCT diagram and the cooling cycles way more complex, meaning that composition may vary in an unpredictable way.

In the case of sample 1, the macrohardness measurement happened to be placed into the HAZ of the substrate, hinting a high hardness. On the other hand, the macrohardness test on sample 2 did not reveal high hardness, since it was outside the very thin HAZ.

To further explore this topic, both samples were etched using 2% Nital and observed under an optic microscope. The results are presented in Figure 4.23 and 4.24, for samples 1 and 2, respectively.

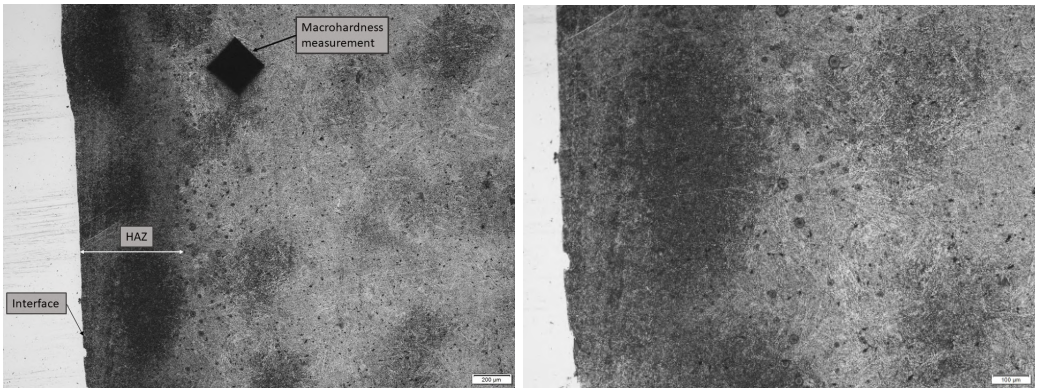

(a) (b)

Figure 4.23: Optical images of sample 1.

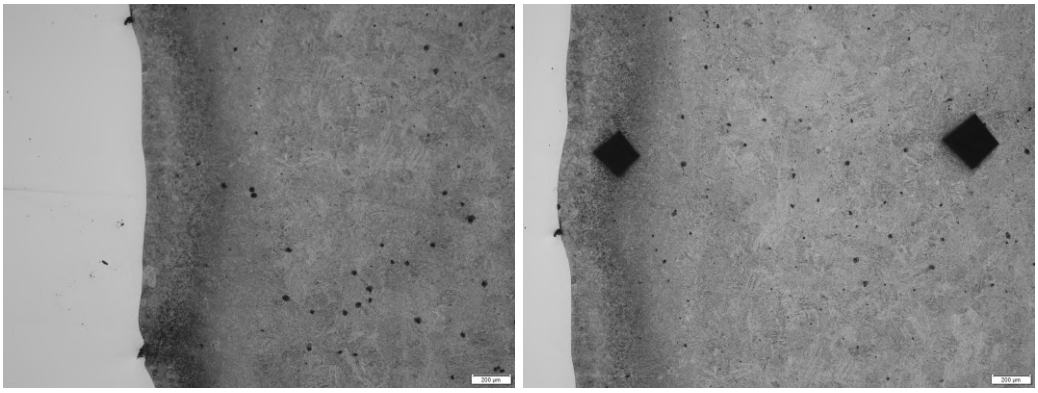

(a) (b)

Figure 4.24: Optical images of sample 2.

It can be clearly seen a thin HAZ near the interface, where a more shaded area is present. Despite not being possible to distinguish microstructure, it can be said that a region near the interface ($\approx 400\ \mu$m) was affected by the process, and its properties are different from the remaining substrate. This zone might be the explanation for the high hardness found near the interface.

Three other measurements were taken in sample 2, at two different heights, to verify if notorious changes would arise from horizontal measuring and to validate the previous measurements. The results are presented in Table 4.8.

Table 4.8: Hardness measurements of sample 2 at two different heights.

z Position [mm]	-4	8
Measurement 1 (HV)	241	224
Measurement 2 (HV)	244	226
Measurement 3 (HV)	240	215
Average (HV)	241.67	221.67

The differences within measurements at the same height are small, as the slight variations can be seen as errors in measurements. Therefore, it can be concluded that hardness is not as influenced by width as it is by height.

M. Fujishima et. al [119] investigated the evolution of hardness of Inconel 625 fabricated by DED with the height and width, reaching similar values and conclusions. The author stated that in multi-layered deposits, there was a variation in hardness depending on the analysed layer, which he also attributed to differences in cooling velocities between layers. The author recorded values of hardness ranging from around 225 HV to 260 HV.

J. Nguejio et. al [88], during his investigation on Inconel 625 fabricated by LMD, recorded higher values for as-deposited samples- 313 HV. F. Xu et. al [86] ran similar tests in samples of Inconel 625 made by Pulsed Plasma Arc Deposition, listing values between 260 and 275 HV. The author stated that the hardness of the bottom of the sample was higher than that of the upper sample because of the finer columnar dendrites and discrete precipitates.

4.1.5 Surface roughness measurement

The results of the surface roughness measurements for the bottom flat and lateral surfaces of the machined Nicoletto specimens are presented in Table 4.9 and 4.10, respectively.

Table 4.9: Surface roughness measurements of the bottom flat surface of sample 5 and 6.

	Longitudinal		Transverse	
Sample 5	R_a (μm)	R_z (μm)	R_a (μm)	R_z (μm)
Measurement 1	0.107	0.727	0.109	0.589
Measurement 2	0.139	0.853	0.158	1.156
Average	0.123	0.790	0.134	0.873
Sample 6	R_a (μm)	R_z (μm)	R_a (μm)	R_z (μm)
Measurement 1	0.107	0.727	0.137	0.852
Measurement 2	0.139	0.853	0.111	0.614
Average	0.123	0.790	0.124	0.733

Table 4.10: Surface roughness measurements of a lateral surface of sample 5 and 6.

	Longitudinal	
Sample 5	R_a (μm)	R_z (μm)
Measurement 1	0.127	0.913
Measurement 2	0.102	0.714
Average	0.115	0.814
Sample 6	R_a (μm)	R_z (μm)
Measurement 1	0.092	0.494
Measurement 2	0.060	0.373
Average	0.076	0.434

The purpose of these measurements is to give a context of the surface quality of the analysed specimen. It can be seen that both surfaces were properly grinded, as requested, and will not negatively impact the fatigue life of the specimen. In addition, it should be noted that the surface roughness of the machined specimen are according to the specimen specifications that can be found in Appendix A.

4.2 Tensile testing

The measurements made on the two tensile specimen before testing are presented in Table 4.11.

Table 4.11: Results of the measurements on the tensile specimen.

	L1 [mm]	L2 [mm]	L3 [mm]	H1 [mm]	H2 [mm]	H3 [mm]
Specimen 1	5.055	4.998	4.943	2.994	3.009	3.010
Specimen 2	5.086	5.044	4.999	3.025	3.018	3.041

In Table 4.12, the cross section of each location measured is presented.

Table 4.12: Results of the measurements on the tensile specimen.

	Cross section L1 x H1 [mm^2]	Cross section L2 x H2 [mm^2]	Cross section L3 x H3 [mm^2]	Average [mm^2]
Specimen 1	15.135	15.039	14.878	15.017
Specimen 2	15.385	15.223	15.202	15.270

Specimen 1 had a medium cross section of 15.017 mm^2 and specimen 2 had 15.270 mm^2. These average values of the cross section were the ones inserted in the DIC technique. The fracture of both specimen is presented in Figure 4.25.

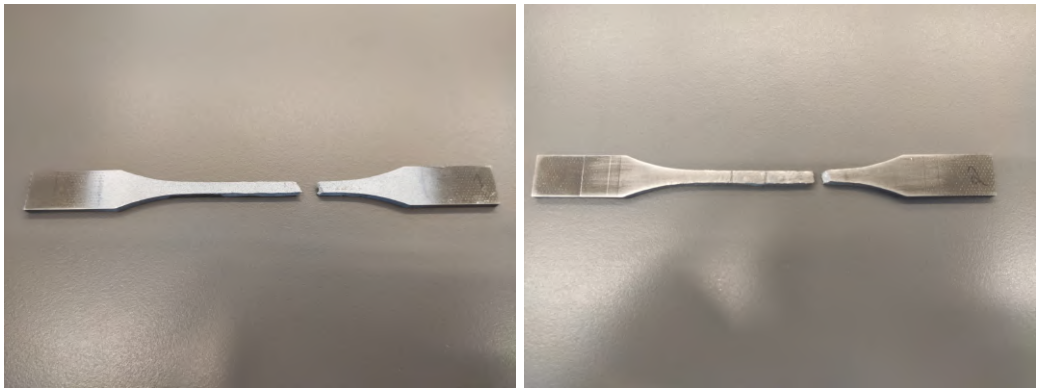

(a) (b)

Figure 4.25: Tensile specimen after failure: (a) specimen 1; (b) specimen 2.

As it can be observed, the fracture did not happen in the middle of the specimens. In fact, both specimens fractured near the L3 x H3 cross section. For specimen 1, this cross section was the smallest of the three analysed, which may justify the fact that the fracture occurred there, since less resistant area existed. For specimen 2, the same can be said, although cross section L2 x H2 presented a similar area as section L3 x H3.

The contrasting speckle utilised in the DIC analysis can be observed in Figure 4.26.

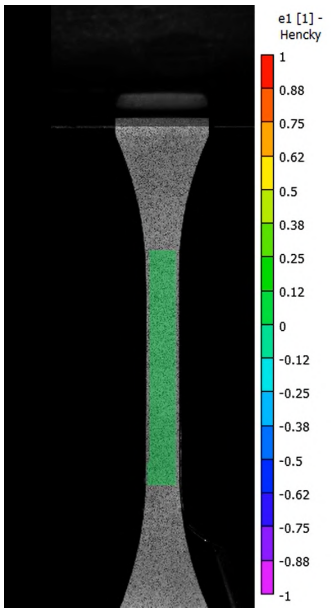

Figure 4.26: Speckle utilised for DIC.

The engineering and real stress-strain curve are presented in Figure 4.27 and 4.28, respectively, for specimen 1 and 2. Note that each curve was obtained by using the force and displacement measured by the tensile testing machine, by utilising the initially measured mean cross sectional area of both specimen and recurring to the DIC technique. This technique uses the cross sectional measurements of the specimen and the information provided by the tensile machine to calculate the stresses and strains.

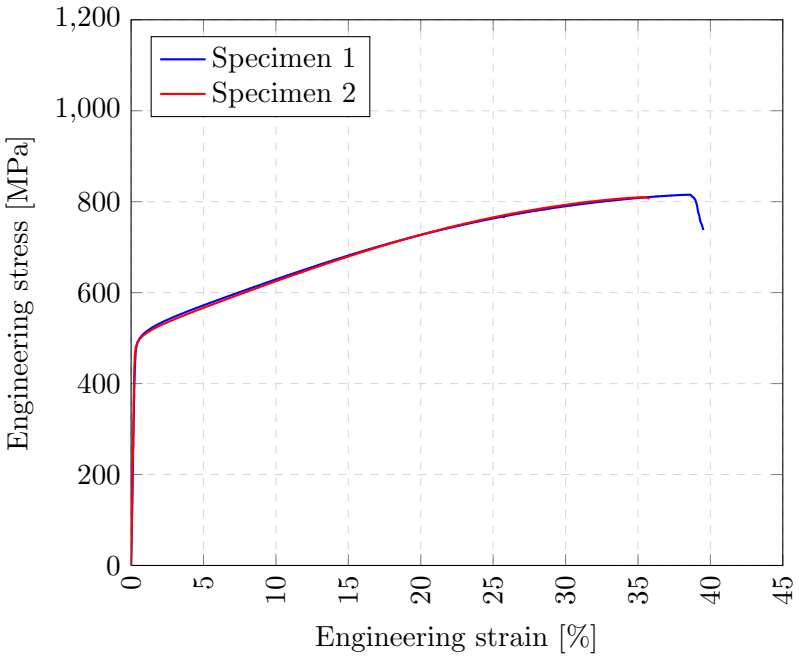

Figure 4.27: Engineering stress-strain curve.

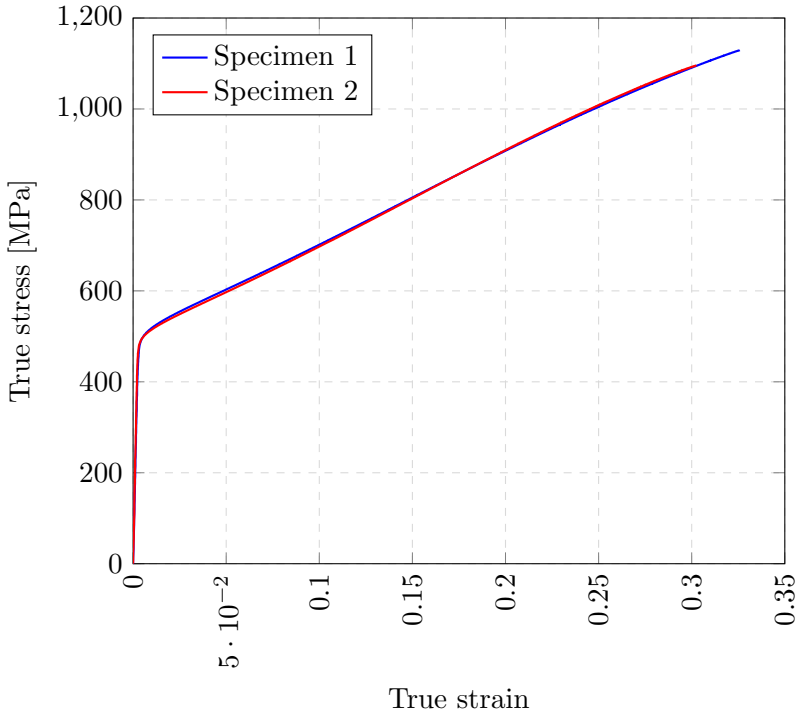

Figure 4.28: Real stress-strain curve.

The main tensile properties obtained from the tests are presented in Table 4.13.

Table 4.13: Experimental tensile properties.

	Young Modulus [GPa]	Yield strength (0.2%) [MPa]	Engineering ultimate tensile strength [MPa]	Real ultimate tensile strength [MPa]
Specimen 1	179	491	815	1129
Specimen 2	196	496	809	1095

These properties were obtained taking into account information monitored during testing by the tensile test machine and the digital image correlation technique. Although the yield strength and the ultimate tensile strength present similar values for both specimen, the Young Modulus is slightly different.

The Young modulus was calculated through the slope of the stress-strain curve in the linear region. The yield strength corresponds to the stress at which 0.2% deformation occurs and the ultimate tensile stress is equal to the maximum value of stress in each curve- either real or engineering stress-strain curve.

By observation of Figure 4.27, it is possible to verify that Inconel 625 presents close to no necking behaviour, as it fails right after the ultimate tensile strength. This behaviour was not expected, since Inconel 625 is a material with high ductility properties. Nevertheless, the material presents a very high elongation to failure value. The tensile properties experimentally obtained are within the ones exposed in the reviewed literature.

In Figure 4.29, it is possible to visualise the region of the specimen 1 that underwent higher strain, around 0.48, just before fracture. That same region led to fracture.

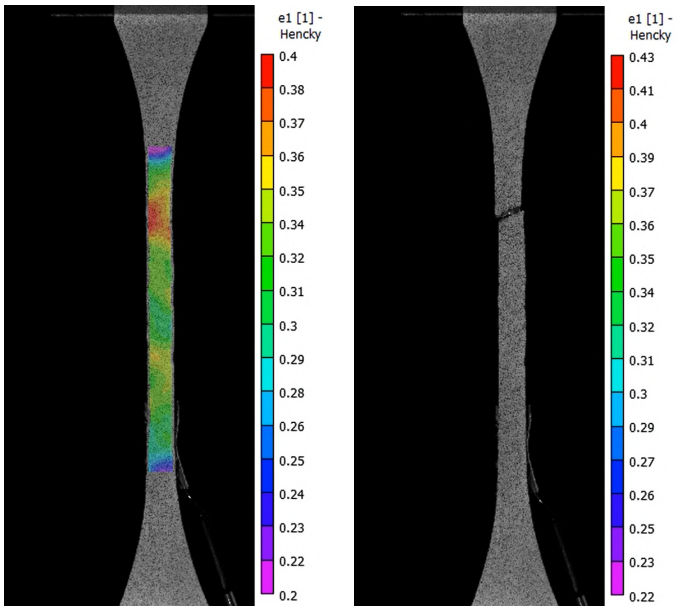

(a) (b)

Figure 4.29: Tensile specimen 1: (a) before and (b) after fracture.

In Figure 4.30, specimen 2 in the beginning of the test and moments before its failure can be observed.

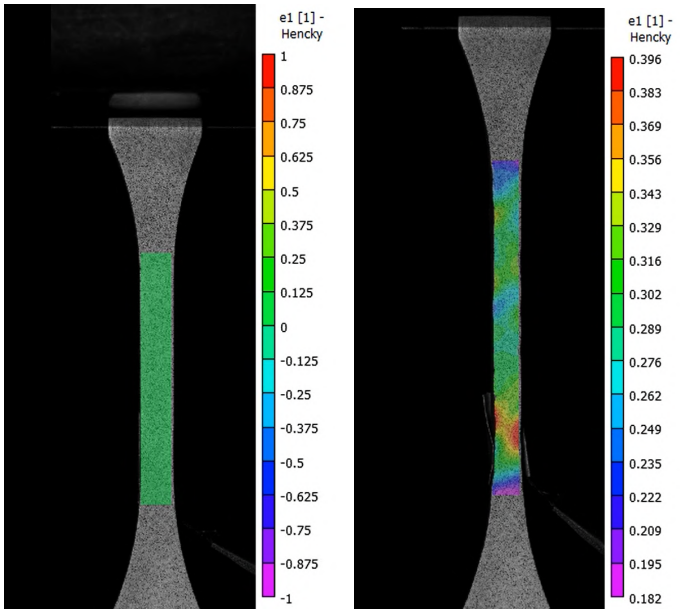

(a) (b)

Figure 4.30: Tensile specimen 2: (a) before and (b) after fracture.

One interesting aspect found was that, during testing in the plastic region, the strain within the DIC grid was not constant at a given time. In Figure 4.31, an example of such behaviour is presented, for specimen 1.

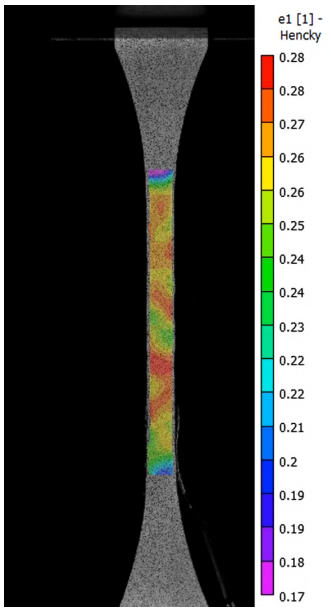

Figure 4.31: Different strains within the DIC grid, at a given time, for specimen 1.

This behaviour of the material might be due to different grain sizes within the specimen, as well as different microstructure morphology, although the tensile testing zone is within the same three or four layers. Another feature that may have given rise to this behaviour is shown in Figure 4.32, for specimen 2.

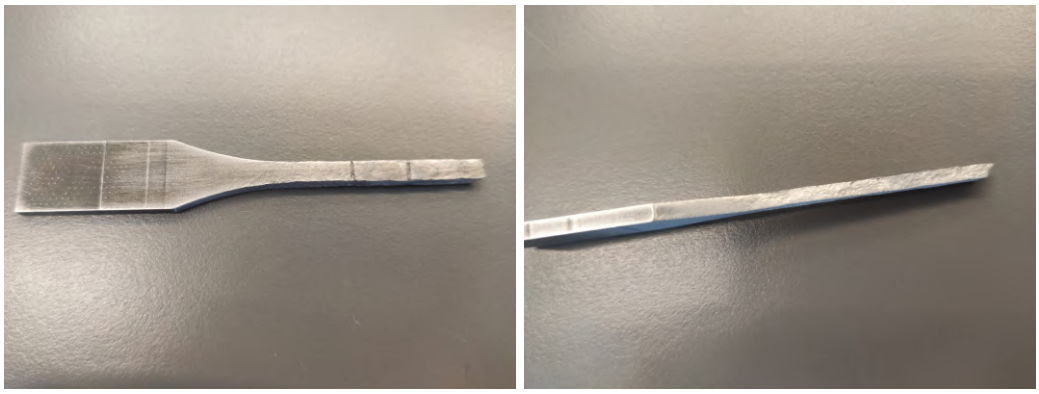

(a) (b)

Figure 4.32: Tensile specimen 2: (a) frontal view (b) lateral view.

As it can be seen in Figure 4.32, after fracture, the specimen presented a very irregular texture in frontal and lateral surface in the testing region. This texture is probably a result of the plastic deformation of the specimen during testing and can also be the reason that the DIC technique presented different strains in the testing section, during the trial.

4.3 FEM simulations

In this section, a convergence study on the mesh, as well as a few results of the numerical simulations are presented. A parametric study of the pre-load and displacement was also performed, to better cope with the influence of both these parameters on the stress profile

of the specimen. Furthermore, some changes to the specimen holder were made with the intent of lowering its stiffness and reducing stress concentration at gripping contact vicinity. It is important to note that these simulations were performed only considering the elastic behaviour of the material.

To evaluate the convergence of the built numerical model, four simulations with four different meshes were carried out. The four nodes considered in the analysis are shown in Figure 4.33.

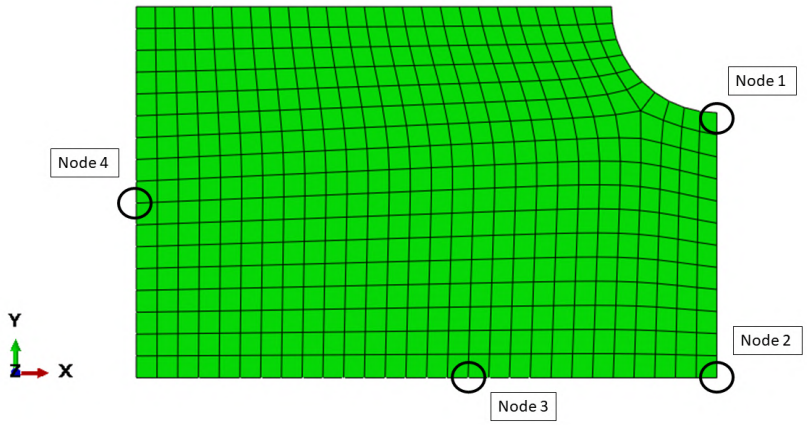

Figure 4.33: Chosen nodes for the convergence study.

Node 1 and 2 are the most relevant to the study, since they belong to the symmetry plane and the cross sectional area that is going to be fatigue tested. Node 3 is one close to the contact with the specimen holder. The stress relevant to these three aforementioned nodes are the normal stresses in the XX-direction (S11). On the other hand, Node 4 is mostly influenced by the pre-load, which means the stress in the YY-direction (S22) is more representative of its stress state.

In Table 4.14, the description of the meshes are presented. Note that every mesh had the same Abaqus elements, C3D8 and C3D8R.

Table 4.14: Different meshes used in the parametric study.

Mesh	Number of Elements	Number of Nodes	Specimen element average size [mm]	Computational Time [hours]
Mesh 1	61001	68625	0.8	0:7:32
Mesh 2	74135	83230	0.6	0:12:10
Mesh 3	107413	120255	0.4	0:18:17
Mesh 4	206534	227428	0.5	1:45:48

The results of the convergence study can be seen in Figure 4.34, while the numerical values are exposed in Table 4.15.

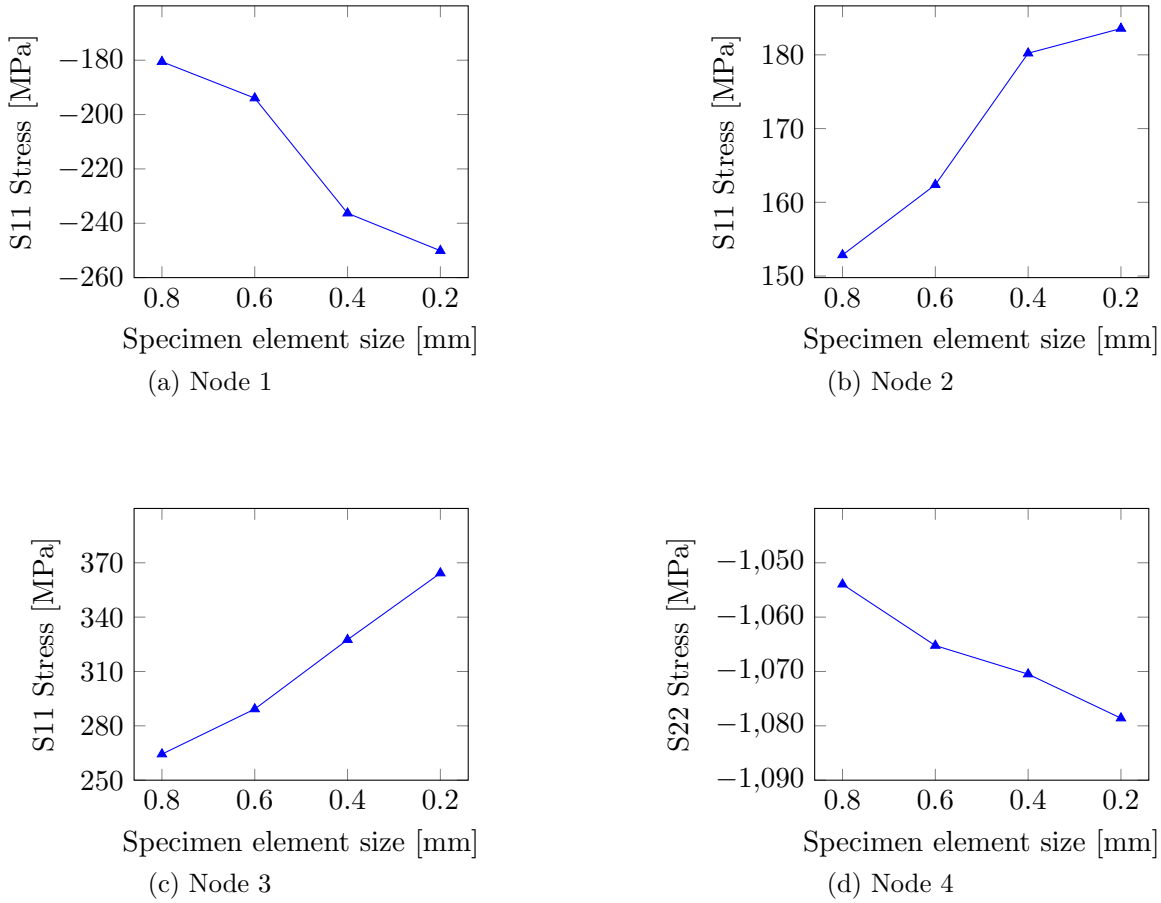

(a) Node 1 (b) Node 2

(c) Node 3 (d) Node 4

Figure 4.34: Effect of mesh refinement in the stress of four different nodes.

Table 4.15: Convergence study results. Node 1, 2 and 3 analysed in S11, while node 4 in S22.

Mesh	Node 1 [MPa]	Node 2 [MPa]	Node 3 [MPa]	Node 4 [MPa]
Mesh 1	-180.55	152.86	264.37	-1053.96
Mesh 2	-193.95	162.38	289.26	-1065.23
Mesh 3	-236.31	180.22	327.53	-1070.49
Mesh 4	-250.10	183.57	364.28	-1078.59

Regarding nodes 1 and 2, it can be seen that a convergence is obtained. In fact, from mesh 3 to mesh 4, the stress of nodes 1 and 2 change 5.83 % and 1.86 %, respectively. The difference in computational time between these two meshes is not worth the increase in numerical result accuracy. As already mentioned, the crack is expected to nucleate at node 2, making it one of the most relevant nodes to analyse. A 2% change in stress can almost be neglected, hence mesh 3 proves to be the most time-efficient mesh for these two nodes.

When it comes to node 3, no convergence is obtained. This node is located near the contact zone between the specimen and its holder, meaning that it is most likely a stress concentration node, i.e a numerical singularity. In these cases, the convergence would not be obtained even with more refined meshes, so further re-meshing was not considered necessary.

Regarding node 4, a convergence was achieved with less than 1% stress variation between mesh 3 and 4.

Weighting the pros and cons of the four considered meshes, it was decided that mesh 3 was the one that provided the most reliable results in the least amount of time. Hence, the following analyses were performed using mesh 3.

The first few simulations were performed with a pre-load of 10602 N, which is equivalent to 10 N.m torque, and a maximum displacement of 0.1 mm, as already mentioned. The Von Mises stress, in MPa, of the overall model after maximum displacement application is presented in Figure 4.35a, while a zoom-in in the most critical nodes is shown in Figure 4.35b.

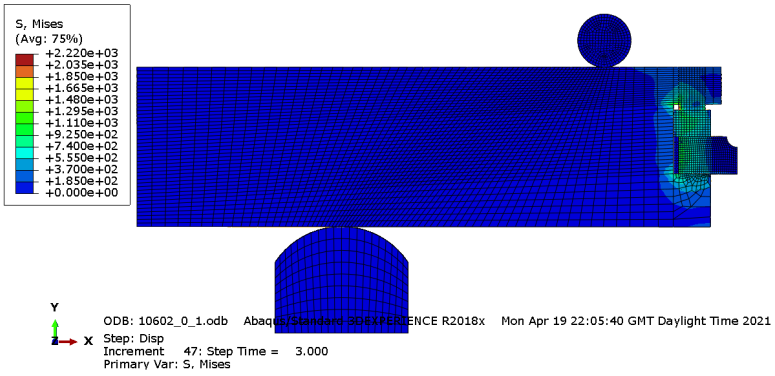

(a)

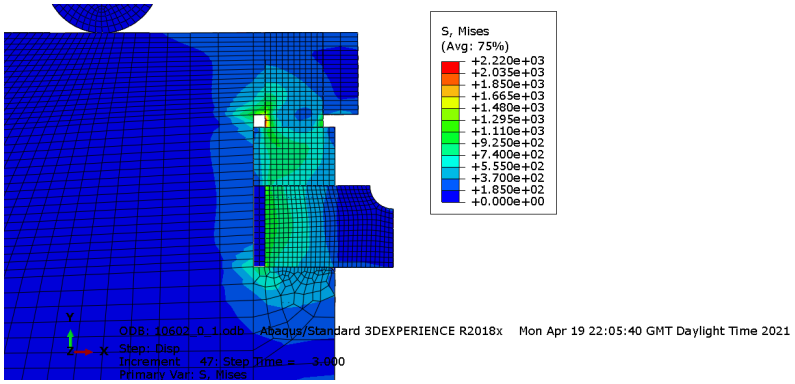

(b)

Figure 4.35: Von Mises stress after maximum displacement application.

As it can be seen, after the displacement step, the maximum Von Mises stress in the model, around 2220 MPa, is located at the surface of the "threaded" element. Since the regions near this stress peak are exposed to stresses around 1300 MPa, that mentioned spike was attributed to low mesh refinement in that area.

Analysing the Von Mises stress is not enough to understand the behaviour of the specimen during the simulation. Hence, a more detailed analysis on the specimen is provided next.

Firstly, when it comes to specimen behaviour, the most relevant results to be analysed are the stress in the YY-direction (S22) after the pre-load step, which indicates the stress profile imposed by the tightening of the screw. In Figure 4.36, it is presented the stress profiles in the YY-direction (S22) and XX-direction (S11), in MPa, of the miniature specimen, at the end of pre-load application step.

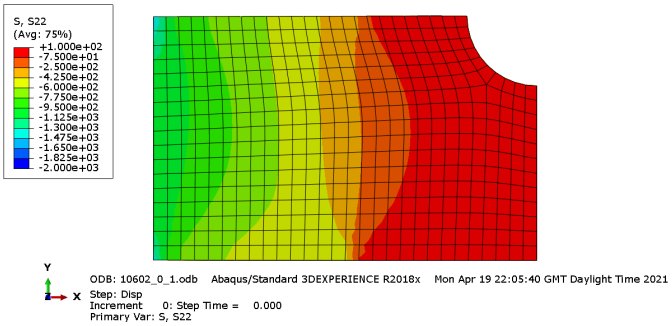

(a) Stress in YY-direction

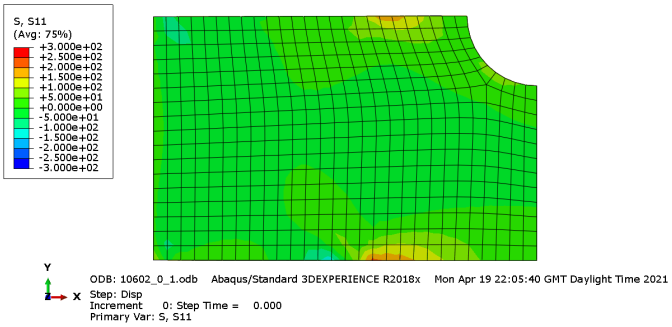

(b) Stress in XX-direction

Figure 4.36: Stress profile of the specimen at the end of pre-load step.

From Figure 4.36a, it can be seen that most of the specimen is being compressed, especially the left region, since it is there that the specimen is being gripped. The compression stress, in the middle horizontal section of the specimen is about 1000 MPa, which is more than enough to secure the specimen during testing. In fact, this value is higher than the Yield strength of the material, meaning that it would plastic deform during pre-load application, which did not occur during testing. This might mean that the tightening torque conversion to pre-load overestimates the normal stress that compresses the specimen. Although some simplifications were made, the applied torque might be excessively high and it could be lowered in further simulations and when experimentally testing the specimen. On the other hand, the numerical model might also be overestimating the influence of the tightening torque on the stress profile of the specimen.

Secondly, the stress profile in the XX-direction after the displacement step is also of upmost importance, since it reveals the stress in the specimen that promotes crack propagation. In Figure 4.37, the stress profiles in the XX-direction (S11) and the YY-direction (S22) are presented, in MPa, of the miniature specimen, at the end of the simulation.

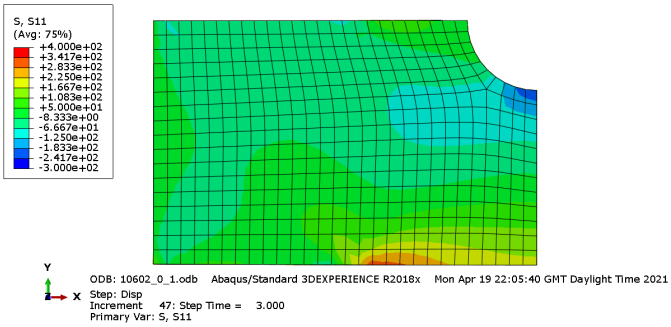

(a) Stress in XX-direction

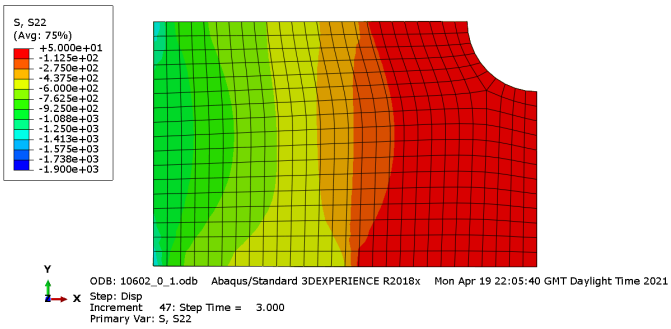

(b) Stress in YY-direction

Figure 4.37: Stress profile of the specimen at the last step of the simulation.

A few conclusions can be drawn by observation of Figure 4.37. Firstly, it is clear that the application of displacement has more influence on the stress profile in the XX-direction than in the YY-direction. The latter is more influenced by the pre-load. By analysing the right side of the specimen, i.e. the nodes in the symmetry plane, one can see that while the nodes in the notch are sustaining compressive loads, the bottom part of the specimen is subjected to tensile loading, which corresponds to the expectations. This way, the crack is expected to nucleate in the bottom part of the specimen, promoted by the tensile load, and to propagate towards the notch, where compressive loads dominate.

However, the numerical simulation allowed to realise that the highest stress was not located at the symmetry nodes. Instead, a stress peak was verified at the middle bottom of the specimen, most likely due to the gripping and the support holder geometry. In Figure 4.38, the location of that stress peak, marked with node 3, can be seen in the overall model. It becomes clear that its origin is related to the shape of the specimen holder.

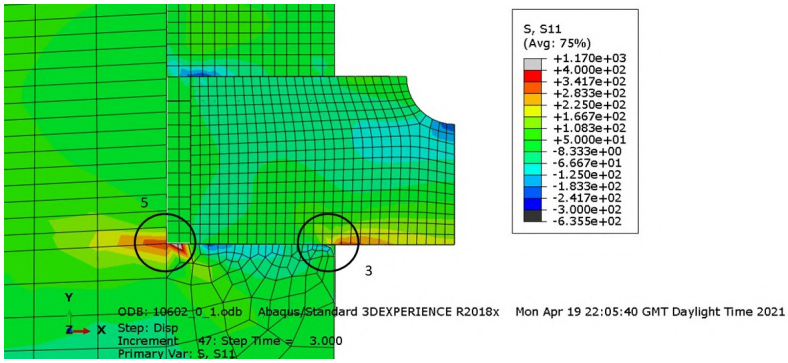

Figure 4.38: Stress peaks in the specimen region.

Marked by number 5 is another observed stress peak. This one might be due to the sharp corner (90 °) which originates a numerical singularity.

The stress peak marked by number 3, being the region with the most stress, may cause crack nucleation *in situ.*, instead of nucleating in the middle region of the specimen. G. Nicoletto [63] gripping system exhibited a similar stress peak due to gripping of the specimen. However, his specimens cracked in the middle section, which leads to believe that the same will occur during the experimental work.

To better understand the variation of stress profile with changing pre-load and displacement, nine other simulations were made. Three levels of pre-load- 10602 N, 5301 N and 3534 N, corresponding to a tightening torque of around 10.6 N.m, 5.3 N.m and 3.5 N.m, respectively, and three levels of maximum displacement- 0.1 mm, 0.2 mm and 0.3 mm, were considered. Analysing the whole model is impractical, hence four nodes were chosen and their stress were registered and plotted. The numerical values of each simulation is exposed in Table 4.16. Moreover, plots of these results are presented in Figure 4.39. The nodes picked for the analysis are the same as the ones presented in Figure 4.33.

Table 4.16: Numerical plan to study the influence of maximum displacement and pre-load on the stress profile, in MPa.

Max. displacement [mm]	Pre-load [N]		
Node 1	10602	5301	3534
0.1	-236.31	-246.46	-247.30
0.2	-557.16	-555.06	-545.80
0.3	-870.51	-848.88	-827.39
Node 2			
0.1	180.22	164.99	158.30
0.2	367.00	344.52	331.83
0.3	549.20	515.15	495.13
Node 3			
0.1	327.53	212.83	173.38
0.2	454.15	330.20	283.71
0.3	572.38	436.63	384.70
Node 4			
0.1	-1070.49	-534.82	-357.77
0.2	-1070.76	-538.21	-363.73
0.3	-1073.14	-544.76	-373.18

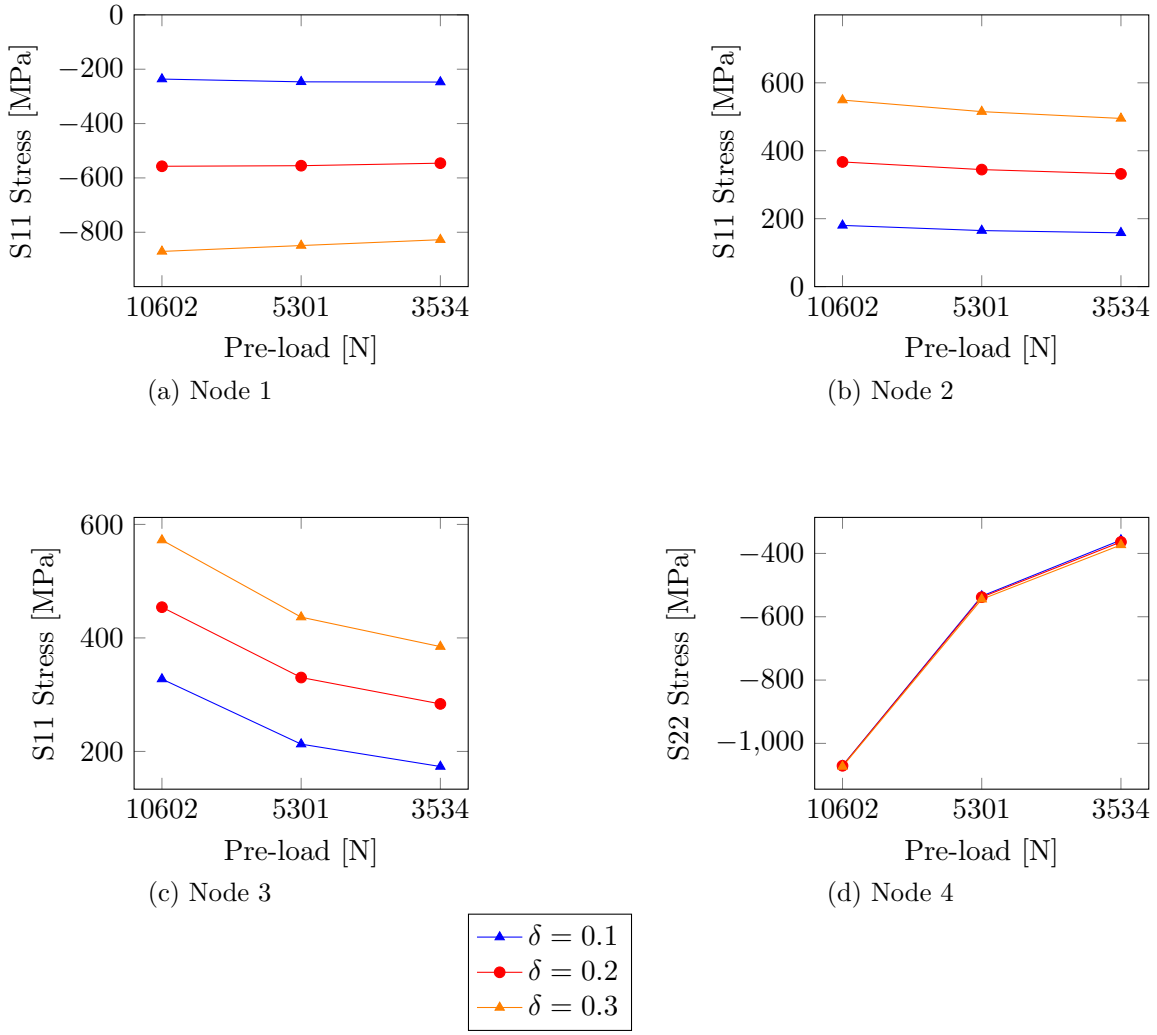

Figure 4.39: Effect of pre-load and displacement in the stress of four different nodes.

Regarding node 1, 2 and 3, it can be seen that with increasing maximum displacement, the stress in XX-direction (S11) also increases. This conclusion is in line with expectations, as a higher displacement originates a higher bending moment on the specimen.

For the nodes in the symmetry boundary (nodes 1 and 2), the pre-load does not have a relevant influence, as a decrease of load does not induce a significant change in the S11 stress. This observation makes sense, since the aforementioned nodes are far from the contact zone of the specimen with its holder. Nevertheless, it is intuitive that with a decrease in load, comes a decrease in stress, which can be observed in the shown results.

When it comes to node 3, it is important to note that it is influenced by both displacement and pre-load. Hence, the S11 stress felt in the node decreases with decreasing pre-load and with decreasing maximum displacement. As before, this result comes as expected, as this node is located in a more central part of the specimen, where it can be influenced by the gripping strength and by the displacement imposed by the actuator.

As for node 4, it can be concluded that its stress in the YY-direction (S22) is only influenced by the pre-load, as a change in maximum displacement has no effect on its S22 stress. This node is far from the symmetry boundary of the specimen, where the displacement is felt the most. Moreover, the node is highly influenced by the gripper load.

With this study, it can be concluded that the pre-load influences the S22 stress direction the most, while displacement takes its toll on the S11 direction. It also allows to conclude that, perhaps, a pre-load of 10602 N is too high to be used in testing. For instance, in node 4, it can be felt a compressive stress of around -1100 MPa, which is higher than the expected ultimate tensile strength of the material. Since only the elastic behaviour is considered, the stresses are obviously higher than those expected with plastic behaviour. Nevertheless, this value seems extremely high for the applied loads, meaning that the current numerical model might be overestimating the influence of the pre-load.

With a pre-load of about 5301 N, the stresses felt in all four nodes are below the ultimate tensile strength of the material, indicating that 5.4 N.m torque applied to the screw is adequate for testing.

Moreover, maximum displacements of 0.1, 0.2 and 0.3 mm, with pre-loads of 5301 N, are within the testing limits of the material, meaning that these could be chosen as levels to extract the S-N curve of the material.

Another useful study is to compare and analyse the evolution of the stress peak observed in Figure 4.38 (marked by point 2) and the node where the crack is expected to begin, i.e. nodes 3 and 2, with changing pre-loads and maximum displacements. With this in mind, in Figure 4.40 the evolution of these nodes is presented for further discussion.

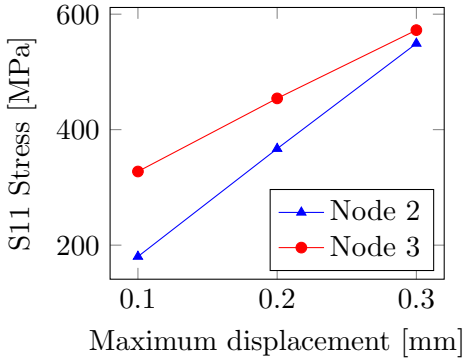

(a) Pre-load= 10602 N

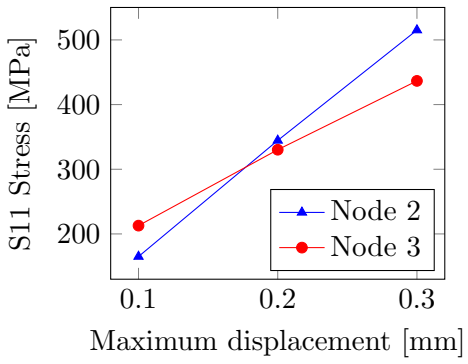

(b) Pre-load= 5301 N

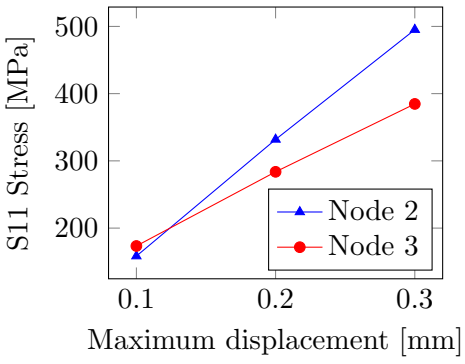

(c) Pre-load= 3534 N

Figure 4.40: Stress evolution of nodes 2 and 3 with different pre-loads and displacements.

The first conclusion that can be drawn is that node 3 is not always the most stressed node of the specimen in the XX-direction. In fact, when the displacement applied increases,

node 2 tends to have a higher stress than node 3. With decreasing pre-load, this shift occurs sooner (for smaller displacements). As already mentioned, stress in node 2 is highly affected by the applied displacement, while displacement contribution to the stress of node 3 is smaller. It is very important for this study that the higher stresses are felt in the middle of the specimen (node 2), since it is expected that the fatigue crack nucleates there and not in node 3, in the interface between the specimen and the gripping system.

One last try at lowering the stress at node 3 was made, by slightly changing the design of the specimen holder. If one could lower the stiffness of the specimen holder part below the specimen, lower gripping stresses could be achieved. With this in mind, three different designs were proposed, and the evolution of stress on the bottom part of the specimen was analysed.

In Figure 4.41, the three designs are revealed and, in Figure 4.42 the analysed nodes, from 10 to 38 are presented.

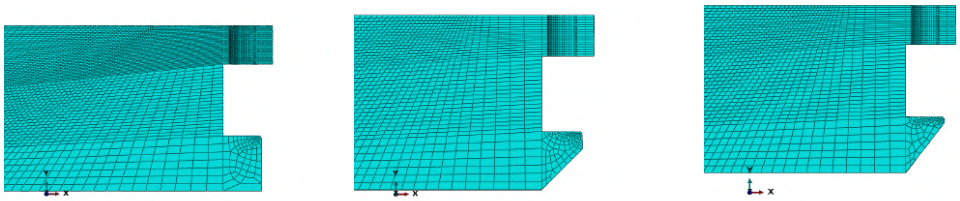

(a) Design 1 (b) Design 2 (c) Design 3

Figure 4.41: Different designs considered.

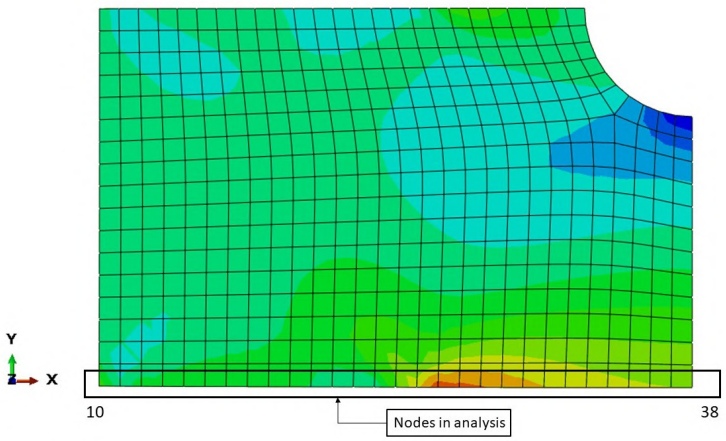

Figure 4.42: Nodes in analysis.

The results of the simulations are presented in Figure 4.43. Note that these were performed with a pre-load of 10602 N and a maximum displacement of 0.1 mm.

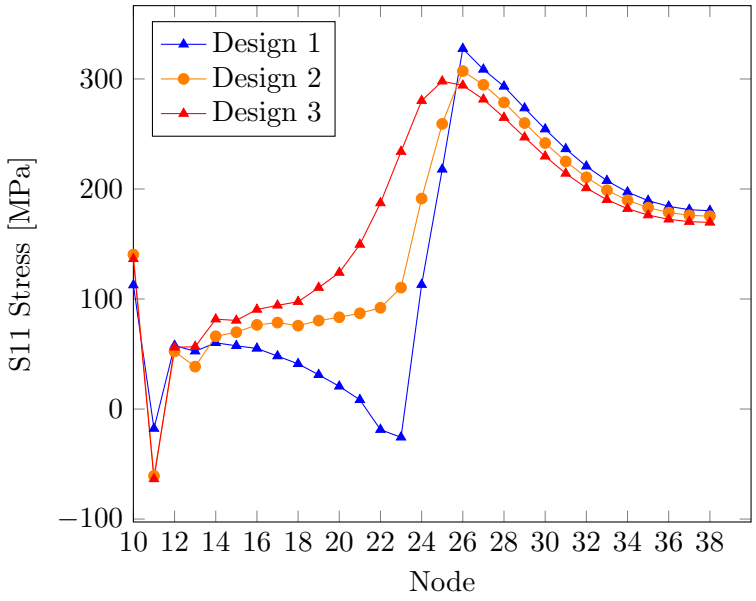

Figure 4.43: Stress profile of the bottom nodes of the specimen with three different designs.

It is clear that the type of design and its stiffness has an influence of the stress peak of the specimen. However, only a change of about 25 MPa was obtained across the three designs. Hence, the second design was chosen to be the final design, since it has enough stiffness not to fail and slightly lowers the stress peak.

4.4 Fatigue testing

The results of the fatigue testing are presented in Table 4.17. Specimen 1 achieved run-out.

Table 4.17: Fatigue testing results.

Specimen	$\Delta\delta$ [mm]	F_{max} [N]	F_{min} [N]	ΔF [N]	$\Delta\sigma_0$ [MPa]	$\sigma_{max,0}$ [MPa]	N_i
1	0.25	168.5	0	168.5	400	400	4000000
2	0.44	257.5	0	257.5	612	612	1246581
3	0.44	230	0	230	546	546	2500000
4	0.44	300.5	0	300.5	714	714	786741
5	0.55	323	0	323	767	767	393079
6	0.55	322.5	0	322.5	766	766	2820300
14	0.55	355.5	0	355.5	845	845	271151
7	0.55	352.5	13	339.5	807	838	412768
8	0.55	429	40	389	924	1019	142238
9	0.55	428.5	28.5	400	950	1018	200871
10	0.55	307.5	1.5	306	727	730	724523
11	0.34	425	50.5	374.5	890	1010	98116
12	0.34	253	19	234	556	601	1773500

where $\Delta\delta$ is the displacement range of the actuator, F_{max} is average of the maximum load acquired by the load cells, F_{min} is average of the minimum load acquired by the load cells, ΔF is the difference between maximum and minimum load, N_i is the number of cycles to crack initiation, $\Delta\sigma_0$ is the nominal stress range and $\sigma_{max,0}$ is the maximum nominal stress. These last two parameters can be calculated using Equation 3.4,

The resulting S-N curves are presented in Figure 4.44 and Figure 4.45, as a function of maximum nominal stress and nominal stress range, respectively. The arrow represents a run-out test. Note that the run-out test was not considered when calculating the experimental regression.

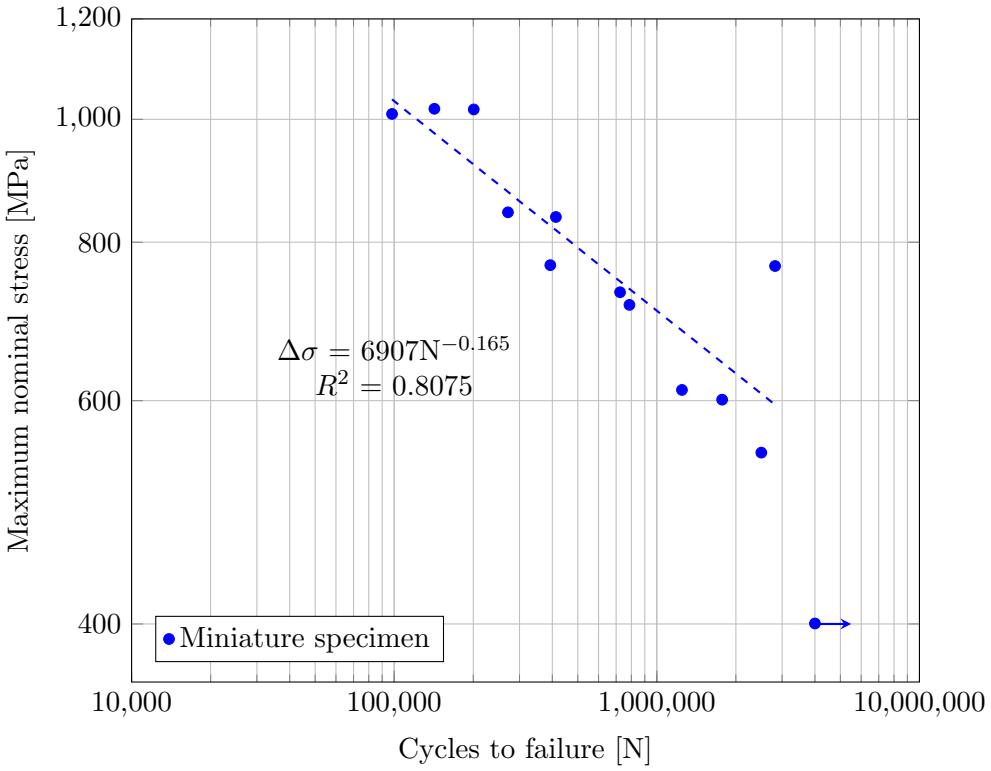

Figure 4.44: Experimental S-N curve. Maximum nominal stress in the Y-axis.

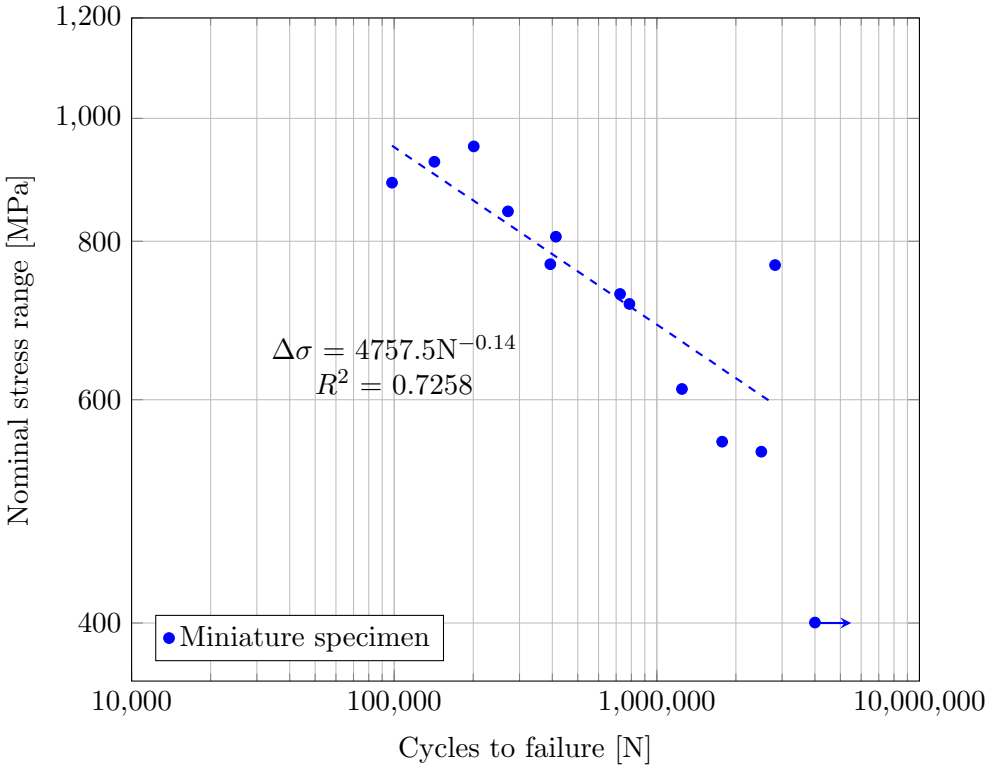

Figure 4.45: Experimental S-N curve. Nominal stress range in the Y-axis.

It should be reminded that the nominal stresses are calculated through the reaction forces measured by the load cells, using Equation 3.4. It is, therefore, an analytical elastic value that does not take into account the complex variations of geometry in the specimen, and specially, in the notch area that occur during the plastic regime.

The R^2 correlation values obtained for both experimental S-N curves are quite satisfactory, as the scatter is typical of S-N curve fatigue testing. Due to time restrictions, the fatigue limit criterion for the experiment was 3×10^6, as already stated. Therefore, it was not possible to determine whether Inconel 625 produced by DED has a fatigue limit or not.

The crack nucleation of the specimen did not always start in the same place. Some of the them started in the middle section, other somewhere near it. Nevertheless, the crack always propagated towards the notch, which was the main focus of the trials.

In the bottom flat part of the specimen, the stress varied due to the gripping system, as shown in Chapter 4.3. Through the numerical simulations, it could be concluded that higher the displacement of the actuator, higher would be the stress in the middle section of the miniature specimen. The stresses in the S11 direction (σ_{xx}) of the specimen for 0.56 mm of actuator displacement and 10 N.m torque are shown in Figure 4.46.

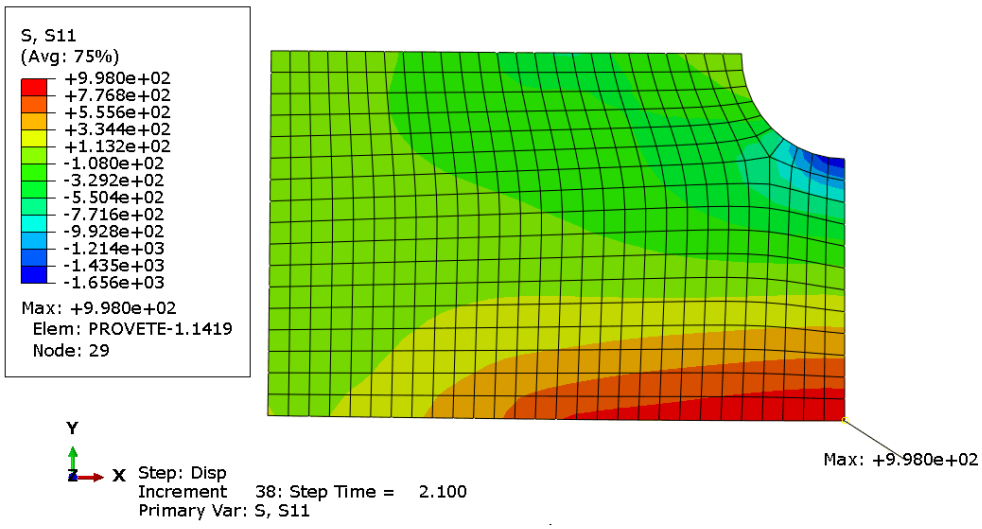

Figure 4.46: Stresses (MPa) in the S11 direction of the bottom region of the specimen.

Crack nucleation depends on many variables. The presence of defects near the surface originates stress concentration factors that promote cracks. As the stress in the bottom flat surface are very similar, as shown in Figure 4.46, the crack will begin somewhere in that region, perhaps where the biggest defect is located. Thus, as verified through this experiment, crack nucleation location varies from sample to sample, being probabilistic. However, all of them progressed towards the notch, where the biggest concentration factor is present. Some of the cracks are presented in Figure 4.47.

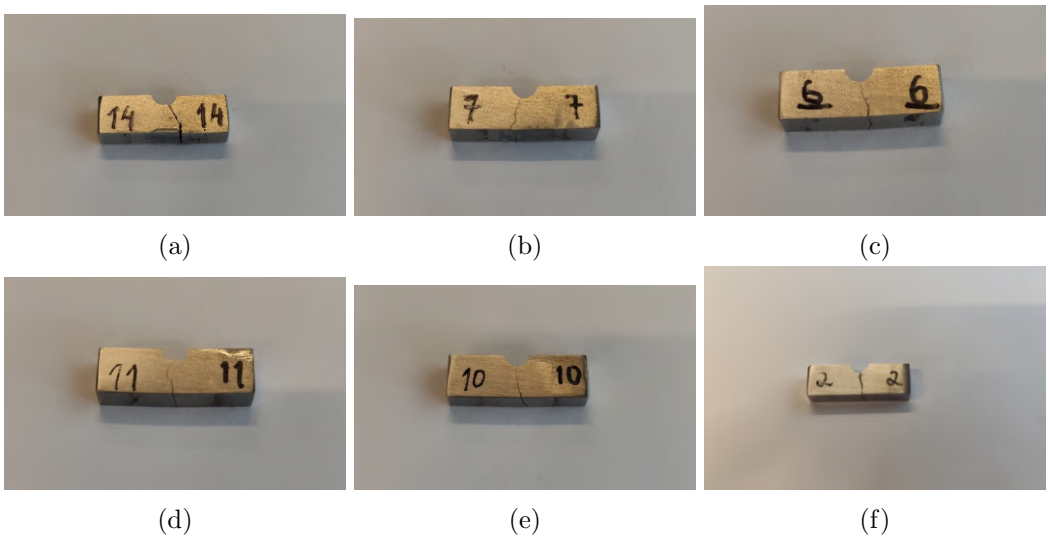

(a) (b) (c)

(d) (e) (f)

Figure 4.47: Cracks in different specimen.

4.4.1 Comparison with literature

In this chapter, S-N curves of Inconel 625 from the available literature were gathered. The main purpose was the comparison of the fatigue life of the material produced by several different processes with the one obtained experimentally.

To the author's knowledge, no fatigue data from Inconel 625 produced by DED was

published yet, at least in the free literature. The researched fatigue curves are plotted in Figure 4.48, as a function of maximum nominal stress.

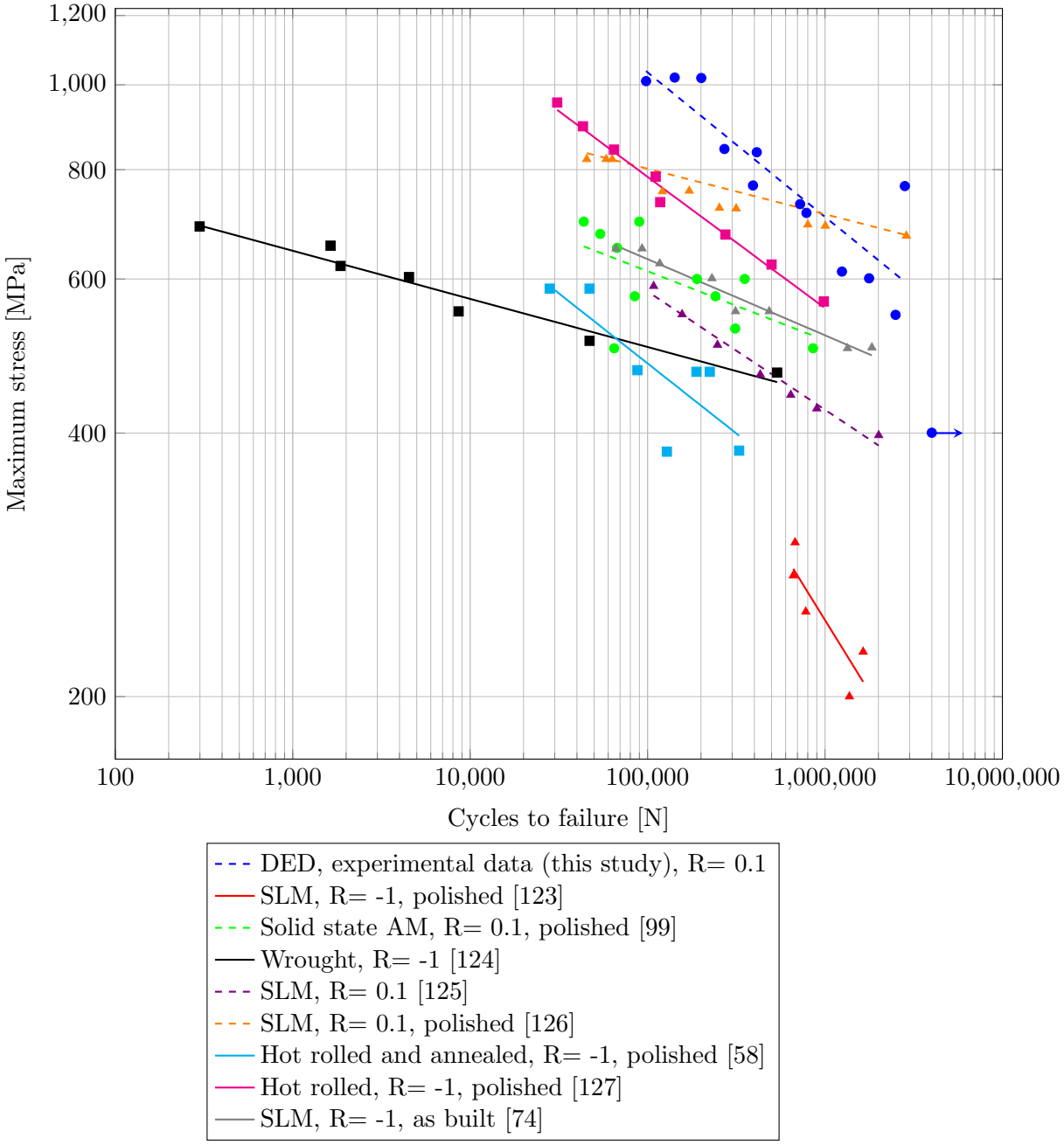

Figure 4.48: Comparison of the experimental S-N curve with the reviewed literature. Maximum stress in the Y-axis

Note that the curves gathered from literature present different load ratios. The trend-line of the curves obtained with R= 0.1 are presented as dashed lines, while the ones obtained with R=-1 are shown as continuous lines.

By observation of Figure 4.48, it would seem that the experimental S-N curve obtained during this work presents a higher fatigue strength than those of the literature. However, presenting the S-N curve as a function of maximum stress for curves with different stress ratios might be misleading in interpretation.

In reality, for the same maximum stress, if one increases the load ratio, the mean stress increases, but the stress range decreases at the same time. This way, it is hard to compare curves with different load ratios, as two damage influencing parameters change simultaneously.

In Figure 4.48, by comparing the curves with R=-1 and R=0.1, it could be said that, in general, the ones with positive load ratios originate higher fatigue strength. This is not true, as tensile mean stresses are detrimental to fatigue life. This interpretation is tightly connected with the variable that is plotted in the Y-axis. An alternative is representing the S-N curves as a function of stress range, as shown in Figure 4.49.

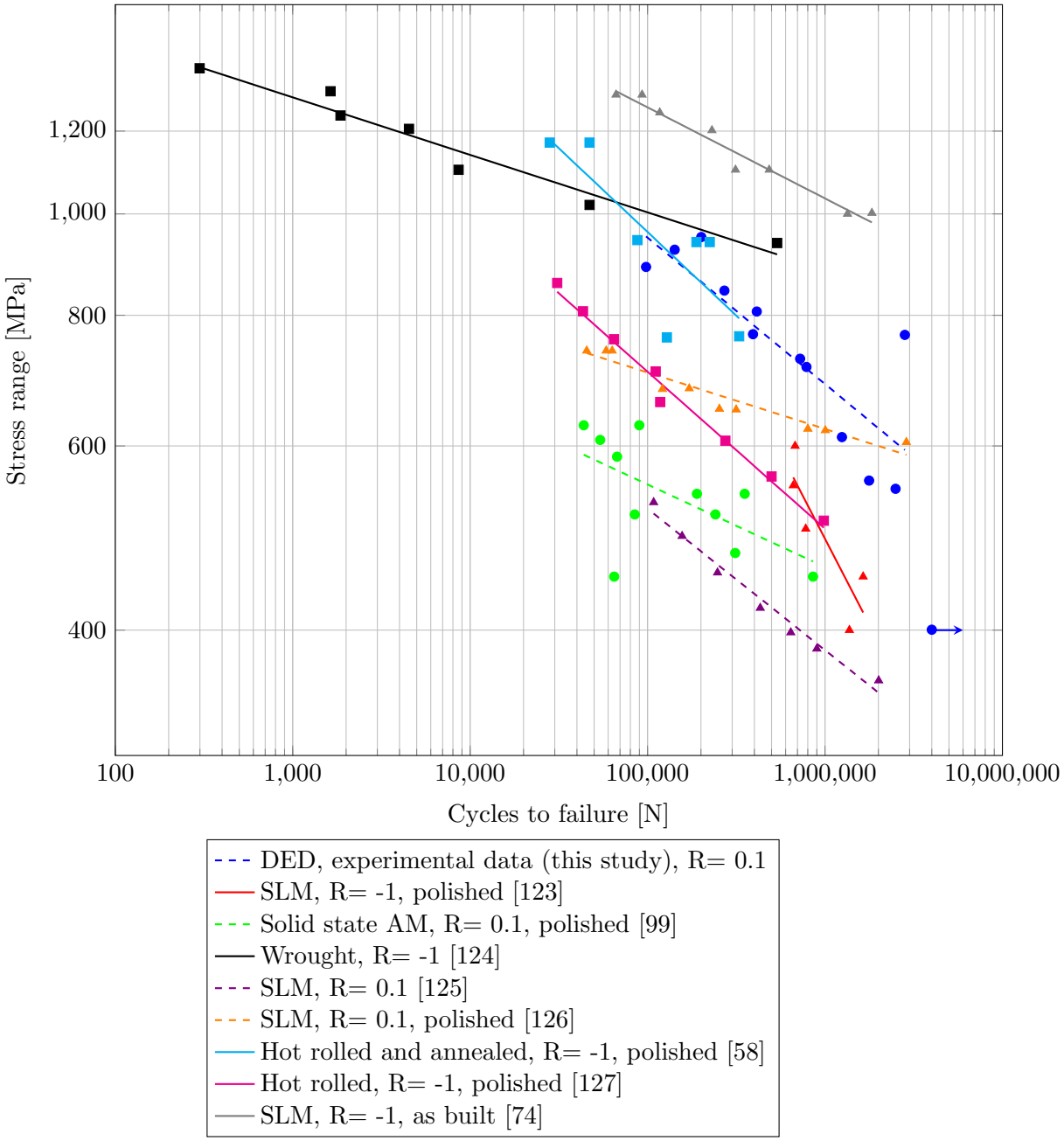

Figure 4.49: Comparison of the experimental S-N curve with the reviewed literature. Stress amplitude on the Y-axis.

Once again, the trendline of the curves obtained with R= 0.1 are presented as dashed lines, while the ones obtained with R=-1 are shown as continuous lines. This time, material produced during this work is no longer the one with the highest fatigue strength. Nevertheless, within the data with load ratio of 0.1, the material of this work is the one that presents higher fatigue life, which is a good indicator that the production process was reliable.

Overall, the S-N curves obtained from tests with negative load ratios provide higher fatigue life for the same stress level, since tensile mean stresses are very detrimental to fatigue life. Moreover, load ratios of -1 imply that $\sigma_{max} = -\sigma_{min}$ and, while tensile stresses promote crack growth, compressive ones tend to avoid this growth, promoting crack closure.

This comparison is also not free of flaws. Comparing S-N curves with different load ratios is not easy and few conclusions can be drawn. A good idea would be to apply one of the criteria that relate the stress amplitude with the mean stresses, such as the Soderberg, Walker [128] or other models. However, being able to apply these models require that the tensile properties of the tested materials are known, which is not feasible since that information is not available all the time.

In addition, the results from the experimental tests are still preliminary. The specimens used were not conventional and the stresses were calculated based on the reaction forces measured by the load cells, which means that these stresses are nominal and "elastic", which overestimates the real stresses.

Instead of representing the S-N curve with the $\Delta\sigma = K \cdot N^n$ power law like in the S-N curve presented in Figure 4.45, a different power law relation can be utilised to describe the curves, such as $\Delta\sigma^m \cdot N = C$, where $\Delta\sigma$ is the stress range, m is the slope of the S-N curve, N is the number of cycles to failure and C a material constant. The slope of each S-N curve reviewed in the literature can be calculated either by using $-1/n$ from the previous power law, or by using two points of each S-N curve.

According to Eurocode 3: design of steel structures [129], a reference value of fatigue strength can be used to characterise the fatigue strength of a material. This reference is defined as the critical stress range that corresponds to 2 million cycles, $\Delta\sigma_c$. Using the power law mentioned before, it is possible to calculate the critical stress range of each S-N curve. In Table 4.18, the slope and the critical stress range for each S-N curve of the reviewed literature and for the one obtained during this work are presented.

Table 4.18: S-N curves slope and critical stress range.

S-N curve	Slope (m)	$\Delta\sigma_c[MPa]$
DED, experimental data, R= 0.1 (Dark blue)	7.14	624
SLM, R= -1 (Red) [123]	3.05	390
Solid state AM, R= 0.1 (Green) [99]	12.66	435
Wrought, R= -1 (Black) [124]	18.18	851
SLM, R= 0.1 (Violet) [125]	7.41	349
SLM, R= 0.1, (Orange) [126]	18.52	600
Hot rolled and annealed, R= -1 (Cyan) [58]	6.25	595
Hot rolled, R= -1 (Magenta) [127]	6.67	451
SLM, R= -1 (grey) [74]	11.49	974

The slopes of the S-N curves reviewed in the literature vary a lot, for the same material, ranging from a value of 3.05 for an SLM process [123] to 18.52 from, interestingly enough, another SLM process [126]. The slope of the curve provides a way to relate the increase in number of cycles, with the reduction is stress range. For instance, for the same variation of number of cycles, a curve with higher slope has less variation in stress range. A material with a S-N curve with low slope, such as 3, has generally many defects that act as pre-existing cracks, so crack nucleation occurs faster. Hence, the fatigue process is more about the propagation of those cracks, rather than their nucleation.

In opposition, the materials with S-N curves with higher slopes during fatigue take longer to nucleate a crack, since it has less defects. This way, crack nucleation is most likely controlled by local plasticity of the matrix and the fatigue process is more about crack initiation rather than its propagation.

The material obtained in this work has a slope of 7.14. The material produced has a slope consistent with three other materials: a material produced by SLM with a slope of 7.41, marked as violet [125], and two hot rolled materials, with slopes of 6.67 and 6.25 marked by magenta [127] and cyan [58], respectively.

In terms of critical stress range, it can be said that only two materials have a higher value of critical stress range than the produced during this work: one produced by SLM and marked as grey [74] and the other is a wrought material, marked as black [124]. Both these materials were tested with a load ratio of -1, which means they had lower mean stresses than the material produced during this work. Hence, it is possible to state that the fatigue strength presented by the manufactured material is higher than the majority of the literature data.

4.4.2 Fracture surface

Typically, fatigue cracks nucleate from the surface of the specimen [74]. Defects, such as pores, inclusions or un-melted particles are local stress raisers that promote crack initiation. As stresses in the bottom flat surface of the specimen are very similar, the largest stress raiser could be the preferred location to start a crack.

However, in the absence of major defects, cracks can still initiate due to the formation of micro-notches or micro-cracks due to slip band effects [74]. With the application of

cyclic load or strain, some materials tend to form ordered structures, which may appear as localised bands of deformation and instabilities, which are also called persistent slip bands [130]. The bands might also act as stress raisers and promote cracks. The resulting profile of the grain is irregular, showing alternating extrusions and intrusions [74].

The maximum stress, as well as number of cycles to crack initiation for each of the samples analysed in terms of fracture surface, is shown in Table 4.19.

Table 4.19: Maximum stress and number of cycles to crack initiation for the samples analysed.

	$\sigma_{max,0}$ [MPa]	N_i
Sample 3	546	2500000
Sample 6	766	2820300
Sample 9	950	200870

where $\sigma_{max,0}$ is the maximum nominal stress. The two halves of the fracture surface of sample 3 can be observed in Figure 4.50.

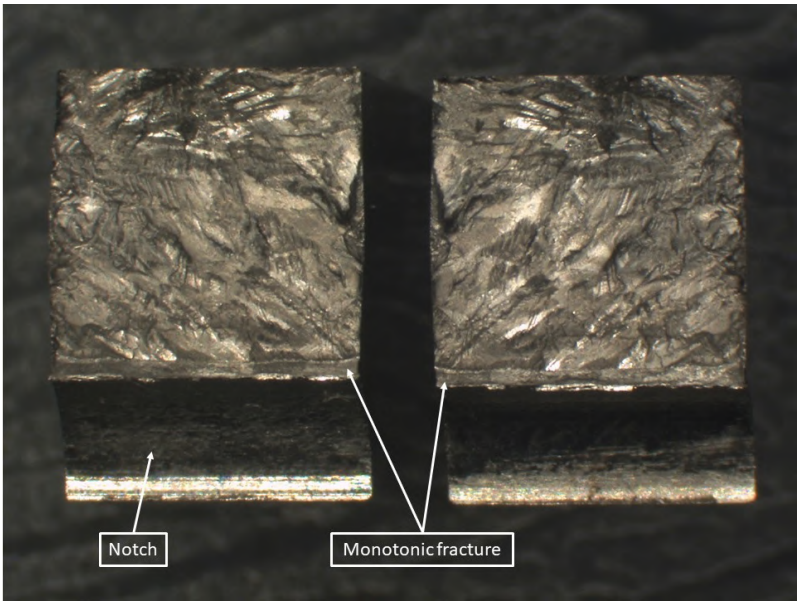

Figure 4.50: Fracture surface of sample 3 with a 7.5x amplification.

By analysis of the fracture surface of sample 3, a few different regions can be distinguished. Fracture seems to have started in the top region of the specimen, which was subjected to tensile loading, and propagated towards the notch. The flat surface near the notch is a result of manual splitting of the sample, since full fracture did not occur during testing.

The two halves are the mirror of one another. That being said, where one half has a material shortage, the other has excess material attached, the exception being when there is a pore present.

Both surfaces seem extremely irregular and the fracture did not propagate in the same plane. Although the selected lens lacks depth perception, a side view of the sample clarifies this aspect, as will be soon discussed.

No visible defects to the naked eye could be observed at the surface of the specimen, so cracks might have initiated in the material matrix, controlled by local plasticity [123]. Nevertheless, with bigger amplifications, there is a chance that observation of defects could be possible. In Figure 4.51, possible crack initiation sites are indicated with white arrows.

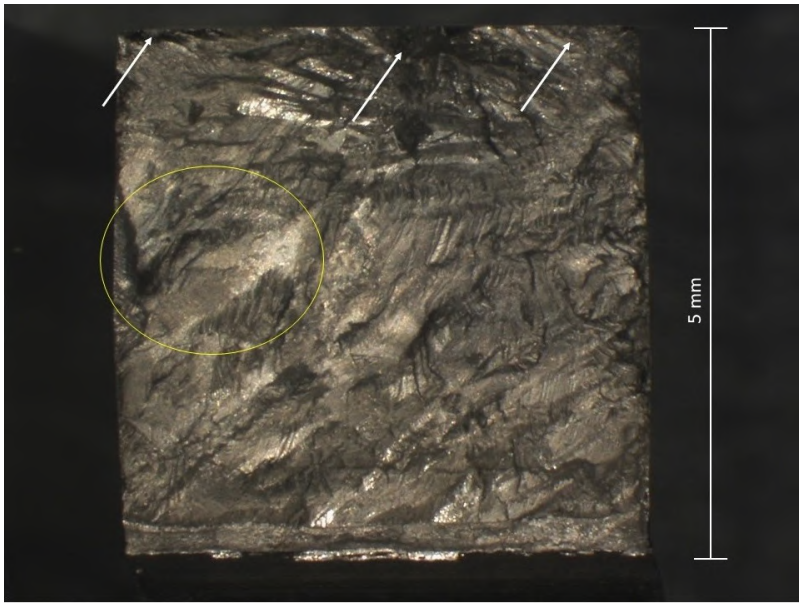

Figure 4.51: Fracture surface of sample 3 with a 12x amplification. Possible crack initiation sites marked by white arrows. Transgranular cleavage-like fracture in yellow.

Although difficult to be certain just by using an optical microscope, it appears that multiple discrete cracks initiated from the surface and, as they progress towards the notch, they coalesce into just one. The more pronounced crack looks to have formed in the centre region of the sample, leaving radial stripes along the crack propagation direction, which could probably be beachmarks.

Beachmarks, also known as clamshell marks, are progressive marks on a fatigue fracture surface that locates the position of the crack propagation front. They often radiate outward one or more origins of the crack [131, 132]. It could be hypothesised that these stripes can be observed in Figure 4.52.

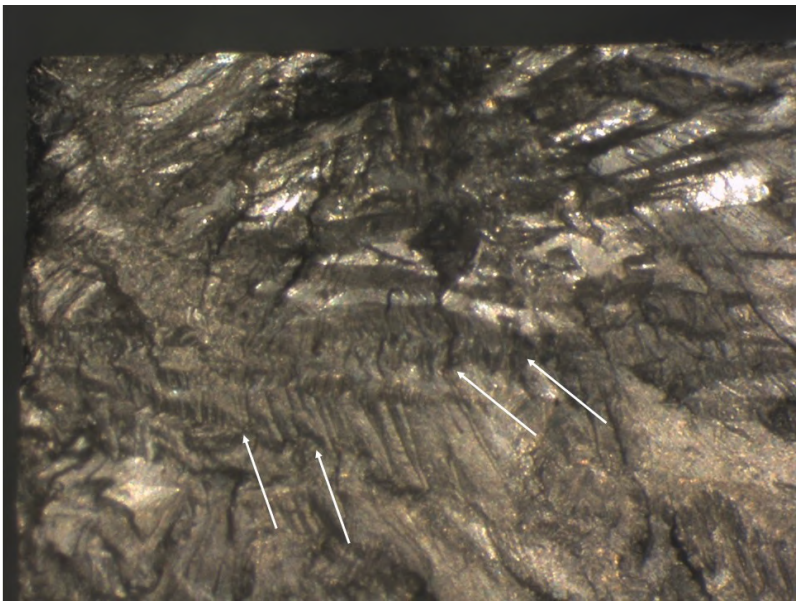

Figure 4.52: Possible fatigue beachmarks visible with a 20x amplification, marked by white arrows, in sample 3.

In the middle region of the sample a transgranular cleavage-like fracture seems to have taken place. This feature is marked in yellow, in Figure 4.51. Sample 3 failed in the high cycle fatigue region (around 2 500 000 cycles) and seems to have a wide crack initiation zone. The opposite occurs in sample 9, which failed much sooner, at 200870 cycles, due to higher stresses. The same behaviour was observed by other authors [74]. An interesting feature was found near the notch. This feature is presented in Figure 4.53 marked by red arrows.

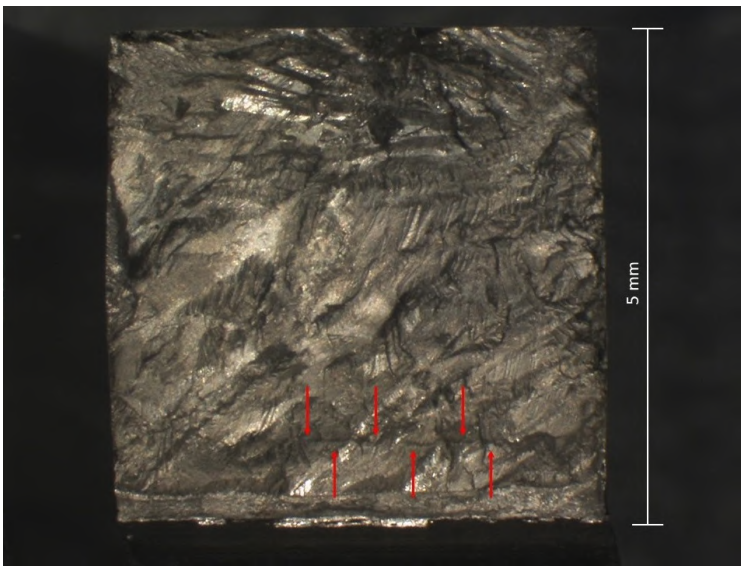

Figure 4.53: Distinctive feature visible with a 12x amplification, marked by red arrows, in sample 3.

It could not be determined what the straight horizontal line is due to. Nevertheless, it should not be overlooked. The two halves of the fracture surface of sample 6 can be

observed in Figure 4.54.

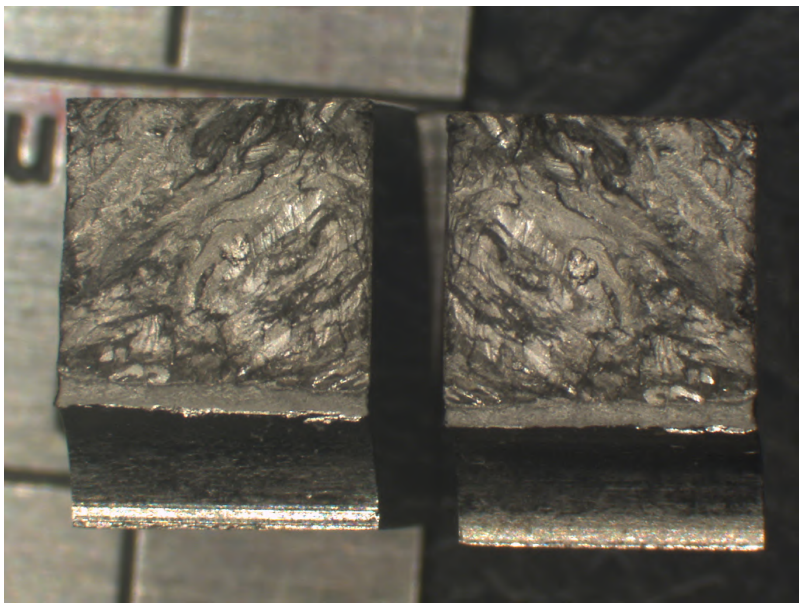

Figure 4.54: Fracture surface of sample 6 with a 7.5x amplification.

This fracture surface is very similar to the one analysed before. The cracked initiated at the top surface, where tensile stresses were felt, and propagated towards the notch. Near the notch, a small flat area is visible, signal of the monotonic fracture post fatigue testing. In Figure 4.55, possible locations of crack nucleation are identified.

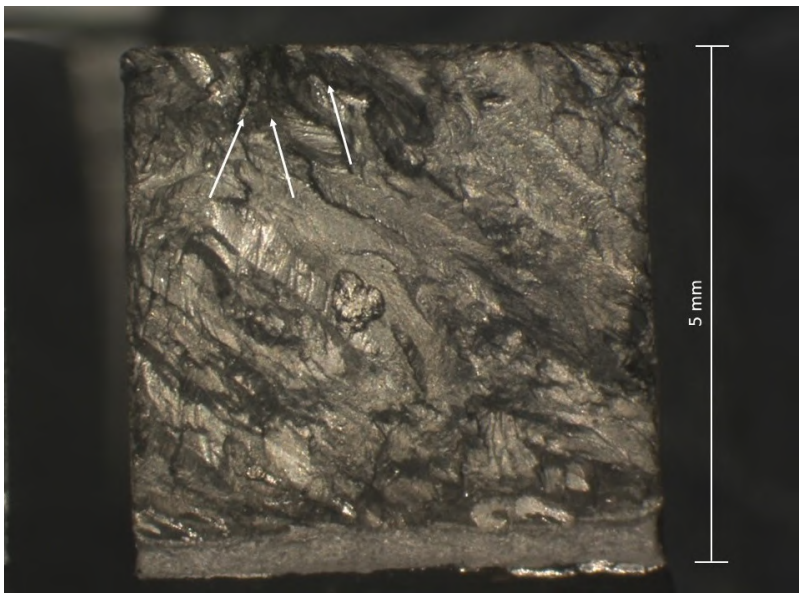

Figure 4.55: Fracture surface of sample 6 with a 12.5x amplification. Possible crack initiation spots marked by white arrows.

Once again, the crack initiation zone seems to be wide. It is hard to tell if a single crack began from a defect or if multiple ones were present and converged in the central region. In Figure 4.56, a few possible beachmarks can be noted, as well as transgranular cleavage-like fracture zone, similar as before.

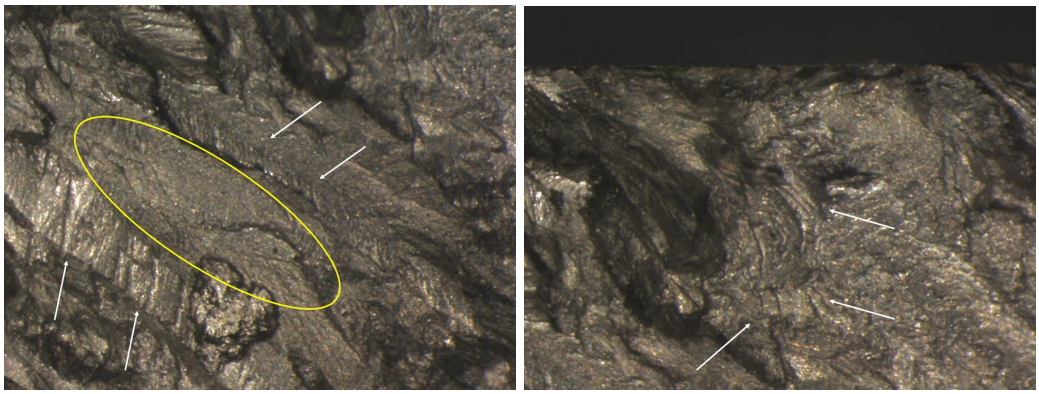

(a) 35x amplification (b) 40x amplification

Figure 4.56: Fracture surface of sample 6 with different amplifications. Possible beachmarks identified by white arrows. Cleavage-like fracture marked in yellow.

As already mentioned, the surfaces of fracture are not flat- they are very irregular, with different planes, depths, peaks and valleys. In Figure 4.57, a lateral and a top view of the fracture surfaces of sample 6 are presented.

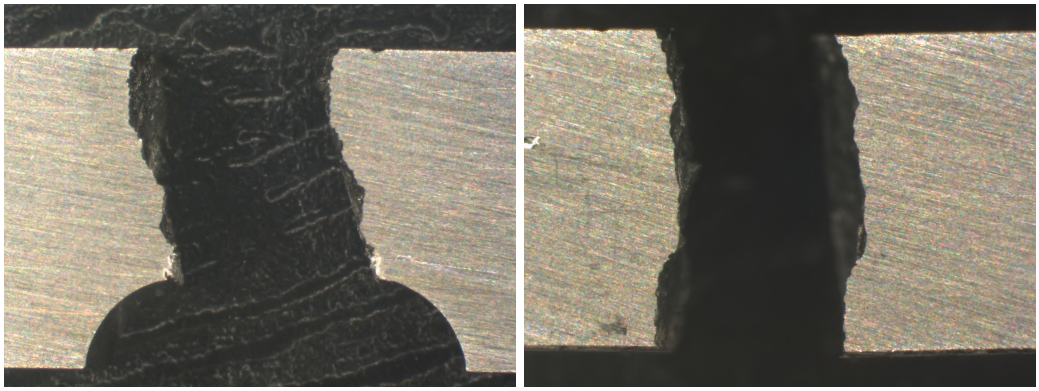

(a) Lateral view (b) Top view (opposite to the notch)

Figure 4.57: Lateral and top view of the fracture surface of sample 6 with a 20x amplification.

The crack naturally progresses taking the easiest path, which often leads it to a defect location. This way, it is natural that the fracture has an irregular shape.

Finally, the fracture surface of sample 9 can be visualised in Figure 4.58.

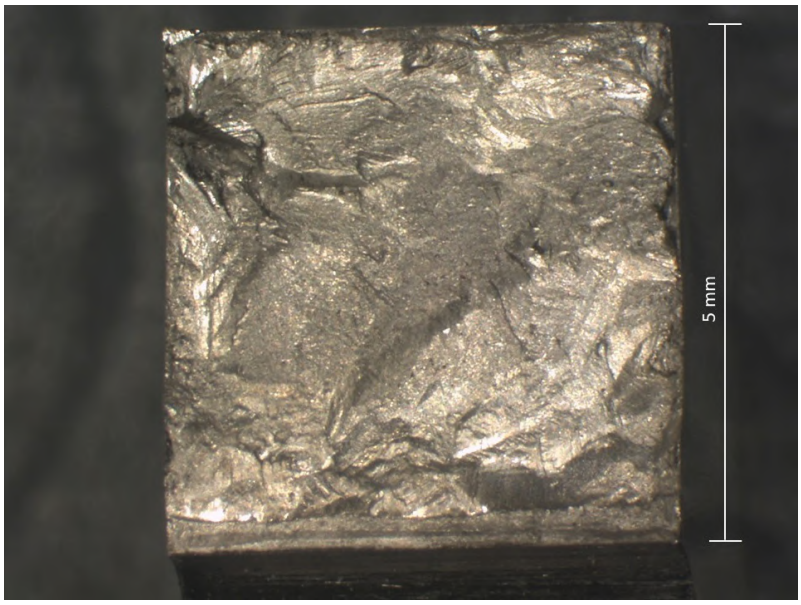

Figure 4.58: Fracture surface of sample 9 with a 10x amplification.

The fracture surface of sample 9 seems different than the other two analysed. This sample lasted a shorter number of cycles and was subjected to a higher load. This time, the crack initiation zone seems to be narrower and harder to visualise the location of crack nucleation. Nevertheless, the crack began in the top region of the specimen, where tensile stresses are felt, and progressed towards the centre. Near the notch, the flat surface indicates a manual monotonic fracture. This time, the presence of a few pores is disclosed, as it can be seen in Figure 4.59.

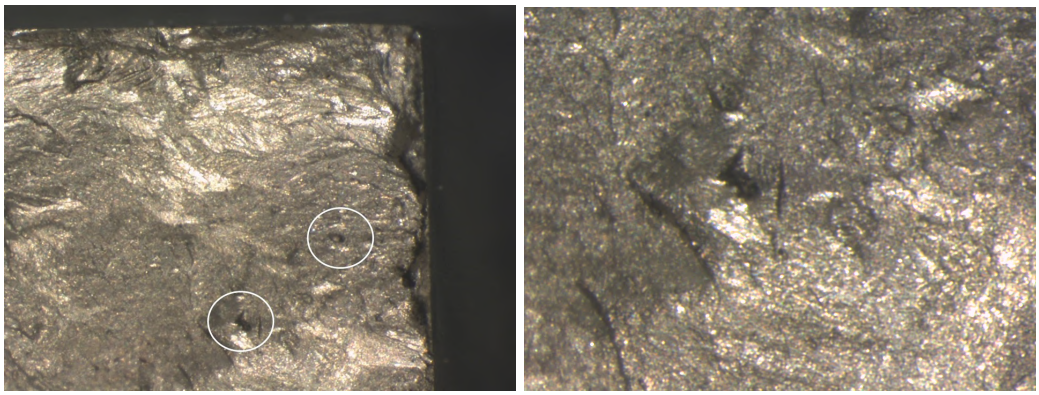

(a) 20x amplification (b) 65x amplification

Figure 4.59: A few pores were detected with different amplifications, in sample 9.

The fracture surfaces of the three analysed samples are irregular and difficult to analyse by optical microscopy. Commonly, fracture surfaces consist of three characteristic regions: stable crack growth, shear lip and fast fracture. However, these regions cannot be clearly distinguished in the analysed surfaces.

Nevertheless, it should be noted that no visible debonding between layers or major defects could be observed in the fracture surface, validating once more the parametrisation process of DED.

4.4.3 Fatigue life prediction

The values needed to build the S-N curve based on the C. Bandara model are presented in Table 4.20.

Table 4.20: Values used to build the S-N curve proposed by C. Bandara.

HB	σ_u	σ_k	N_k	N_{GCF}	i	σ_{GCF}	o	p	B
223	950	379.1	67980	10^9	-0.2	287.04	998.75	271.21	7

In Figure 4.60 and 4.61, the experimental S-N curve as well as the fatigue life prediction curves are plotted. In the first one, maximum stress is in the Y-axis, while in the second one, in the Y-axis is the stress range. Note that both models imply tests with load ratio of -1.

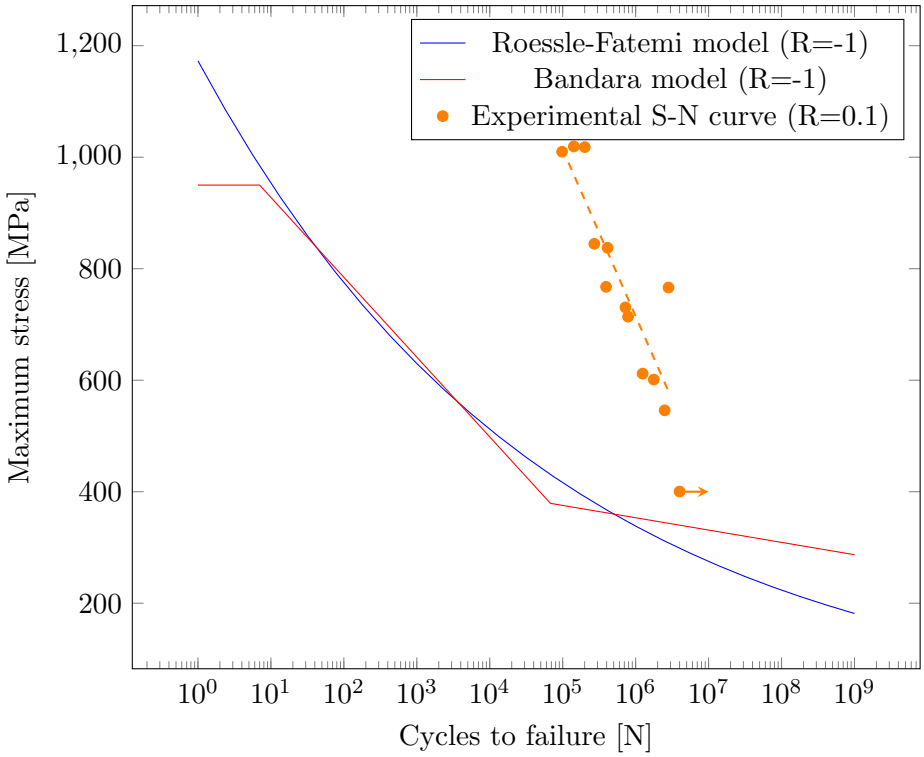

Figure 4.60: Predicted and experimental S-N curves. Maximum stress in the Y-axis.

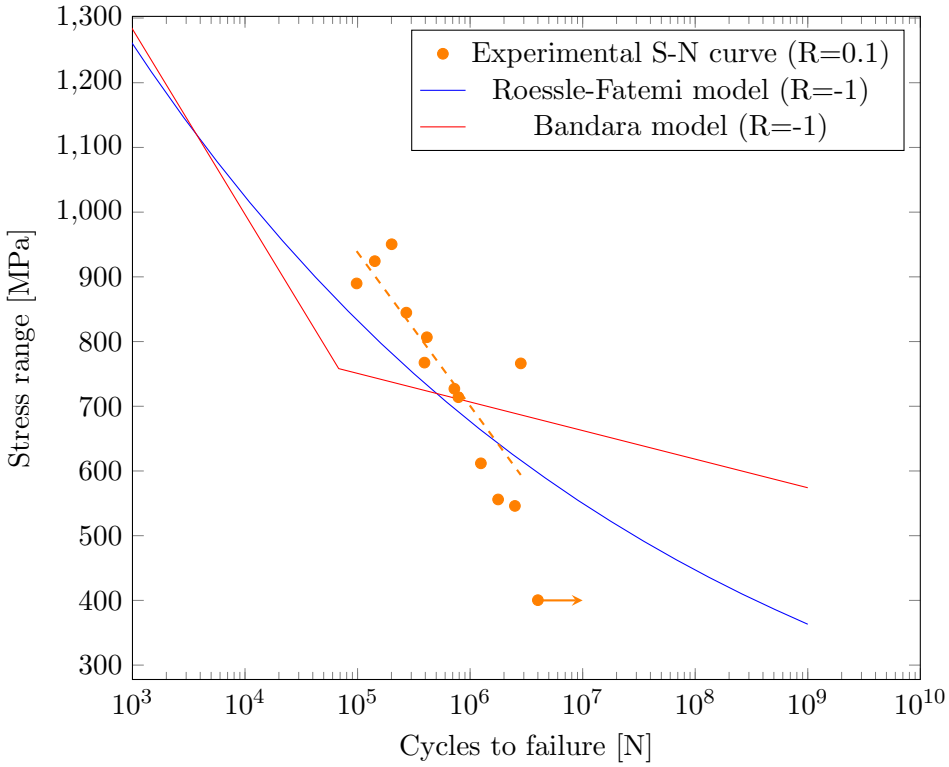

Figure 4.61: Predicted and experimental S-N curves. Stress range in the Y-axis.

Once again, comparing curves obtained by tests with different load ratios is a challenge. By observation of Figure 4.60, it can be said that neither model can predict the fatigue life of Inconel 625. The same problem arises from using the S-N curve as a function of maximum stress: it might be misleading and difficult to establish a legitimate comparison. However, plotting the curve as a function of stress range, the experimental S-N curve intersects both prediction models.

As already mentioned, the experimental stresses are the nominal ones, calculated through the reaction forces. The real stresses must be lower than the nominal ones, as they take into account the plastic behaviour of the material. Therefore, the real stresses might translate the experimental S-N curve downwards to lower stress ranges, or even changing the slope of the S-N curve, making it appear below both prediction models. Nevertheless, the Fatemi model seems to be more adequate for the manufactured material than the Bandara model. In fact, for the current preliminary S-N curve based on the measured reaction forces, the Fatemi prediction model correlates in a satisfactory fashion with the experimental results. It should be noted that these models do not take into account the natural scatter of the S-N curves.

In Figure 4.62, the experimental S-N curve is plotted, with the two scatter bands. One being the mean plus two times the standard deviation, $\hat{\sigma}$, and the other being the mean minus two times the standard deviation.

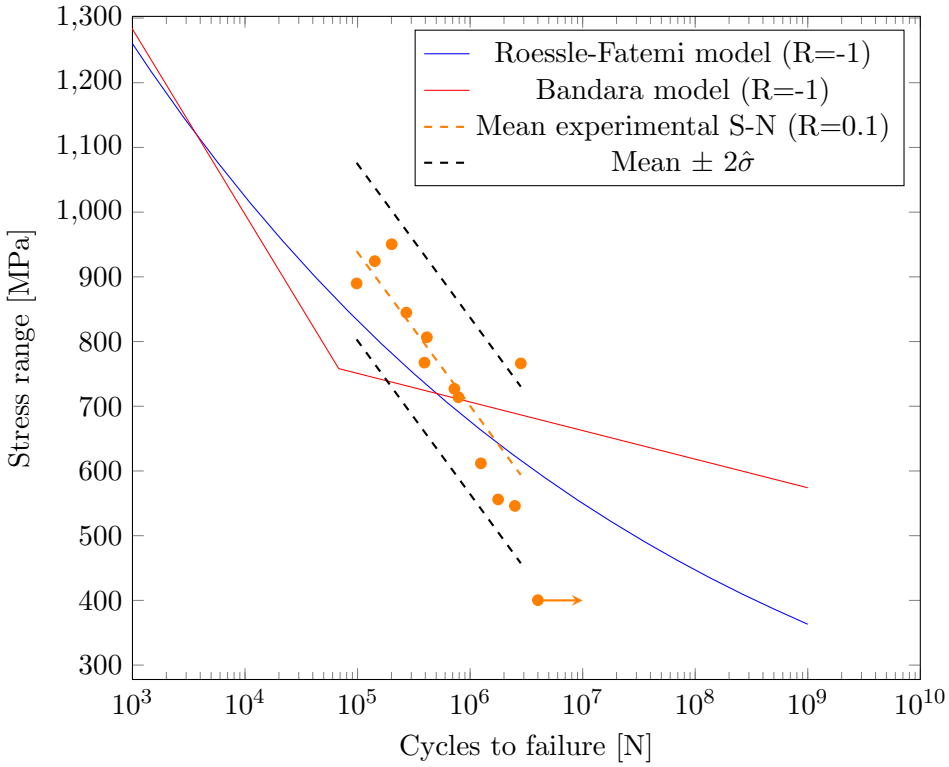

Figure 4.62: Predicted and experimental S-N curves with experimental scatter bands based on the standard deviation. Stress range in the Y-axis.

By analysing Figure 4.62, it can be said that if the scatter band is taken into account, it is possible that both models can predict the experimental data with a high degree of accuracy.

It should be noted that both proposed models plot the stress as a function of the number of cycles to failure. The S-N curve obtained experimentally is a function of number of cycles to crack nucleation. Overall, this fact would not change the values too much, as the crack propagates rapidly.

As already mentioned, both models were proposed for steels, which have a very different behaviour from Inconel 625. Similar models of estimating mechanical properties based on hardness values of steels have been proposed, showing good correlation between the two properties. For instance, Z. Lopez et. al [133] mention a relationship between Brinell hardness, HB, and ultimate tensile strength, S_{ut}:

$$S_{ut} = 0.0012HB^2 + 3.3HB \tag{4.1}$$

M. Meggiolaro et. al [134] proposed a similar relationship between Brinell hardness and ultimate tensile strength by statistical evaluation of experimental data for steels:

$$S_{ut} = 3.4HB \tag{4.2}$$

If one tried to apply these relationships to Inconel, the ultimate tensile strength obtained for a 223 HB hardness would be 750 MPa, which is around 200 MPa below the actual value for Inconel 625. Hence, it is likely that these kinds of models that work for steels, need to be tunned to superalloys.

4.4.4 Experimental and numerical calibration of the test setup

In this section, the results of the experiments performed with strain gauges are presented and discussed.

Influence of the tightening torque

Initial simulations of the numerical model of the specimen/gripping system indicated that using half of the recommended torque on the screws (5 N.m) would be a good compromise between screw induced stresses and gripping of the specimen.

After the first trials, an alarming fact could be observed. Despite starting with a load ratio higher than zero, after around 50000 cycles the ratio would tend to zero, as it can be observed in Figure 4.63.

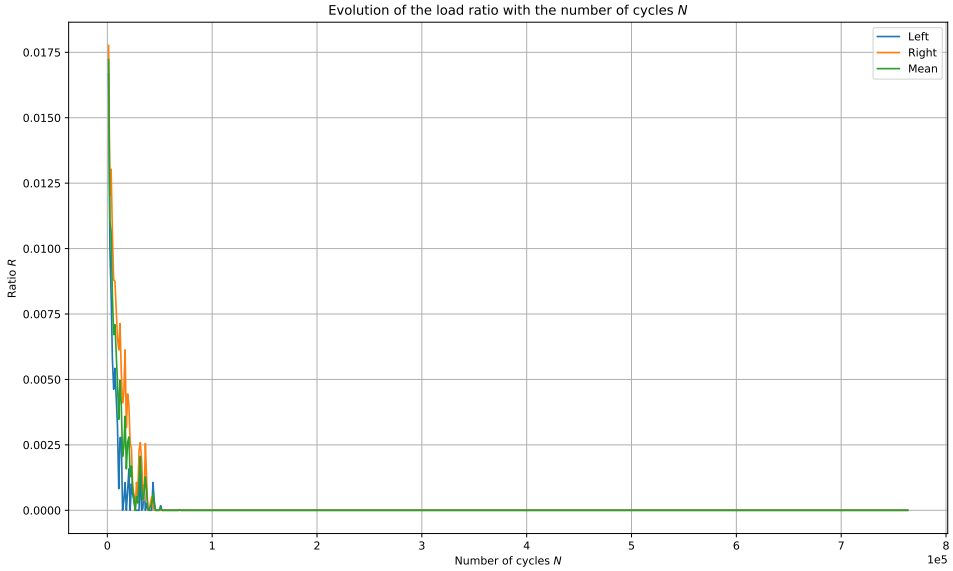

Figure 4.63: Evolution of the load ratio, R, with the number of cycles, N, with a 5 Nm pre-load.

The maximum reaction was kept approximately constant throughout the trial, but the minimum reaction would tend to zero, leading to a zero load ratio. By zooming in the first few cycles of Figure 4.63, Figure 4.64 can be created.

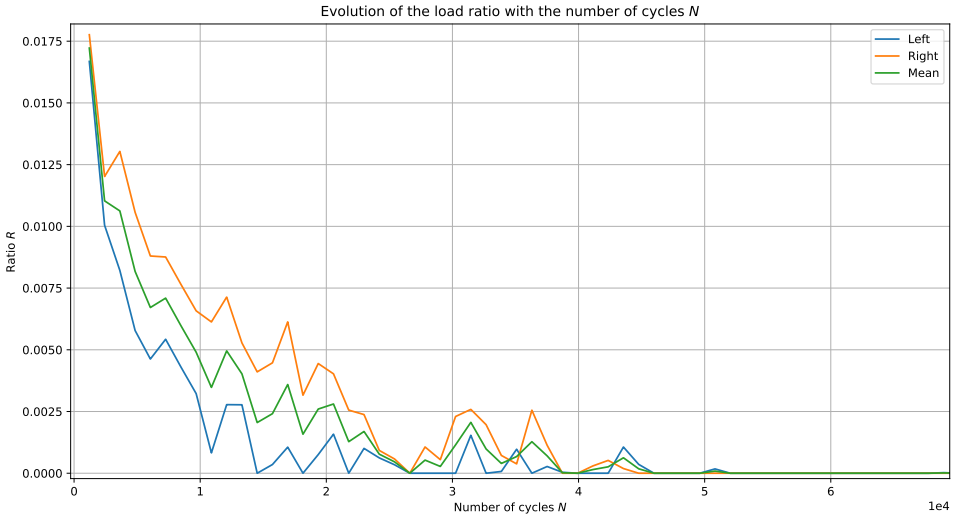

Figure 4.64: Evolution of the load ratio in the first few cycles.

This behaviour could have two possible explanations or, perhaps, a combination of two different effects:

1. The material would undergo plastic deformation in the first few cycles and would not return to its original position, leading to a reaction force of zero at the upper position of the actuator;

2. The tightening torque is not enough to ensure gripping between the specimen and the part that is above the specimen, meaning that " slippage" could occur, leading to a 0 N reaction force in the upper position of the actuator.

If plastic deformation was the reason, nothing could be done other than adjusting the movable platform under the gripping system to calibrate the reaction forces during testing. This way, it was prudent to tackle the possible " slippage" problem.

It was important to understand how the tightening torque would really affect the stress on the specimen, so strain gauges were utilised. The obtained strain was plotted as a function of time in Figure 4.65.

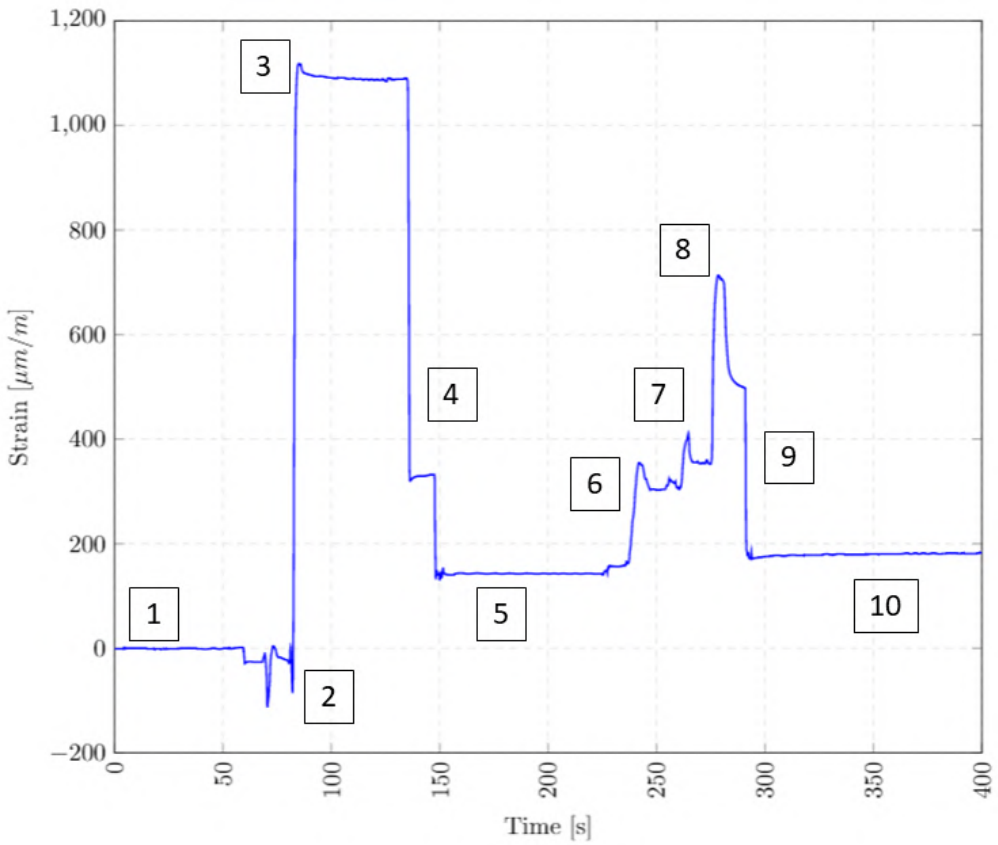

Figure 4.65: Influence of the tightening torque on the strain gauge results. Main stages are numbered from 1 to 10.

The most important stages of the experiment were numbered and are described next.

1. The gripping system was placed on the bench clamps;
2. The bench clamps were slightly tightened;
3. The first and second screw were tightened using 5 N.m torque;
4. The bench clamps were loosened;
5. At this point, the strain obtained is solely due to 5 N.m applied torque on the screws;
6. The bench clamps were slightly tightened;
7. The first screw was tightened with 10 N.m torque;
8. The second screw was tightened with 10 N.m torque;
9. The bench clamps were once again loosened;
10. At this point, the strain obtained is solely due to 10 N.m applied torque on the screws.

A few interesting occurrences can be discussed. For instance, when the bench clamps were tightened, the strain given by the gauge was negative. When the first screw with 5 N.m was tightened, no change in strain was verified, as the other side of the specimen was loose. However, when the first screw with 10 N.m was tightened, a peak in strain can be observed (stage 7), as the other side was not loose. Note that before applying 10 N.m of torque, there was no loosening of the screws.

During stage 4, two slopes can be seen which may be caused by an irregular loosening of the clamps. Another interesting aspect of the experiment was the fact that tightening with 5 N.m induced more strain in the specimen that with 10 N.m, initially (stages 3 and 10). The same cannot be said about the strain induced by the sole application of the screws (stage 5 and 10).

The strain caused by a torque of 5 N.m was 142 $\mu m/m$, while the strain caused by 10 N.m was 180 $\mu m/m$. Assuming that the deformation occurred in the elastic regime, Hooke's law can be applied. Hence, the stress caused by the application of 5 N.m and 10 N.m torque was 29 MPa and 37 MPa, respectively.

An increase by 5 N.m would provoke an increase in stress of 8 MPa, which can almost be neglected. Since a tightening torque of 10 N.m would not increase the stress levels on the specimen, it could be used for the remaining fatigue tests.

In order to verify if this change would solve the problem of the loading ratio, the gripping system was placed on the fatigue testing machine and manual reversals of the electric motor shaft were done, gradually increasing the maximum reaction force. Simultaneously, the minimum reaction would be analysed to verify if it would tend to zero. In Figure 4.66, the reaction forces were plotted as a function of time.

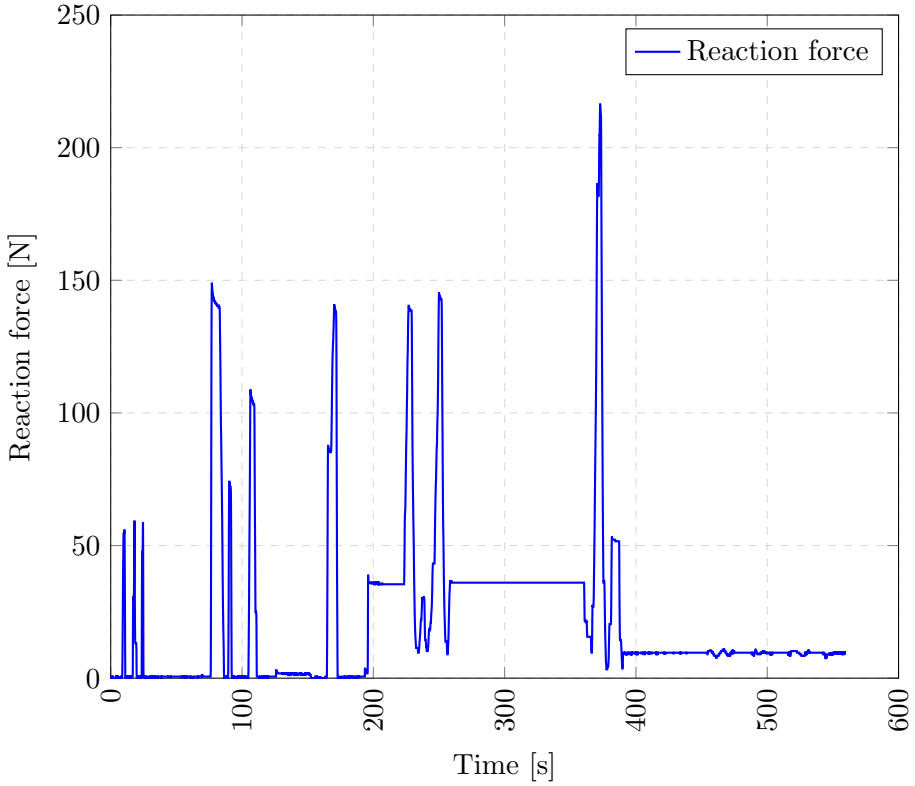

Figure 4.66: Load ratio bigger than zero when using a 10 N.m tightening torque, after 400 seconds.

As it can be observed in Figure 4.66, after a few cycle reversals, the load ratio could be kept higher than zero, at least for maximum loads of at least 220 N. Until the 200 second mark, the reaction force was zero because the actuator was not in contact with the gripping system in its lowest position, since the displacement range was too large.

Specimen 8 was the first to be tested with 10 N.m torque, which allowed to conclude that the load ratio could be kept roughly constant and higher than zero, until crack initiation. In Figure 4.67, the evolution of the load ratio with the number of cycles with a 10 N.m applied torque is shown.

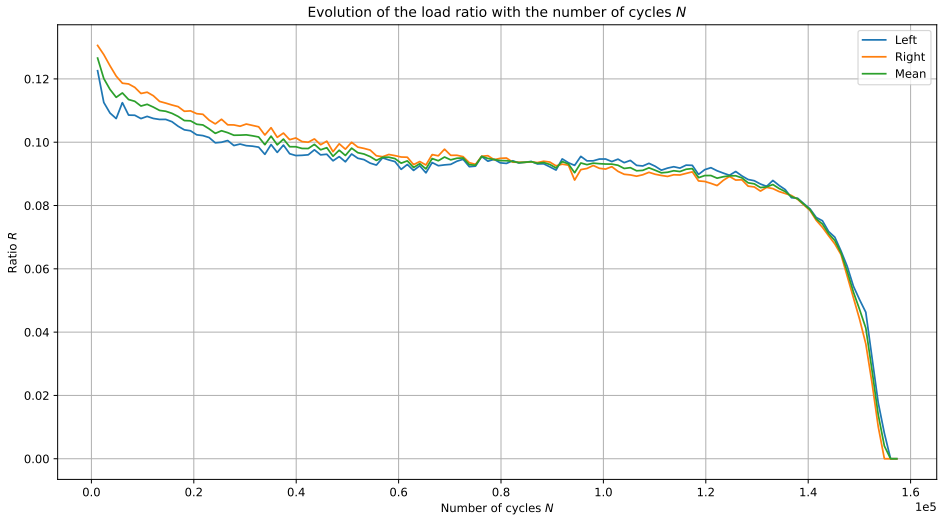

Figure 4.67: Evolution of the load ratio with the number of cycles for 10 N.m tightening torque.

After this test, every specimen was tested with such torque, which is the reason why the load ratio of the S-N obtained experimentally varies between 0 and 0.1. It should be said that this difference is not alarming, since the variations of load are very little.

Finally, the experiment allowed to confirm the suspicion that the numerical model was overestimating the effect of torque in the stress of the specimen, since no visible plastic deformation had occurred after application of the torque.

Relation between deformation and reaction force

The signals received by the Catman software, either reaction forces measured by the load cells, or the strain measured by the strain gauge, were plotted as a function of time. The result is presented in Figure 4.68.

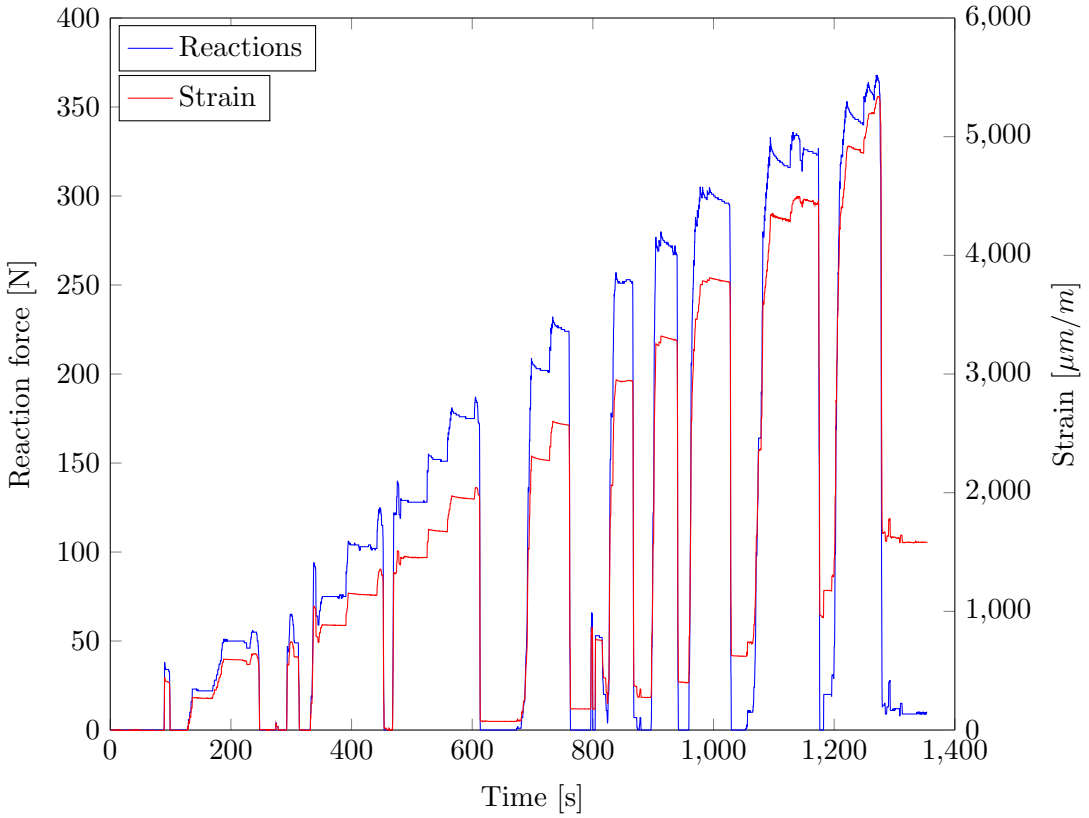

Figure 4.68: Evolution of strain with different reaction forces over time.

The strain gauge was able to measure strains up to 5300 $\mu m/m$ or, in terms of reaction forces up to around 350 N. As already mentioned, after some increments of load, the load would be removed and the strain measured was observed. By observation of Figure 4.68, it can be seen that at 613 seconds, with zero load application, the strain was no longer zero- the gauge had a permanent strain, which means that somewhere between 462 and 613 seconds, the material had plastified.

However, that does not mean that the specimen plastified where the strain gauge was placed. Due to the notch that is present in the specimen, there is a stress concentration factor, K_t, that raises the stress in that area of the specimen, meaning that the notch is the region that plastifies first. That being said, the strain measured in the flat bottom part of the specimen (where the strain gauge was placed) must be lower than the strain felt on the notched area.

To find the approximate stress value at which the notch entered the plastic regime, the stress concentration factor must be utilised. Recurring to the numerical model, the stress values of the notched area was divided by the stress of the bottom flat surface at the symmetry plane, for different actuator displacements, originating a K_t of around 1.7. In Figure 4.69, the evolution of the K_t with the displacement is presented.

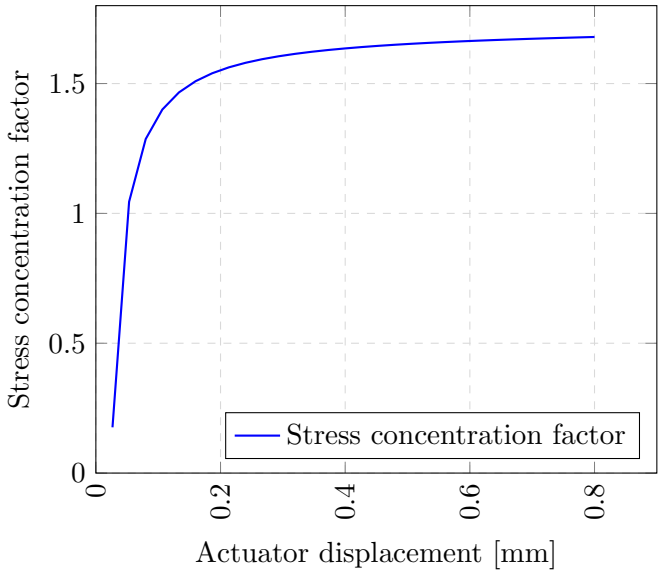

Figure 4.69: Evolution of K_t with the displacement of the actuator.

As it can be observed in Figure 4.69, after 0.3 mm of displacement, the stress concentration factor tends to be around 1.7. The stress in the notch, σ_{notch}, is equal to $K_t\sigma_0$, being σ_0 the nominal stress obtained by the strain gauge strain's measurement.

Between 462 and 613 seconds, different loads were measured. In Table 4.21 some loads with corresponding strain values between 415 and 718 seconds are presented. The nominal stress is calculated using Hooke's law and the stress in the notch by applying the stress concentration factor.

Table 4.21: Reaction forces and corresponding strains as a function of time.

Time [s]	Reaction [N]	Strain [$\mu m/m$]	σ_0 [MPa]	σ_{notch} [MPa]
415	100	1142	236	401
500	128	1455	301	512
540	150	1680	348	592
590	172	1952	404	687
718	198	2277	471	801

It was previously mentioned that the specimen plastified between 462 and 613 seconds, which means between the application of 127.5 and 183 N (the maximum reaction force registered within that period of time), or 512 and 717 MPa. With that being said, the Yield strength of the material should range between those two values. In the current case, this was not verified, as the yield strength measured by the tensile tests was slightly lower, around 496 MPa.

Above this stress, it is no longer accurate to calculate the stress from strain using Hooke's law. Note that the Young modulus used for this analysis was 207 GPa, as found in literature. However, as seen from the tensile tests, this is not the case for the current material.

Almost every fatigue test performed during this work had reaction forces higher than

200 N, which leads to believe that they were all performed in the plastic regime of the material.

Taking the raw data presented in Figure 4.68, a plot of strain vs. reaction force can be made. The result is featured in Figure 4.70.

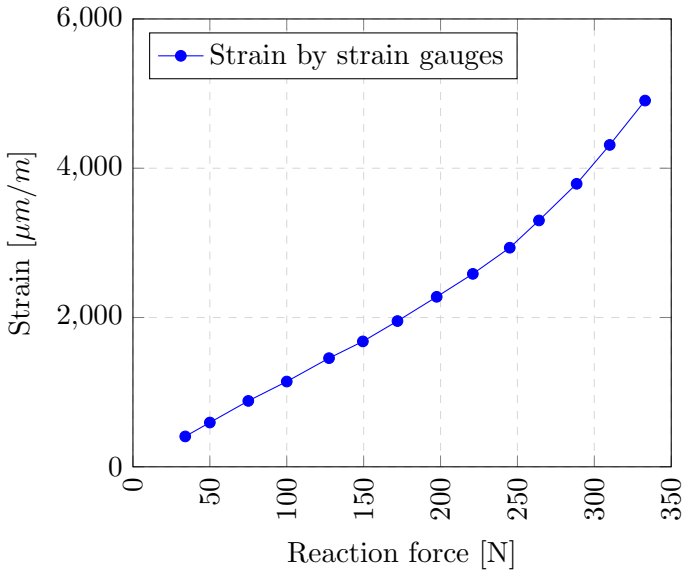

Figure 4.70: Strain as a function of reaction force.

The same plot can be created, but instead of strain, using nominal stress in the Y-axis, as shown in Figure 4.71, by applying Hooke's law. The Young modulus used is 207 GPa.

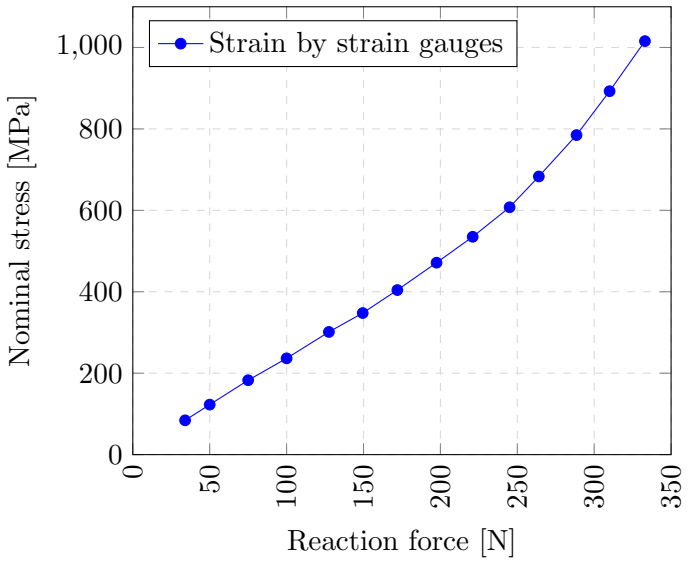

Figure 4.71: Nominal stress as a function of reaction force.

It can be observed that the plot has a constant slope up until around 200 N, at which point the material starts to plastically deform. After the constant slope, the curve gains a steeper slope, as expected. In the plastic regime, a variation in stress or reaction originates a larger variation of strain.

The experimental setup can be validated analytically. The nominal stress, σ_0, can be

obtained by Equation 3.4 as a function of the reaction force. Then, applying Hooke's law with a Young modulus of 207 GPa, the strain can be calculated. A plot can be made with the reactions and the corresponding analytically calculated strains and compared to the strains given by the strain gauge (experimental strains). The resulting plot is presented in Figure 4.72.

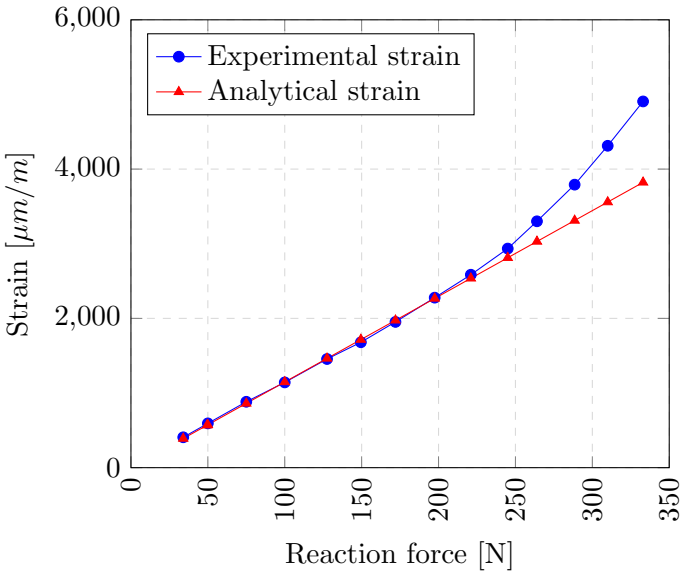

Figure 4.72: Analytical and measured strain as a function of reaction force.

Likewise, the same plot can be built featuring stress as a function of reaction force, as shown in Figure 4.73.

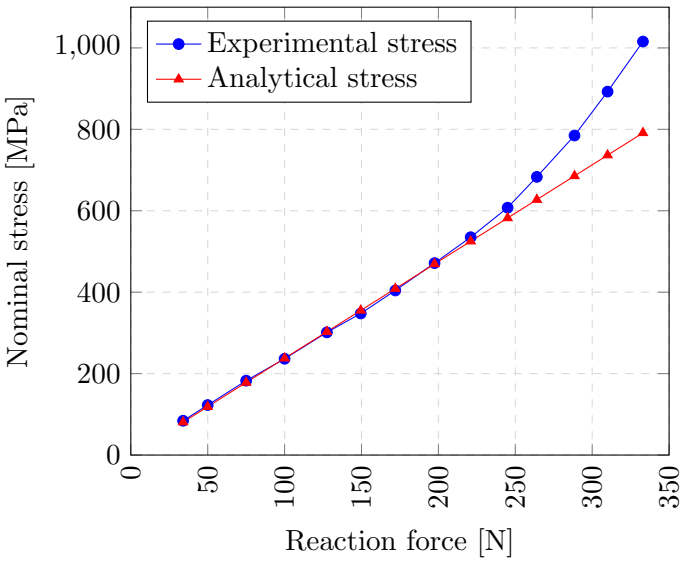

Figure 4.73: Analytical and measured nominal stress as a function of reaction force.

As it can be observed in Figure 4.72, in the elastic regime, the strain measured by the gauges and the analytically calculated strains are very similar, validating the experimental setup for such regime. In the plastic region, the strains get slightly different, as the analytical strains are calculated using Hooke's law, which is only applicable in the elastic

regime.

The experimental and analytical values of reaction force and strain are presented in Table 4.22, as well as the relative error between the values.

Table 4.22: Experimental and analytical strain as a function of reaction forces.

Reaction Force [N]	Experimental strain [$\mu m/m$]	Analytical strain [$\mu m/m$]	|Relative error| [%]
34	406.95	390.26	4.10
50	593.21	573.91	3.25
75	882.76	860.87	2.48
100	1142.29	1147.83	0.48
128	1455.67	1463.48	0.54
150	1669.89	1716.00	2.15
172	1952.66	1974.26	1.11
198	2277.52	2266.96	0.46
221	2584.72	2536.70	1.86
245	2935.17	2812.17	4.19
264	3300.63	3030.26	8.19
288.5	3791.45	3311.48	12.66
310	4312.28	3558.26	17.49
333	4906.37	3822.26	22.10

As expected, the relative error becomes larger as the strain transits from the elastic regime to the plastic one. During the elastic regime, the maximum error is around 4%, a very acceptable value.

The experimental and analytical strains can also be compared to the ones obtained by the numerical model. For that, a new simulation with other conditions was performed. The pre-load considered in the FEM model was 10602N (or 10 N.m of torque) and, instead of the actuator displacement proposed in Chapter 3.5.2, one that increased from 0 mm to 0.8 mm was considered.

The reaction forces were recorded at each increment step. The partition of the specimen made in the numerical model to replicate the strain gauge grid was utilised, and an average of the stresses (σ_{xx}) in the nodes within that grid was made, in each increment step, and the strain was calculated using Hooke's law, since only the linear-elastic behaviour of the material was considered in the model.

As a result, a relationship between reaction force and strain was achieved. The results can be plotted and compared to the ones obtained experimentally and analytically, as seen in Figure 4.74.

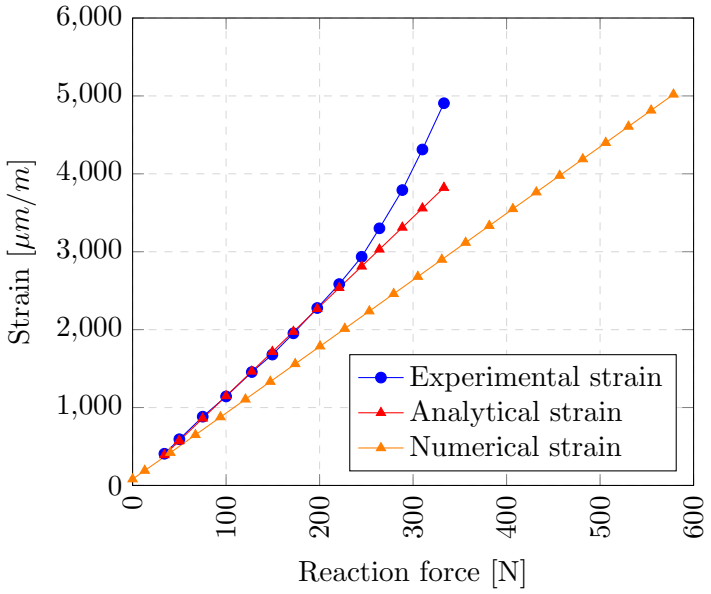

Figure 4.74: Experimental, analytical and numerical strain as a function of reaction force.

Once again, the same plot can be created but in terms of nominal stresses, as shown in Figure 4.75.

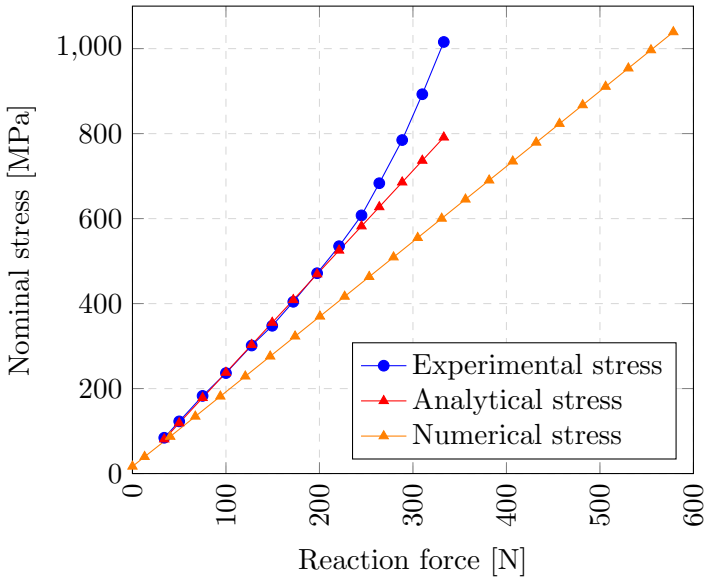

Figure 4.75: Experimental, analytical and numerical nominal stress as a function of reaction force.

A linear trendline was applied to the numerical data to obtain the strain as a function of reaction force. This way, they could be directly comparable to the strains obtained by the strain gauges. The experimental and numerical values of reaction force and strain are presented in Table 4.23, as well as the relative error between the values.

Table 4.23: Experimental and numerical strain as a function of reaction forces.

Reaction Force [N]	Experimental strain strain [$\mu m/m$]	Numerical strain [$\mu m/m$]	|Relative error| [%]
34	406.95	368.15	9.53
50	593.21	511.91	13.70
75	882.76	736.56	16.56
100	1142.29	961.19	15.85
127.5	1455.67	1208.29	16.99
149.5	1669.89	1405.97	16.63
172	1952.66	1608.15	17.64
197.5	2277.52	1837.28	19.33
221	2584.72	2048.44	20.75
245	2935.17	2264.44	22.86
264	3300.63	2434.82	26.23
288.5	3791.45	2654.96	29.97
310	4312.28	2848.15	22.95
333	4906.37	3054.8	37.74

The relative error within the linear-elastic region seems to vary between 10% and 20%. For each reaction, the strain obtained numerically is smaller than the strain measured by the strain gauges. This difference may have to do with the simplifications made in the model, which means that the numerical model might be more flexible than the experimental setup. It can be said that the model can still be upgraded and improved by adjusting a few parameters, such as the friction coefficient between parts, the pre-load application since in the experimental setup some pre-load might be lost during testing (by loosening of the screws) and even the gripping system material properties. Moreover, the plastic behaviour of Inconel 625 should be modelled.

Chapter 5

Conclusions and Future Work

5.1 Conclusions

The main goal of the present work was to characterise the fatigue behaviour of Inconel 615 produced by Directed Energy Deposition. The goal was successfully achieved and the fatigue life results were quite satisfactory. The experimental setup was accurately validated through strain gauge application, while the numerical model could be validated with some degree of precision for the current experimental setup, in the elastic regime. Being directly in contact with the complete cycle of testing, from production process optimisation, to the specimen production and testing allowed the author to capture the bigger picture and acknowledge the adversities of such cycle. The main conclusions of this work are:

- Although the DED process can be used to produce fully functional parts, it requires extensive testing to optimise the process parameters that lead to an almost defect free part with good mechanical properties. Despite having a high build rate, post-processing such as machining is always required;
- The designed gripping system allowed the four point bending tests to be carried out properly. However, the machine used to fatigue testing was not adequate to perform tests with such a small variation of displacement. Since it had to be adjusted manually, it was hard to accurately measure the displacement range used;
- The experimental setup was validated in the elastic regime through use of strain gauges, as the strain measured by them was very similar to the analytical strains calculated based on the reaction forces acquired by the load cells;
- A tightening torque of 5 N.m was insufficient to maintain a load ratio higher than zero;
- Although convergence was obtained in the numerical model, the strains obtained are underestimating the ones of the experimental setup. The average error between strains in the linear-elastic regime was found to be around 15%;
- The chemical composition of the specimen produced was within the ranges provided by the supplier, with the exception of Ni, meaning that some alloying elements might have been lost during the process production;
- The specimen produced presented a relative density of 99.8 % due to the presence of lack-of-fusion and trapped gas pores. These values are in line with the reviewed literature and should not degrade the fatigue life of the material;

- The specimen presented hardness values of around 232 HV, with variations in height. A hardness of 412 HV was obtained in the heat affected zone of the interface, indicating a good bonding between the deposited material and the substrate;
- The surface roughness of the samples was around 0.1 μm, meaning that the surface condition should not negatively affect the fatigue performance of the material;
- The microstructural analysis revealed some minor and very sparse defects, specially near the interface between melt pools. The microstructure found was a mixture of columnar dendrites and cell-like equiaxed structures that progressed through different tracks and layers, indicating good bonding between them. The microstructure presented variations with height and cutting plane;
- The fracture surface analysis allowed to visualise that cracks nucleated in the surface that was subjected to tensile stresses and progressed towards the notch due to the stress concentration factor associated with it. The surface revealed to be very irregular;
- The tensile tests with digital image correlation allowed to define the elastoplastic behaviour of Inconel 625;
- Fatigue testing results showed a good correlation coefficient;
- The preliminary fatigue strength of the tested specimens revealed to be higher than the majority of the literature data, which demonstrates the reliability of the DED process production and even its parametrisation;
- The obtained results correlate satisfactorily with the predictive model proposed by Roessle-Fatemi despite the different underlined stress ratios, when stress range is used as the main fatigue damage parameter.

5.2 Future work

With the intent of continuing to develop the work carried out in this thesis, some suggestions are provided:

- Improving the FEM model, calibrating the contacts between parts, the coupling between the bolts and the gripping system, and modelling the plastic behaviour of Inconel 625 with the data from the tensile tests and DIC;
- Performing fatigue tests with smaller loads to verify whether fatigue limit of Inconel 625 exists for a higher number of cycles;
- Producing other sets of miniature specimen with different build orientations and studying its influence on fatigue behaviour;
- Performing other fatigue tests in conventional specimens to further characterise fatigue and crack growth behaviour, such as axial fatigue, compact tension or even gigacycle fatigue;
- Analysing fracture surfaces with SEM to understand crack nucleation spots and to identify possible causes of failure;
- Carrying out microhardness measurements of particular phases of the microstructure;

- Investigating grain size and identifying carbides or intermetallic phases that were generated during the AM process;
- Trying to relate grain size with the strain measured in the tensile tests by DIC;
- Performing a heat treatment to minimise potential residual stresses and analysing its influence on fatigue behaviour;
- Executing fatigue tests at high temperatures and under corrosive environments to replicate the in-service conditions to which most Inconel parts are subjected to;
- Performing fatigue tests in wrought specimens and compare them with the AM produced ones.

References

[1] Special Metals. Inconel 625. URL https://www.specialmetals.com/. [Accessed February 23rd, 2021].

[2] S. Kumar. *Additive Manufacturing Processes*. Springer, 2020.

[3] Isaac Alves Ferreira. *Fibre-Reinforced Thermoplastic Composite Parts Produced by Additive Manufacturing: A Comprehensive Characterization Study*. PhD thesis, Faculdade de Engenharia da Universidade do Porto, 2020.

[4] A. Manshadi, M. J. Bermingham, M. S. Dargusch, D. H. John, and M. Qian. Metal injection moulding of titanium and titanium alloys: Challenges and recent development. *Powder Technology*, 319:289–301, 2017. doi: https://doi.org/10.1016/j.powtec.2017.06.053.

[5] P. Panjan, M. Čekada, R. Kirn, and M. Soković. Improvement of die-casting tools with duplex treatment. *Surface and Coatings Technology*, 180(1), 2004. doi: https://doi.org/10.1016/j.surfcoat.2003.10.119.

[6] K. S. Prakash, T. Nancharaih, and V. V. S. Rao. Additive manufacturing techniques in manufacturing -an overview. *Materials Today: Proceedings*, 5:3873–3882, 2018. doi: https://doi.org/10.1016/j.matpr.2017.11.642.

[7] L. D. Bourell, W. Frazier, H. Kuhn, and M. Seifi. *ASM Handbook, Volume 24 - Additive Manufacturing Processes*. ASM International, 2020. ISBN 978-1-62708-288-4. URL https://app.knovel.com/hotlink/toc/id:kpASMHVA23/asm-handbook-volume-24/asm-handbook-volume-24.

[8] G. H. Loh, E. Pei, D. Harrison, and M. D. Monzón. An overview of functionally graded additive manufacturing. *Additive Manufacturing*, 23:34–44, 2018. doi: https://doi.org/10.1016/j.addma.2018.06.023.

[9] J. Liu, A. T. Gaynor, S. Chen, Z. Kang, K. Suresh, A. Takezawa, L. Li, J. Kato, J. Tang, C. C. L. Wang, L. Cheng, X. Liang, and A. C. To. Current and future trends in topology optimization for additive manufacturing. *Structural and Multidisciplinary Optimization*, 57:2457–2483, 2018. doi: https://doi.org/10.1007/s00158-018-1994-3.

[10] S. M. Thompson, L. Bianc, N. Shamsaeia, and A. Yadollahia. An overview of direct laser deposition for additive manufacturing; part i: Transport phenomena, modeling and diagnostics. *Additive Manufacturing*, 8:36–62, 2015. doi: https://doi.org/10.1016/j.addma.2015.07.001.

[11] F. Chen, G. Mac, and N. Gupta. Security features embedded in computer aided design (cad) solid models for additive manufacturing. *Materials Design*, 128(15): 182–194, 2017. doi: https://doi.org/10.1016/j.matdes.2017.04.078.

[12] ISO/ASTM 52900:2015. Additive manufacturing – general principles – terminology. Standard, ASTM, 2015.

[13] J. Gutierrez, F. Arbeiter, T. Schlauf, C. Kukla, and C. Holzer. Tensile properties of sintered 17-4ph stainless steel fabricated by material extrusion additive manufacturing. *Materials Letters*, 248:165–168, 2019. doi: https://doi.org/10.1016/j.matlet.2019.04.024.

[14] M. Doyle, K. Agarwal, W. Sealy, and K. Schull. Effect of layer thickness and orientation on mechanical behavior of binder jet stainless steel 420 + bronze parts. *Procedia Manufacturing*, 1:251–262, 2015. doi: https://doi.org/10.1016/j.promfg.2015.09.016.

[15] AMFG. All you need to know about metal binder jetting. URL `https://amfg.ai/2019/07/03/metal-binder-jetting-all-you-need-to-know/`. [Accessed March 8th, 2021].

[16] F. P. Bowden and G. W. Rowe. The adhesion of clean metals. *Proceedings of the Royal Society A*, 233:429–442, 1956. doi: 10.1098/rspa.1956.0001.

[17] J. J. Lewandowski and M. Seifi. Metal additive manufacturing: A review of mechanical properties. *Annual Review of Materials Research*, 46(1):151–186, 2016. doi: 10.1146/annurev-matsci-070115-032024.

[18] W. E. Frazier. Metal additive manufacturing: A review. *Journal of Materials Engineering and Performance*, 23:1917–1928, 2014. doi: 10.1007/s11665-014-0958-z.

[19] J. L. A. Prata. Fatigue behaviour of miniature specimens produced by additive manufacturing. Master's thesis, Faculty of Engineering of the University of Porto, 2019.

[20] I. Corral, A. Otero, and F. Artés. Development of am technologies for metals in the sector of medical implants. *Metals*, 10, 2020. doi: 10.3390/met10050686.

[21] Y. Y. Woo, S. Han, I. Oh, Y. Moon, and W. Ha. Control of directed energy deposition process to obtain equal-height rectangular corner. *International Journal of Precision Engineering and Manufacturing*, 20:2129–2139, 2019. doi: https://doi.org/10.1007/s12541-019-00226-6.

[22] A. Dass and A. Moridi. State of the art in directed energy deposition: From additive manufacturing to materials design. *Coatings*, 9(418), 2019. doi: 10.3390/coatings9070418.

[23] M. J. Kim and C. Saldana. Thin wall deposition of in625 using directed energy deposition. *Journal of Manufacturing Processes*, 56:1366–1373, 2020. doi: https://doi.org/10.1016/j.jmapro.2020.04.032.

[24] Adira. Adira ac addcreator. URL `https://adira.pt/product/additive-manufacturing-2/`. [Accessed March 20th, 2021].

[25] P. Lin, F. Shen, K. Wu, S. Hwang, and H. Lee. Process optimization for directed energy deposition of ss316l components. *The International Journal of Advanced Manufacturing Technology*, 111:1387–1400, 2020. doi: https://doi.org/10.1007/s00170-020-06113-z.

[26] H. Lee. Effects of the cladding parameters on the deposition efficiency in pulsed nd:yag laser cladding. *Journal of Materials Processing Technology*, 202:321–327, 2008. doi: https://doi.org/10.1016/j.jmatprotec.2007.09.024.

[27] E. Toyserkani, A. Khajepour, and S. Corbin. *Laser Cladding*. CRC PRESS, 2005. ISBN 9780849321726.

[28] D. Bergstrom, J. Powell, and A. F. H. Kaplan. Formation and evolution of persistent slip bands in metals. *Applied Surface Science*, 253:5017–5028, 2007. doi: 10.1016/j.apsusc.2006.11.018.

[29] M. Pantawane, S. Joshi, and N. Dahotre. *Laser Beam Machining of Aluminum and Aluminum Alloys*, pages 519–541. ASM International, 2018. doi: 10.31399/asm.hb.v02a.9781627082075.

[30] J. Choia and Y. Chang. Characteristics of laser aided direct metal/material deposition process for tool steel. *International Journal of Machine Tools Manufacture*, 45:597–607, 2005. doi: doi:10.1016/j.ijmachtools.2004.08.014.

[31] S. Mondal, C. P. Paul, L. M. Kukreja, A. Bandyopadhyay, and P. K. Pal. Application of taguchi-based gray relational analysis for evaluating the optimal laser cladding parameters for aisi1040 steel plane surface. *The International Journal of Advanced Manufacturing Technology*, 66:91–96, 2013. doi: 10.1007/s00170-012-4308-8.

[32] C. Kledwig, H. Perfahl, M. Reisacher, F. Brückner, J. Bliedtner, and C. Leyens. Analysis of melt pool characteristics and process parameters using a coaxial monitoring system during directed energy deposition in additive manufacturing. *Materials*, 12(2), 2019. doi: 10.3390/ma12020308.

[33] Y. Li and J. Ma. Study on overlapping in the laser cladding process. *Surface and Coatings Technology*, 90:1–5, 1997. doi: https://doi.org/10.1016/S0257-8972(96)03022-8.

[34] K. Shah, A. J. Pinkerton, A. Salman, and L. Li. Effects of melt pool variables and process parameters in laser direct metal deposition of aerospace alloys. *Materials and Manufacturing Processes*, 25:1372–1380, 2010. doi: 10.1080/10426914.2010.480999.

[35] D. J. Corbin, A. R. Nassar, E. W. Reutzel, A. M. Beese, and N. A. Kistler. Effect of directed energy deposition processing parameters on laser deposited inconel® 718: External morphology. *Journal of Laser Applications*, 29(2), 2017. doi: 10.2351/1.4977476.

[36] P. A. Kobryn, E. H. Moore, and S. L. Semiatin. The effect of laser power and traverse speed on microstructure, porosity, and build height in laser-deposited ti-6al-4v. *Scripta Materialia*, 43(4):299–305, 2000. doi: 10.1016/S1359-6462(00)00408-5.

[37] J. P. Davim, C. Oliveira, and A. Cardoso. Predicting the geometric form of clad in laser cladding by powder using multiple regression analysis (mra). *Materials and Design*, 29:554–557, 2008. doi: doi:10.1016/j.matdes.2007.01.023.

[38] K. Zhanga, W. Liu, and X. Shang. Research on the processing experiments of laser metal deposition shaping. *Optics Laser Technology*, 39:549–557, 2005. doi: doi:10.1016/j.optlastec.2005.10.009.

[39] K. C. Mills, B. J. Keene, R. F. Brooks, and A. Shirali. Marangoni effects in welding. *Philosophical Transactions of the Royal Society A*, 356:911–925, 1998. doi: https://doi.org/10.1098/rsta.1998.0196.

[40] P. K. Samal and J. W. Newkirk. *ASM Handbook, Volume 7 - Powder Metallurgy (2015)*. ASM International, 2015. ISBN 978-1-62708-087-3. URL `https://app.knovel.com/hotlink/khtml/id:kt010RTYX1/asm-handbook-volume-7/ferrous-nonferrous-powders`.

[41] Cambridge Dictionary. Atomize. URL `https://dictionary.cambridge.org/dictionary/english/atomize`. [Accessed March 20th, 2021].

[42] A. Popovich and V. Sufiiarov. Metal powder additive manufacturing. 2016. doi: 10.5772/63337.

[43] L. C. Ardila, F. Garciandia, J. B. González-Díaz, P. Álvarez, A. Echeverria, M. M. Petite, R. Deffley, and J. Ochoa. Effect of in718 recycled powder reuse on properties of parts manufactured by means of selective laser melting. *Physics Procedia*, 56: 99–107, 2014. doi: https://doi.org/10.1016/j.phpro.2014.08.152.

[44] A. Saboori, A. Aversa, F. Bosio, E. Bassini, E. Librera, M. de Chirico, S. Biamino, D. Ugues, P. Fino, and M. Lombardi. An investigation on the effect of powder recycling on the microstructure and mechanical properties of aisi 316l produced by directed energy deposition. *Materials Science and Engineering: A*, 766, 2019. doi: https://doi.org/10.1016/j.msea.2019.138360.

[45] A. Soltani-Tehrani P. E. Carrion, N. Phan, and N. Shamsaei. Powder recycling effects on the tensile and fatigue behavior of additively manufactured ti-6al-4v parts. *JOM*, 71:963–973, 2019. doi: https://doi.org/10.1007/s11837-018-3248-7.

[46] NFPA 484. Standard for combustible metals. Standard, National Fire Protection Association, 2019.

[47] J. C. L. P. de Melo. Comportamento à fadiga de aço maraging produzido por fabrico aditivo. Master's thesis, Faculty of Engineering of the University of Porto, 2020.

[48] EB Industries. Conduction mode and keyhole mode welding. URL `https://www.ebindustries.com/conduction-mode-and-keyhole-mode-welding/`. [Accessed March 12th, 2021].

[49] A. Angelastro, S. L. Campanelli, and A. D. Ludovico. Characterization of colmonoy 227-f samples obtained by direct laser metal deposition. *Trans Tech Publications Ltd*, 83:842–849, 2010. doi: 10.4028/www.scientific.net/AMR.83-86.842.

[50] P. Jaiswal, J. Patel, and R. Rai. Build orientation optimization for additive manufacturing of functionally graded material objects. *The International Journal of Advanced Manufacturing Technology*, 96:223–235, 2018. doi: https://doi.org/10.1007/s00170-018-1586-9.

[51] C. Li, Z. Y. Liu, X. Y. Fang, and Y. B. Guo. Residual stress in metal additive manufacturing. *Procedia CIRP*, 71:348–353, 2018. doi: https://doi.org/10.1016/j.procir.2018.05.039.

[52] X. Lu, X. Lin, M. Chiumenti, M. Cervera, X. Ji, Y. L. Hu, L. Ma, and W. Huang. Residual stress and distortion of rectangular and s-shaped ti-6al-4v parts by directed energy deposition: Modelling and experimental calibration. *Additive Manufacturing*, 26:166–179, 2019. doi: 10.1016/j.addma.2019.02.001.

[53] L. Li, X. Zhang, W. Cui, F. Liou, W. Deng, and W. Li. Temperature and residual stress distribution of fgm parts by ded process: modeling and experimental validation. *The International Journal of Advanced Manufacturing Technology*, 109: 451–462, 2020. doi: https://doi.org/10.1007/s00170-020-05673-4.

[54] A. S. Wu, D. W. Brown, M. Kumar, G. F. Gallegos, and W. E. King. An experimental investigation into additive manufacturing-induced residual stresses in 316l stainless steel. *Metallurgical and Materials Transactions A*, 45:6260–6270, 2014. doi: 10.1007/s11661-014-2549-x.

[55] P. Mercelis and J. Kruth. Residual stresses in selective laser sintering and selective laser melting. *Rapid Prototyping Journal*, 12(5):254–265, 2006. doi: https://doi.org/10.1108/13552540610707013.

[56] K. Nisbett and R. Budynas. *Shigley's Mechanical Engineering Design, 10th Edition.* McGraw-Hill Education, 2015.

[57] R. I. Stephens, A. Fatemi, R. R. Stephens, and H. O. Fuchs. *Metal Fatigue in Engineering (2nd Edition).* John Wiley Sons, 2001. ISBN 978-0-471-51059-8. URL `https://app.knovel.com/hotlink/toc/id:kpMFEE0008/metal-fatigue-in-engineering/metal-fatigue-in-engineering`.

[58] F. G. Pereira, J. M. Lourenço, R. M. do Nascimento, and N. A. Castro. Fracture behavior and fatigue performance of inconel 625. *Materials Research*, 21, 2018. doi: 10.1590/1980-5373-mr-2017-1089.

[59] J. C. R. Pereira, A. De Jesus, J. Xavier, and A. Fernandes. Ultra low-cycle fatigue behaviour of a structural steel. *Engineering Structures*, 60:214–222, 2014. doi: 10.1016/j.engstruct.2013.12.039.

[60] Q. Wang, M. K. Khan, and C. Bathias. Current understanding of ultra-high cycle fatigue. *Theoretical and Applied Mechanics Letters*, 2(3), 2012. doi: https://doi.org/10.1063/2.1203102.

[61] Y. Lee, J. Pan, R. B. Hathaway, and M. E. Barkey. *Fatigue Testing and Analysis - Theory and Practice.* Elsevier, 2005.

[62] J. W. Gil. Finite element analysis of residual stresses in parts manufactured by laser powder-bed fusion. Master's thesis, Faculty of Engineering of the University of Porto, 2020.

[63] G. Nicoletto. Anisotropic high cycle fatigue behavior of ti–6al–4v obtained by powder bed laser fusion. *International Journal of Fatigue*, 94:255–262, 2017. doi: https://doi.org/10.1016/j.ijfatigue.2016.04.032.

[64] Aerospace materials: past, present and future. In A. P. Mouritz, editor, *Introduction to Aerospace Materials*, pages 15–38. Woodhead Publishing, 2012. doi: https://doi.org/10.1533/9780857095152.15.

[65] Langley Alloys. What is inconel? URL `https://www.langleyalloys.com/en/what-is-inconel/`. [Accessed March 1st, 2021].

[66] Stephen Floreen, Gerhard E. Fuchs, and Walter J. Yang. The metallurgy of alloy 625. *Superalloys*, pages 13–37, 1994. doi: 10.7449/1994/SUPERALLOYS_1994_13_37.

[67] Vani Shankar, K. Bhanu Sankara Rao, and S.L. Mannan. Microstructure and mechanical properties of inconel 625 superalloy. *Journal of Nuclear Materials*, 288(2-3): 222–232, 2001. doi: 10.1016/S0022-3115(00)00723-6.

[68] H. L. Eiselstein and D. J. Tillack. The invention and definition of alloy 625. *Superalloys*, pages 1–14, 1991. doi: 10.7449/1991/SUPERALLOYS_1991_1_14.

[69] Rupert Wickens. Introduction to alloy 625 - part 1, . URL `https://www.lff-group.com/posts/introduction-to-alloy-625-part-1`. [Accessed February 12th, 2021].

[70] Rupert Wickens. Introduction to alloy 625 - part 2, . URL `https://www.lff-group.com/posts/introduction-to-alloy-625-part-2`. [Accessed February 15th, 2021].

[71] L.E. Shoemaker. Alloys 625 and 725: Trends in properties and applications. Superalloys, pages 409–418. Proceedings of the International Symposium on Superalloys and Various Derivatives, 2005. doi: 10.7449/2005/Superalloys_2005_409_418.

[72] P. Petrzak, K. Kowalski, and M. Blicharski. Analysis of phase transformations in inconel 625 alloy during annealing. *Acta Physica Polonica A*, 130:1041–1044, 2016. doi: 10.12693/APhysPolA.130.1041.

[73] J.N. DuPont. Solidification of an alloy 625 weld overlay. *Metallurgical and Materials Transactions A*, 27(11):3612–3620, 1996. doi: https://doi.org/10.1007/BF02595452.

[74] Md Ashabul Anam. *Microstructure and mechanical properties of selective laser melted superalloy inconel 625*. PhD thesis, University of Louisville, 8 2018.

[75] H. Okamoto, M. E. Schlesinger, and E. M. Mueller. *ASM Handbook, Volume 03 - Alloy Phase Diagrams (2016 edition)*. ASM International, 2016. ISBN 978-1-62708-070-5. URL `https://app.knovel.com/hotlink/toc/id:kpASMHVA0B/asm-handbook-volume-03/asm-handbook-volume-03`.

[76] M. J. Cieslak. The welding and solidification metallurgy of alloy 625. *Welding Journal*, 70, 1991.

[77] M. J. Cieslak. The solidification behaviour of an alloy 625/718 variant. Superalloys, pages 71–80. Special emphasis symposium on superalloys 718, 625, and various derivatives, 1991.

[78] Rupert Wickens. Introduction to alloy 625 - part 3, . URL `https://www.lff-group.com/posts/introduction-to-alloy-625-part-3`. [Accessed February 20th, 2021].

[79] U. Heubner and M. Kohler. Effect of carbon content and other variables on yield strength, ductility and creep properties of alloy 625. *Superalloys*, pages 479–488, 1994. doi: 10.7449/1994/SUPERALLOYS_1994_479_488.

[80] L. Jiang, W. Zhang, Z. Xu, H. Huang, X. Ye, B. Leng, L. Yan, Z. Li, and X. Zhou. M2c and m6c carbide precipitation in ni-mo-cr based superalloys containing silicon. *Materials Design*, 112:300–308, 2016. doi: https://doi.org/10.1016/j.matdes.2016.09.075.

[81] M. Sundararaman, P. Mukhopadhyay, and S. Banerjee. Precipitation of the δ-ni$_3$nb phase in two nickel base superalloys. *Materials Design*, 19(3):453–465, 1988. doi: 10.1007/BF02649259.

[82] A. N. M. Tanvir, Md. R. U. Ahsan, C. Ji, W. Hawkins, B. Bates, and D. B. Kim. Heat treatment effects on inconel 625 components fabricated by wire + arc additive manufacturing (waam)—part 1: microstructural characterization. *The International Journal of Advanced Manufacturing Technology*, 103(9):3785–3798, 2019. doi: 10.1007/s00170-019-03828-6.

[83] M. Rombouts, G. Maes, M. Mertens, and W. Hendrix. Laser metal deposition of inconel 625: Microstructure and mechanical properties. *Journal of Laser Applications*, 24(5), 2012. doi: https://doi.org/10.2351/1.4757717.

[84] C. Pleass and S. Jothi. Influence of powder characteristics and additive manufacturing process parameters on the microstructure and mechanical behaviour of inconel 625 fabricated by selective laser melting. *Additive Manufacturing*, 24:419–431, 2018. doi: https://doi.org/10.1016/j.addma.2018.09.023.

[85] B. Dubiel and J. Sieniawski. Precipitates in additively manufactured inconel 625 superalloy. *Materials*, 12(7), 2019. doi: 10.3390/ma12071144.

[86] F. Xu, Y. Lv, Y. Liu, F. Shu, P. He, and B. Xu. Microstructural evolution and mechanical properties of inconel 625 alloy during pulsed plasma arc deposition process. *Journal of Materials Science Technology*, 29(5):480–488, 2013. doi: https://doi.org/10.1016/j.jmst.2013.02.010.

[87] G.P. Dinda, A.K. Dasgupta, and J. Mazumder. Laser aided direct metal deposition of inconel 625 superalloy: Microstructural evolution and thermal stability. *Materials Science and Engineering: A*, 509(1):98–104, 2009. doi: https://doi.org/10.1016/j.msea.2009.01.009.

[88] J. Nguejio, F. Szmytka, S. Hallais, A. Tanguy, S. Nardone, and M. G. Martinez. Comparison of microstructure features and mechanical properties for additive manufactured and wrought nickel alloys 625. *Materials Science and Engineering: A*, 764, 2019. doi: https://doi.org/10.1016/j.msea.2019.138214.

[89] Y. L. Hu, X. Lin, S. Y. Zhang, Y. M. Jiang, X. F. Lu, H. O. Yang, and W. D. Huang. Effect of solution heat treatment on the microstructure and mechanical properties of inconel 625 superalloy fabricated by laser solid forming. *Journal of Alloys and Compounds*, 767:330–344, 2018. doi: https://doi.org/10.1016/j.jallcom.2018.07.087.

[90] G. Marchese, M. Lorusso, S. Parizia, E. Bassini, J. Lee, F. Calignano, D. Manfredi, M. Terner, H. Hong, D. Ugues, M. Lombardi, and S. Biamino. Influence of heat treatments on microstructure evolution and mechanical properties of inconel 625 processed by laser powder bed fusion. *Materials Science and Engineering: A*, 729:64–75, 2018. doi: https://doi.org/10.1016/j.msea.2018.05.044.

[91] G. Marchese, X. G. Colera, F. Calignano, M. Lorusso, S. Biamino, P. Minetola, and D. Manfredi. Characterization and comparison of inconel 625 processed by selective laser melting and laser metal deposition. *Advanced Engineering Materials*, 19(3), 2017. doi: https://doi.org/10.1002/adem.201600635.

[92] S. Li, Q. Wei, Y. Shi, Z. Zhu, and D. Zhang. Microstructure characteristics of inconel 625 superalloy manufactured by selective laser melting. *Journal of Materials Science Technology*, 31(9):946–952, 2015. doi: https://doi.org/10.1016/j.jmst.2014.09.020.

[93] M. R. Stoudt, E. A. Lass, D. S. Ng, M. E. Williams, F. Zhang, C. E. Campbell, G. Lindwall, and L. E. Levine. The influence of annealing temperature and time on the formation of δ-phase in additively-manufactured inconel 625. *Metallurgical and Materials Transactions A*, 49:3028–3037, 2018. doi: https://doi.org/10.1007/s11661-018-4643-y.

[94] G. Lindwall, C. E. Campbell, E. A. Lass, F. Zhang, M. R. Stoudt, A. J. Allen, and L. E. Levine. Simulation of ttt curves for additively manufactured inconel 625. *Metallurgical and Materials Transactions A*, 50:457–467, 2019. doi: https://doi.org/10.1007/s11661-018-4959-7.

[95] M. D. Fullen and J. A. Schneider. Effects of varying heat treatments on the microstructure and mechanical properties of blown powder inconel 625. *JOM*, 71: 1127–1133, 2019. doi: https://doi.org/10.1007/s11837-019-03339-5.

[96] P. Ganesh, R. Kaul, C. P. Paul, P. Tiwari, S. K. Rai, R. C. Prasad, and L. M. Kukreja. Fatigue and fracture toughness characteristics of laser rapid manufactured inconel 625 structures. *Materials Science and Engineering: A*, 527(29):7490–7497, 2010. doi: https://doi.org/10.1016/j.msea.2010.08.034.

[97] S. Sui, J. Chen, E. Fan, H. Yang, X. Lin, and W. Huang. The influence of laves phases on the high-cycle fatigue behavior of laser additive manufactured inconel 718. *Materials Science and Engineering: A*, 695:6–13, 2017. doi: https://doi.org/10.1016/j.msea.2017.03.098.

[98] K. Kim, T. Kang, M. E. Kassner, K. Son, and K. Lee. High-temperature tensile and high cycle fatigue properties of inconel 625 alloy manufactured by laser powder bed fusion. *Additive Manufacturing*, 35, 2020. doi: https://doi.org/10.1016/j.addma.2020.101377.

[99] D. Z. Avery, O. G. Rivera, C. J. T Mason, B. J. Phillips, J. B Jordon, J. Su, N. Hardwick, and P. G. Allison. Fatigue behavior of solid-state additive manufactured inconel 625. *JOM*, 70:2475–2484, 2018. doi: 10.1007/s11837-018-3114-7.

[100] Fraunhofer USA. Nozzle technology, coax12. URL `https://www.cmw.fraunhofer.org/en/expertise/LaserTechnologies/products/coax_12.html`. [Accessed March 28th, 2021].

[101] P. M. B. M. de Sousa. Parametrization study for 316l additive manufacturing using direct energy deposition (ded). Master's thesis, Faculty of Engineering of the University of Porto, 2020.

[102] Fraunhofer IWS. Modular powder nozzle system coaxn. URL `https://www.iws.fraunhofer.de/en/technologyfields/surface_treatment/laser_cladding/system_technology/COAXn.html`. [Accessed March 28th, 2021].

[103] Hitachi High-Tech GlobalTV. What is optical emission spectroscopy (oes)? URL https://www.youtube.com/watch?v=jkyZtuAkVYc&ab_channel=HitachiHigh-TechGlobalTV. [Accessed May 16th, 2021].

[104] Element. Optical emission spectroscopy (oes) analysis, . URL https://www.element.com/materials-testing-services/chemical-analysis-labs/oes-analysis. [Accessed May 16th, 2021].

[105] ImageJ. Image processing and analysis in java. URL https://imagej.nih.gov/ij/. [Accessed May 5th, 2021].

[106] ASTM E8 / E8M-21. Standard test methods for tension testing of metallic materials. Standard, ASTM International, West Conshohocken, PA.

[107] Testing the mechanical, thermal and chemical properties of adhesives for marine environments. In J. R. Weitzenböck, editor, *Adhesives in Marine Engineering*, pages 99–154. Woodhead Publishing, 2012. doi: https://doi.org/10.1533/9780857096159.2.99.

[108] Beam Guru. Beam calculator online. URL https://beamguru.com/online/beam-calculator/. [Accessed April 2nd, 2021].

[109] Ramada Aços. Pm300, . URL https://www.ramada.pt/pt/produtos/acos/aa-os-de-construa-ao-ligados/pm300-.html. [Accessed April 20th, 2021].

[110] Fuller fasteners. Torque information. URL https://fullerfasteners.com/tech/torque-information/. [Accessed March 30th, 2021].

[111] Roymech. Bolt loading notes. URL https://roymech.org/Useful_Tables/Screws/Preloading.html. [Accessed April 6th, 2021].

[112] Element. Scanning electron microscopy (sem) with edx analysis, . URL https://www.element.com/materials-testing-services/scanning-electron-microscopy-sem. [Accessed May 1st, 2021].

[113] C. Bandara, S. Siriwardane, U. Dissanayake, and R. Dissanayake. Full range s–n curves for fatigue life evaluation of steels using hardness measurements. *International Journal of Fatigue*, 82:325–331, 2016. doi: https://doi.org/10.1016/j.ijfatigue.2015.03.021.

[114] M. L. Roessle and A. Fatemi. Strain-controlled fatigue properties of steels and some simple approximations. *International Journal of Fatigue*, 22(6):495–511, 2000. doi: https://doi.org/10.1016/S0142-1123(00)00026-8.

[115] S. Sharifimehr and A. Fatemi. Evaluation of estimation methods for shear fatigue properties and correlations with uniaxial fatigue properties for steels and titanium alloys. *MATEC Web Conf.*, 165, 2018. doi: 10.1051/matecconf/201816516012.

[116] J. Li, Z. Zhang, Q. Sun, C. Li, and R. Li. A modified method to estimate fatigue parameters of wrought aluminum alloys. *Journal of Materials Engineering and Performance*, 20:1323–1329, 2010. doi: 10.1007/s11665-010-9765-3.

[117] H. Xin, J.A.F.O. Correia, M. Veljkovic, F. Berto, and L. Manuel. Residual stress effects on fatigue life prediction using hardness measurements for butt-welded joints made of high strength steels. *International Journal of Fatigue*, 147, 2021. doi: https://doi.org/10.1016/j.ijfatigue.2021.106175.

[118] P. Strzelecki and T. Tomaszewski. Analytical models of the s-n curve based on the hardness of the material. *Procedia Structural Integrity*, 5:832–839, 2017. doi: 10.1016/j.prostr.2017.07.065.

[119] M. Fujishimaa, Y. Oda, R. Ashida, K. Takezawa, and M. Kondoa. Study on factors for pores and cladding shape in the deposition processes of inconel 625 by the directed energy deposition (ded) method. *CIRP Journal of Manufacturing Science and Technology*, 19:200–204, 2017. doi: https://doi.org/10.1016/j.cirpj.2017.04.003.

[120] P. Wang, B. Zhang, C. C. Tan, S. Raghavan, Y. Lima, C. Sun, J. Wei, and D. Chi. Microstructural characteristics and mechanical properties of carbon nanotube reinforced inconel 625 parts fabricated by selective laser melting. *CIRP Journal of Manufacturing Science and Technology*, 112:290–299, 2016. doi: https://doi.org/10.1016/j.matdes.2016.09.080.

[121] sij Group. Simold 2311 steel. URL `https://steelselector.sij.si/steels/UTOPNEX.html`. [Accessed April 17th, 2021].

[122] Ramada Aços. 2311, . URL `https://www.ramada.pt/pt/produtos/acos/aa-os-de-construa-ao-ligados/2311-.html`. [Accessed April 17th, 2021].

[123] I. Koutiri, E. Pessard, P. Peyre, O. Amlou, and T. De Terris. Influence of slm process parameters on the surface finish, porosity rate and fatigue behavior of as-built inconel 625 parts. *Journal of Materials Processing Technology*, 255:536–546, 2018. doi: https://doi.org/10.1016/j.jmatprotec.2017.12.043.

[124] D. Celli, M. H. Shen, T. George, O. Scott-Emuakpor, and C. Holycross. Development of a fatigue damage and lifing assessment method for inconel 625 and aluminum 6061-t6. Turbo Expo: Power for Land, Sea, and Air, 2017. doi: 10.1115/GT2017-63775.

[125] A. E. Abela. High cycle fatigue of additively manufactured inconel 625. Master's thesis, Georgia Institute of Technology, 2020.

[126] J.-R. Poulin, A. Kreitcberg, P. Terriault, and V. Brailovski. Fatigue strength prediction of laser powder bed fusion processed inconel 625 specimens with intentionally-seeded porosity: Feasibility study. *International Journal of Fatigue*, 132, 2020. doi: https://doi.org/10.1016/j.ijfatigue.2019.105394.

[127] M. Horstmann, N. Kashaev, V. Ventzke, S. Riekehr, and N. Huber. Comparative study of mechanical properties using standard and micro-specimens of base materials inconel 625, inconel 718 and ti-6al-4v. *Journal of Materials Research and Technology*, 2:43 – 47, 2013. doi: 10.1016/j.jmrt.2013.03.003.

[128] S. Lu, Y. Su, M. Yang, and Y. Li. A modified walker model dealing with mean stress effect in fatigue life prediction for aeroengine disks. *Mathematical Problems in Engineering*, 2018, 2018. doi: 10.1155/2018/5148278.

[129] *Eurocode 3: Design of steel structures - Part 1-9: Fatigue*. BSI, London, 2005. URL `https://www.academia.edu/30074852/Eurocode_3_Design_of_steel_structures_Part_1-9_Fatigue_Incorporating_Corrigenda_Nos._1_and_2`.

[130] A. Trochidis, E. Douka, and B. Polyzos. Formation and evolution of persistent slip bands in metals. *Journal of the Mechanics and Physics of Solids*, 48:1761–1775, 2000. doi: https://doi.org/10.1016/S0022-5096(99)00077-0.

[131] Tec-Eurolab. Striations or beachmarks? URL https://www.tec-eurolab.com/eu-en/striations-or-beachmarks.aspx. [Accessed June 14th, 2021].

[132] Corrosionpedia. Beach marks. URL https://www.corrosionpedia.com/definition/146/beach-marks. [Accessed June 15th, 2021].

[133] Z. Lopez and A. Fatemi. A method of predicting cyclic stress-strain curve from tensile properties for steels. *Materials Science and Engineering A*, 556:540–550, 2012. doi: https://doi.org/10.1016/j.msea.2012.07.024.

[134] M. A. Meggiolaro and J. T. P. Castro. Statistical evaluation of strain-life fatigue crack initiation predictions. *International Journal of Fatigue*, 26:463–476, 2004. doi: https://doi.org/10.1016/j.ijfatigue.2003.10.003.

Appendix A

Miniature Specimen

This appendix presents the technical drawing of the adopted miniature specimens for this work. The drawing is presented in Figure A.1.

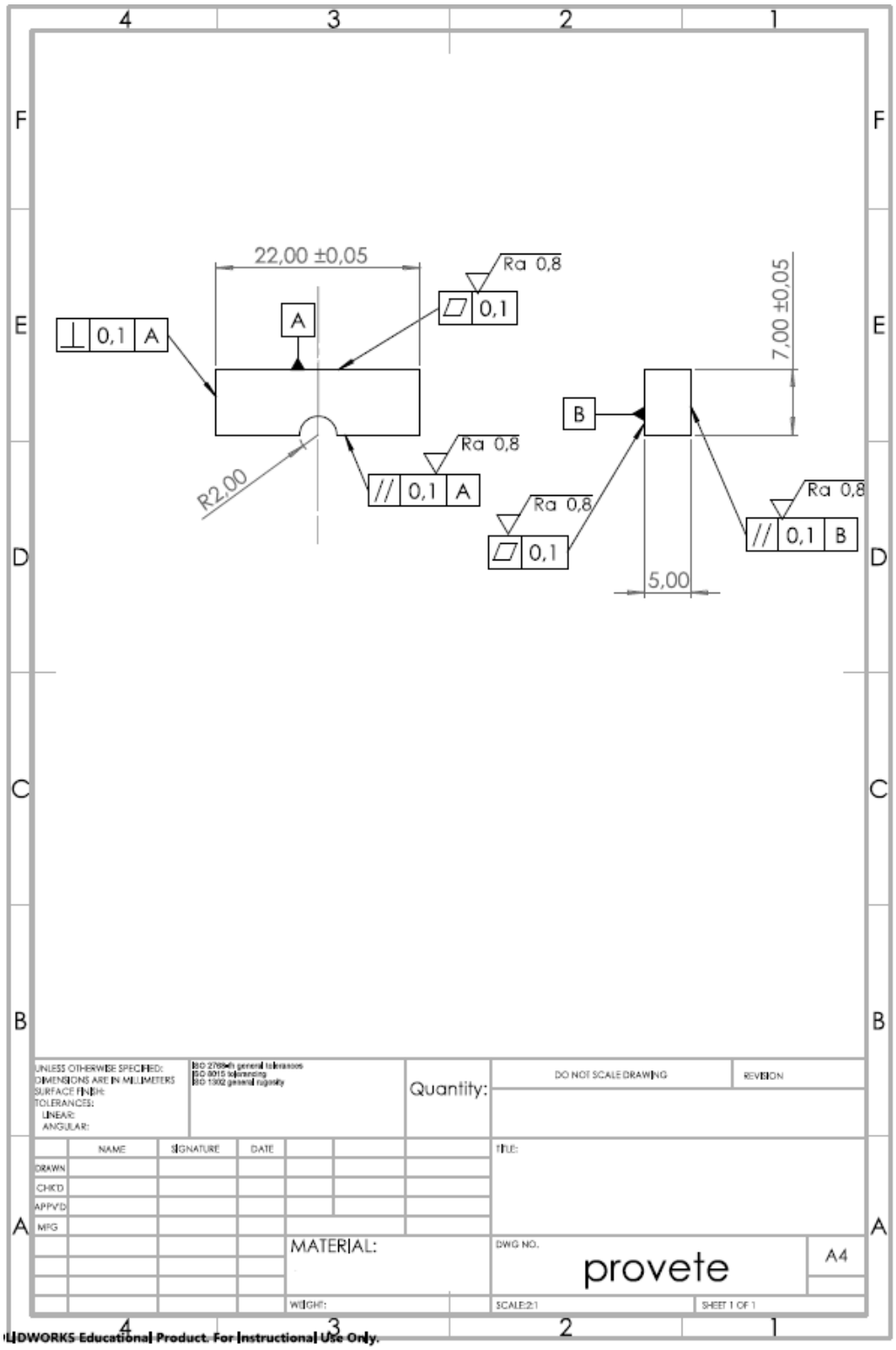

Figure A.1: Miniature specimen with dimensions in mm

Appendix B

Tensile specimen

This appendix presents the technical drawing of the adopted tensile specimens for this work. The drawing is presented in Figure B.1.

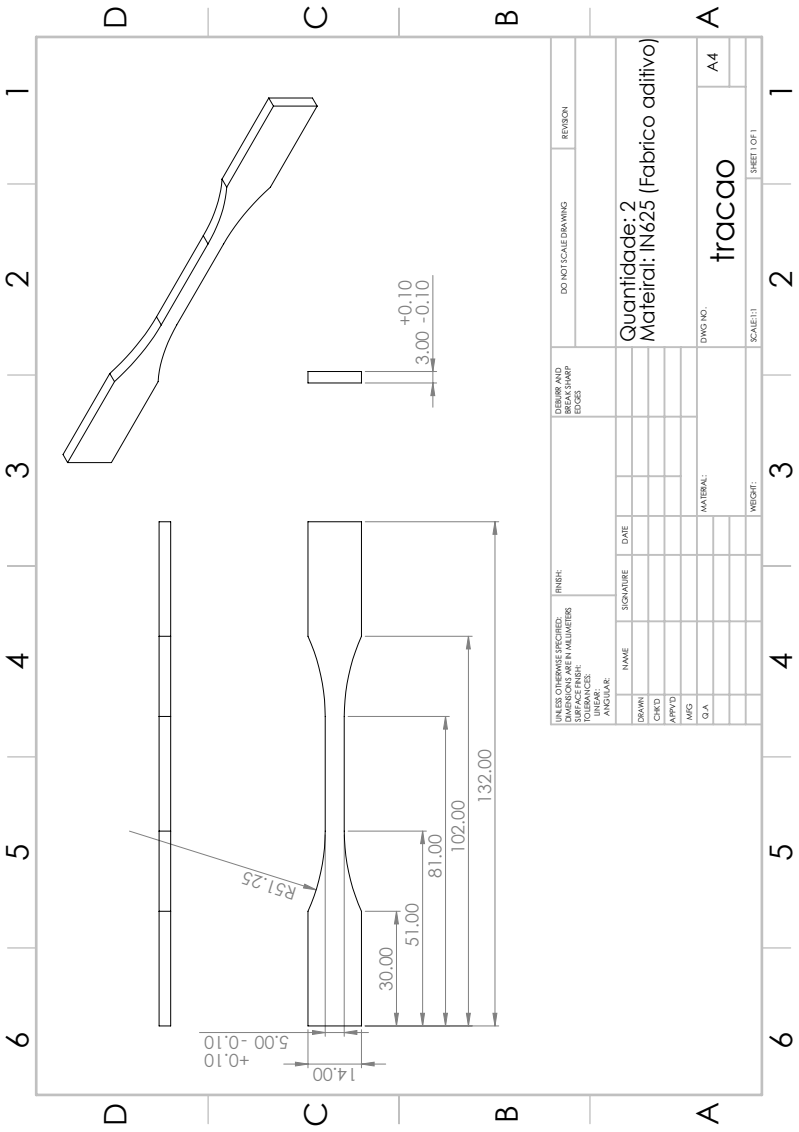

Figure B.1: Tensile specimen with dimensions in mm.